Mathematical modelling of groundwater flow beneath the Antarctic Ice Sheet



Gabriel Cairns
Lady Margaret Hall
University of Oxford

A thesis submitted for the degree of
Doctor of Philosophy

Trinity 2026

Acknowledgements

I am very thankful to Prof. Ian Hewitt and Prof. Graham Benham for much valuable support, guidance and encouragement as my supervisors. I also thank the Engineering and Physical Sciences Research Council (EPSRC) for providing the funding to carry out this project.

I am also thankful to my colleagues, in particular my office mates and the Icy Maths group, for many helpful and enjoyable discussions. Finally, thank you to the many family and friends who have supported me in numerous ways throughout this DPhil.

Declaration of Authorship

I, Gabriel Cairns, declare that the work presented in this thesis is my own, performed under the supervision of Professor Ian Hewitt and Professor Graham Benham. I hereby certify that all material obtained from published or unpublished sources of any type have been fully acknowledged at the proper point in the text and included in the list of references or in this declaration.

Much of the work in Chapter 3 is adapted from our work published in *The Cryosphere* in the paper *'Groundwater dynamics beneath a marine ice sheet'* (Cairns et al., 2025).

Declaration of generative AI use

I confirm that I have read the University and MPLS Division guidance on generative AI and have complied with it in preparing this thesis.

I have not used generative AI to generate mathematical content, code, figures, text, or any substantive part of the argument.

I used standard local software tools for spelling, grammar, LaTeX syntax checking, reference formatting, and code diagnostics. These tools made only local corrections and did not generate or alter substantive mathematical content. I have not directly used any output from a generative AI system.

Abstract

Sedimentary basins are large rock aquifers that lie underneath much of Antarctica, including many of its fastest-flowing glaciers. It is thought that sedimentary basins could influence ice dynamics by exchanging groundwater with a 'subglacial hydrological system' consisting of water stored at the ice-bed interface, which modulates the sliding of many Antarctic glaciers, and by modifying geothermal heat flux to the ice bed. However, little is currently known about the factors controlling discharge ('exfiltration') and recharge ('infiltration') of Antarctic groundwater, the size of these fluxes, or the implications for ice dynamics. In this thesis, I seek to investigate the dynamics of groundwater in Antarctic sedimentary basins using mathematical modelling.

I first estimate the permeability of an Antarctic sedimentary basin by modelling seawater intrusion into the basin, and comparing the results to field observations. I next couple the groundwater flow model to idealised models of a subglacial hydrological system and an ice sheet, finding that groundwater exfiltration and infiltration locally promote and hinder ice sliding respectively, and that feedbacks associated with groundwater can slow the rate of ongoing ice sheet advance and retreat. Finally, by modelling the effect of groundwater flow on heat transport beneath the ice, I estimate how groundwater flow could modify geothermal heat flux across Antarctica, and identify potential positive feedbacks, wherein groundwater flow enhances geothermal heat flux beneath where the ice is flowing fastest or thinning most rapidly.

The results of this thesis highlight the potential importance of sedimentary basins for the Antarctic ice sheet, shed light on some of the associated feedbacks, and give insight into the future work needed to better understand the significance of Antarctic sedimentary basins.

Contents

1 Introduction and literature review **1**

1.1 Introduction 1

1.2 Literature review 2

1.2.1 Antarctic Ice Sheet dynamics 2

1.2.2 Groundwater flow in Antarctic sedimentary basins 3

1.2.3 Modelling of subglacial groundwater 5

1.2.3.1 Groundwater approaches to subglacial hydrology . . 5

1.2.3.2 Groundwater and palaeo-ice sheets 7

1.2.3.3 Recent modelling of Antarctic sedimentary basins . . 7

1.2.4 Summary 9

2 Depth-integrated models of groundwater flow and ice sheets **11**

2.1 The groundwater flow equation 11

2.2 The Dupuit approximation 17

2.2.1 Short-time solution 21

2.3 Saltwater intrusion 22

2.4 Heterogeneity and anisotropy 25

2.5 The shallow-shelf approximation (SSA) ice sheet model 27

3 Seawater intrusion beneath a marine ice sheet **34**

3.1 Introduction 34

3.2 Model design 35

3.2.1 Governing equations 35

3.2.2 Non-dimensionalisation 39

3.2.3 Ice sheet forcing 41

3.3 Solutions in an idealised aquifer geometry 42

3.3.1 Steady states 42

3.3.2 Periodic forcing 44

3.4 Solutions in a non-uniform aquifer geometry 48
3.4.1 "Pocket" steady states 48
3.4.2 Stability of pocket steady states 50
3.4.3 Pocket creation by grounding line advance 52
3.5 Application: Ross Sea, West Antarctica 54
3.5.1 Design 54
3.5.2 Aquifer geometry 55
3.5.3 Grounding line and ice sheet model 55
3.5.4 Aquifer properties and timescales 56
3.5.5 Results 57
3.5.6 Effect of heterogeneity 62
3.6 Discussion 64
3.7 Conclusions 68

4 A coupled model of ice streams, subglacial hydrology and sedimentary basins 70
4.1 Introduction 70
4.2 Model development 71
4.2.1 Ice sheet 73
4.2.2 Subglacial hydrological system 74
4.2.3 Sedimentary basin 76
4.2.4 Non-dimensionalisation 77
4.3 Steady ice sheet with weak groundwater flow 82
4.3.1 Ice sheet and effective pressure for weak groundwater flow . . 83
4.3.2 Streamlines of groundwater flow 85
4.4 Steady ice sheet with strong groundwater flow 86
4.4.1 Low-moderate melt rate 87
4.4.2 High melt rate 88
4.4.3 Effects of sedimentary basin geometry 91
4.5 Groundwater feedback during grounding line motion 92
4.6 Discussion 98
4.7 Conclusions 101

5 Modification of Antarctic geothermal heat flux by groundwater flow 102
5.1 Introduction . . . 102
5.2 Model . . . 105
5.2.1 Governing equations . . . 105
5.2.2 Non-dimensionalisation . . . 109
5.3 Example solution for a synthetic geometry in 2D . . . 111
5.3.1 Additional example . . . 113
5.4 Asymptotic solution for small Péclet number . . . 115
5.4.1 Additional example . . . 118
5.5 Application to Antarctic data . . . 119
5.5.1 Heat flux modification . . . 119
5.5.2 Basal melt modification correlates with exfiltration . . . 125
5.6 Discussion . . . 126

6 Conclusions 130
6.1 Summary . . . 130
6.2 Future work . . . 133
6.3 Concluding remarks . . . 135

A Numerical methods 136
A.1 Saltwater intrusion . . . 136
A.2 Shallow-shelf ice sheet model . . . 137
A.3 Subglacial hydrology model . . . 139
A.4 Heat equation in sedimentary basin . . . 140

Bibliography 141

Chapter 1

Introduction and literature review

1.1 Introduction

The Antarctic Ice Sheet is the largest body of ice on the planet, but is currently losing mass at an accelerating rate (Otosaka et al., 2022). Current mass loss is dominated by Antarctica's fastest-flowing glaciers, known as ice streams (Smith et al., 2020), whose sliding is modulated by a subglacial hydrological system at the ice bed (Engelhardt et al., 1990). This hydrological system is therefore a key source of uncertainty in predicting future sea-level rise due to Antarctic ice loss (Dow et al., 2022; Fricker et al., 2025).

One potentially important component of the subglacial hydrological system is the exchange of groundwater with sedimentary basins. Sedimentary basins underlie large portions of Antarctica, and host substantial volumes of groundwater (Gustafson et al., 2022; Aitken et al., 2023). This groundwater is discharged into, or recharged from, the hydrological system at the base of the ice in a process known as exfiltration (or infiltration when water enters the sedimentary basin), which may contribute significantly to water budgets at the base of ice streams (Christoffersen et al., 2014). However, little is known about the rate of exfiltration or infiltration, its geographical distribution, or its wider consequences for ice dynamics.

In this thesis, I will use mathematical modelling to investigate the role of sedimentary basins in Antarctic subglacial hydrology and their wider implications for ice flow. In the remainder of this chapter I review the existing literature on Antarctic sedimentary basins and the modelling of subglacial groundwater, and in Chapter 2 I derive the general models used throughout the thesis.

In Chapter 3, I aim to estimate the permeability of the sedimentary basin, which determines the size of the exfiltration flux. This is done by modelling the process of seawater intrusion into the sedimentary basin, the results of which can be compared

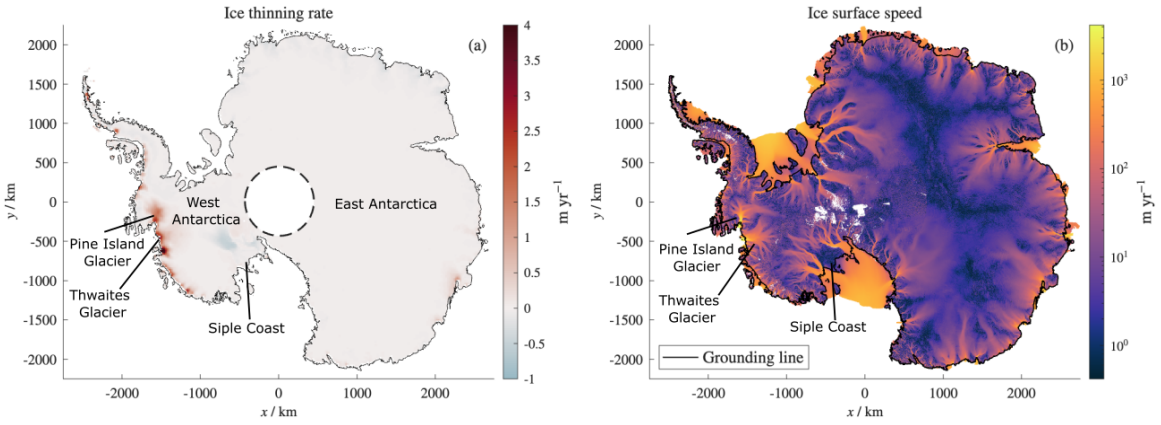


Figure 1.1: (a) Current ice sheet thinning rates (Smith et al., 2020) and (b) ice surface speeds (Mouginot et al., 2017). The former contains a gap around the South Pole denoted with a dashed circle, whereas the latter contains smaller gaps within a similar region, in both cases because the data are obtained via satellite remote sensing whose coverage does not extend to high latitudes. West and East Antarctica are labelled along with selected locations.

to geophysical measurements. This modelling also enables a first prediction of where groundwater is exfiltrated or infiltrates.

In Chapter 4, I investigate the consequences of this exfiltration and infiltration for subglacial hydrology and ice sliding, by coupling the model of groundwater flow to models of the hydrological system and ice sheet. Chapter 5 then considers the effect of groundwater flow on heat transport in the sedimentary basin, with implications for melting at the bed of the ice.

1.2 Literature review

1.2.1 Antarctic Ice Sheet dynamics

The Antarctic Ice Sheet contains more than 27 million km^3 of ice, which would contribute 58 m of sea-level rise if melted in its entirety (Pritchard et al., 2025; Morlighem et al., 2020). Future projections suggest that Antarctica could contribute an estimated 30 cm of sea-level rise by 2100 and up to 6.9 m by 2300 under high-emission climate scenarios (Seroussi et al., 2024). However, significant uncertainty remains in these projections, making the Antarctic Ice Sheet one of the largest sources of uncertainty in future sea-level projections (Arias et al., 2021; Edwards et al., 2021).

Antarctic mass loss is due to an imbalance between ice accumulation via compacting snow and ice sinks such as calving, melting and sublimation. For sea-level rise predictions, the flux of ice across the grounding line, where ice transitions from

a grounded ice sheet to a floating ice shelf, is also of importance, since a mass of floating ice displaces an equal mass of seawater. Both recent (Smith et al., 2020) and projected (Seroussi et al., 2023) mass loss are dominated by marine-terminating glaciers known as ice streams. Ice streams are characterised by ice surface velocities of hundreds to thousands of m yr^{-1}, compared to less than 10 m yr^{-1} over the majority of Antarctica (Mouginot et al., 2017). Figure 1.1 shows current ice thinning rates (Figure 1.1(a)) and ice surface speeds (Figure 1.1(b)). The ice streams are visible as the regions of highly elevated velocity within the grounded portion of Antarctica, many of which flow into ice shelves beyond the grounding line. The ice thinning rate is dominated by these ice streams, and in particular Pine Island and Thwaites glaciers in West Antarctica.

The rapid sliding of ice streams is modulated by a subglacial hydrological system, consisting of pressurised water at the ice-bed interface (Engelhardt et al., 1990). This water can be located in subglacial lakes, conduits or cavities, or in porous sediments known as till (Flowers, 2015). Subglacial till is typically metres to tens of metres thick, and is usually taken to consist of unconsolidated sediments, which are highly deformable as a result. The connection between hydrology and ice stream dynamics has been evidenced through observations of subglacial lakes at the onset of ice streams (Bell et al., 2007) and of subglacial floods linked to ice acceleration (Stearns et al., 2008; Scambos et al., 2011; Siegfried et al., 2016), as well as through modelling of ice flow coupled to hydrology (*e.g.* Bougamont et al., 2011). Accurate modelling of subglacial hydrology and its interaction with the overlying ice is therefore a key challenge in reducing the uncertainty of sea-level rise projections from Antarctica (Dow, 2022; Fricker et al., 2025).

1.2.2 Groundwater flow in Antarctic sedimentary basins

Large regions of the Antarctic ice bed, including the most prominent ice streams, lie above sedimentary basins, consisting of sedimentary rock hundreds to thousands of metres thick (Li et al., 2022; Aitken et al., 2023; Li and Aitken, 2024). A map of estimated sedimentary basin coverage and thickness beneath Antarctica is shown in Figure 1.2. Such sedimentary basins have been identified as a control on ice streaming, because their erosion produces till over which the ice can slide (Bell et al., 1998; Anandakrishnan, 2003; Peters et al., 2006; Bamber et al., 2006; Smith et al., 2013). However, more recently, sedimentary basins have emerged as a possible contributor to subglacial hydrology through the exchange of groundwater with the ice bed (Siegert

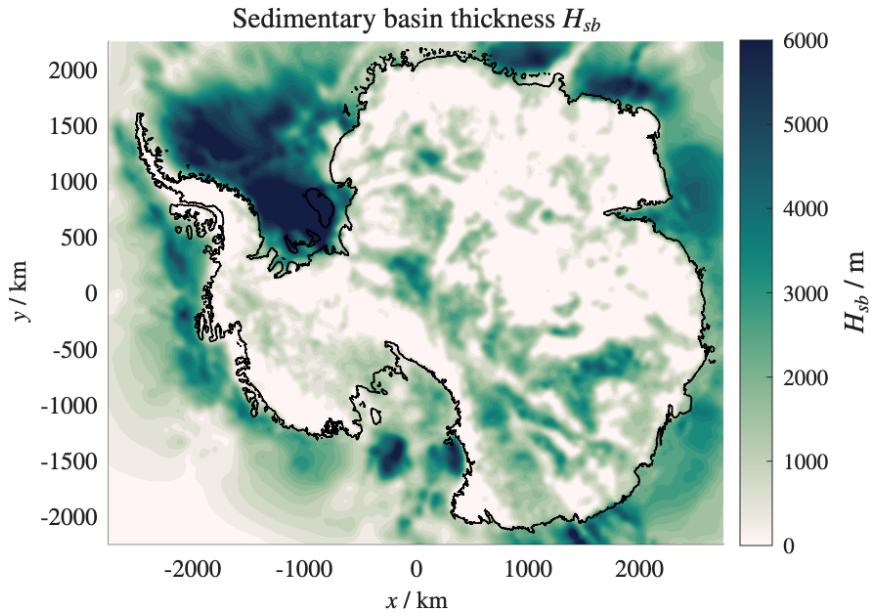


Figure 1.2: Sedimentary basin thickness beneath Antarctica and the surrounding ocean, as estimated by Li and Aitken (2024). The grounding line is denoted in black. The color scale is chosen to saturate at 6 km for visibility.

et al., 2018). Modelling by Christoffersen et al. (2014) suggested that groundwater must contribute substantially to water budgets beneath several Siple Coast ice streams. Using a simple model of groundwater flow, Gooch et al. (2016) estimated that groundwater exfiltration beneath East Antarctica could reach up to 1 mm yr^{-1}, comparable to modelled basal melt rates, which range from millimetres per year to centimetres per year (*e.g.* Seroussi et al., 2019). In addition, these authors postulated that groundwater flow could significantly modify geothermal heat flux to the ice bed by advecting heat.

As a result, several recent studies have used geophysical methods to obtain insight into Antarctic sedimentary basins and the groundwater stored therein. Using magnetotelluric and passive seismic data, Gustafson et al. (2022) obtained the first direct geophysical observations of Antarctic groundwater beneath the Siple Coast in West Antarctica, and in addition inferred an increase in groundwater salinity with depth attributed to seawater intrusion. In the same region, Tankersley et al. (2022) used airborne magnetic data to estimate sedimentary basin thickness and infer the locations of faults. In addition, Zhou et al. (2022) used passive seismics to estimate sedimentary basin thickness across West and Central Antarctica. Li et al. (2022) used machine learning to identify likely regions of sedimentary basin coverage across the whole of Antarctica, and Li and Aitken (2024) used gravity inversion to extend

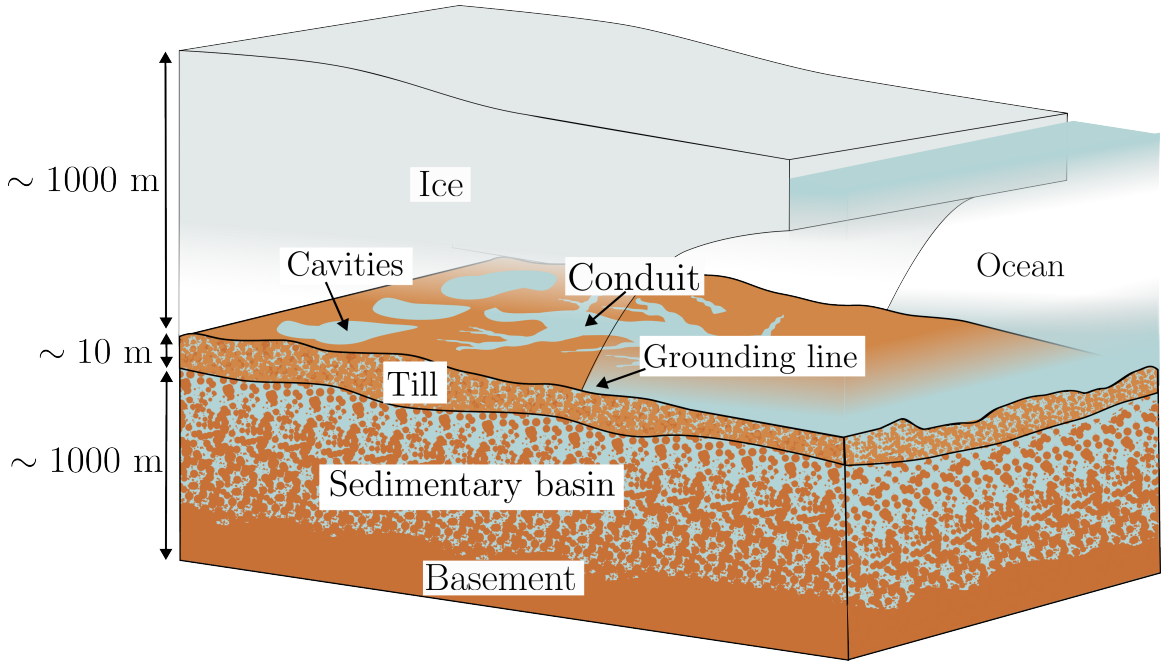


Figure 1.3: Schematic of a marine-terminating glacier and the subglacial hydrological system. Many previous studies have considered water transport in the thin 'shallow' layer of till, conduits and cavities, whereas this thesis considers groundwater flow in the much thicker sedimentary basin.

this to an estimate of sedimentary basin thickness. This estimated thickness is shown in Figure 1.2, and can be seen to reach a kilometre or more beneath large regions of Antarctica, including many ice streams. However, geophysical methods have not to date been able to provide insight into the direction or rate of groundwater flow, or estimate regions of exfiltration and infiltration or the size of such fluxes. This motivates the use of mathematical modelling as an approach to quantify such effects.

1.2.3 Modelling of subglacial groundwater

The mathematical theory of regional groundwater flow modelling is richly developed and wide-ranging (Freeze and Cherry, 1979; Bear, 2013). Here I will review in particular the applications of this theory in subglacial contexts which are relevant to Antarctic subglacial hydrology.

1.2.3.1 Groundwater approaches to subglacial hydrology

The earliest studies of groundwater beneath contemporary ice sheets considered water flow through the relatively thin layer of till beneath the ice (see Figure 1.3). The

till layer is distinct from the sedimentary basin in that a portion of it consists of unconsolidated sediments rather than consolidated rock. Shoemaker (1986) considered till as a route for subglacial water drainage, but concluded that the majority of such drainage would occur through subglacial conduits.

Interest in groundwater flow through till re-emerged with the recognition that water storage in till could affect ice sliding, both by modifying the till strength, and by enabling freeze-on of the till to the ice (Tulaczyk et al., 2000b). To describe the latter, Christoffersen and Tulaczyk (2003a) developed a one-dimensional model of groundwater flow through till including heat transport, and Christoffersen and Tulaczyk (2003b) showed using this model that freeze-on could drive exfiltration from the upper tens of metres of sediment. Several subsequent models of subglacial hydrology have built on this approach to couple groundwater transport in till to basal ice sliding (*e.g.* Bueler and van Pelt, 2015; Gowan et al., 2023).

Porous medium approaches have also been used to model other components of a subglacial hydrological system (Flowers, 2015). For example, so-called cavity-sheet models treat subglacial water as a thin film in an interconnected network of cavities, which is treated as a macroporous medium (*e.g.* Alley, 1996; Creyts and Schoof, 2009; Le Brocq et al., 2009; Kyrke-Smith et al., 2014). A further option is the 'equivalent porous medium' approach, in which all forms of subglacial drainage are modelled as porous media with various hydraulic properties (*e.g.* de Fleurian et al., 2014; Beyer et al., 2018).

While the modelling of till and subglacial hydrology described above bears some physical similarities to the case of an sedimentary basin, there are also significant differences. Firstly, sedimentary basins are much thicker (hundreds to thousands of metres thick) than the till layer, which is tens of metres thick at most. Till is also likely to significantly deform in response to ice sliding and water flow (*e.g.* Tulaczyk et al., 2000a), whereas the sedimentary rock likely only undergoes linear poro-elastic deformations (*e.g.* Neuzil, 2012). Finally, models of subglacial hydrology generally have a water source or sink term due to melting as well as a prescribed overburden pressure from the ice (Flowers, 2015), whereas models of sedimentary basins only have a pressure (and/or vertical stress) imposed by the combined ice and hydrology (Gooch et al., 2016; Li et al., 2022; Robel et al., 2023, *e.g.*).

Most models of subglacial hydrology to date omit a potential groundwater contribution, although some studies have included a subglacial aquifer in models of mountain glacier hydrology (Flowers and Clarke, 2000, 2002b; Flowers, 2008). Notably,

Flowers and Clarke (2002a) identify basal topography as a driver of groundwater discharge and recharge, with recharge generally occurring upstream and discharge near the glacier terminus.

1.2.3.2 Groundwater and palaeo-ice sheets

Several studies have considered the interaction of palaeo-ice sheets with groundwater systems. Early examples argued that meltwater from such ice sheets drained through aquifers, and investigated the geological implications (Boulton and Dobbie, 1993; Boulton et al., 1995; Boulton and Caban, 1995). Fowler and Noon (1999) updated this theory but argued that such drainage was implausible, and a channelised system must form instead. These authors appealed to the fact that the timescales of groundwater flow are likely to be comparable with those of ice sheet growth and retreat, and therefore groundwater flow is unlikely to reach a steady state. Boulton et al. (2007) used a numerical model of groundwater flow to investigate the development of channels during an idealised ice sheet advance.

Several studies in particular have used numerical modelling to investigate the impact of the Laurentide ice sheet on North American groundwater systems during Quaternary glaciations (Person et al., 2007; Bense and Person, 2008; Lemieux et al., 2008c,a; Neuzil, 2012; Person et al., 2012). Lemieux et al. (2008b) obtained an analytical solution for a one-dimensional column undergoing loading at a constant rate, in order to validate the numerical model used in three dimensions.

These numerical solutions, in particular the formulation of the model, are a useful contribution to a framework for modelling Antarctic sedimentary basins. However, the palaeo-ice sheets considered are land-terminating, as opposed to Antarctic ice streams, which are mostly marine-terminating, so that a different set of boundary conditions is required. Moreover, the use of a complex numerical model is better suited to aquifers of Europe and North America, whose properties are well-constrained, than to the Antarctic sedimentary basins, about which relatively little is known.

1.2.3.3 Recent modelling of Antarctic sedimentary basins

Several recent studies consider the particular question of Antarctic sedimentary basins that forms the subject of this thesis. Gooch et al. (2016) conducted two numerical experiments in one vertical dimension. The first, similarly to Lemieux et al. (2008b), considered compaction-driven groundwater flow in response to prescribed ice thickening and thinning, while the second considered the effect of a prescribed groundwater flow on heat transport. Using these models, the authors estimated that groundwater

exfiltration or infiltration could reach 1 mm yr^{-1} and that geothermal heat flux could be modified by tens to hundreds of mW m^{-2}, though their results depended strongly on the permeability of the sedimentary basin.

Li et al. (2022) conducted a numerical experiment considering groundwater flow in one horizontal direction in addition to the vertical, again including compaction. Their setup included an idealised rectangular sedimentary basin, with layers of varying permeability, over which an idealised ice sheet profile advances and retreats. They found that the excess subglacial water flux could reach tens of mm yr^{-1}, and scaled with the rate of ice sheet thinning as well as the sedimentary basin thickness. They also found that groundwater infiltration generally occurred upstream and exfiltration downstream (although aquifer geometry and heterogeneity also played a role), and that groundwater flow during ice sheet retreat could enhance heat flux to the ice bed by up to 5 mW m^{-2} (in supplementary material).

Most recently, Robel et al. (2023) again considered a model of one-dimensional vertical groundwater flow driven by sediment compaction, and recovered the analytical solution of Lemieux et al. (2008b) for the exfiltration (or infiltration) under a constant ice thinning rate, in addition to a new solution for a step change in ice thickness. These solutions assumed that the sedimentary basin is effectively infinite in depth. Using these solutions, the authors estimated exfiltration for current ice sheet thinning rates across Antarctica, and compared this to estimated basal melt rates. The resulting estimated rates could reach tens to hundreds of millimetres per year beneath the fastest thinning parts of the Antarctic Ice Sheet.

A notable source of uncertainty across these models is the sedimentary basin permeability, which could vary across several orders of magnitude: Gooch et al. (2016) used values between 10^{-18} and 10^{-10} m^2 whereas Robel et al. (2023) considered values from 10^{-17} to 10^{-13} m^2. Constraining this permeability is an important step in understanding the role of groundwater beneath Antarctica.

Of the three studies, only Li et al. (2022) included horizontal groundwater flow, but only considered a single sedimentary basin geometry (up to scaling the thickness) and a uniform bed topography, and did not characterise the horizontal groundwater flow in detail. Therefore, a significant gap exists in describing horizontal groundwater flow for a more general set of cases, and the resulting exfiltration and infiltration in the steady state.

Moreover, none of the above studies couple the groundwater flow to a model of subglacial hydrology, instead assuming a layer of water at the ice-bed interface which is held at the pressure imposed by the overlying ice (zero effective pressure). In

reality, a subglacial hydrological system may lead to pressure variations at the ice-bed interface which feed back on the groundwater flow, as well as transporting exfiltrated groundwater and heat downstream.

1.2.4 Summary

Overall, there is a substantial body of evidence suggesting that groundwater flow in Antarctic sedimentary basins could play a significant role in subglacial hydrology, and that ongoing research is required to quantify and characterise this role. This evidence includes geophysical observations of subglacial groundwater (Gustafson et al., 2022), as well as modelling that suggests groundwater exfiltration could contribute substantially to basal water budgets, both by considering the basal water budget (Christoffersen et al., 2014) and from the dynamics of the sedimentary basin itself (Gooch et al., 2016; Li et al., 2022; Robel et al., 2023).

However, despite richly developed theories of several similar topics, the study of modelling groundwater in Antarctic sedimentary basins is in its early stages, with several opportunities for investigation. Analytical solutions are particularly scarce, being limited to the one-dimensional solutions found by Lemieux et al. (2008b) and Robel et al. (2023). However, such approaches could provide more general insights than are offered by specific numerical experiments, especially since parameters such as the permeability and specific storage are highly ill-constrained.

One priority is to characterise the effect of horizontal groundwater flow, and identify the importance of bed topography, sedimentary basin geometry, and ice sheet thickness in driving infiltration and exfiltration. These features can drive groundwater flow in the absence of ice thinning or thickening.

There is also a need to constrain the permeability of Antarctic sedimentary basins (along with other hydraulic properties such as the specific storage), in order to estimate the true scale of groundwater exfiltration. As discussed in Chapter 3, modelling seawater intrusion beneath an Antarctic Ice Sheet and comparing to the results of Gustafson et al. (2022) provides a possible method to estimate this permeability.

Another gap in the literature concerns the coupling of groundwater flow to Antarctic subglacial hydrology. Current models of the latter tend not to consider the former, which could act as an important source or sink of basal water. The reverse coupling also warrants consideration, as subglacial hydrology could modify the water pressure at the ice-bed interface, violating the 'zero effective pressure' condition assumed in existing models. There is therefore scope to investigate how groundwater exfiltration and infiltration impact the distribution of water in the subglacial hydrological system

and vice versa. This can be further extended to explore the effects of exfiltration and infiltration on ice sliding, as I seek to do in Chapter 4.

Finally, there is potential to investigate the effect of groundwater on geothermal heat flux and basal melting, building on the models of Gooch et al. (2016) and Li et al. (2022, supplementary material). I consider this problem in Chapter 5, by finding analytical solutions for the modified heat flux, building horizontal groundwater flow into the model, and estimating the modification heat flux and basal melt rate for current ice sheet thinning rates.

Chapter 2

Depth-integrated models of groundwater flow and ice sheets

2.1 The groundwater flow equation

I begin by deriving from first principles the model of groundwater flow used in this thesis. A more detailed and general derivation of the governing equation is found in Lemieux (2006). In the following derivation, I use a coordinate system (x, y, z, t), where x and y are horizontal, z is vertically upwards, and t is time. I use bold type vectors and the del symbol

$$\nabla = \left(\frac{\partial}{\partial x}, \frac{\partial}{\partial y} \right) \tag{2.1}$$

to refer to horizontal vectors and derivatives (*i.e.* x and y components only), as the models used in this thesis are mostly depth-integrated.

The domain under consideration consists of a sedimentary basin with thickness $H_{sb}(x, y)$ and upper surface at $z = b(x, y)$, so that the domain is $b - H_{sb} < z < b$. The lower surface of the sedimentary basin is considered impermeable, whereas the upper surface is permeable and exchanges water with a thin subglacial hydrological system lying between the sedimentary basin and an overlying ice sheet. The ice sheet and the hydrological system impose dynamic conditions on the water pressure and vertical stress at the top of the sedimentary basin, as detailed below.

A poroelastic medium is considered with porosity $\phi + \phi'(x, y, z, t)$, where dash denotes a linear perturbation about a constant value. The pores are filled with water, which occupies a volume fraction $\phi + \phi'(x, y, z, t)$ and has density $\rho + \rho'(x, y, z, t)$. The water is assumed to be weakly compressible, meaning that the density undergoes small changes in response to changes in the water pressure $p(x, y, z, t)$. The rock matrix occupies a volume fraction $1 - \phi - \phi'$ and has density ρ_r. It is assumed for

simplicity that ρ_r is constant, although the derivation may be generalised to include compressibility of the rock grains (which in reality may be comparable with that of the water). In this case, the resulting equation is the same except that the definitions below of the specific storage and loading efficiency are modified. It is assumed that the sedimentary rock is sufficiently rigid that the weak compressibility of the water produces an effect comparable with the deformation of the porous medium as a whole, although the limit of incompressible water can be straightforwardly recovered (see below).

The solid undergoes a linear elastic displacement (X, Y, Z), and moves with velocity $(U, V, W) = \partial(X, Y, Z)/\partial t$. The fluid moves with a Darcy flux (u, v, w), representing the volume flux of fluid per unit area. The Darcy flux is defined to be relative to the solid matrix, *i.e.* given by

$$(u, v, w) = (\phi + \phi')\big((u_p, v_p, w_p) - (U, V, W)\big) \tag{2.2}$$

where (u_p, v_p, w_p) is the pore-average velocity of the fluid.

The pore-average equation of fluid mass conservation therefore is given in full by

$$\frac{\partial}{\partial t}\left((\rho + \rho')(\phi + \phi')\right) + \nabla \cdot \left((\rho + \rho')(\mathbf{u} + \phi\mathbf{U})\right) + \frac{\partial}{\partial z}\left((\rho + \rho')(w + \phi W)\right) = 0, \tag{2.3}$$

where $\mathbf{u} = (u, v)$ and $\mathbf{U} = (U, V)$. These equations may be linearised in ϕ', ρ', $\mathbf{U}$, W, $\mathbf{u}$ and w around an unperturbed state in which all of these quantities are zero. This assumes not just that the deformation of the porous medium and resulting displacements are small, but also that the pore-average fluid velocity is comparably small, *i.e.* other drivers of groundwater flow produce a flux comparable with that due to poroelastic deformation. (If this is not the case, *i.e.* other drivers of groundwater flow produce a much larger flux than poroelastic deformation, then it suffices to neglect poroelasticity altogether and consider the rigid limit of the model.) Expanding Equation (2.3) gives

$$\frac{\partial \phi'}{\partial t} + \frac{\phi}{\rho}\frac{\partial \rho'}{\partial t} + \nabla \cdot (\mathbf{u} + \phi\mathbf{U}) + \frac{\partial}{\partial z}(w + \phi W) = 0. \tag{2.4}$$

Solid mass conservation is given by

$$\frac{\partial}{\partial t}\left(\rho_r(1 - \phi - \phi')\right) + \nabla \cdot \left(\rho_r(1 - \phi - \phi')\mathbf{U}\right) + \frac{\partial}{\partial z}\left(\rho_r(1 - \phi - \phi')W\right) = 0, \tag{2.5}$$

which linearises to

$$-\frac{\partial \phi'}{\partial t} + \nabla \cdot \left((1 - \phi)\mathbf{U}\right) + \frac{\partial}{\partial z}\left((1 - \phi)W\right) = 0. \tag{2.6}$$

Adding Equations (2.4) and (2.6) gives

$$\frac{\phi}{\rho}\frac{\partial \rho'}{\partial t} + \nabla \cdot \mathbf{U} + \frac{\partial W}{\partial z} + \nabla \cdot \mathbf{u} + \frac{\partial w}{\partial z} = 0. \tag{2.7}$$

The Darcy flux of the fluid is assumed to be given by Darcy's law (Bear, 2013), which states that the flux is proportional to the gradient of the hydraulic head,

$$\mathbf{u} = -\frac{k_{sb}}{\mu}\nabla p, \quad w = -\frac{k_{sb}}{\mu}\left(\frac{\partial p}{\partial z} + \rho g\right), \tag{2.8}$$

where p is the pore pressure, and where the density perturbation $\rho' \ll \rho$ has been neglected in the definition of w. Here μ is the viscosity of water and k_{sb} is the permeability of the sedimentary basin, which depends on properties of the solid matrix such as the grain size and arrangement. The permeability is assumed to be isotropic, though in general k_{sb} may be replaced by a tensor.

A Terzaghi poroelastic constitutive law for incompressible grains is assumed, in which the components of the strain tensor ε_{ij} are related to those of the bulk Cauchy stress tensor σ_{ij} and pore pressure p by (Lemieux, 2006)

$$\varepsilon_{ij} = \frac{1}{2}\left(\frac{\partial X_i}{\partial x_j} + \frac{\partial X_j}{\partial x_i}\right) = \frac{1}{2G}\left(\sigma_{ij} - \frac{\nu}{1+\nu}\mathrm{tr}\boldsymbol{\sigma}\delta_{ij}\right) + \frac{1}{3K}p\delta_{ij}, \tag{2.9}$$

where δ_{ij} is the Kronecker delta. Here K is the bulk modulus of the porous medium, G is the shear modulus, and ν is the undrained Poisson's ratio, which together obey the relation

$$\frac{1}{2G} = \frac{1+\nu}{1-2\nu}\frac{1}{3K}. \tag{2.10}$$

Finally, the weak compressibility of the fluid is expressed as a linear relationship to the pressure,

$$\frac{1}{\rho}\frac{\partial \rho'}{\partial t} = \frac{1}{K_f}\frac{\partial p}{\partial t}, \tag{2.11}$$

where K_f is the fluid compression modulus. Noting that

$$\nabla \cdot \mathbf{U} + \frac{\partial W}{\partial z} = \frac{\partial}{\partial t}\mathrm{tr}\boldsymbol{\varepsilon} = \frac{1}{K}\frac{\partial}{\partial t}\left(\frac{\mathrm{tr}\boldsymbol{\sigma}}{3} + p\right), \tag{2.12}$$

this may be substituted along with Equation (2.11) into Equation (2.7) to obtain

$$\frac{\phi}{K_f}\frac{\partial p}{\partial t} + \frac{1}{K}\frac{\partial}{\partial t}\left(\frac{\mathrm{tr}\boldsymbol{\sigma}}{3} + p\right) + \nabla \cdot \mathbf{u} + \frac{\partial w}{\partial z} = 0. \tag{2.13}$$

The simplifying assumption is now made of uniaxial vertical strain, so that ε_{xx} and ε_{yy} are negligible compared to ε_{zz}. This assumption is reasonable because the

horizontal extent of the ice sheet is much larger than the thickness of the sedimentary basin, meaning that on the scale of the latter the loading stress appears approximately uniform in x and y (Lemieux, 2006). By Equations (2.9) and (2.10), the horizontal strains are zero if

$$\sigma_{xx} = \sigma_{yy} = \frac{\nu}{1-\nu}\sigma_{zz} - \frac{1-2\nu}{1-\nu}p. \tag{2.14}$$

This implies that

$$\frac{\mathrm{tr}\boldsymbol{\sigma}}{3} + p = \frac{1}{3}\frac{1+\nu}{1-\nu}\left(\sigma_{zz} + p\right), \tag{2.15}$$

which may be substituted into Equation (2.13) to give

$$\frac{\phi}{K_f}\frac{\partial p}{\partial t} + \frac{1}{K_e}\frac{\partial}{\partial t}\left(\sigma_{zz} + p\right) + \nabla \cdot \mathbf{u} + \frac{\partial w}{\partial z} = 0, \tag{2.16}$$

where the effective compaction modulus is

$$K_e = 3K\frac{1-\nu}{1+\nu}. \tag{2.17}$$

Equation (2.16) may be written as

$$S_s\frac{\partial p}{\partial t} + \rho g\left(\nabla \cdot \mathbf{u} + \frac{\partial w}{\partial z}\right) = -S_s\xi\frac{\partial \sigma_{zz}}{\partial t}, \tag{2.18}$$

defining the one-dimensional specific storage S_s and one-dimensional loading efficiency ξ as (Lemieux, 2006)

$$S_s = \rho g\left(\frac{1}{K_e} + \frac{\phi}{K_f}\right), \quad \xi = \frac{\frac{1}{K_e}}{\frac{1}{K_e} + \frac{\phi}{K_f}} = \frac{1}{1 + \frac{\phi K_e}{K_f}}. \tag{2.19}$$

The limit of incompressible water is recovered by setting $\xi = 1$, which would be appropriate for a porous medium that deforms much more freely than its constituent phases (such as soil). Measurements of formerly glaciated sedimentary rocks by Neuzil (2012) suggest that values of ξ strictly less than 1 are reasonable, *i.e.* water compressibility is non-negligible. Setting $S_s = 0$ recovers the limit in which both the porous medium and the water are incompressible.

Finally, the vertical loading stress satisfies Cauchy's momentum equation in the porous medium, which reads (ignoring the effect of the small perturbations ρ' and ϕ' at leading order)

$$0 = \frac{\partial \sigma_{zz}}{\partial z} + (\phi\rho + (1-\phi)\rho_r)g. \tag{2.20}$$

The model therefore consists of Equation (2.18), together with the Darcy flux components given by Equation (2.8) and Equation (2.20) for the vertical stress. The

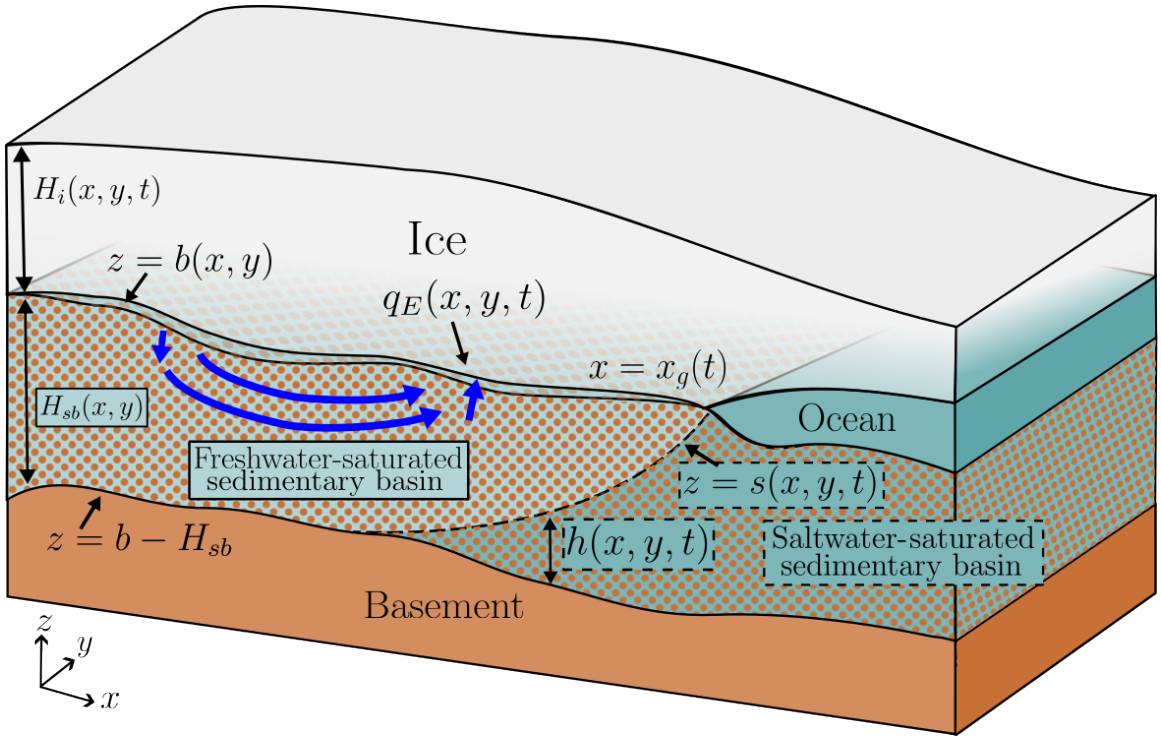


Figure 2.1: Schematic of the model. The sedimentary basin with thickness H_{sb} lies between the ice-bed interface at $z = b$ and an impermeable basement at $z = b - H_{sb}$. An ice sheet of thickness H_i lies on top of a thin layer of pressurised water at $z = b$. The flux of water from the sedimentary basin to the thin layer is denoted by q_E. In Section 2.3 and Chapter 3, the model additionally includes a saltwater-saturated layer with thickness h, with the freshwater-saltwater interface at $z = s = b - H_{sb} + h$.

latter can be substituted in to give the 'groundwater flow equation' (Lemieux, 2006; Li et al., 2022; Robel et al., 2023)

$$S_s \frac{\partial p}{\partial t} = \nabla \cdot \left[\frac{k_{sb}\rho g}{\mu} \nabla p \right] + \frac{\partial}{\partial z} \left[\frac{k_{sb}\rho g}{\mu} \left(\frac{\partial p}{\partial z} + \rho g \right) \right] - S_s \xi \frac{\partial \sigma_{zz}}{\partial t}. \tag{2.21}$$

As described above Equations (2.8), (2.18) and (2.20) are solved in a sedimentary basin occupying $b - H_{sb} < z < b$, where $H_{sb}(x, y)$ is the sedimentary basin thickness and $z = b(x, y)$ is the upper surface, The sedimentary basin is overlain by an ice sheet with thickness H_i, together with a subglacial hydrological system that resides along the interface between the two. The subglacial hydrological system is modelled as a macroporous layer of pressurised water with pressure $p_b(x, y, t)$ (which is taken to be a local-space average over features such as water-filled cavities and conduits). This pressure may be written as

$$p_b = \rho_i g H_i - N, \tag{2.22}$$

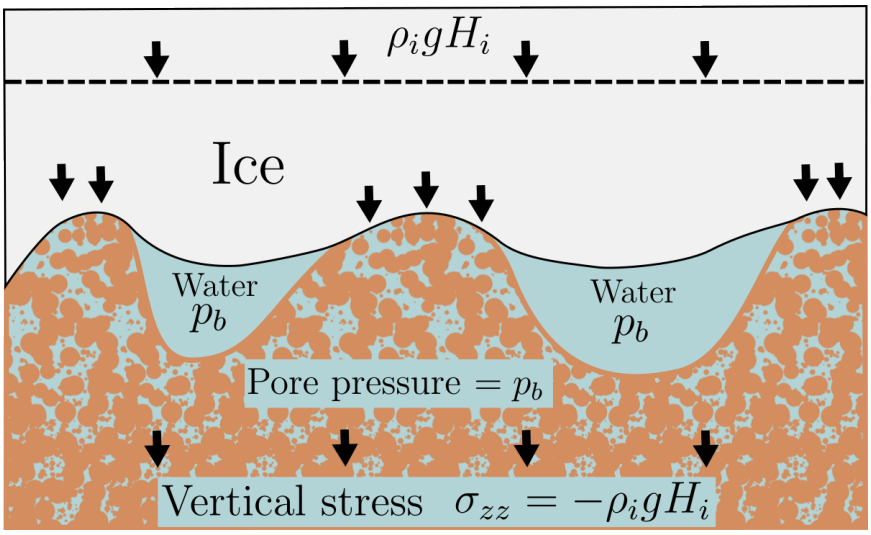


Figure 2.2: Zoomed-in schematic of the ice-bed interface. The ice is supported by protrusions in the bed, with water-filled cavities in between. The water pressure in the cavities p_b is equal to the pore pressure in the sedimentary basin. Averaging in space, the ice imposes an overburden $\rho_i g H_i$, which is transferred to the vertical stress σ_{zz} at the top of the porous medium (also a spatial average).

where ρ_i is the density of ice and N is the 'effective pressure' in the hydrological system, defined as the difference between the overburden imposed by the ice and the water pressure in the subglacial system. The effective pressure is an additional variable that must be determined by an additional model for the subglacial hydrological system (as is done in Chapter 4) or otherwise parameterised (as in Chapters 3 and 5).

At the ice-bed interface, the sedimentary basin supports the weight of the overlying ice (since the regions of the bed between water-filled cavities and conduits are assumed to directly contact the ice), so that

$$\sigma_{zz} = -\rho_i g H_i \quad \text{on} \quad z = b. \tag{2.23}$$

Integrating Equation (2.20) subject to Equation (2.23) gives

$$\sigma_{zz} = -\rho_i g H_i - (\phi\rho + (1-\phi)\rho_r) g (b - z). \tag{2.24}$$

It is assumed that the water in the hydrological system is continuous with that in the sedimentary basin, meaning that continuity of pressure gives

$$p = p_b \quad \text{on} \quad z = b. \tag{2.25}$$

Figure 2.2 shows a zoomed-in schematic of the ice-bed interface.

In addition to the boundary condition (2.25), it is assumed that the bottom of the sedimentary basin is impermeable, so that

$$w - \mathbf{u} \cdot \nabla(b - H_{sb}) = 0 \quad \text{on} \quad z = b - H_{sb}. \tag{2.26}$$

Finally, the exfiltration q_E (or infiltration if $q_E < 0$) is defined to be the normal Darcy flux from the sedimentary basin into the hydrological through $z = b$ (Robel et al., 2023),

$$q_E := \frac{1}{\sqrt{1 + |\nabla b|^2}} \left(w - \mathbf{u} \cdot \nabla b\right)\big|_{z=b}. \tag{2.27}$$

2.2 The Dupuit approximation

The shallow geometry of the sedimentary basin may be exploited in order to facilitate the solution of Equations (2.8) and (2.18). For this purpose, it is useful to non-dimensionalise the model. This is achieved by setting

$$x = [x]\hat{x}, \quad \mathbf{u} = [u]\hat{\mathbf{u}}, \quad p = [p]\hat{p}, \quad \ldots \tag{2.28}$$

where square brackets $[\cdot]$ denote constant scales, and hats denote dimensionless variables. Hats are hereafter dropped from notation.

A natural horizontal lengthscale $[x] = [y]$ is assumed to be provided by the geometry of the sedimentary basin. A vertical lengthscale $[z]$ can also be inferred from the sedimentary basin geometry, or re-used from the ice sheet model (see Section 2.4 below), since typical ice sheet thicknesses are comparable to those of sedimentary basins. Throughout this thesis, the latter is chosen. A timescale $[t]$ is also assumed to be provided, which can also be obtained from the ice sheet model.

The lengthscales are assumed to be such that the aspect ratio is small,

$$\varepsilon = [z]/[x] \ll 1. \tag{2.29}$$

Since Antarctic sedimentary basins are typically hundreds to thousands of kilometres long and wide and hundreds of metres to a few kilometres thick (*e.g.* Li and Aitken, 2024), this is a reasonable assumption. Pressures and stresses are scaled with the hydrostatic scale $[p] = \rho g[z]$, and horizontal Darcy fluxes with $[u] = [v] = k_{sb}[p]/\mu[x]$ motivated by Darcy's law (2.8). The vertical Darcy flux is scaled with $[w] = \varepsilon[u]$, based on Equation (2.18). However, a scale $[q_E]$ for the exfiltration is assumed to be given (*e.g.* by the subglacial melt rate), and the parameter

$$\kappa = \frac{[w]}{[q_E]} \tag{2.30}$$

is defined. The parameter κ is introduced (rather than just scaling q_E with $[w]$, say), as later in this thesis different scales $[q_E]$ will be used depending on the problem under consideration.

Under these scalings, Equation (2.8) becomes

$$\mathbf{u} = -\nabla p, \tag{2.31}$$

$$\varepsilon^2 w = -\left(\frac{\partial p}{\partial z} + 1\right). \tag{2.32}$$

Equation (2.18) becomes

$$\zeta \frac{\partial p}{\partial t} + \nabla \cdot \mathbf{u} + \frac{\partial w}{\partial z} = \zeta \xi (1 - \delta_i) \frac{\partial H_i}{\partial t}, \tag{2.33}$$

where

$$\delta_i = 1 - \frac{\rho_i}{\rho} \approx 0.1, \tag{2.34}$$

and

$$\zeta = \frac{S_s[x][z]}{[t][u]} = \frac{S_s \mu [x]^2}{k_{sb} \rho g [t]}, \tag{2.35}$$

is a parameter representing the relative importance of compaction. This is related to the hydraulic diffusivity $D = k_{sb}\rho g / S_s \mu$ by $\zeta = [x]^2/D[t]$. In order to use the Dupuit approximation, it is required in addition to $\varepsilon \ll 1$ that $\zeta \varepsilon^2 \ll 1$. This condition may fail if k_{sb} is small, or if the ice changes rapidly so that the timescale $[t]$ is short. The corresponding case is discussed below.

After non-dimensionalising, the boundary conditions (2.25) and (2.26) are unchanged from their dimensional form, whereas the definition of q_E becomes at leading order in ε

$$q_E := \kappa \left(w - \mathbf{u} \cdot \nabla b\right)\big|_{z=b}. \tag{2.36}$$

Equation (2.33) may therefore be integrated from $z = b - H_{sb}$ to $z = b$ to obtain

$$q_E := -\kappa \nabla \cdot \left[\int_{b-H_{sb}}^{b} \mathbf{u} \, \mathrm{d}z\right] - \Sigma \int_{b-H_{sb}}^{b} \left(\frac{\partial p}{\partial t} - \xi(1-\delta_i)\frac{\partial H_i}{\partial t}\right) \mathrm{d}z, \tag{2.37}$$

where

$$\Sigma = \zeta \kappa = \frac{S_s [z]^2}{[t][q_E]}. \tag{2.38}$$

The parameters κ and Σ are generally treated in this thesis as $O(1)$ unless stated otherwise, although realistic values range from small to $O(1)$ in both cases. In particular, the values of κ considered in this thesis range from 6×10^{-5} to 6, based on the assumption that permeabilities for coarse-grained sedimentary rocks range from

$k_{sb} = 10^{-17}$–10^{-12} m^2 (Freeze and Cherry, 1979). Realistic values of Σ are considered as ranging from 0.07–70 (although occasionally higher values are used for illustrative purposes), based on measurements of S_s for formerly glaciated aquifers (Neuzil and Provost, 2014) and inferred values for subglacial till (Stone et al., 1997). However, the precise definitions of κ and Σ depend on how the exfiltration scale $[q_E]$ is chosen, as well as the scales $[z]$ and $[t]$, all of which vary from chapter to chapter. Neuzil and Provost (2014) also measure values of ξ ranging from 0.3–1.0, though generally between 0.75–0.95. The value $\xi = 0.8$ is therefore used throughout this thesis.

Since the aspect ratio is small ($\varepsilon \ll 1$), Equation (2.32) implies that the pressure is approximately hydrostatic,

$$\frac{\partial p}{\partial z} + 1 \approx 0, \tag{2.39}$$

so that

$$p \approx p_b + b - z. \tag{2.40}$$

The assumption that the pressure is roughly hydrostatic is commonplace in models of regional groundwater flow, where it is known as the Dupuit approximation (Bear, 2013). Under this approximation, the horizontal Darcy flux is given by Equation (2.31) as

$$\mathbf{u} = -\nabla(p_b + b). \tag{2.41}$$

This enables Equation (2.37) to be simplified,

$$q_E = \kappa \nabla \cdot [H_{sb} \nabla(p_b + b)] - \Sigma H_{sb} \left(\frac{\partial p_b}{\partial t} - \xi(1 - \delta_i) \frac{\partial H_i}{\partial t} \right). \tag{2.42}$$

The vertical Darcy flux may be obtained by integrating Equation (2.33) subject to the boundary condition (2.26),

$$w = (z - b + H_{sb}) \left(\nabla^2(p_b + b) - \zeta \left(\frac{\partial p_b}{\partial t} - \xi(1 - \delta_i) \frac{\partial H_i}{\partial t} \right) \right) - \nabla(p_b + b) \cdot \nabla(b - H_{sb}). \tag{2.43}$$

Throughout this thesis, these equations are often simplified by defining the hydraulic potential,

$$\psi = p_b + b. \tag{2.44}$$

The exfiltration in Equation (2.42) consists of a 'topographic' term (with prefactor κ) and 'compaction' term (with prefactor Σ). The topographic term accounts for changes in the horizontal groundwater flux, which may result from variations in the hydraulic gradient $\nabla(p_b + b)$ or in the sedimentary basin thickness. For example,

if the sedimentary basin becomes narrower in the direction of groundwater flow, the groundwater flux through the sedimentary basin is reduced and water is exfiltrated as a result. Conversely, thickening of the sedimentary basin increases the groundwater flux and drives infiltration of groundwater.

The compaction term accounts for poroelastic deformation of the porous medium. The origin of this term may be understood by rewriting it in terms of the effective pressure N, defined in Equation (2.22), which after non-dimensionalisation (scaling with $[p]$) becomes

$$N = (1 - \delta_i)H_i - p_b. \tag{2.45}$$

The compaction term can then be written as

$$q_{E,c} = \Sigma H_{sb} \left(\xi \frac{\partial N}{\partial t} - (1 - \xi) \frac{\partial p_b}{\partial t} \right). \tag{2.46}$$

The term with prefactor ξ is due to the deformation of the porous medium, being proportional to the rate of change of the 'effective stress' in the the sedimentary basin, which is equal to the rate of change of the effective pressure N at the bed. This term produces exfiltration when the effective pressure increases ($\partial N/\partial t > 0$), as the porous medium contracts, expelling water. The term with prefactor $(1 - \xi)$ is due to weak compressibility of the water. This term produces exfiltration when the pressure decreases, as the water then expands, causing some water to be discharged. Generally in this thesis, the effective pressure is expected to be small compared to $(1 - \xi)$ times the overburden (borehole observations by Engelhardt and Kamb (1997) in West Antarctica found effective pressures $< 2\%$ of the overburden, whereas Neuzil and Provost (2014) measured values of ξ generally between 0.75–0.95 for formerly glaciated aquifers in North America). In this case, the second term dominates, giving

$$q_{E,c} \approx -\Sigma H_{sb}(1 - \xi)(1 - \delta_i) \frac{\partial H_i}{\partial t}. \tag{2.47}$$

This leads to exfiltration when the ice sheet is thinning, and infiltration when the ice sheet is thickening. However, for a strongly deformable porous medium such as unconsolidated till, the loading efficiency ξ would be close to 1, and the effective stress term would dominate instead.

The sizes of the topographic and compaction terms are controlled to a large extent by the permeability k_{sb} of the sedimentary basin and specific storage S_s of the porous medium. These properties are difficult to estimate from direct measurements, although appropriate values can be estimated using values from similar sedimentary aquifers (Gooch et al., 2016; Li et al., 2022; Robel et al., 2023). The size of q_E can

also be estimated from the required groundwater contribution to modelled subglacial water budgets (Christoffersen et al., 2014).

Other than topographic and compaction effects, exfiltration can be driven by other phenomena, such as basal freeze-on of subglacial water (Christoffersen and Tulaczyk, 2003b; Meyer et al., 2018; Gerber et al., 2022). However, detailed modelling of this process is beyond the scope of this thesis.

2.2.1 Short-time solution

As mentioned above, the use of the Dupuit approximation requires that both $\varepsilon \ll 1$ and $\zeta\varepsilon^2 \ll 1$. The latter fails if the hydraulic diffusivity is small, or if the timescales under consideration are short. In terms of the dimensionless variables described above, this failure occurs if Σ/κ is large ($O(\varepsilon^{-2})$). Although it is not the main focus of this work, a brief consideration what happens to the model in this case is included here. This case is investigatied using a rescaled time variable $\tau = t/\zeta\varepsilon^2$. Substituting this timescale into Equation (2.33), along with the Darcy flux components (2.31) and (2.32), gives

$$\frac{\partial p}{\partial \tau} = \varepsilon^2 \nabla^2 p + \frac{\partial^2 p}{\partial z^2} + \xi(1-\delta_i)\frac{\partial H_i}{\partial \tau}, \tag{2.48}$$

solved subject to

$$p = p_b \quad \text{on} \quad z = b, \quad \frac{\partial p}{\partial z} + 1 - \varepsilon^2 \nabla p \cdot \nabla(b - H_{sb}) = 0 \quad \text{on} \quad z = b - H_{sb}. \tag{2.49}$$

Substituting Equations (2.31) and (2.32) into Equation (2.36) for the exfiltration gives

$$q_E = -\frac{\kappa}{\varepsilon^2}\left(\frac{\partial p}{\partial z} + 1 - \varepsilon^2 \nabla p \cdot \nabla b\right)\bigg|_{z=b}. \tag{2.50}$$

Under this rescaling, the horizontal fluxes become negligible due to the prefactor ε^2, and the model used by Robel et al. (2023) is recovered, where the pressure satisfies a forced heat equation in one dimension. In this case, the vertical groundwater flow undergoes a time-dependent response to loading changes. Robel et al. (2023) obtain analytical solutions for p and q_E for the cases of a step change in H_i and for a constant thinning / thickening rate $\partial H_i/\partial\tau$.

In general, the solution of Equation (2.48), after neglecting the small horizontal fluxes, can be analysed using a Laplace transform in time. The transform variable is denoted by s, and overbars denote the Laplace transform. Assuming that at time $\tau = 0$ the basal pressure and ice thickness are $p_{b0}(x)$ and $H_{i0}(x)$, and that the pressure is initially hydrostatic, Equation (2.48) becomes

$$s\bar{p} - (p_{b0} + b - z) = \frac{\partial^2 \bar{p}}{\partial z^2} + \xi(1-\delta_i)(s\bar{H}_i - H_{i0}), \tag{2.51}$$

and Equation (2.50) becomes

$$\bar{q}_E = -\frac{\kappa}{\varepsilon^2}\left(\frac{\partial \bar{p}}{\partial z} + \frac{1}{s}\right)\bigg|_{z=b}. \tag{2.52}$$

The boundary conditions are

$$\bar{p} = \bar{p}_b \quad \text{on} \quad z = b, \quad \frac{\partial \bar{p}}{\partial z} + \frac{1}{s} = 0 \quad \text{on} \quad z = b - H_{sb}. \tag{2.53}$$

Equation (2.51) can be solved to give

$$\bar{p} = \left(\bar{p}_b - \xi(1-\delta_i)\left(\bar{H}_i + \frac{H_{i0}}{s}\right)\right)\frac{\cosh((z-b+H_{sb})\sqrt{s})}{\cosh(H_{sb}\sqrt{s})} + \frac{b-z}{s} + \xi(1-\delta_i)\left(\bar{H}_i - \frac{H_{i0}}{s}\right), \tag{2.54}$$

resulting in the transformed exfiltration

$$\bar{q}_E = -\frac{\kappa}{\varepsilon^2}\left(\bar{p}_b + \frac{p_{b0}}{s} - \xi(1-\delta_i)\left(\bar{H}_i + \frac{H_{i0}}{s}\right)\right)\sqrt{s}\tanh(H_{sb}\sqrt{s}). \tag{2.55}$$

The solution for p and q_E is then given by inversion of the Laplace transform. It can be shown using the final value theorem for the Laplace transform that, in the limit $\tau \to \infty$, this solution tends to the compaction-driven exfiltration found in the Dupuit solution (2.42) above. Namely, it can be found that

$$\lim_{\tau\to\infty} q_E = \lim_{s\to 0} s\bar{q}_E \tag{2.56}$$

$$= -\frac{\kappa}{\varepsilon^2} H_{sb} \lim_{s\to 0}\left(s\bar{p}_b + p_{b0} - \xi(1-\delta_i)\left(s\bar{H}_i + H_{i0}\right)\right). \tag{2.57}$$

$$= -\frac{\kappa}{\varepsilon^2} H_{sb} \lim_{\tau\to\infty}\left(\frac{\partial p_b}{\partial \tau} - \xi(1-\delta_i)\frac{\partial H_i}{\partial \tau}\right) \tag{2.58}$$

$$= \Sigma H_{sb} \lim_{t\to 0}\left(\frac{\partial p_b}{\partial t} - \xi(1-\delta_i)\frac{\partial H_i}{\partial t}\right), \tag{2.59}$$

using the fact that $\tau = t/\zeta\varepsilon^2 = \kappa t/\Sigma\varepsilon^2$. The Dupuit approximation and short-time solution are therefore consistent limiting approximations of the groundwater flow problem.

2.3 Saltwater intrusion

In the previous sections it was assumed that the (unperturbed) density of water ρ is constant. However, in the following chapter, I will model the particular phenomenon of seawater intrusion into the sedimentary basin. For this purpose, it is necessary to

distinguish between freshwater, produced by melting of the ice, with density ρ_f, and saltwater from the ocean, with a higher density ρ_s.

In this model, the sharp-interface approximation is employed, a frequent assumption in saltwater intrusion problems, which asserts that mixing between freshwater and saltwater through molecular diffusion and hydrodynamic dispersion is negligible (Bear, 2013). The aquifer therefore consists of a saltwater-saturated region, whose thickness is denoted by $h(x, y, t)$, underneath a freshwater-saturated region with thickness $H_{sb} - h$. The two are separated by a sharp kinematic interface at $z = s(x, y, t) = b - H_{sb} + h$. This satisfies the condition

$$\phi \frac{\partial s}{\partial t} = w_{\pm} - \mathbf{u}_{\pm} \nabla s \quad \text{on} \quad z = s, \tag{2.60}$$

where the subscript $\pm$ indicates that the Darcy flux components $\mathbf{u}$ and w can be taken on either side of the interface, although they are not continuous across the interface. Equation (2.60) ensures that mass is conserved across the interface.

The sharp-interface approximation is warranted provided that the Péclet numbers associated with molecular diffusion and hydrodynamic dispersion are large (Bear, 2013; Dentz et al., 2006; Koussis and Mazi, 2018). Although a sharp interface is assumed between the two regions, the fluids are miscible, meaning that there is no surface tension between them. The possibility of residual trapping at the pore scale can therefore be ignored (Bear, 2013).

It is possible to adapt the working from the previous section, assuming that the freshwater density is used as the density scale ($\rho = \rho_f$). This introduces an additional dimensionless constant representing the density difference between freshwater and saltwater,

$$\delta_s = \frac{\rho_s - \rho_f}{\rho_f}. \tag{2.61}$$

The water viscosity μ is assumed to be independent of salinity, since the effect of salinity thereupon is relatively small compared to that of the density Bear (2013). It is also assumed for simplicity here that the porous medium is rigid so that the compaction terms and solid displacements are zero. This is consistent provided that the model is applied on a long timescale $[t]$, which leads to a small value of the parameter Σ (see Equation (2.38)). For the purposes of this model, an exfiltration scale is chosen that is comparable with the motion of the saltwater interface,

$$[q_E] = \frac{\phi[z]}{[t]}, \quad \kappa = \frac{k_{sb}\rho_f g[z][t]}{\phi \mu [x]^2}. \tag{2.62}$$

In dimensionless variables, the salinity difference modifies Equation (2.39) to

$$\frac{\partial p}{\partial z} = \begin{cases} -1 & \text{for} \quad s < z < b, \\ -1 - \delta_s & \text{for} \quad b - H_{sb} < z < s. \end{cases} \tag{2.63}$$

As a result, the pressure is given by

$$p = \begin{cases} p_b + b - z & \text{for} \quad s < z < b, \\ p_b + b + \delta_s s - (1 + \delta_s) z & \text{for} \quad b - H_{sb} < z < s, \end{cases} \tag{2.64}$$

using Equation (2.25) and the fact that p must be continuous across the sharp interface. The horizontal Darcy flux is accordingly

$$\mathbf{u} = \begin{cases} -\nabla(p_b + b) & \text{for} \quad s < z < b, \\ -\nabla(p_b + b + \delta_s s) & \text{for} \quad b - H_{sb} < z < s. \end{cases} \tag{2.65}$$

As before, an equation for the exfiltration may be obtained by evaluating the integral in Equation (2.37)

$$q_E = \kappa \nabla \cdot \left[H_{sb} \nabla (p_b + b) + \delta_s h \nabla s \right]. \tag{2.66}$$

To find the location of the freshwater-saltwater interface $z = s(x, y, t)$, the kinematic condition (2.60) is used, which is given by

$$\frac{\partial s}{\partial t} = \kappa (w_\pm - \mathbf{u}_\pm \nabla s) \quad \text{on} \quad z = s. \tag{2.67}$$

Equation (2.33) may then be depth-integrated over the saltwater region, *i.e.* from $z = b - H_{sb}$ to $z = s$, to obtain

$$\frac{\partial s}{\partial t} = \kappa \nabla \cdot \left[h \nabla (p_b + b + \delta_s s) \right]. \tag{2.68}$$

Equation (2.68) holds provided that $b - H_{sb} \leq s < b$. However, it also also possible for the aquifer to become saturated with saltwater throughout its depth, so that $s = b$ (*i.e.* $h = H_{sb}$). In this case, saltwater rather than freshwater is discharged across the upper surface with a flux

$$q_E = \kappa \nabla \cdot \left[H_{sb} \nabla \left(p_b + (1 + \delta_s) b \right) \right]. \tag{2.69}$$

This flux must be non-negative in order to maintain the $s = b$ state; otherwise, freshwater influx will create a freshwater layer.

To account for this case, Equation (2.68) must be replaced by the complementarity problem

$$\begin{aligned} (H_{sb} - h) \left(-\frac{\partial s}{\partial t} + \kappa \nabla \cdot \left[h \nabla \left(p_b + b + \delta_s s \right) \right] \right) &= 0, \\ -\frac{\partial s}{\partial t} + \kappa \nabla \cdot \left[h \nabla \left(p_b + b + \delta_s s \right) \right] &\geq 0, \\ H_{sb} - h &\geq 0. \end{aligned} \tag{2.70}$$

This formulation establishes that either Equation (2.68) applies and $s \leq b$, or $s = b$ and saltwater is discharged according to Equation (2.69).

2.4 Heterogeneity and anisotropy

Throughout the majority of this thesis, the sedimentary basin is treated as homogeneous and isotropic on the grounds that the geological structure of Antarctic sedimentary basins is not well known. However, this assumption is unlikely to be accurate, as sedimentary rocks typically consist of layered strata whose permeabilities vary significantly. In this section, I therefore discuss briefly how the model in this thesis may be generalised to include heterogeneity and anisotropy of the aquifer.

Anisotropy is usually accounted for by replacing the scalar permeability k_{sb} with a permeability tensor in Darcy's law (2.8) (Freeze and Cherry, 1979; Bear, 2013). Assuming that the anisotropy is due to stratification in the vertical direction, this amounts to having distinct horizontal and vertical permeabilities k_{sb}^H and k_{sb}^V, so that (2.8) becomes

$$\mathbf{u} = -\frac{k_{sb}^H}{\mu}\nabla p, \quad w = -\frac{k_{sb}^V}{\mu}\left(\frac{\partial p}{\partial z} + \rho g\right). \tag{2.71}$$

If k_{sb}^H is used as the permeability in the non-dimensionalisation above, then a result of the Dupuit approximation is that k_{sb}^V drops out of the model. This is because the vertical component of Darcy's law (2.8) states that the pressure is approximately hydrostatic, and w is determined instead by mass conservation. However, in order to use the Dupuit approximation, it must be the case that

$$k_{sb}^V / k_{sb}^H \gg \varepsilon^2, \tag{2.72}$$

as otherwise the assumption of near-hydrostatic pressure breaks down (see Equation (2.32)).

Heterogeneity results in variables that are dependent on space rather than constant therein. This section focuses in particular on heterogeneity in the porosity $\phi = \phi(x, y, z)$ and permeability $k = k(x, y, z)$, although a similar treatment can be extended to heterogeneous S_s. Often, the latter inherits heterogeneity from the former, via the prescription of a relation $k = k(\phi)$. The porosity perturbation ϕ' is then taken as a perturbation about the nonuniform steady distribution $\phi(x, y, z)$.

Writing $\phi = \phi_0\hat{\phi}$ and $k_{sb} = k_0\hat{k}$, where ϕ_0 and k_0 are typical scales, these scales can be used in the non-dimensionalisation as before. The horizontal velocity in Equation (2.41) is modified to

$$\mathbf{u} = \hat{k}\nabla(p_b + b). \tag{2.73}$$

Integrating over the depth of the sedimentary basin leads to the exfiltration (originally given by Equation (2.42))

$$q_E = \kappa\nabla\cdot\left[H_{sb}\bar{k}\nabla(p_b+b)\right] - \Sigma H_{sb}\left(\frac{\partial p_b}{\partial t} - \xi(1-\delta_i)\frac{\partial H_i}{\partial t}\right), \tag{2.74}$$

where the depth-averaged permeability is

$$\bar{k}(x,y) = \frac{1}{H_{sb}}\int_{b-H_{sb}}^{b}\hat{k}(x,y,z)\,\mathrm{d}z. \tag{2.75}$$

It can therefore be seen that the shallow geometry of the problem enables vertical heterogeneity to be averaged out, provided the assumptions of the Dupuit approximation remain valid. The thickness H_{sb} is replaced by the 'effective thickness' $\bar{k}H_{sb}$. This means that the horizontal variation in $\bar{k}$ is, within the topographic term, equivalent to variation in H_{sb}, and thus the consideration of the latter in this thesis can be generalised to describe the former.

For the seawater intrusion problem, the exfiltration in Equation (2.66) becomes

$$q_E = \kappa\nabla\cdot\left[\bar{k}H_{sb}\nabla(p_b+b) + \delta_s\bar{k}_h h\nabla s\right], \tag{2.76}$$

and the evolution equation of the interface (2.68) becomes

$$\hat{\phi}\frac{\partial s}{\partial t} = \kappa\nabla\cdot\left[\bar{k}_h h\nabla(p_b+b+\delta_s s)\right], \tag{2.77}$$

where

$$\bar{k}_h = \frac{1}{h}\int_{b-H_{sb}}^{s}\hat{k}\,\mathrm{d}z. \tag{2.78}$$

An example of a heterogeneous ϕ previously used to model sedimentary basins is the so-called Athy profile (Gooch et al., 2016; Gustafson et al., 2022, supplementary material),

$$\phi = \phi_0\exp(-\beta_A(b-z)), \tag{2.79}$$

in which the porosity decays exponentially with depth at a constant rate β_A (Athy, 1930). This can be combined with the frequently-used Kozeny-Carman equation for the permeability (Bear, 2013)

$$k(\phi) = k_0\frac{\phi^3}{1-\phi^2}\left(\frac{\phi_0^3}{1-\phi_0^2}\right)^{-1}, \tag{2.80}$$

where the prefactor is introduced so that $k(\phi_0) = k_0$. (This is chosen by way of example, since for rocks containing a high amount of marine clays, as Antarctic

sedimentary basins are likely to, the Kozeny-Carman law is unsuitable (Revil and Cathles III, 1999).) For these choices, it can be calculated analytically that

$$\bar{k}_h = \frac{1}{\beta_A h}\left(\frac{\phi_0^3}{1-\phi_0^2}\right)^{-1}\big[\tanh^{-1}(\exp(\beta_A(s-b+H_{sb})))\\ -\phi_0(\exp(-\beta_A(b-s))-\exp(-\beta_A H_{sb}))\big], \quad (2.81)$$

and in particular

$$\bar{k} = \frac{1}{\beta_A H_{sb}}\left(\frac{\phi_0^3}{1-\phi_0^2}\right)^{-1}\left[\tanh^{-1}(\exp(\beta_A H_{sb}))-\phi_0(1-\exp(-\beta_A H_{sb}))\right]. \quad (2.82)$$

The Athy profile may be derived by considering a model of non-linear compaction of sediments, in which the porous medium undergoes large deformations in response to loading stress (Audet and Fowler, 1992). Such a model is appropriate for the initial formation of a sedimentary rock from deposited sediments. However, it is assumed that subsequent cementation of the sediments via diagenesis results in a rigid rock, which obeys the poroelastic theory of small deformations used in this chapter.

2.5 The shallow-shelf approximation (SSA) ice sheet model

The overburden p_b on the sedimentary basin is dominated by the ice sheet, which has thickness $H_i(x, y, t)$. It is therefore necessary to select an appropriate model for the ice sheet.

Ice is typically modelled as a highly viscous fluid, which deforms through creep on long timescales, and whose dynamics are governed by the equations of Stokes flow. Often, these equations are simplified by exploiting the fact that the horizontal extent of the ice sheet is much larger than its thickness. Throughout this thesis, I use the shallow-shelf approximation (Muszynski and Birchfield, 1987; MacAyeal, 1989), which is appropriate for rapidly sliding ice such as Antarctic ice streams. An alternative model, the shallow ice approximation, is sometimes used when internal shearing of the ice is more important than basal sliding.

In this section, I describe the derivation of the shallow-shelf model, working initially in dimensional variables. For simplicity, this derivation considers one horizontal dimension (*i.e.* x only, representing distance along an ice flowline), although the derivation may be generalised to include both x and y. The model described in this section and its derivation are standard in the literature, but are included in this thesis for completeness.

The ice is assumed to be an incompressible viscous fluid with horizontal and vertical velocity components u_i and w_i respectively, obeying

$$\frac{\partial u_i}{\partial x} + \frac{\partial w_i}{\partial z} = 0. \tag{2.83}$$

The pressure in the ice is denoted by $p_i(x, z, t)$ and the deviatoric stress tensor by $\boldsymbol{\tau}$, so that the total stress tensor is $\boldsymbol{\sigma} = -p_i\mathbf{I} + \boldsymbol{\tau}$, where $\mathbf{I}$ is the identity matrix.

The deviatoric stress is related to the strain rate tensor,

$$\dot{\boldsymbol{\varepsilon}} = \begin{pmatrix} \dot{\varepsilon}_{xx} & \dot{\varepsilon}_{xz} \\ \dot{\varepsilon}_{xz} & \dot{\varepsilon}_{zz} \end{pmatrix} := \begin{pmatrix} \frac{\partial u_i}{\partial x} & \frac{1}{2}\left(\frac{\partial u_i}{\partial z} + \frac{\partial w_i}{\partial x}\right) \\ \frac{1}{2}\left(\frac{\partial u_i}{\partial z} + \frac{\partial w_i}{\partial x}\right) & \frac{\partial w_i}{\partial z} \end{pmatrix}, \tag{2.84}$$

by a flow law. The most common choice for ice is Glen's law, which takes ice to be a shear-thinning viscous fluid,

$$\dot{\boldsymbol{\varepsilon}} := A\boldsymbol{\tau}|\tau|^{n-1}, \quad |\tau| := \sqrt{\frac{1}{2}(\tau_{xx}^2 + 2\tau_{xz}^2 + \tau_{zz}^2)}, \tag{2.85}$$

where the prefactor A is assumed constant and the exponent is taken as $n = 3$. In reality, A is temperature-dependent, so the value of A taken represents a depth-average. Equations (2.83), (2.84) and (2.85) together imply $\tau_{zz} = -\tau_{xx}$, so that the stress tensor is given by

$$\boldsymbol{\sigma}_i = \begin{pmatrix} -p_i + \tau_{xx} & \tau_{xz} \\ \tau_{xz} & -p_i - \tau_{xx} \end{pmatrix}. \tag{2.86}$$

It is also assumed that the ice undergoes a shallow extensional flow, in which the horizontal lengthscale $[x]$ is much larger than the vertical lengthscale $[z]$, and in which the extensional stress τ_{xx} is much larger than the shear stress τ_{xz} (so that $|\tau| \approx |\tau_{xx}|$). The latter assumption comes from the fact that the grounded ice must transition to an ice shelf, where there is no shear stress applied on either the upper or lower surface, and therefore where extensional stress must dominate. Equation (2.83) then implies that

$$\frac{[w_i]}{[u_i]} \sim \frac{[z]}{[x]} \ll 1. \tag{2.87}$$

The fact that the extensional stresses dominate the shear stresses, $\tau_{xx} \gg \tau_{xz}$, implies the same is true of the strains, $\dot{\varepsilon}_{xx} \gg \dot{\varepsilon}_{xz}$, by Glen's law (2.85). By the definition of the strain rate in Equation (2.84), this further implies $\partial u_i/\partial z$ must be small compared to $\partial u_i/\partial x$, so the velocity $u_i \approx u_i(x, t)$ is roughly uniform in z.

The mass conservation equation (2.83) must be supplemented with boundary conditions. On the upper surface of the ice, a kinematic condition is imposed,

$$\frac{\partial H_i}{\partial t} + u_i\left(\frac{\mathrm{d}b}{\mathrm{d}x} + \frac{\partial H_i}{\partial x}\right) = w_i - a \quad \text{on} \quad z = H_i + b, \tag{2.88}$$

where $a(x,t)$ is the net accumulation, representing the mass added or lost due to the balance of snowfall and ablation. At the ice bed, there is no normal flux of ice

$$w_i - u_i \frac{\mathrm{d}b}{\mathrm{d}x} = 0 \quad \text{on} \quad z = b. \tag{2.89}$$

Using the fact that u_i is uniform in z, integration of Equation (2.83) from $z = b$ to $z = b + H_i$ subject to these conditions gives the mass conservation equation

$$\frac{\partial H_i}{\partial t} + \frac{\partial}{\partial x}\left(H_i u_i\right) = a. \tag{2.90}$$

To determine the ice velocity u_i, a momentum balance must be considered. The viscous flow of the ice at low Reynolds number is described by the equations of Stokes flow under gravity, which are given at leading order by

$$0 = -\frac{\partial p_i}{\partial x} + \frac{\partial \tau_{xx}}{\partial x} + \frac{\partial \tau_{xz}}{\partial z}, \tag{2.91}$$

$$0 = -\frac{\partial p_i}{\partial z} - \frac{\partial \tau_{xx}}{\partial z} - \rho_i g, \tag{2.92}$$

where ρ_i is the density of ice. In the latter the small term $\partial \tau_{xz}/\partial x$ is neglected (on the basis of the scaling arguments above that $\tau_{xz} \ll \tau_{xx}$ and $z \ll x$) and used the fact that $\tau_{zz} = -\tau_{xx}$.

The stress vector acting on a surface is given by $\boldsymbol{\sigma}_i \mathbf{n}$, where $\mathbf{n}$ is a unit normal vector to the surface. On the upper surface $z = H_i + b$, this normal vector is given by

$$\mathbf{n} = \frac{\left(-\left(\frac{\partial H_i}{\partial x} + \frac{\mathrm{d}b}{\mathrm{d}x}\right), 1\right)^{\mathrm{T}}}{\sqrt{1 + \left(\frac{\partial H_i}{\partial x} + \frac{\mathrm{d}b}{\mathrm{d}x}\right)^2}} \approx \left(-\left(\frac{\partial H_i}{\partial x} + \frac{\mathrm{d}b}{\mathrm{d}x}\right), 1\right)^{\mathrm{T}}, \tag{2.93}$$

using the shallow approximation $[z] \ll [x]$ to treat the slope $\partial H_i/\partial x + \partial b/\partial x$ as small. On this surface, a condition of no stress is imposed, so that

$$\mathbf{0} = \boldsymbol{\sigma}_i \mathbf{n} \sim \begin{pmatrix} -\left(\frac{\partial H_i}{\partial x} + \frac{\mathrm{d}b}{\mathrm{d}x}\right)\left(-p_i + \tau_{xx}\right) + \tau_{xz} \\ -p_i - \tau_{xx} \end{pmatrix} \quad \text{on} \quad z = H_i + b, \tag{2.94}$$

using Equations (2.86) and (2.93), and using the relative smallness of $\partial H_i/\partial x + \partial b/\partial x$ and τ_{xz} to neglect the product of these terms.

Using the smallness of the slope as in Equation (2.93), an approximate unit normal and tangent at the ice bed $z = b$ are given by

$$\mathbf{n} \approx \left(-\frac{\mathrm{d}b}{\mathrm{d}x}, 1\right)^{\mathrm{T}}, \quad \mathbf{t} \approx \left(1, \frac{\mathrm{d}b}{\mathrm{d}x}\right)^{\mathrm{T}}, \tag{2.95}$$

The shear stress at the bed of the ice τ_b is therefore given by

$$\tau_b \sim \mathbf{t}^{\mathrm{T}} \boldsymbol{\sigma}_i \mathbf{n} \approx -2\frac{\mathrm{d}b}{\mathrm{d}x}\tau_{xx} + \tau_{xz}, \tag{2.96}$$

again using the relative smallness of $\partial b/\partial x$ and τ_{xz} to neglect the product of these terms. It is assumed that $\tau_b = \tau_b(u_i, N)$ is determined by a so-called sliding law, which may include dependence on the ice velocity and subglacial effective pressure N, and which encapsulates the physics of the ice sliding over the bed (Cuffey and Paterson, 2010). The choice of sliding law is discussed below.

Integrating Equation (2.91) over the depth of the ice and applying the Leibniz integral rule, it is found that

$$\begin{aligned} 0 = \frac{\partial}{\partial x}\left[\int_b^{H_i+b} -p_i + \tau_{xx}\,\mathrm{d}z\right] - \left[\left(\frac{\mathrm{d}b}{\mathrm{d}x} + \frac{\partial H_i}{\partial x}\right)(-p_i + \tau_{xx})\right]\Bigg|_{z=H_i+b} \\ + \left[\frac{\mathrm{d}b}{\mathrm{d}x}(-p_i + \tau_{xx})\right]\Bigg|_{z=b} + \Big[\tau_{xz}\Big]_{z=b}^{H_i+b}. \end{aligned} \tag{2.97}$$

The boundary terms on the upper surface $z = H_i + b$ are zero by the boundary condition (2.94). The boundary terms on the bed $z = b$ can also be simplified using the expression (2.96) for the basal shear stress. This leads to

$$\frac{\partial}{\partial x}\left[\int_b^{H_i+b} -p_i + \tau_{xx}\,\mathrm{d}z\right] - \tau_b - \left[\frac{\mathrm{d}b}{\mathrm{d}x}(p_i + \tau_{xx})\right]\Bigg|_{z=b} = 0. \tag{2.98}$$

It remains to find τ_{xx} and p_i. Integrating the vertical stress balance (2.92) from b to z subject to the boundary condition (2.94) gives

$$p_i + \tau_{xx} = \rho_i g(H_i + b - z). \tag{2.99}$$

Substituting this into Equation (2.98) and evaluating the integral gives

$$\frac{\partial}{\partial x}\left[\int_b^{H_i+b} 2\tau_{xx}\,\mathrm{d}z\right] - \frac{\partial}{\partial x}\left[\frac{1}{2}\rho_i g H_i^2\right] - \tau_b - \rho_i g H_i \frac{\mathrm{d}b}{\mathrm{d}x} = 0. \tag{2.100}$$

Finally, Glen's flow law (2.85) gives the extensional stress as

$$\tau_{xx} = A^{-1/n}\left|\frac{\partial u_i}{\partial x}\right|^{n-1}\frac{\partial u_i}{\partial x}. \tag{2.101}$$

Substituting this into Equation (2.100) leads to the final momentum equation

$$\frac{\partial}{\partial x}\left[2A^{-1/n}H_i\left|\frac{\partial u_i}{\partial x}\right|^{1/n-1}\frac{\partial u_i}{\partial x}\right] - \tau_b - \rho_i g H_i \frac{\partial}{\partial x}(H_i + b) = 0. \tag{2.102}$$

The shallow-shelf approximation model consists of Equations (2.90) and (2.102), together with appropriate boundary conditions. It is also necessary to prescribe the sliding law τ_b. The simplest case is the so-called Weertman sliding law (Weertman, 1957; Fowler, 1981)

$$\tau_b = C_W |u_i|^{m_W - 1} u_i, \tag{2.103}$$

where C_W is a constant, and the exponent is taken as $m_W = 1/3$. Equation (2.103) is obtained by assuming that ice moves around obstacles via either regelation (melting and re-freezing) or viscous creep, and using a scaling argument to obtain a relationship between the sliding velocity and shear stress. Other sliding laws account for cavitation, the formation of water-filled pockets between the ice and the bed. Such laws are discussed in Chapter 4.

Equations (2.90) and (2.102) are typically solved in a domain $0 < x < x_g$, where $x = 0$ is the ice divide, and where $x = x_g$ represents the grounding line at which the ice transitions to a floating ice shelf. At the ice divide, zero ice flux is imposed *i.e.*

$$u_i = 0 \quad \text{at} \quad x = 0. \tag{2.104}$$

At the grounding line, the thickness of the ice must be such as to achieve flotation by Archimedes' principle,

$$\rho_i H_i = -\rho b \quad \text{at} \quad x = x_g. \tag{2.105}$$

taking $z = 0$ as sea level. If the grounding line is taken as a free boundary, an additional condition is required, which takes the form of a stress condition (Schoof, 2007a)

$$2A^{-1/n} H_i \left| \frac{\partial u_i}{\partial x} \right|^{1/n-1} \frac{\partial u_i}{\partial x} - \frac{1}{2} \rho_i g \left(1 - \frac{\rho_i}{\rho} \right) {H_i}^2 = 0 \quad \text{at} \quad x = x_g, \tag{2.106}$$

which represents the balance between extensional and driving stresses that must hold in the ice shelf.

More precisely, if the ice shelf occupies $x_g < x < x_t$, then the momentum balance is the same as for the grounded portion, except that the basal shear stress τ_b is zero, and the lower surface of the ice is at $b = -(\rho_i/\rho_w) H_i$, assuming the ice is at flotation throughout. Therefore, the momentum balance in the shelf is given by

$$\frac{\partial}{\partial x} \left[2A^{-1/n} H_i \left| \frac{\partial u_i}{\partial x} \right|^{1/n-1} \frac{\partial u_i}{\partial x} \right] - \rho_i \left(1 - \frac{\rho_i}{\rho} \right) g H_i \frac{\partial H_i}{\partial x} = 0 \quad \text{for} \quad x_g < x < x_t. \tag{2.107}$$

At the terminus, the extensional stress in the ice must be balanced by the water pressure from the ocean,

$$\int_{-(\rho_i/\rho)H_i}^{(1-\rho_i/\rho)H_i} -p_i + \tau_{xx}\,\mathrm{d}z = \int_{-(\rho_i/\rho)H_i}^{0} \rho g z\,\mathrm{d}z \quad \text{at} \quad x = x_t. \tag{2.108}$$

Using Equation (2.99) to eliminate p_i as before and using Equation (2.101) for the strain rate, evaluation of these integrals gives

$$2A^{-1/n}H_i\left|\frac{\partial u_i}{\partial x}\right|^{1/n-1}\frac{\partial u_i}{\partial x} - \frac{1}{2}\rho_i g {H_i}^2 = -\frac{1}{2}g\frac{\rho_i^2}{\rho}{H_i}^2 \quad \text{at} \quad x = x_t. \tag{2.109}$$

Finally, integrating Equation (2.107) subject to Equation (2.109) implies that the balance in Equation (2.109) holds throughout the ice shelf, hence Equation (2.106) (Schoof, 2007a).

Given the choice of a sliding law (2.103), the shallow-shelf model may be non-dimensionalised, by assuming a horizontal lengthscale $[x]$ and accumulation scale $[a]$ are provided. A vertical lengthscale $[z]$ and velocity scale $[u_i]$ are then found by solving (motivated by Equations (2.90) and (2.102))

$$[z][u_i] = [a][x], \quad C_W[u_i]^m = \rho_i g[z]^2/[x]. \tag{2.110}$$

The timescale is then given by

$$[t] = [x]/[u_i] = [z]/[a]. \tag{2.111}$$

Applying these scalings, the dimensionless problem reads

$$\frac{\partial H_i}{\partial t} + \frac{\partial}{\partial x}\left(H_i u_i\right) = a, \tag{2.112}$$

$$4\varepsilon_i\frac{\partial}{\partial x}\left[H_i\left|\frac{\partial u_i}{\partial x}\right|^{1/n-1}\frac{\partial u_i}{\partial x}\right] - |u_i|^{m_W-1}u_i - H_i\frac{\partial}{\partial x}\left(H_i + b\right) = 0, \tag{2.113}$$

with boundary conditions

$$u_i = 0 \quad \text{at} \quad x = 0, \tag{2.114}$$

$$H_i = -\frac{b}{1-\delta_i} \quad \text{at} \quad x = x_g, \tag{2.115}$$

$$4\varepsilon_i H_i\left|\frac{\partial u_i}{\partial x}\right|^{1/n-1}\frac{\partial u_i}{\partial x} - \frac{1}{2}\delta_i {H_i}^2 = 0, \tag{2.116}$$

where

$$\varepsilon_i = \frac{A^{-1/n}\left([u_i]/[x]\right)^{1/n}}{2\rho_i g[z]} \ll 1, \tag{2.117}$$

and δ_i is as above. The fact that the parameter ε_i is small implies that the extensional stress terms are much smaller than the basal stress in the interior of the ice sheet. However, the extensional stress becomes important in the floating ice shelf, where there is no longer any basal friction to balance the driving stress, as seen in the boundary condition (2.116). This suggests the existence of a boundary layer near $x = x_g$, where the extensional stress becomes significant. Resolving this boundary layer determines the grounding line position x_g, after which Equations (2.112) and (2.113) may be solved subject to (2.114) and (2.115), neglecting the extensional stress at leading order (Schoof, 2007b). I further consider this boundary layer and its effect on the grounding line position in Chapter 4.

Chapter 3

Seawater intrusion beneath a marine ice sheet

3.1 Introduction

Despite the potential importance of Antarctic sedimentary basins for subglacial water budgets and heat flux, there has been little investigation to date into the effect of horizontal groundwater flow, and the resulting patterns of groundwater exfiltration and infiltration. Moreover, hydraulic properties such as the permeability remain poorly constrained. In order to quantify the magnitude of Antarctic groundwater flow and hence its importance, it is essential to obtain estimates of these properties.

While geophysical methods have been used to estimate the geometry of Antarctic sedimentary basins (Tankersley et al., 2022; Aitken et al., 2023; Li and Aitken, 2024), geophysical measurements of Antarctic groundwater itself have generally proved elusive. In a notable exception, Gustafson et al. (2022) used magnetotelluric measurements of bulk electrical conductivity to infer the presence of groundwater hundreds of metres deep beneath Whillans Ice Stream on the Siple Coast, West Antarctica. These authors also observed an increase in conductivity with depth in the sedimentary basin, which they interpreted as an increase in salinity and attributed to seawater intrusion during a Holocene glacial minimum.

Outside of Antarctica, evidence of historic seawater intrusion has been used to infer the effects of continental ice sheets on groundwater systems during glaciations (Aquilina et al., 2015). Modelling the process of seawater intrusion could therefore provide insight into groundwater flow in Antarctica.

Existing models to date of groundwater flow in Antarctic sedimentary basins (*e.g.* Gooch et al., 2016; Li et al., 2022; Robel et al., 2023) have not considered differences in salinity. However, the mathematical theory of seawater intrusion in coastal aquifers

is of longstanding interest due to its implications for groundwater management, beginning with the investigations of Badon-Ghyben and Herzberg (1896). A rich array of mathematical and numerical techniques have emerged to investigate the effects of overextraction and, more recently, sea level rise on coastal groundwater flow (Bear, 2013; Werner et al., 2013; Ketabchi et al., 2016; Mondal et al., 2019; Richardson et al., 2024). However, such models are yet to be applied to a subglacial context.

In this chapter, I consider a mathematical model for groundwater flow in a sedimentary basin beneath a marine ice sheet on geological timescales, accounting for seawater intrusion, ice sheet growth and retreat, and basin geometry. I show that grounding line motion and basin geometry may give rise to "saltwater trapping", where seawater remains resident in portions of the aquifer that would be saturated with freshwater in the simplest steady state. The phenomenon of saltwater trapping depends heavily on the permeability of the aquifer, along with past grounding line motion.

I then apply this model to the sedimentary basin beneath the Ross Ice Shelf in West Antarctica, enabling a prediction of how groundwater is exchanged with the shallow hydrological system. By comparing modelled saltwater trapping to field observations, I estimate the permeability of the sedimentary basin required to reproduce these observations. My results evidence the importance of accounting for horizontal flow and saltwater intrusion when modelling groundwater dynamics in a subglacial sedimentary basin, and when considering the wider implications of these sedimentary basins for subglacial hydrology.

3.2 Model design

3.2.1 Governing equations

In this chapter, the model presented in Section 2.3 of the previous chapter is used, working in one horizontal dimension for simplicity. The setup is depicted in Figure 3.1. The region $0 < x < x_g(t)$ is considered, where x_g represents the grounding line, where the grounded ice sheet transitions to a floating ice shelf, and $x = 0$ represents the water divide within the aquifer. For $x > x_g$, the upper surface of the aquifer is therefore exposed to the ocean, which rapidly saturates this region of the aquifer with seawater. The water pressure in these region is hydrostatic, as the floating ice shelf weighs the same as the seawater it displaces in Archimedean equilibrium. The present-day sea level is taken as the reference $z = 0$.

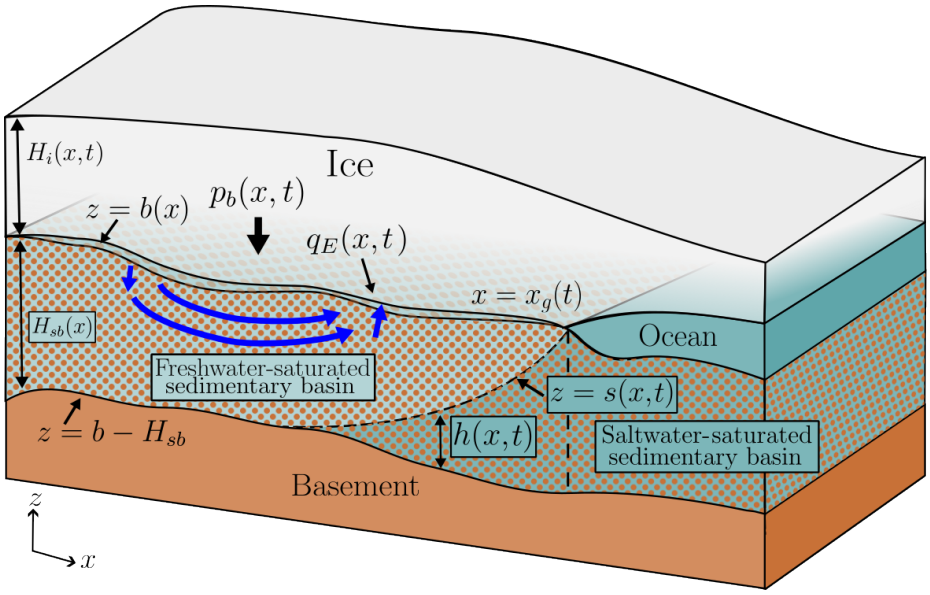


Figure 3.1: Schematic of the model used in this chapter. The aquifer has thickness $H_{sb}(x)$, and is bounded by $z = b(x)$ above and $z = b(x) - H_{sb}(x)$ below. The saltwater region occupies $b(x) - H_{sb}(x) < z < s(x)$ and has thickness $h(x) = s(x) - b(x) + H_{sb}(x)$, and the freshwater region occupies $s(x) < z < b(x)$ and has thickness $H_{sb}(x) - h(x)$. The subglacial hydrological system is depicted as a layer of water between the ice and the aquifer at $z = b(x)$. The grounding line $x = x_g(t)$ is marked by a vertical dashed line.

The aquifer has a thickness $H_{sb}(x)$, with an upper surface at $z = b(x)$ and basement at $z = b(x) - H_{sb}(x)$. For simplicity, it is assumed for the majority of this chapter that the aquifer is homogeneous and isotropic, with porosity ϕ and permeability k_{sb}. However, in Section 3.5.6 I investigate the effect of heterogeneity on the results of this chapter, using the generalised model previously discussed in Chapter 2, Section 2.4. For $x < x_g(t)$, the upper surface $z = b(x)$ is overlain by an ice sheet above a thin layer of freshwater, which represents an idealised subglacial hydrological system. The aquifer is assumed to be saturated at all times, but exchanges water with this freshwater layer at a rate $q_E(x,t)$, where $q_E > 0$ corresponds to exfiltration of water from the sedimentary basin. This layer is treated in the model as having zero thickness, on the basis that the corresponding subglacial hydrological system has a thickness on the order of metres to tens of metres, whereas the sedimentary basin is hundreds to thousands of metres thick (Gustafson et al., 2022).

As in Chapter 2 Section 2.3, it is also assumed for simplicity that the sedimentary basin is rigid, which corresponds to neglecting the compaction-related terms appearing in other chapters. Therefore, the only exfiltration q_E considered is the

'topographic' exfiltration resulting from horizontal flow and driven by ice thickness, bed elevation, sedimentary basin geometry and seawater intrusion, given by Equation (2.69). Since seawater intrusion requires horizontal groundwater flow in order to occur, it is reasonable to assume that these drivers of flow are significant over the locations and timescales considered here. On the other hand, the compaction-related terms, which scale with the rate of ice sheet thickening or thinning, are likely to be small when considering the slow evolution of the ice sheet over millennia. However, the same terms may become significant or dominant where an ice sheet undergoes thinning on decadal timescales (Robel et al., 2023).

As in Chapter 2, Section 2.3, a sharp interface is assumed at $z = s(x,t)$, separating freshwater above from saltwater below. The saltwater-saturated layer occupies $b(x) - H_{sb}(x) < z < s(x,t)$ and has thickness $h(x,t)$, whereas the freshwater-saturated layer occupies $s(x,t) < z < b(x)$ and has thickness $H_{sb}(x) - h(x,t)$. The sharp-interface assumption is reasonable provided that the Péclet numbers associated with molecular diffusion and hydrodynamic dispersion are large (Bear, 2013; Dentz et al., 2006; Koussis and Mazi, 2018). For a molecular diffusivity $D = 10^{-9}$ m^2 s^{-1} and a hydrodynamic dispersivity length $A_d = 10^{-2}$ m, which are suitable for salt in groundwater in sedimentary rocks (Aquilina et al., 2015), these Péclet numbers are respectively

$$\mathrm{Pe}_{\mathrm{diff}} = \frac{[z]^2}{D[t]} \approx 300, \quad \mathrm{Pe}_{\mathrm{disp}} = \frac{[z]^2}{A_d[x]} \approx 200, \tag{3.1}$$

suggesting that the sharp-interface assumption is reasonable here. More precisely, existing theory (Van Duijn and Peletier, 1992; Paster and Dagan, 2007, *e.g.*) suggests that saltwater mixing exerts an influence over a layer of thickness $[z]/\sqrt{\mathrm{Pe}}$, which is around 60–70 m for these Péclet numbers. Since the inversion results of Gustafson et al. (2022) suggest a smooth variation in salinity through the aquifer rather than a distinct sharp interface, a discussion is included in Section 3.6 of how a similar model could account for diffusion and dispersion, although it is possible that this smoothness could be in part or in full due to the inversion method used.

The governing equations are as derived in Section 2, Chapter 2.3. In dimensional variables, the evolution equation for $s(x,t)$ is given by

$$\phi \frac{\partial s}{\partial t} = \frac{k_{sb}\rho_f g}{\mu} \frac{\partial}{\partial x}\left[h \frac{\partial}{\partial x}\left(\frac{p_b}{\rho_f g} + b + \delta_s s\right)\right], \tag{3.2}$$

and the exfiltration is given by

$$q_E = \frac{k_{sb}\rho_f g}{\mu} \frac{\partial}{\partial x}\left[H_{sb} \frac{\partial}{\partial x}\left(\frac{p_b}{\rho_f g} + b\right) + \delta_s h \frac{\partial s}{\partial x}\right], \tag{3.3}$$

where p_b is the water pressure at the ice-bed interface. For this chapter, the simplifying assumption is made of zero effective pressure ($N = 0$), so that p_b is simply given by the overburden,

$$p_b = \rho_i g H_i. \tag{3.4}$$

However, in the subsequent chapters of this thesis, and particularly Chapter 4, the effect of a nonzero effective pressure on groundwater flow is considered in the absence of saltwater intrusion.

Note that in addition to the first term of Equation (3.3) which accounts for the ice pressure, bed elevation and sedimentary basin geometry, there is a second term involving s. The latter accounts for the effect of the intruding salt wedge on freshwater exfiltration and infiltration.

Equation (3.2) requires two boundary conditions in x. At the water divide $x = 0$, it is imposed that there is no horizontal flux of saltwater or freshwater,

$$hu = (H_{sb} - h)u = 0 \quad \text{at} \quad x = 0. \tag{3.5}$$

Since u is given by Equation (2.65), this requires that the sedimentary basin thickness and hydraulic gradient satisfy

$$H_{sb}u = -H_{sb}\frac{\partial}{\partial x}\left(\frac{p_b}{\rho_f g} + b\right) = 0 \quad \text{at} \quad x = 0. \tag{3.6}$$

In addition, having no flux of saltwater requires that

$$h\frac{\partial}{\partial x}\left(\frac{p_b}{\rho_f g} + b + \delta_s s\right) = 0 \quad \text{at} \quad x = 0. \tag{3.7}$$

(Note that Equation (3.7) can be satisfied by either $h = 0$ or $\partial s/\partial x = 0$.)

At the grounding line $x = x_g(t)$, the ice sheet weighs the same as the displaced ocean,

$$p_b = \rho_i g H_i = -\rho_s g b \quad \text{at} \quad x = x_g. \tag{3.8}$$

The aquifer is also saturated with seawater beyond the grounding line, so that the water pressure is equal to the hydrostatic ocean pressure,

$$p = -\rho_s g z \quad \text{at} \quad x = x_g, \tag{3.9}$$

taking the atmospheric pressure as the reference pressure. Since the pressure in the sedimentary basin is given by (Equation (2.64)),

$$p = \begin{cases} p_b + \rho_f g(b - z) & \text{for} \quad s < z < b, \\ p_b + \rho_f g(b - z) + (\rho_s - \rho_f)gs - \rho_s g z & \text{for} \quad b - H_{sb} < z < s, \end{cases} \tag{3.10}$$

Equation (3.9) is equivalent to

$$s = b \quad \text{at} \quad x = x_g. \tag{3.11}$$

3.2.2 Non-dimensionalisation

The equations are non-dimensionalised using the process described in Chapter 2. For this chapter, a vertical lengthscale $[z]$ is chosen based on approximate sedimentary basin thickness, along with a timescale $[t]$ appropriate for paleo-ice sheet growth and retreat, imposed by the rate of grounding line movement. As described in Section 2.3, an exfiltration scale $[q_E]$ is chosen to be comparable with the vertical motion of the freshwater-saltwater interface. The scalings of the model are listed in Table 3.1, and resulting dimensionless parameters in Table 3.2. From here onwards, variables are dimensionless unless otherwise stated, but dimensional values are used in figures, based on the scalings provided in Tables 3.1 and 3.2 unless otherwise stated.

As stated in Section 2.3, the dimensionless problem for the evolution of the freshwater-saltwater interface is then

$$\begin{aligned}(H_{sb}-h)\left(-\frac{\partial s}{\partial t}+\kappa\frac{\partial}{\partial x}\left[h\frac{\partial}{\partial x}\left(p_b+b+\delta_s s\right)\right]\right)&=0,\\ -\frac{\partial s}{\partial t}+\kappa\frac{\partial}{\partial x}\left[h\frac{\partial}{\partial x}\left(p_b+b+\delta_s s\right)\right]&\geq 0,\\ H_{sb}-h&\geq 0.\end{aligned} \tag{3.12}$$

The problem (3.12) is solved for s (noting that $h = s - b + H_{sb}$), assuming that p_b and x_g are provided along with b and H_{sb}. The parameter

$$\kappa = \frac{k_{sb}\rho_f g[z][t]}{\phi\mu[x]^2}, \tag{3.13}$$

is the dimensionless hydraulic conductivity of the groundwater flow. A larger κ corresponds to faster groundwater flow, and vice versa. The conditions (3.7) and (3.11) become

$$h\frac{\partial}{\partial x}\left(p_b+b+\delta_s s\right)=0 \quad \text{at} \quad x=0, \tag{3.14}$$

$$s=b \quad \text{at} \quad x=x_g. \tag{3.15}$$

The numerical method used to solve this problem is described in the Appendix, Section A.1. The dimensionless exfiltration is given by

$$q_E=\kappa\frac{\partial}{\partial x}\left[H_{sb}\frac{\partial}{\partial x}\left(p_b+b\right)+\delta_s h\frac{\partial s}{\partial x}\right]. \tag{3.16}$$

In Section 3.3 I consider the solution of Equation (3.12) in a uniform aquifer geometry, firstly looking at steady-state solutions, before moving to a periodic time-dependent solution, which introduces the possibility of saltwater trapping via grounding line movement. In Section 3.4, this is generalised to non-uniform aquifer geometries, which enables further potential saltwater trapping via so-called pockets. Finally

Scaling	Value used (Range)	Units
Vertical lengthscale $[z]$	1×10^3	m
Horizontal lengthscale $[x]$	5×10^5	m
Gravitational acceleration g	9.81	m s^{-2}
Viscosity μ	1×10^{-3}	Pa s
Permeability k_{sb}	(3×10^{-14}–3×10^{-12})	m^2
Freshwater density ρ_f	1.0×10^3	kg m^{-3}
Saltwater density ρ_s	1.025×10^3	kg m^{-3}
Porosity ϕ	0.3 (0.05–0.3)	
Timescale $[t]$	100	kyr
Ice density ρ_i	917	kg m^{-3}
Sliding parameter C_W (Section 3.5)	(2.6×10^5–2.6×10^6)	Pa $m^{-\frac{1}{3}}$ $s^{\frac{1}{3}}$
Accumulation a (Section 3.5)	0.1	m yr^{-1}

Table 3.1: Dimensional scalings used in numerical solutions. The lengthscales $[x]$ and $[z]$ are based on sedimentary basin geometry from Gustafson et al. (2022) and Li et al. (2022). The range of possible porosities ϕ and permeabilities k_{sb} are based on values for coarse-grained sedimentary rocks in Freeze and Cherry (1979), focusing on relatively high values of k_{sb} to avoid very small values of κ. The timescale $[t]$ roughly corresponds to the period of the most recent glacial cycle (Pollard and DeConto, 2009; Willeit et al., 2019).

Parameter	Value (Range)	Definition
Aspect ratio ε	2×10^{-3}	$\varepsilon = [z]/[x]$
Density difference δ_s	0.025	$\delta_s = (\rho_s - \rho_f)/\rho_f$
Dimensionless hydraulic conductivity κ	(0.0012–1.2)	Equation (3.13)
Dimensionless accumulation α	(0.005–5)	Equation (3.20)

Table 3.2: Values of dimensionless parameters used in numerical solutions.

in Section 3.5, Equation (3.12) is used to model groundwater flow in the sedimentary basin beneath the Ross Ice Shelf.

3.2.3 Ice sheet forcing

To model the ice sheet thickness H_i, the shallow-shelf approximation model laid out in Chapter 2, Section 2.5 is used, but neglecting the small extensional stress terms and the corresponding boundary condition (2.116). The grounding line position $x_g(t)$ is also prescribed explicitly, rather than as the solution of a free-boundary problem, which is permissible due to the neglect of the aforementioned boundary condition. It is also assumed that the dynamics of the ice sheet are quasi-steady for a given x_g, leading to dimensional equations of mass and momentum conservation

$$H_i u_i = ax, \quad C_W |u_i|^{-2/3} u_i = -\rho_i g H_i \frac{\partial}{\partial x} (H_i + b), \tag{3.17}$$

where a is the accumulation rate (assumed constant) and C_W is the sliding-law parameter. These combine to give

$$-\left(\frac{\rho_i g}{C_W}\right)^3 H_i^4 \left|\frac{\partial}{\partial x}(H_i + b)\right|^2 \frac{\partial}{\partial x}(H_i + b) = ax, \tag{3.18}$$

subject to the boundary condition (3.8). In dimensionless variables, this becomes

$$-H_i^4 \left|\frac{\partial}{\partial x}(H_i + b)\right|^2 \frac{\partial}{\partial x}(H_i + b) = \alpha x, \tag{3.19}$$

where

$$\alpha = \frac{a C_W^3 [x]^4}{(\rho_i g)^3 [z]^7}. \tag{3.20}$$

The boundary condition (3.8) becomes

$$H_i = -\frac{1 + \delta_s}{1 - \delta_i} b \quad \text{at} \quad x = x_g, \tag{3.21}$$

where δ_i is defined as in Section 2.5 with $\rho = \rho_f$. Equation (3.19) is consistent with the condition (3.6) provided that $\partial b / \partial x = 0$ at $x = 0$, and can in general be solved by numerical integration. Assuming zero effective pressure at the ice-bed interface, the pressure at the ice-bed interface is then given by

$$p_b = (1 - \delta_i) H_i. \tag{3.22}$$

Since δ_i is known, for a specified bed topography $b(x)$ this ice sheet model effectively contains one parameter α, which is treated as constant (although another

version of this model could have α varying with time to reflect changes in accumulation). Sensitivity of p_b to α is low due to the high powers appearing in Equation (3.19). The chosen value of α in Section 3.5 is based on present-day measurements and historic reconstructions of ice thickness, and is consistent with realistic values of C_W and a. In Section 3.3 and Section 3.4, a lower but plausible value of α is chosen for illustrative purposes.

The above ice sheet model is chosen because it is simple and quick to solve for a given grounding line position, and is physically appropriate for an ice stream context, where fast ice flow is dominated by basal slip (Cuffey and Paterson, 2010). This is because the main objective of this chapter is to model the dynamics of groundwater, rather than those of the ice sheet. A more general model could replace the Weertman sliding law with other sliding laws, and in particular a sliding law coupled to the effective pressure N in the subglacial hydrological system. In Chapter 4, I consider the consequences of using such a sliding law, and explore a fully coupled model of ice, subglacial hydrology and groundwater flow.

3.3 Solutions in an idealised aquifer geometry

3.3.1 Steady states

Although, for realistic parameter values (see Table 3.1), the system is usually far from a steady state, it is useful to understand these states in order to gain insight into solutions of Equation (3.12) more generally. The steady states of Equation (3.12) (with $s < b$) satisfy

$$h\frac{\partial}{\partial x}\left(p_b + b + \delta_s s\right) = 0, \tag{3.23}$$

using the no-flux condition (3.14). This implies that

$$h = 0 \quad \text{or} \quad p_b + b + \delta_s s = \text{const.} \tag{3.24}$$

By the condition (3.15), the latter must hold near the grounding line x_g. There are therefore two basic forms of steady-state solution (excluding possible steady states in which $s = b$ over some region), a "lens" case and "nose" case, which are discussed below.

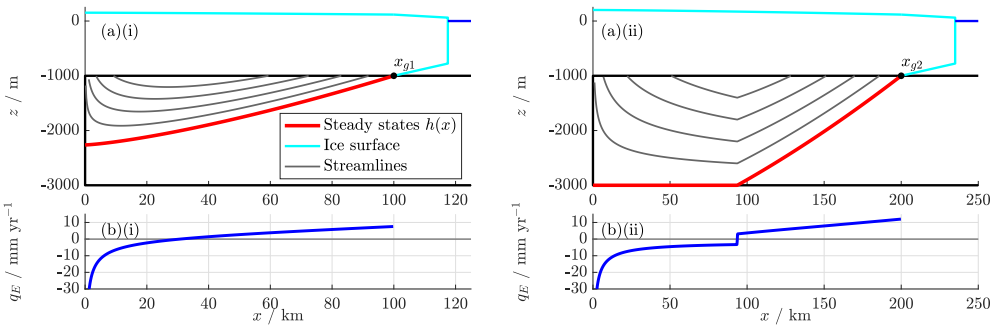


Figure 3.2: (a) Freshwater-saltwater interface $s(x)$ and (b) exfiltration q_E, for (i) "lens" and (ii) "nose" steady states arising from different grounding line positions x_{g1} and x_{g2}, for a uniform thickness aquifer with $H_{sb} = 2000$ m, $b = -1000$ m. Parameters are as listed in Tables 3.1 and 3.2, with $k_{sb} = 10^{-12}$ m^2 ($\kappa = 0.41$) and $\alpha = 0.1$.

Lens case

One possibility is that $h > 0$ everywhere, resulting in a freshwater "lens" beneath the ice sheet. In this case, conditions (3.8) and (3.15) imply

$$p_b + b + \delta_s s = 0 \quad \text{for} \quad 0 < x < x_g. \tag{3.25}$$

Since it must be the case that $s > b - H_{sb}$, such a solution requires that

$$p_b + b + \delta_s(b - H_{sb}) < 0 \quad \text{for} \quad 0 < x < x_g. \tag{3.26}$$

This generally occurs when the ice sheet is thin relative to the thickness of the sedimentary basin, or when the grounding line has retreated far inland. The interface in the lens solution does not coincide with the upper surface $z = b$, provided that $s < b$, *i.e.*

$$(1 + \delta_s)b - \delta_s H_{sb} \leq -p_b \leq (1 + \delta_s)b. \tag{3.27}$$

The alternative that $p_b + (1 + \delta_s)b < 0$ would imply the ice is thinner than its saltwater flotation thickness, which is unrealistic in general. This possibility is therefore dismissed henceforth.

Nose case

If the condition (3.26) is violated for some x, then the lens solution must be replaced locally by the solution $h = 0$, since h cannot become negative. The solution therefore displays a saltwater "nose" at $x = x_n$, where

$$x_n = \max\{x < x_g : p_b(x) + b(x) + \delta_s(b(x) - H_{sb}(x)) = 0\}. \tag{3.28}$$

The basic nose solution is given by (3.25) for $x > x_n$, and by $h = 0$ for $0 < x < x_n$, though such a steady state is not always unique, as discussed shortly.

Examples of the lens and nose cases are shown in Figure 3.2. (Note that here and in subsequent figures in this chapter, the aspect ratio is exaggerated and a schematic ice shelf is depicted for illustrative purposes only.) Freshwater infiltrates into the aquifer far inland, and is exfiltrated closer to the grounding line, with the total infiltration and exfiltration balancing one another in the steady state. There is no flow in the saltwater region in the steady state. The infiltration $q_E < 0$ is large in magnitude but finite at $x = 0$, because the ice overburden gradient $\partial p_b/\partial x$ is zero at $x = 0$ whilst changing over a relatively short distance.

In the nose case, $\partial s/\partial x$ has a discontinuity at x_n, leading to a kink in the streamlines and a jump discontinuity in q_E at this point. This is a quirk of the steady state solution, and is only possible because the flux of saltwater is identically zero: as will be shown in Section 3.4.1, the transient solution never reaches the $h = 0$ state from a nonzero initial condition, meaning that this kink in h and the corresponding jump in q_E are smoothed out in practice. However, the presence of this jump is an indication that saltwater intrusion can affect exfiltration by diverting the flow of fresh groundwater.

3.3.2 Periodic forcing

The above steady states can only be realised if the grounding line position $x_g(t)$ and ice overburden $p_b(x, t)$ remain steady. However, Antarctic ice streams such as those on the Siple Coast have undergone significant grounding line movement on timescales of tens to hundreds of millennia. For typical rates of groundwater flow, which scale with the dimensionless hydraulic conductivity κ (see Table 3.2), the present-day groundwater dynamics are therefore unlikely to have reached a steady state since the most recent grounding line migration.

This motivates an investigation dynamic solutions of Equation (3.12), considering in particular periodic solutions. This is motivated by the fact that global temperatures during the Pleistocene display periodicity of around 100 kyr (the 100-kyr Milankovitch cycle), associated with variations in the Earth's orbit of the sun (Willeit et al., 2019), which suggests that a periodic form of the grounding line forcing $x_g(t)$ is appropriate. In particular, a forcing

$$x_g(t) = \bar{x}_g - \Delta x_g \cos\left(2\pi t/100\,\mathrm{kyr}\right) \tag{3.29}$$

is used, wherein $\bar{x}_g$ and Δx_g are constants (in particular $\bar{x}_g = 150$ km and $\Delta x_g = 50$ km).

Figure 3.3 shows solutions to Equation (3.12) for periodic grounding line forcing at various values of κ. The solution $z = s(x,t)$ is initialised in a steady state, then calculated over several cycles of advance and retreat until it reaches a stable periodic solution. Only the final cycle of advance and retreat, which represents this periodic solution, is plotted. As explained below, this figure illustrates how the interface position during ongoing grounding line motion (plotted in colour) might differ substantially from its quasi-steady state for the current grounding line position (examples of which are plotted in black dashed lines).

For all values of κ, the interface lies between the would-be steady states at the minimum and maximum grounding line positions within the cycle. Although the forcing is symmetric in time, the interface $z = s(x,t)$ takes different shapes during advance and retreat, illustrating the history dependence of the saltwater intrusion dynamics.

When $\kappa = 10$ (Figure 3.3(a)(i)), groundwater flow is fast compared to grounding line movement. The interface therefore adjusts relatively rapidly, and is consequently close to the quasi-steady state corresponding to the instantaneous grounding line position. It can be seen that the steady-state solutions are most relevant in the limit of large κ. In the limit $\kappa \to \infty$, the groundwater flow would be able to instantaneously adjust to the movement of the grounding line, and therefore would agree at all times with the steady state position for the present value of x_g.

When $\kappa = 1$ (Figure 3.3(b)(i)), groundwater flow takes place at a moderate speed. There is now a substantial region of saltwater, which lies below the interface $z = s$ throughout the whole cycle, but above the steady-state position of the interface at the most advanced grounding line position (black dashed line). This region can be regarded as dynamically "trapped" saltwater, in the sense that it remains saltwater-saturated in the periodic solution at all times, although the steady-state solution for certain grounding line positions would suggest it is freshwater-saturated. For this particular value of κ, the lens thickness $H_{sb}(0,t) - h(0,t)$ achieves its maximum near the minimum grounding line position, so that the dynamics of the freshwater lens thickness at $x = 0$ are nearly in antiphase with those at the grounding line. This results in an additional region of trapped *freshwater*, in the sense that the freshwater lens is deeper at all times than predicted by the steady-state solution for the minimum grounding line position.

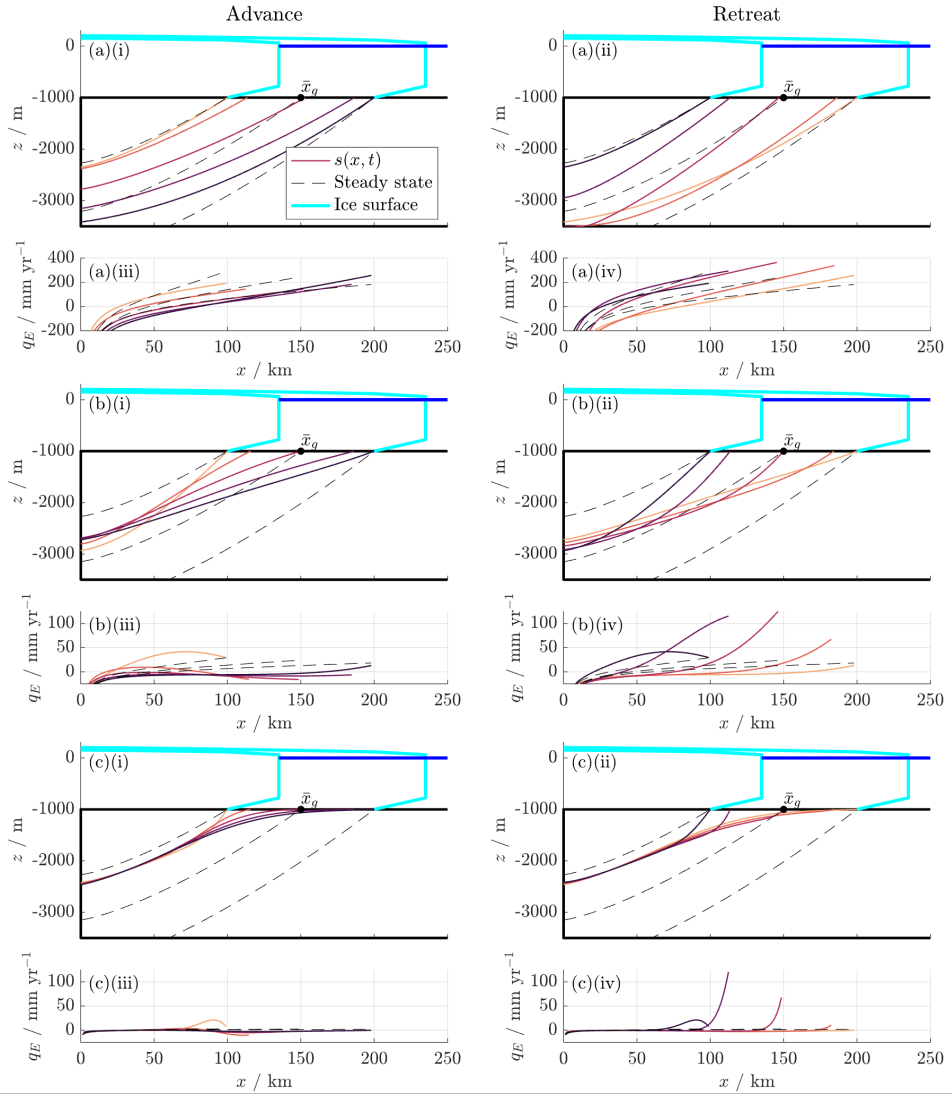


Figure 3.3: Stable periodic solution for $s(x,t)$ during (i) advance and (ii) retreat, and $q_E(x,t)$ during (iii) advance and (iv) retreat, with periodic grounding line forcing given by (3.29), for (a) $\kappa = 10$ (high permeability) (b) $\kappa = 1$ (moderate permeability) (c) $\kappa = 0.1$ (low permeability). The solution is plotted at times 0, 13, 25, 38, 50 kyr for advance and 50, 63, 75, 98, 100 kyr for retreat, with darker colours corresponding to later times. Instantaneous steady states are plotted with dashed lines for $x_g = \bar{x}_g$, $\bar{x}_g \pm \Delta x_g$. Parameters are as listed in Tables 3.1 and 3.2 with $\alpha = 0.1$.

Conversely, when $\kappa = 0.1$ (Figure 3.3(c)(i)), groundwater flow is slow compared to grounding line movement. In this case, $s(x,t)$ is near-steady over much of the domain, apart from a thin region alternating between freshwater and saltwater below the moving grounding line. The amount of saltwater trapped by the periodic motion is very large, while the corresponding amount of trapped freshwater is small; that is, taking the steady-state solution for almost any x_g overestimates the size of the freshwater lens.

Notably, the quasi-steady portion of the solution for small κ does not correspond to the steady state at the mean grounding line position $\bar{x}_g$. As $\kappa \to 0$, this state approaches the steady state for the most retreated grounding line position $\min_t x_g(t)$. This is because, during grounding line retreat, seawater instantaneously displaces any freshwater from the newly exposed region $x > x_g$. However, during re-advance, the freshwater lens grows at a finite rate, determined by the infiltration $q_E < 0$, and depending on κ. This is the key cause of asymmetry between grounding line advance and retreat. It can be inferred from this example that the furthest inland grounding line position is most important for determining the extent of saltwater intrusion whenever grounding line movement is fast compared to the natural timescale of groundwater flow.

The limiting behaviour of $s(x,t)$ as $\kappa \to 0$ can also be seen from Equation (3.12). For $x > \min_t x_g$, the saltwater thickness is identically $h = H_{sb}$ (*i.e.* $s = b$) whenever $x \geq x_g$, and when $x < x_g$ $\partial s/\partial t = O(\kappa)$ is small enough that s remains close to b. For $x < \min_t x_g$, the solution will slowly drift towards a small oscillation about a quasi-steady state, and, since $s = b$ for $x > \min_t x_g$, the only available quasi-steady state is that corresponding to $x_g = \min_t x_g$,

The exfiltration flux q_E also depends strongly on κ, as shown in Figures 3.3(a)–(c)(ii). Equation (2.69) shows that q_E is multiplied through by a factor of κ, but also depends on the position of the interface s, which is itself affected by κ. When κ is large (Figures 3.3(a)(iii) and (iv)), q_E therefore follows s in being close to the value implied by the steady state for the current x_g, and resembles that shown in Figure 3.2(b)(i). However, when κ is small (Figures 3.3(c)(iii) and (iv)), exfiltration is small apart from a prominent peak near x_g during grounding line retreat, where freshwater is rapidly flushed out of the aquifer as seawater saturates the region beyond the grounding line. Seawater intrusion could therefore significantly influence the shallow hydrological system via its effect on q_E, as will be shown again in Section 3.5.

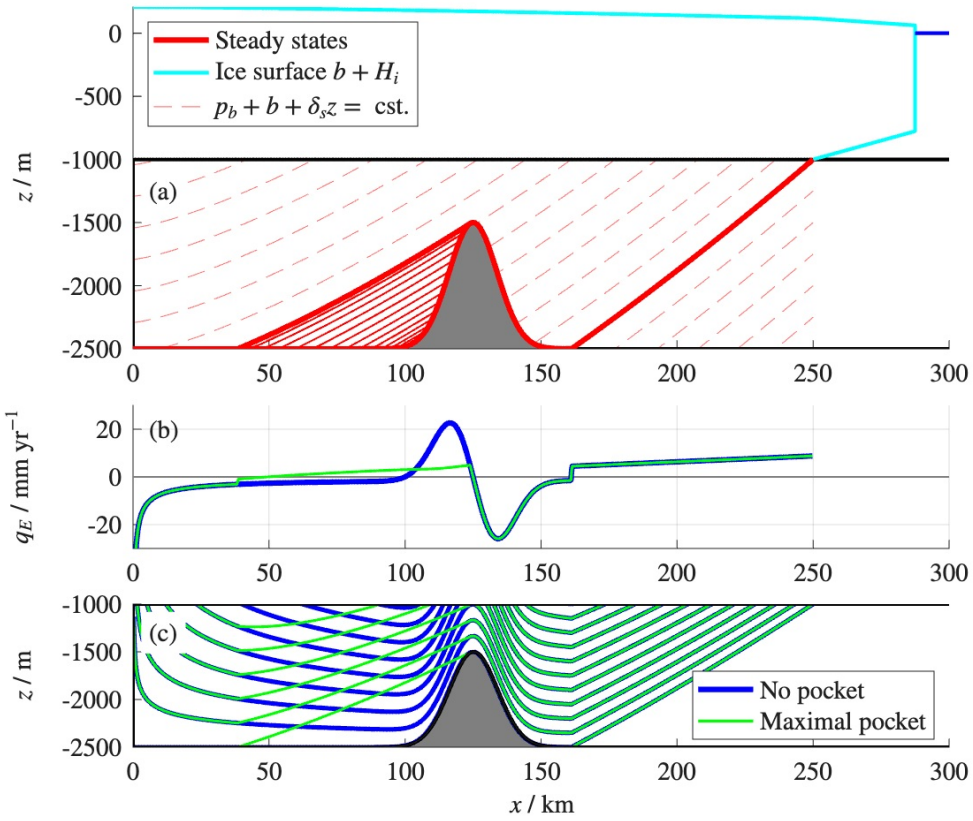


Figure 3.4: (a) A case with infinitely many possible "pocket" steady states, with curves satisfying the general solution (3.30) illustrated. The geometry is given by $b = -1000$ m, $H_{sb} = (1500 - 1000\exp(-((x - 125\text{ km})/12.5\text{ km})^2))$ m. (b) Freshwater exfiltration and (c) streamlines, with no pocket and the largest possible pocket. Parameters are as listed in Tables 3.1 and 3.2, with $k_{sb} = 10^{-12}$ m^2, $\kappa = 0.41$ and $\alpha = 0.05$.

3.4 Solutions in a non-uniform aquifer geometry

3.4.1 "Pocket" steady states

For certain basement geometries b and H_{sb} and overburdens p_b, Equation (3.23) also admits steady states that, in addition to a nose, contain saltwater "pockets", where $h > 0$ on a discrete region that is not connected to the saltwater nose. An illustrative example of these "pocket" steady states is shown in Figure 3.4. Such a pocket may be formed, for example, if the ice has advanced sufficiently rapidly to its current position that saltwater is still present relatively far inland once the ice has halted (see later Figures 3.5 and 3.6). These pockets represent another form of saltwater trapping,

which can occur in the steady state solution rather than requiring ongoing grounding line movement. For a single pocket in $x_q < x < x_p$, where $x_p < x_n$, the solution satisfies

$$p_b(x) + b(x) + \delta_s s(x) = p_b(x_p) + b(x_p) + \delta_s s(x_p) \quad \text{for} \quad x_q < x < x_p, \tag{3.30}$$

$$h = 0, \quad \frac{\partial h}{\partial x} \leq 0 \quad \text{at} \quad x = x_{p-}, \tag{3.31}$$

where the "$-$" subscript denotes a limiting value taken from the left-hand side, and

$$h = 0 \quad \text{at} \quad x = x_q. \tag{3.32}$$

Such a pocket is therefore possible if and only if

$$\frac{\partial}{\partial x}\left(p_b + b + \delta_s(b - H_{sb})\right) \geq 0 \quad \text{at} \quad x = x_{p-}. \tag{3.33}$$

The pocket solution is then given by

$$h = \frac{1}{\delta_s}\Big[p_b(x_p) - p_b(x) + b(x_p) - b(x)\Big] + b(x_p) - H_{sb}(x_p) - b(x) + H_{sb}(x) \quad \text{for} \quad x_q \leq x \leq x_p. \tag{3.34}$$

where x_q is the largest $x < x_p$ for which this expression is zero. It is imposed that $h = 0$ for $x < x_q$ to avoid the above solution becoming negative, making x_q effectively a second nose (although in general, further pockets could exist in the region $x < x_q$). (It is also possible for a pocket to form a saltwater lens, if the above expression for h is positive for $0 \leq x \leq x_p$.)

Since $\partial p_b/\partial x < 0$ in a realistic setting, and $|\partial b/\partial x|$ is usually small compared to $|\partial H_{sb}/\partial x|$ (see Section 3.5), Equation (3.33) effectively requires that $\partial H_{sb}/\partial x$ is negative and relatively large (of order $1/\delta_s \approx 40$). However, the Dupuit approximation remains valid in such a geometry, since the aspect ratio of the aquifer is around $1/500$ (see Table 3.2).

In the example of Figure 3.4, the sedimentary basin contains an idealised bottleneck due to a local rise in the basement rock. Behind this obstacle, the basement $b(x) - H_{sb}(x)$ is sufficiently steep for pockets to form via the criterion (3.33).

It can be seen that the bottleneck in the sediment geometry also produces local exfiltration and subsequent infiltration of freshwater, as the flux of freshwater (set by the ice overburden) is forced through a thinning and subsequently thickening aquifer. However, the presence of a trapped saltwater pocket extends the distance over which the freshwater region grows thinner, leading to smaller exfiltration over a larger area

and substantially modifying the spatial dependence of q_E. It can be inferred that potential saltwater pockets, and saltwater intrusion more generally, may significantly impact the effect of sedimentary basins on subglacial hydrology.

When pocket steady states exist, they are non-unique, since any x_p may be chosen from the interval on which Equation (3.33) holds, or it may simply be the case that $h = 0$ for all $x < x_n$. Figure 3.4 also illustrates this infinite family of steady states and their relation to the criterion (3.33). Choosing the largest such x_p leads to the "maximal" pocket, which contains the largest possible volume of trapped saltwater. Depending on the geometry, it may also be possible to satisfy Equation (3.33) on multiple disjoint intervals, so that steady states exist with several discrete saltwater pockets. However, it is not yet clear how, if at all, the existence of pocket steady states affects the transient solution of Equation (3.12). It is natural to ask, firstly, whether pocket steady states are stable, and, if so, whether a realistic combination of initial conditions and forcings can lead to such states. These questions are addressed in the following subsection.

3.4.2 Stability of pocket steady states

For the case of a steady ice sheet p_b and grounding line x_g, the transient solution of Equation (3.12) relaxes towards a steady state. However, in the case where there are multiple possible steady states, it is unclear which will be achieved. In this and the following subsection, it is demonstrated that a range of final steady states with or without pockets can be obtained, depending on initial conditions and on the dimensionless hydraulic conductivity κ.

Figure 3.5(a) shows a transient solution for the geometry and ice sheet shown in Figure 3.4, in which the aquifer is initially saturated with saltwater throughout ($h = H_{sb}$). As freshwater enters the aquifer from above, a significant volume of saltwater is trapped behind the obstacle, resulting in an eventual pocket steady state. However, as becomes evident after a very long period of time, the final state does not have the largest possible pocket, as might be expected. This overshoot occurs because the slope of the steady interface $\partial s/\partial x$ fails to be continuous at x_p and x_q, where the solution switches between $h = 0$ and $h > 0$. On the other hand, the transient solution $s(x, t)$ has a continuous derivative due to the regularity imposed by Equation (3.12). As a result, this solution is smoothed compared to the steady state, as seen for instance at 10^2 kyr. The smoothed region near x_p in turn allows a small amount of trapped saltwater to escape the pocket.

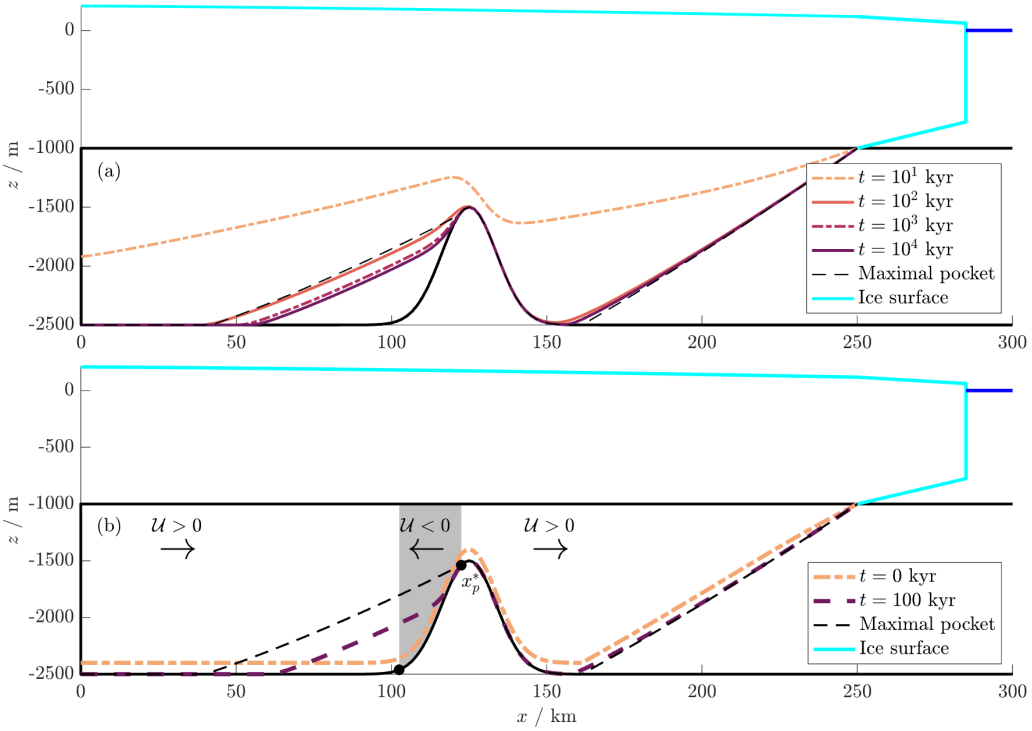


Figure 3.5: (a) Relaxation from an initial state $h = H_{sb}$ towards a pocket steady state. (b) Relaxation towards a steady state from an initially perturbed pocket-free state, with the direction of $\mathcal{U}(x)$ indicated. Note that x_p^* is not at the minimum of $H_{sb}(x)$, but a point where $\partial H_{sb}/\partial x < 0$. Parameters are as in Tables 3.1 and 3.2, with $\kappa = 10$ and $\alpha = 0.05$.

The opposite case of a small initial perturbation to the pocket-free state is shown in Figure 3.5(b). Near $h = 0$, the linearised evolution equation for h (Equation (3.12)) takes the form

$$\frac{\partial h}{\partial t} + \frac{\partial}{\partial x}\left[\mathcal{U}(x)h\right] = 0, \tag{3.35}$$

where

$$\mathcal{U}(x) = -\kappa \frac{\partial}{\partial x}\left(p_b + b + \delta_s(b - H_{sb})\right). \tag{3.36}$$

This is a hyperbolic equation representing advection with velocity $\mathcal{U}$. Equation (3.36) indicates that, at leading order, the flow is driven by the overburden and topographic pressure gradients, and the second-order buoyancy term is negligible.

The direction in which a perturbation (*i.e.* a small volume of saltwater) travels is determined by the sign of $\mathcal{U}$, which is shown in Figure 3.5(b). The condition (3.33) for a possible pocket in $x_q < x < x_p$ is equivalent to $\mathcal{U}(x_p) < 0$, and the largest possible pocket occupies $x_q < x < x_p^*$, where $\mathcal{U}(x_p^*) = 0$. Therefore, a small volume of saltwater in $x < x_p^*$ close to x_p^* will move in the negative x-direction and become trapped in the

region $x < x_p^*$. This trapped saltwater will in turn eventually form a pocket in the final steady state. Meanwhile, a small volume of saltwater in $x_p^* < x < x_n$ will travel in the positive x-direction and reach the saltwater nose.

To illustrate this, Figure 3.5(b) shows the result of initially perturbing a pocket-free state. The eventual steady state towards which the solution relaxes includes a pocket of trapped saltwater. The volume of saltwater in $0 < x < x_p^*$, given by the integral of $h(x,t)$ over this region, changes by less than 2% from the initial to final state, strongly suggesting that this pocket has been formed by trapping the saltwater initially located in this region, via the linearised flow $\mathcal{U}$. Conversely, the saltwater in $x > x_p^*$ has been evacuated towards the ocean.

3.4.3 Pocket creation by grounding line advance

If grounding line movement brings about a change from a system with a unique steady state to one with multiple steady states, it is unclear towards which of the new available steady states the solution of Equation (3.12) will relax. Here it is shown that it is possible for the system to reach either a state with a pocket or one without, depending on the intermediate states, and on the parameter κ. For the purposes of plotting the results, the total volume of freshwater is also defined as

$$V_f = \int_0^{x_g} H_{sb} - h \, \mathrm{d}x. \tag{3.37}$$

Figure 3.6 includes an example wherein the grounding line advances from an inland position past a bottleneck similar to that shown in Figure 3.4. The final grounding line position accommodates multiple steady states, although only the maximal and minimal such states are shown. Different final steady states are reached depending on the relative speed of groundwater flow, described by the parameter κ. In this case, values of κ are selected that illustrate a difference in final states whilst being relatively fast to approach these states, for the sake of readability of the figure.

When groundwater flow is sufficiently slow compared to grounding line movement (*e.g.* for $\kappa = 0.5$), the interface slowly relaxes from above to the maximal pocket state, resulting in trapped saltwater. On the other hand, when groundwater flow is fast (*e.g.* for $\kappa = 10$), the interface rapidly relaxes to the quasi-steady state for the instantaneous grounding line position. If one of these intermediate quasi-steady states inundates the region of the would-be pocket with freshwater, the final steady state has no pocket and no saltwater is trapped.

Similarly to the case of periodic forcing in Section 3.3.2, it can be seen from this example that the trapping of saltwater (in this case via a pocket steady state) is

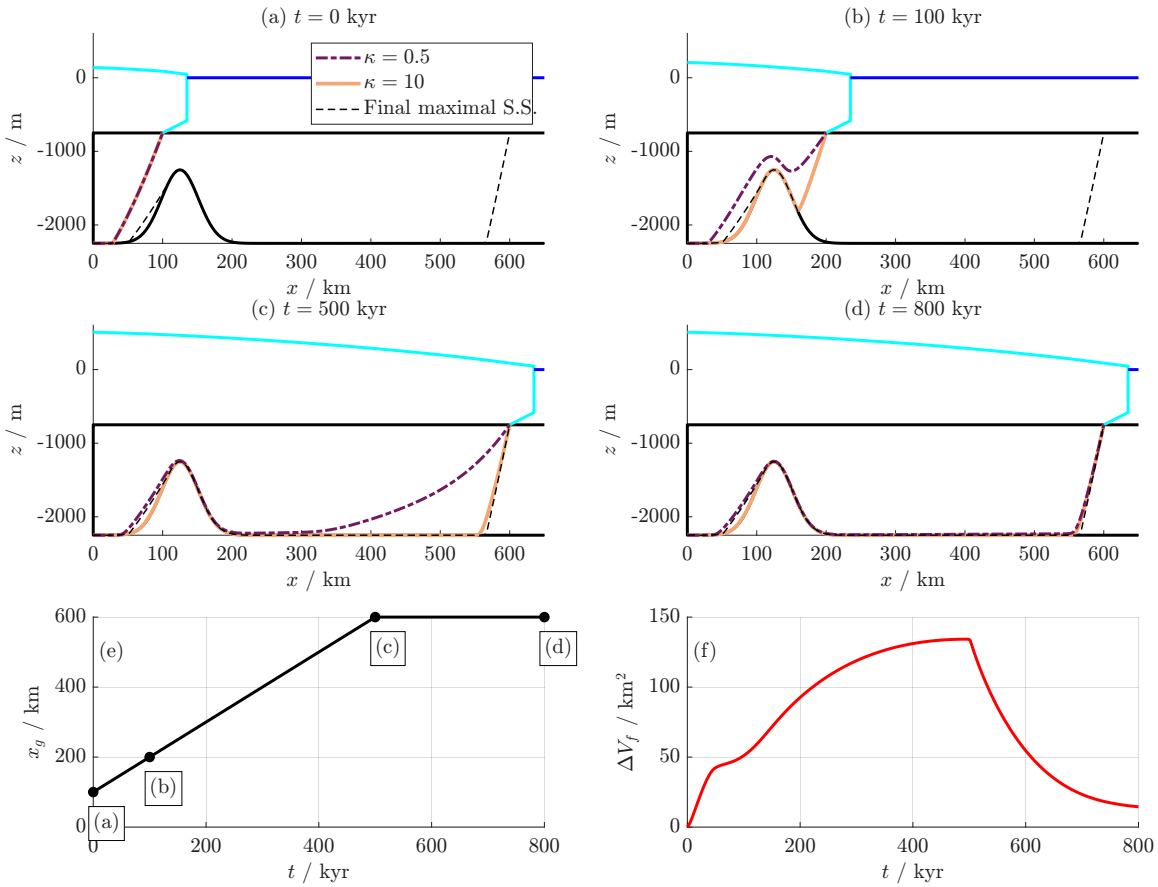


Figure 3.6: (a–d) Solutions $z = s(x, t)$ for the evolution to a steady state following grounding line advance, plotted at various points in time for two different κ. (e) Grounding line position x_g (f) Difference in freshwater volumes $\Delta V_f(t) = V_{f,\kappa=10} - V_{f,\kappa=0.5}$ between the two cases. Parameters are as listed in Tables 3.1 and 3.2, with $\alpha = 0.1$.

dependent on the dimensionless hydraulic conductivity κ as well as previous grounding line forcing. Indeed, this model demonstrates the possibility of "hysteresis", where grounding line retreat and re-advance induces a transition between two possible steady states. This hysteresis would affect the exfiltration q_E into the shallow hydrological system, because the presence of a saltwater pocket influences q_E (*e.g.* as seen in Figure 3.4). This in turn would modify the distribution of water in the shallow hydrological system beneath an ice sheet and could therefore feed back on the dynamics of the ice via basal sliding.

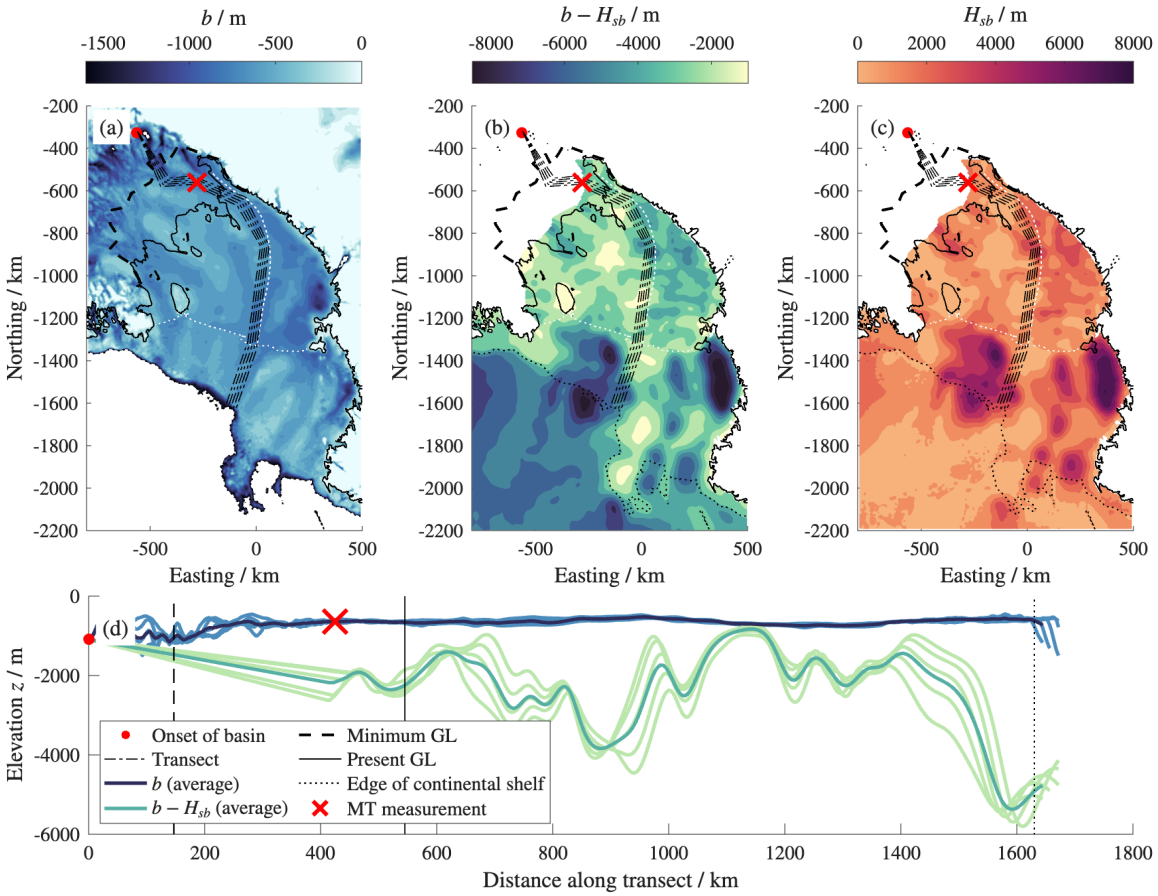


Figure 3.7: Measurements of (a) upper surface b (b) basement $b - H_{sb}$ (c) thickness H_{sb} for the Ross Sea sedimentary basin, which is sampled along transects. (d) Averaged cross-section along transects.

3.5 Application: Ross Sea, West Antarctica

3.5.1 Design

After exploring the above model of seawater intrusion in idealised settings, it can now be applied to a more realistic scenario, using the sedimentary basin beneath the Ross Ice Shelf in West Antarctica as a case study. As well as being the location of observed paleo-seawater intrusions by Gustafson et al. (2022), the thickness of this sedimentary basin has been modelled in detail using airborne magnetic data by Tankersley et al. (2022), and the grounding line history of this region has been subject to extensive investigation and modelling (Venturelli et al., 2023, 2020; Neuhaus et al., 2021; Lowry et al., 2019; Kingslake et al., 2018). A one-dimensional flowline is constructed from the three-dimensional data set by averaging over a set of adjacent transects (in order to reduce uncertainty due to lateral variation). A summary of the basement geometry

and grounding line data used, along with the choices of transect, and the sites of magnetotelluric measurements of salinity by Gustafson et al. (2022), is plotted in Figure 3.7.

3.5.2 Aquifer geometry

The estimate for $H_{sb}(x)$ along the selected flowline comes from the results of Tankersley et al. (2022), which are derived from airborne magnetic data. These are combined with bedrock topography and bathymetry data for $b(x)$ from Fretwell et al. (2013). Since the measurements of H_{sb} only extend a short distance beyond the present-day grounding line, $b - H_{sb}$ is linearly extrapolated in this region, assuming that $H_{sb}(0) = 0$ based on localised seismic measurements (Peters et al., 2006). It is assumed that the onset of the sedimentary basin $x = 0$ corresponds to the onset of ice streaming, which can be roughly estimated from surface ice flow velocity. A point on the flowline, marked with a red cross, is also selected, corresponding to the Subglacial Lake Whillans (SLW) observation site, where the salinity of the sedimentary basin has been modelled by Gustafson et al. (2022).

Note that elsewhere in this thesis, estimated sedimentary basin thicknesses from gravity inversion by Li and Aitken (2024) have been used, which have more comprehensive coverage than the data of Tankersley et al. (2022). However, the former was not yet available when the work in this chapter was conducted.

3.5.3 Grounding line and ice sheet model

The reconstruction of the grounding line position $x_g(t)$ is based on paleo-ice-sheet modelling supported by geophysical observations, which suggests (Kingslake et al., 2018):

1. Slow advance to a maximum, located at the edge of the Antarctic continental shelf, during 100–20 kyr before present,

2. Rapid retreat to a minimum, several hundred kilometres inland of the present-day grounding line position, during 20–10 kyr before present,

3. Re-advance from this minimum to the present-day grounding line during 10–0 kyr before present.

Since there is substantial uncertainty in the precise speed and timing of grounding line advance and retreat, $x_g(t)$ is simply linearly interpolated between the maximum, minimum and present-day position, as shown in Figure 3.10(a) and 3.11(a).

It is assumed that the grounding line behaviour obeys 100-kyr periodicity, in accordance with the periodic behaviour of global temperatures during the Pleistocene (*i.e.* the 100-kyr Milankovitch cycle) (Pollard and DeConto, 2009; McKay et al., 2012). The approach from Section 3.3.2 is therefore repeated, wherein the model is run for a series of forcing cycles until a stable periodic solution is reached (which is independent of the initial condition used).

To model p_b, the quasi-steady shallow ice sheet model described by Equation (3.18) is employed, with the constant $\alpha = 5$ based on the results of paleo-ice sheet reconstructions using more sophisticated models (Huybrechts, 2002; Kingslake et al., 2018). These simplified models are used on the basis that the exact forms of p_b and x_g are a relatively small source of model uncertainty compared to *e.g.* lateral variations in H_{sb}, or heterogeneity in aquifer properties such as k_{sb} and ϕ. This approach therefore prioritises capturing appropriate values for the grounding line maximum and minimum, and their timing. A more sophisticated approach could use ice core data for historic accumulation and temperature to force a model of both p_b and x_g, but such a model may require excessive fine-tuning to reproduce existing estimates of the grounding line extrema.

3.5.4 Aquifer properties and timescales

The largest source of uncertainty is given by the hydraulic properties of the aquifer, namely k_{sb} and ϕ. This includes model uncertainty (*e.g.* possible heterogeneity in ϕ and k_{sb}, dependence of k_{sb} on ϕ, and possible anisotropy in k_{sb}) and parameter uncertainty (assuming that k_{sb} is constant, what should its value be?). Previous studies have accounted for this by solving models for a wide range of possible k_{sb}, typically 10^{-17}–10^{-13} m^2 (Gooch et al., 2016; Li et al., 2022; Robel et al., 2023). In the dimensionless model (Equations (3.12) and (3.16)), the values of k_{sb} and ϕ are both accounted for in the single parameter κ, which takes small to moderate values for the above range of k_{sb} (see Table 3.3). Note that values smaller than $k_{sb} = 3 \times 10^{-14}$ m^2, which gives $\kappa \approx 0.01$, are disregarded on the basis that solutions for very small values of κ ought not to differ substantially, and an artificially high value $k_{sb} = 1 \times 10^{-10}$ m^2 ($\kappa \approx 40$) is included for comparison.

Equation (3.12) may be generalised to the case of heterogeneous $k_{sb}(x, z)$ and $\phi(x, z)$, as described in Section 2.4 of the previous chapter. I consider the effect on the model of using a depth-decaying ϕ and k_{sb} in Section 3.5.6.

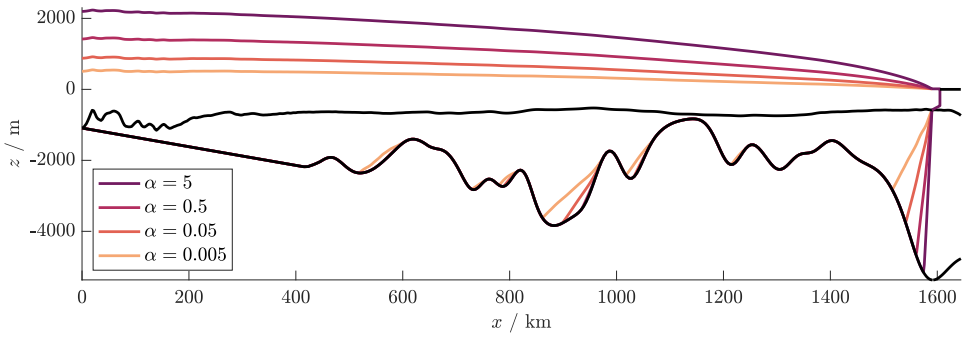


Figure 3.8: Potential steady state pockets for the basement geometry $z = b(x)$ and $z = b(x) - H_{sb}(x)$ (black curves) estimated along a historic flowline of the ice in the Ross Sea, West Antarctica, as shown in Figure 3.7. The freshwater-saltwater interface $z = s(x)$ and ice surface are plotted for various values of the ice sheet parameter α. (Any possible pockets in the region ($x < 400$ km) where $b(x) - H_{sb}(x)$ has been linearly interpolated are ignored.) Parameters are as listed in Tables 3.1 and 3.2.

Table 3.3: Depth of the freshwater lens at the SLW site for various values of k_{sb}.

k_{sb} / m^2	κ	$d_{f,\mathrm{SLW}}$ / m
1×10^{-10}	41	1520
3×10^{-12}	1.2	400
1×10^{-12}	0.41	170
3×10^{-13}	0.12	120
1×10^{-13}	0.041	110
3×10^{-14}	0.012	100

3.5.5 Results

Figure 3.8 shows where potential steady-state saltwater pockets can exist in the above geometry for a range of ice thicknesses, which in the model used are characterised by the dimensionless accumulation α. For the chosen value $\alpha = 5$, which is based on historic ice thickness modelled by Kingslake et al. (2018) and Huybrechts (2002), the ice surface is too steep to permit saltwater pockets from existing in the steady state. However, such pockets are possible for ice sheets with a shallower surface slope, or (more importantly) in the transient case.

The results of the time-dependent simulations are shown in Figures 3.9, 3.10 and 3.11 and Table 3.3. For each value of k_{sb}, the present depth of the freshwater lens at the SLW site

$$d_{f,\mathrm{SLW}} = b(x_{\mathrm{SLW}}) - s(x_{\mathrm{SLW}}, 0) \tag{3.38}$$

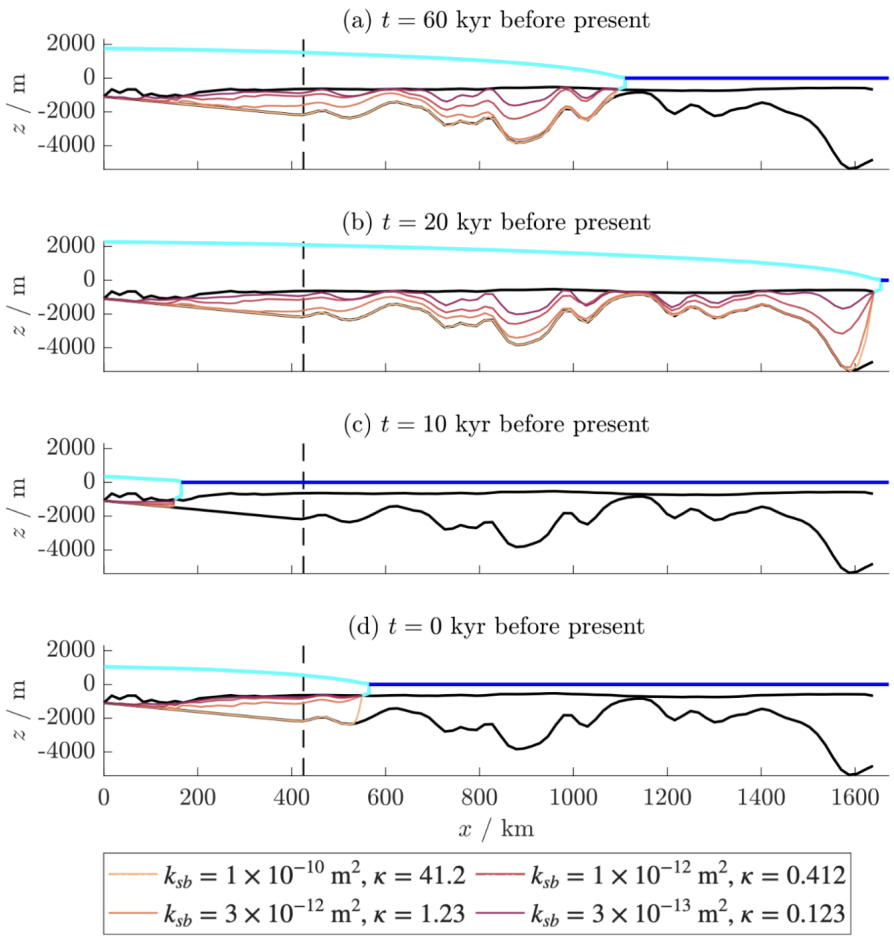


Figure 3.9: Interface $s(x,t)$ for varying k_{sb}, plotted (a) during grounding line advance (b) at grounding line maximum (c) at grounding line minimum (d) at present day, with the SLW site marked by a black dashed line. Parameters are as listed in Tables 3.1 and 3.2, with $\alpha = 5$.

is calculated, along with the space-averaged exfiltration

$$\bar{q}_E(t) = \frac{1}{x_g} \int_0^{x_g(t)} q_E(x,t)\,\mathrm{d}x. \tag{3.39}$$

Figure 3.9 shows the interface $s(x,t)$ at selected points in time for various values of k_{sb}, and Table 3.3 shows the corresponding values of $d_{f,\mathrm{SLW}}$. Figure 3.10 shows a time series of the space-averaged exfiltration $\bar{q}_E$, both dimensionally and dimensionlessly after scaling with κ, and Figure 3.11 shows a space-time plot of $q_E(x,t)$ for the case $k_{sb} = 3 \times 10^{-12}$ m^2 ($\kappa = 1.2$), alongside the basement geometry for comparison.

For the very highly permeable test case ($k_{sb} = 1 \times 10^{-10}$ m^2) in Figure 3.9, the interface is close to the quasi-steady state for the current grounding line position, as expected. The resemblance to the steady state is also observed for $k_{sb} = 3 \times$

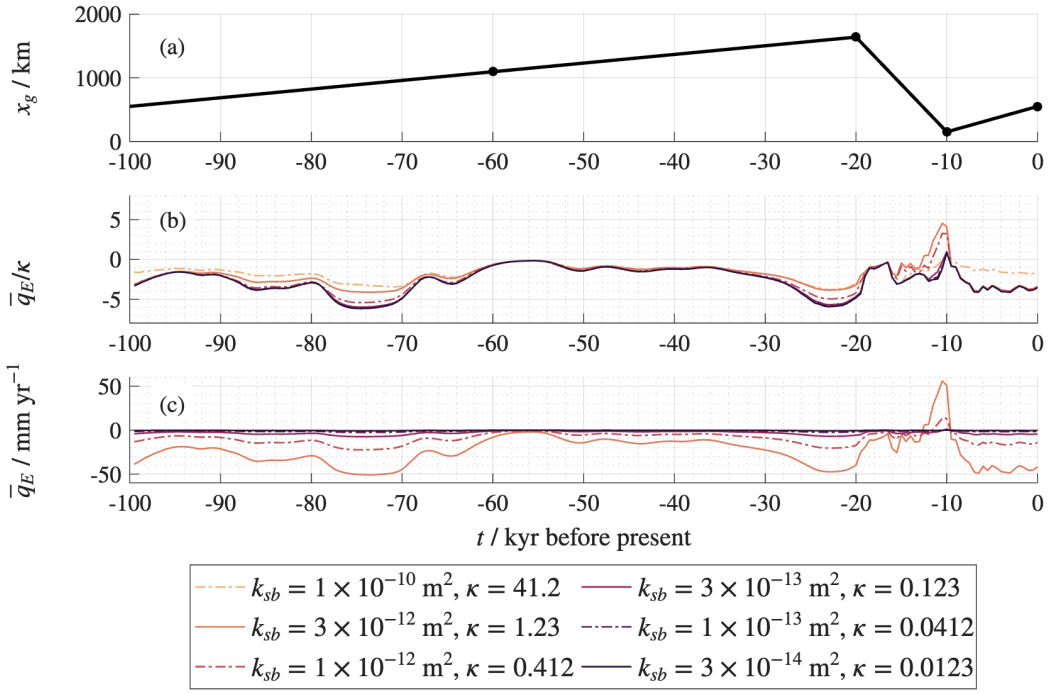


Figure 3.10: (a) Grounding line position $x_g(t)$. (b) Dimensionless spatially averaged exfiltration $\bar{q}_E$ after scaling with κ. (c) Dimensional $\bar{q}_E$. Parameters are as listed in Tables 3.1 and 3.2, with $\alpha = 5$.

10^{-12} m^2, in addition to a thin layer of trapped saltwater. For the successively lower permeabilities, the depth of the transient freshwater lens becomes successively smaller, and correspondingly more saltwater is trapped due to grounding line movement. For the less permeable examples, it can be seen that that both possible solution forms within the complementarity problem (3.12) are required, as the solution exhibits small but significant regions of saltwater exfiltration where $h = H_{sb}$ (for example, near $x = 600$ m and $x = 1200$ m in Figure 3.9(b)).

Table 3.3 shows the present-day depth of the transient freshwater lens $d_{\mathrm{f,SLW}}$ at the location of SLW in the above solutions. This increases with the permeability k_{sb}, reaching the full thickness H_{sb} of the layer for the very high value of 1×10^{-10} m^2, where the solution is near quasi-steady. Modelled salinity profiles found by inversion of magnetotelluric data by Gustafson et al. (2022) suggest that the groundwater salinity reaches that of seawater around 600 m below the ice bed, and 50% of this salinity about 400 m below the ice bed. These profiles show a smooth increase in salinity as opposed to the results in this chapter obtained assuming a sharp freshwater-saltwater interface. This smoothness is largely due to the inversion process used by these authors, which is unable to fully resolve sharp changes in electrical conductivity, but

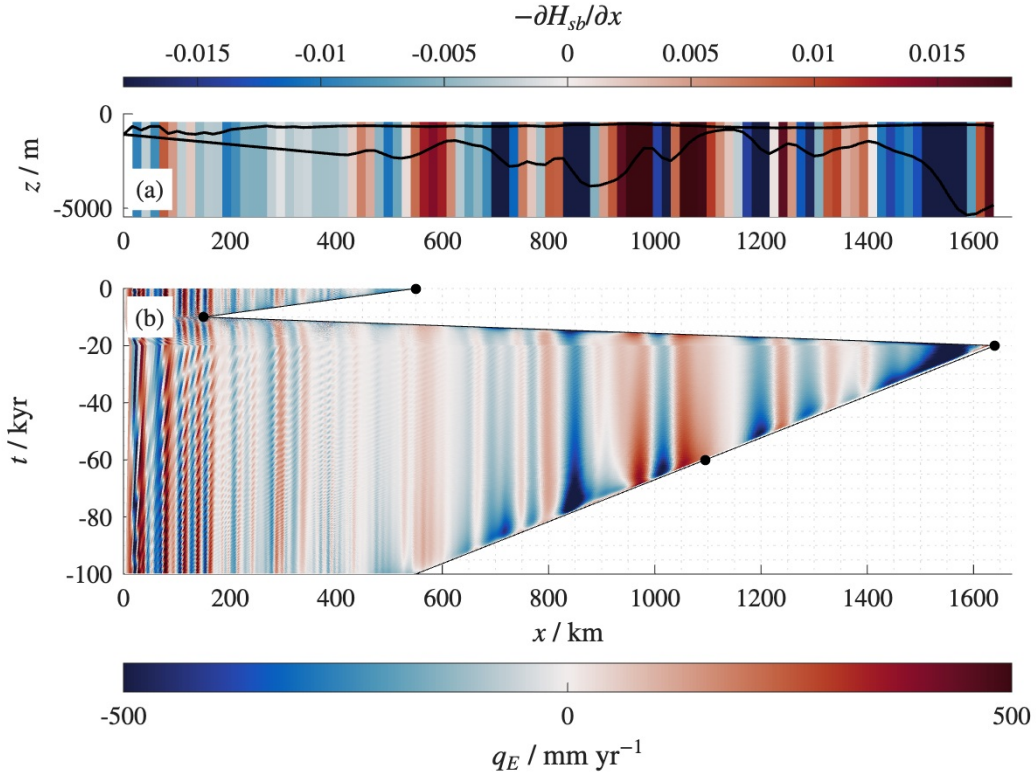


Figure 3.11: (a) Basement geometry $b(x)$ and $H_{sb}(x)$, coloured according to $-\partial H_{sb}/\partial x$. (b) Space-time plot of $q_E(x,t)$, with red corresponding to $q_E(x,t) > 0$ (exfiltration) and blue to $q_E < 0$ (infiltration). Values with $|q_E| > 500$ mm yr^{-1} are plotted using the same colours as ± 500. Parameters are as listed in Tables 3.1 and 3.2, with $\alpha = 5$ and $k_{sb} = 3 \times 10^{-12}$ m^2.

may also result in part from mixing of freshwater and saltwater. This introduces some uncertainty in how best to infer the 'freshwater lens depth' from these results. However, it is clear that the high permeability value $k_{sb} = 3 \times 10^{-12}$ m^2, for which $d_{\mathrm{f,SLW}} = 400$ m, gives the results that can be considered to agree best with those of Gustafson et al. (2022) (bearing in mind the uncertainty regarding the effect of the geothermal heat on resistivity, which when accounted for would result in a smaller salinity gradient and shallower freshwater lens). I discuss how this model might be adapted to allow smoothly varying salinity in Section 3.6.

The exfiltration q_E scales roughly linearly with κ (see Equation (2.69)), but also depends on κ through $s(x,t)$. Figure 3.10(b) illustrates the importance of the latter dependence: if q_E were determined by basement geometry and ice overburden alone (*i.e.* if seawater intrusion were ignored), the curves would collapse onto one another.

However, the magnitude of $\bar{q}_E/\kappa$ is at points several times larger for $k_{sb} = 3 \times 10^{-14}$ m^2, which includes the most trapped saltwater, than for $k_{sb} = 1 \times 10^{-10}$ m^2, where effectively no saltwater is trapped. Saltwater intrusion and trapping may therefore have a substantial effect on groundwater exchange with the shallow hydrological system. It is also noted that $\bar{q}_E < 0$ throughout most of the cycle, meaning that, on average across the basin, more water infiltrates than is exfiltrated (ultimately driven by the downstream hydraulic potential gradient due to the slope of the ice surface). However, around the glacial minimum exfiltration dominates. Over the duration of a periodic cycle, the net flux of freshwater into the domain must be zero, which is achieved by localised discharge of freshwater at the grounding line x_g during retreat.

Figure 3.10(c) allows the dimensional values of $\bar{q}_E$ to be compared. For the large values $k_{sb} = 3\times10^{-12}$ m^2 and $k_{sb} = 1\times10^{-12}$ m^2, the magnitude of $\bar{q}_E$ is in the low tens of millimetres per year, dropping to a few millimetres per year for lower permeabilities. However, local values of q_E may be several times larger than the average $\bar{q}_E$, as seen in Fig. 3.11. Previous modelling has found that groundwater contributes significantly to subglacial hydrological budgets (Christoffersen et al., 2014). This suggests that a realistic value of q_E should be similar in size to other sources of basal water, such as the basal melt rate, which may reach 20–100 mm yr^{-1} beneath an ice stream (Joughin et al., 2009). To achieve a mean exfiltration of this order of magnitude, high permeabilities $k_{sb} \gtrsim 10^{-12}$ m^2 are required, which is consistent with the previous estimate based on freshwater lens depth above. For smaller permeabilities, such values of q_E are locally achievable, but are counterbalanced by infiltration ($q_E < 0$) elsewhere.

Moreover, any estimate obtained under the assumptions of this model will fail to consider short-term exfiltration due to poro-elastic deformation of the sediments, which previous modelling suggests may reach tens to hundreds of mm yr^{-1} for $k_{sb} = 1 \times 10^{-13}$ m^2 (Li et al., 2022; Robel et al., 2023). This short-term exfiltration may enable sedimentary basins to act as a net source of basal water, as is suggested by the modelling of Christoffersen et al. (2014), rather than a sink. However, further modelling is required to understand the combined effects of short-term and long-term exfiltration.

In addition, q_E is highly heterogeneous in space, as seen in Figure 3.11, displaying localised regions of significant exfiltration and infiltration. The sign of q_E is closely correlated to that of $-\partial H_{sb}/\partial x$, with exfiltration generally occurring where the aquifer is becoming thinner in the direction of flow and infiltration where it is thickening.

This correlation occurs because the terms $\partial b/\partial x$ and $\delta_s \partial s/\partial x$ are relatively small in Equation (2.69), so that the exfiltration is approximately

$$q_E \approx \kappa \frac{\partial}{\partial x}\left(H_{sb}\frac{\partial p_b}{\partial x}\right) \approx -\kappa \frac{\partial H_{sb}}{\partial x}\left|\frac{\partial p_b}{\partial x}\right|, \tag{3.40}$$

with the latter approximation holding because $\partial p_b/\partial x$ varies relatively little compared to H_{sb} throughout the aquifer. The striped pattern of Figure 3.11 indicates that this term dominates throughout most of the domain over time. However, there are also visible deviations from this pattern due to the other terms, such as the role of saltwater intrusion as discussed above. These are most prominent near the grounding line, where the interface $s(x,t)$ and ice thickness $H_i(x,t)$ are steepest.

Overall, this experiment finds that a high permeability $k_{sb} \gtrsim 10^{-12}$ m^2 is required to reproduce both the observed depth of the freshwater lens at the SLW site and is consistent with the modelled contribution of groundwater to the basal water budget. This is an unusually high value for a sedimentary rock, which may in part owe to uncertainty in the results of Gustafson et al. (2022) regarding *e.g.* the effect of geothermal heat on conductivity, or the law used to invert for salinity. The high value of k_{sb} may be an indication that geological features such as faults and fractures, which this model has not considered explicitly, but which may macroscopically be captured by a large permeability, may play an important role in subglacial groundwater transport. However, the chosen value of k_{sb} here represents an idealisation of a sedimentary aquifer which may in reality be highly heterogeneous and anisotropic, motivating a consideration of the role of heterogeneity.

3.5.6 Effect of heterogeneity

To investigate the importance of heterogeneity, the previous experiment is repeated using a non-uniform permeability and porosity, following the procedure described in Chapter 2, Section 2.4, and focusing in particular on vertical heterogeneity. The evolution equation for the salt wedge is given by Equation (2.77)

$$\hat{\phi}(x,s)\frac{\partial s}{\partial t} = \kappa \nabla \cdot \left[\bar{k}_h h \nabla (p_b + b + \delta_s s)\right], \tag{3.41}$$

where

$$\bar{k}_h = \frac{1}{h}\int_{b-H_{sb}}^{s} \hat{k}\, \mathrm{d}z, \tag{3.42}$$

and $\hat{\phi}(x,z)$ and $\hat{k}(x,z)$ are the porosity and permeability with the factors ϕ_0 and k_0 scaled out. As in Section 2.4, an Athy profile is used for the porosity (Athy, 1930),

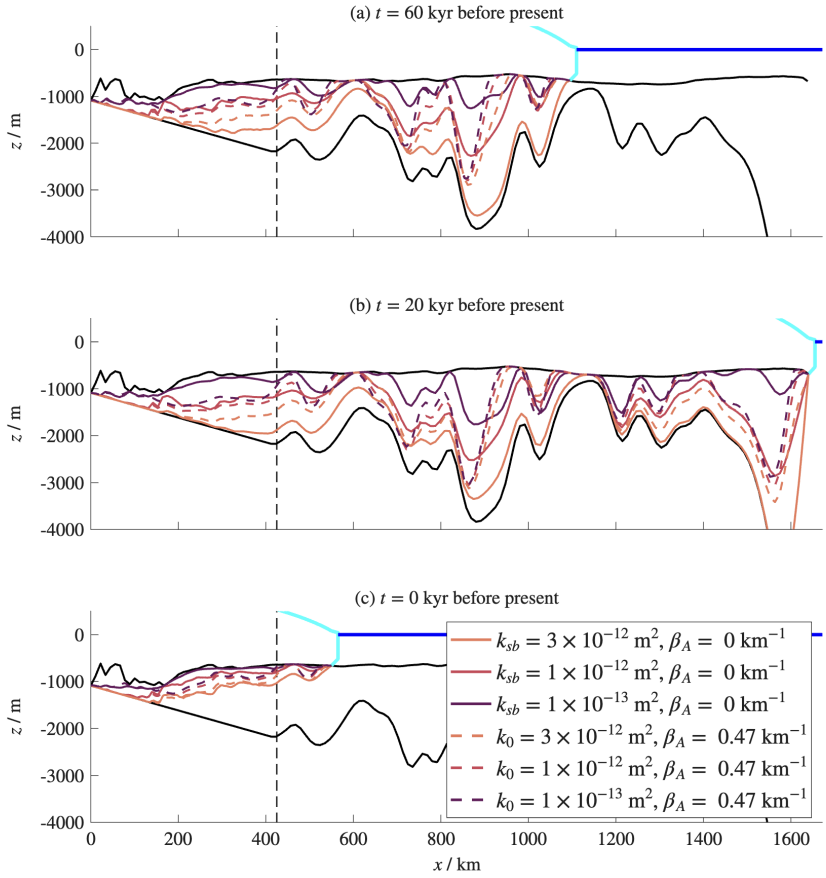


Figure 3.12: Interface $s(x,t)$ for varying k_{sb} and ϕ, as in Figure 3.9(a), (b) and (d). Solid lines denote constant permeability and porosity, whereas dashed lines have these varying with depth.

which gives (see Equation (2.79))

$$\hat{\phi} = \exp(-\beta_A(b-z)), \tag{3.43}$$

and a Kozeny-Carman law for the permeability, giving (see Equation (2.80))

$$\hat{k}(\hat{\phi}) = \left(\frac{1-\phi_0^2}{1-\phi_0^2\hat{\phi}^2}\right)\hat{\phi}^3. \tag{3.44}$$

A value $\beta_A = 4.7 \times 10^{-4}$ m^{-1} is used, based on Gustafson et al. (2022, supplementary material). (However, it is noted that the Kozeny-Carman law might not be the most suitable for Antarctic sedimentary basins, as discussed below.) It is noted that β_A introduces a characteristic lengthscale for porosity decay $1/\beta_A = 2100$ m, and that heterogeneity ought to have a significant effect if this scale is comparable with or smaller than the thickness of the sedimentary basin ($\beta_A H_{sb} = O(1)$ or larger).

The resulting freshwater-saltwater interfaces $s(x,t)$ are shown at selected times in Figure 3.12, for the cases $k_0 = 3 \times 10^{-12}$, 1×10^{-12} and 1×10^{-13} m^2, which are compared with the corresponding cases with no heterogeneity ($\beta_A = 0$ m^{-1}). While it can be seen that the freshwater lens depth continues to increase for higher permeabilities, the curves are closer together overall when heterogeneity is included, making it harder to distinguish between the different permeabilities. The effect of heterogeneity is substantial, dramatically modifying the position of the interface during advance, and significantly changing the present-day lens depth.

This results from the competing effects of porosity and permeability, seen on either side of Equation (3.41). While the decay in permeability with depth slows down the groundwater flow, the decay in porosity accelerates the movement of the freshwater-saltwater interface, because at a lower porosity the same mass flux of water corresponds to a larger pore-average velocity. For the lowest surface permeability $k_0 = 1\times10^{-13}$ m^2, the interface is lower with heterogeneity overall, indicating the effect of the porosity dominates, whereas for the highest value $k_0 = 3\times10^{-12}$ m^2 the interface is higher with heterogeneity, indicating that effect of the decaying permeability is more important. This clustering effect will be stronger the larger the decay in porosity with depth (in this case corresponding to the size of β_A), and is likely to be observed whenever the permeability $k_{sb}(\phi)$ is an increasing function of ϕ.

Since the choices of permeability and porosity here are just one among many possibilities, and introduce parameters (namely β_A) which are themselves uncertain, it is likely that various models of heterogeneity could lead to significant variations in modelled freshwater lens depth and hence in the inferred permeability. In particular, the Kozeny-Carman law used above is inappropriate for rocks containing a high proportion of clay minerals (Revil and Cathles III, 1999), and therefore may be unsuitable for sedimentary basins beneath marine ice sheets. Moreover, the above example only considers heterogeneity in depth z rather than in x. Possible heterogeneity is therefore likely to be one of the largest sources of uncertainty in the above modelling process.

3.6 Discussion

In this chapter, I have applied a mathematical model for groundwater flow and seawater intrusion in the sedimentary basin beneath a marine ice sheet, considering in particular the effects of grounding line advance and retreat and of sedimentary basin geometry. Both of these lead to the phenomenon of saltwater trapping, where

saltwater is permanently resident in regions where a steady-state solution would predict freshwater. Saltwater trapping is also highly dependent on the permeability of the sedimentary basin. The concept of saltwater trapping, via pocket steady states, should generalise from a subglacial context to a wider range of seawater intrusion problems where the aquifer geometry is sufficiently non-uniform.

In order to understand the role of groundwater in the subglacial hydrological system, it is crucial to constrain the permeability k_{sb}, since the flux q_E of water from the sedimentary basins to the shallow hydrological system scales with this value. The appropriate value of k_{sb} is highly uncertain, because of the observational challenges in measuring the porosity and permeability of such an aquifer. The fact that a single value of k_{sb} is used to represent a likely inhomogeneous and anisotropic aquifer compounds these challenges. However, by modelling groundwater flow beneath the Ross Ice Shelf, using existing knowledge grounding line history, it is possible to gain insight into the effect of k_{sb} on saltwater trapping, and estimate the range of values for k_{sb} required to reproduce present-day observations of seawater intrusion. High values of the permeability ($k_{sb} \sim 10^{-12}$ m^2) are found to agree best with observations of the freshwater lens depth, and are also consistent with modelled contributions of groundwater to the basal water budget via exfiltration.

The above modelling also suggests that sedimentary basin geometry has a strong effect on the exchange of groundwater with the subglacial hydrological system. Groundwater is generally exfiltrated where the sedimentary basin is thinning in the direction of flow, and infiltrates where the sedimentary basin is thickening. However, the ice overburden and the freshwater-saltwater interface also affect exfiltration and infiltration. In particular, the presence of trapped or intruding saltwater changes the shape of the freshwater-saturated region of the aquifer, and in some cases saltwater may entirely displace freshwater, so that saltwater is exfiltrated into the groundwater system.

The effect of including heterogeneity has also been considered in the form of a depth-decaying porosity and permeability. This can significantly affect modelled seawater intrusion, and is a large source of uncertainty in estimating the permeability of the sedimentary basin. The impact of heterogeneity is not monotone, since the porosity and permeability have competing effects, but generally reduces the impact of varying the surface permeability k_0. A priority of future work should be to further investigate and characterise the impact of sedimentary basin heterogeneity, as well as anisotropy, on Antarctic groundwater flow. This could include further modelling

using the equations presented in this chapter or the previous, or numerical simulations of non-Dupuit groundwater flow. Geophysical and remote sensing methods could also provide a possible route to gain insight into the heterogeneity of subglacial sedimentary basins.

Another limitation of this model is the idealised treatment of the subglacial hydrological system as an effectively unlimited freshwater layer with effective pressure $N = 0$. In the following Chapter 4, I consider a more complex model for $N(x, t)$, which allows q_E to exert feedback on N. This enables a deeper investigation into the role of groundwater exfiltration and infiltration in subglacial hydrology. A further development not considered in this thesis would be to allow for both freshwater and saltwater in the subglacial hydrological system, as groundwater exfiltration provides a possible route for saltwater to enter this system, which could enhance the basal melting of the ice.

A more complex model of subglacial hydrology also allows for coupling to the ice sheet via the sliding law $\tau_b(u_i, N)$, which is also considered in the following chapter. The use of an ice sheet model coupled to the effective pressure results in a different ice sheet profile, and also allows for feedbacks between the groundwater flow and the ice. For example, groundwater exfiltration could locally lower the basal effective pressure, affecting the sliding of the ice and hence the profile of the ice sheet, whose gradient in turn drives the groundwater flow.

Though seawater intrusion is not considered in the following chapters, a different ice sheet profile would affect this process. For example, if the ice had a shallower surface slope near the grounding line due to faster sliding, there would be more saltwater intrusion in the steady state (due to the smaller pressure gradient) and a higher likelihood of trapping seawater in pockets. This would in turn lead to a shallower freshwater lens and a higher predicted permeability. The exfiltration or infiltration would also be smaller in this region. However, the results of Section 3.5 suggest that, when periodic grounding line movement prevents groundwater dynamics from reaching a steady state, the shape of the ice sheet is less important than the permeability and geometry of the sedimentary basin. The resulting model uncertainty is therefore small compared to that resulting from *e.g.* aquifer heterogeneity and anisotropy, or lateral variations in basement geometry.

Since basement geometry is important for the results of the model, particularly the exfiltration q_E, it should be noted that the use of a cross-sectional model introduces uncertainty even after transverse averaging. Future work should therefore consider the dynamics of subglacial groundwater flow in all 3 dimensions, using the

equations derived in the previous chapter. In Chapter 5 of this thesis, I consider 3-dimensional groundwater flow in order to model the effect of groundwater on heat flux, but saltwater intrusion is not considered in this chapter. A possible way to incorporate transverse geometry while still solving a one-dimensional equation is through a width-averaged model, assuming the sedimentary basin has a transverse width $W(x, z)$ and is bounded by impermeable (curved) walls on either side. In this case, the evolution equation for $s(x, t)$ would read

$$W(x, s)\frac{\partial s}{\partial t} = \kappa \frac{\partial}{\partial x}\left[\overline{W}(x, s)h\frac{\partial}{\partial x}\left(p_b + b + \delta_s s\right)\right], \tag{3.45}$$

where

$$\overline{W}(x, z) = \frac{1}{z - b + H_{sb}} \int_{b-H_{sb}}^{z} W(x, \hat{z})\, \mathrm{d}\hat{z}, \tag{3.46}$$

is the depth-averaged width up to a given height. The exfiltration would be

$$q_E = \frac{\kappa}{W(x, b)}\frac{\partial}{\partial x}\left[\overline{W}(x, b)H_{sb}\frac{\partial}{\partial x}\left(p_b + b\right) + \delta_s \overline{W}(x, s)h\frac{\partial s}{\partial x}\right]. \tag{3.47}$$

Since the sedimentary basin thickness data are themselves the result of inverting magnetic measurements, they are also subject to their own model uncertainty, which should be taken into account (Tankersley et al., 2022). Indeed, estimates of sedimentary basin thickness in the same region using magnetotelluric measurements find significant discrepancies (Killingbeck et al., 2026). Further use of geophysical methods to estimate sedimentary basin geometry (*e.g.* Li and Aitken, 2024) can help to quantify and reduce this uncertainty.

It has been assumed, following Gustafson et al. (2022) and Tankersley et al. (2022), that the basement may be treated as impermeable, although an extension of this model could include a basement which is weakly permeable. The inclusion of basement permeability would weaken the effects of basement geometry on q_E by providing an alternative route for groundwater to leave or re-enter the sedimentary basin.

In this chapter, a rigid aquifer has been assumed for simplicity, and the compaction-related terms introduced in the previous chapter have been neglected. Over long timescales associated with grounding line movement, these terms ought to be small, since the ice thickness will change relatively slowly. However, when considering present-day groundwater flow, the compaction-driven terms are likely important due to ice thickness changes on decadal timescales. I explore the effects of compaction-driven groundwater flow in the following Chapters 4 and 5.

The model in this chapter makes the assumption of a sharp interface dividing freshwater and saltwater, on the basis that the Péclet numbers associated with diffusion and hydrodynamic dispersion are large. This greatly expedites the solution of the problem, at the cost of being unable to reproduce the smoothly varying salinity modelled by Gustafson et al. (2022) (although this smoothness may in part or fully result from the model used to invert the magnetotelluric data). To account for the effect of mixing, it is possible (though more complicated) to solve the full problem of density-coupled salt transport, known as the Henry problem, (*e.g.* Croucher and O'Sullivan, 1995), or to introduce a "mixing layer" around the sharp interface wherein these effects are accounted for (Van Duijn and Peletier, 1992; Paster and Dagan, 2007). The thickness of this layer is of order $[z]/\sqrt{\mathrm{Pe}}$, which is around 60–70 m for the Péclet numbers estimated in Equation (3.1). The salinity profiles modelled by Gustafson et al. (2022) vary smoothly over hundreds of metres, meaning that a higher hydrodynamic dispersivity would be required to explain this variation via mixing alone.

In steady-state seawater intrusion problems, the inclusion of saltwater-freshwater mixing reduces the extent of seawater intrusion by inducing a circulatory flow in the saltwater-saturated region (Cooper Jr, 1959; Koussis and Mazi, 2018). Including mixing ought to therefore result in a more retreated "interface" (which would need to be newly defined, *e.g.* as the 50% salinity contour) than under the sharp-interface assumption for a given permeability. This would lead to a lower permeability estimate than that obtained above. The process of saltwater mixing would also reduce the trapping of saltwater in pockets, via entrainment of saltwater into the freshwater flow, especially over long timescales such as those considered in this chapter.

3.7 Conclusions

In conclusion, I have shown that a model of seawater intrusion in an Antarctic sedimentary basin can be used to estimate the permeability of the sedimentary basin. My results suggest that groundwater fluxes are large, and therefore could play a significant role in Antarctic subglacial hydrology, with sedimentary basin geometry being an important driver of the flow. However, there are several sources of uncertainty, such as heterogeneity of the sedimentary basin or the use of a cross-sectional model, which should form a priority of future work.

My work in this chapter highlights the need for further investigations into the importance of Antarctic groundwater, such as including exfiltration and infiltration

in a model of subglacial hydrology coupled to ice sliding, and modelling the effect of groundwater flow on subglacial heat flux. I consider these in the subsequent chapters.

Chapter 4

A coupled model of ice streams, subglacial hydrology and sedimentary basins

4.1 Introduction

As discussed in Chapter 1, the subglacial hydrological system is a key source of uncertainty in projecting future sea-level rise from Antarctica. In the previous chapter, I found that exfiltration and infiltration could be large enough to significantly affect basal water budgets, agreeing with the findings of existing models of groundwater flow in Antarctic sedimentary basins (*e.g.* Gooch et al., 2016; Li et al., 2022; Robel et al., 2023). However, neither the work in this chapter nor the aforementioned models considered the effect of these fluxes on the subglacial hydrological system, nor its coupling with the ice sheet. Likewise, the majority of current subglacial hydrology models do not include exfiltration from, or infiltration into, sedimentary basins.

Various approaches to modelling subglacial hydrology consider water transport through subglacial conduits, a linked cavity network containing a water film (a "cavity sheet"), or flow through porous sediments (Flowers, 2015). The most frequently used state-of-the-art models combine multiple components, for example by including both a cavity sheet and a conduit system (*e.g.* Werder et al., 2013; Sommers et al., 2018). Such multi-component hydrology models have been used to model Antarctic subglacial hydrology for both individual glacier catchments (Dow et al., 2022; Wearing et al., 2024; Zhang et al., 2024; Hayden et al., 2025) and continent-wide settings (Ehrenfeucht et al., 2025).

While some studies also include feedback of the ice on the hydrology (Cook et al., 2020; Pelle et al., 2024), two-way coupled modelling of ice and hydrology remains

infrequent in state-of-the art models due to its high computational demand and the large parameter space required (Dow, 2022). As a result, relatively idealised models are more popular as a means of gaining insight into the coupling between ice sheets and subglacial hydrology (*e.g.* Lu and Kingslake, 2023; Kazmierczak et al., 2024; Haseloff et al., 2025). Such models may, for instance, work in two rather than three spatial dimensions, or consider only one component in a subglacial hydrology model (*e.g.* a conduit or a cavity sheet).

In this chapter, I therefore seek to develop a simple mathematical model for ice sheet flow in one horizontal dimension, coupled to a subglacial hydrological system, which includes exfiltration and infiltration from a sedimentary basin due to both compaction and horizontal flux variation. This model enables an investigation of how groundwater contributes towards or against the sliding of the ice, and where this effect is most important. I also investigate the consequences for the hydrology and ice sheet of compaction-driven exfiltration and infiltration during retreat.

I introduce the governing equations of this model in Section 4.2, and non-dimensionalise to find that the influence of the groundwater flow in the sedimentary basin is characterised by the parameters κ and Σ, effectively a dimensionless permeability and specific storage. Section 4.3 describes the steady states of the model when the feedback from groundwater flow on the hydrological system (and therefore the ice sheet) is weak. In Section 4.4, I then investigate the effect of strong groundwater flow coupling on these steady states, finding that the presence of a sedimentary basin can lead to thicker and slower-flowing ice in the steady state. In Section 4.5, I consider transient solutions when the ice is retreating or advancing to a new steady state, and show in particular that compaction-driven infiltration and exfiltration can decelerate ice sheet retreat and advance respectively. In Section 4.6, I conclude with a discussion of my results and possible developments of the model.

4.2 Model development

In this chapter, I consider a model with one horizontal dimension in addition to the vertical, in which the ice flows along the x-direction, as shown in Figure 4.1. The ice has thickness $H_i(x,t)$, and lies on a bed at $z = b(x,t)$, where $z = 0$ refers to sea level. The ice divide is located at $x = 0$, and is is assumed that this point also corresponds to the onset of the subglacial hydrological system. The grounded ice flow transitions into a floating ice shelf at the grounding line $x = x_g(t)$, a point which in this chapter must be determined as part of the solution. (In the previous chapter x_g could be

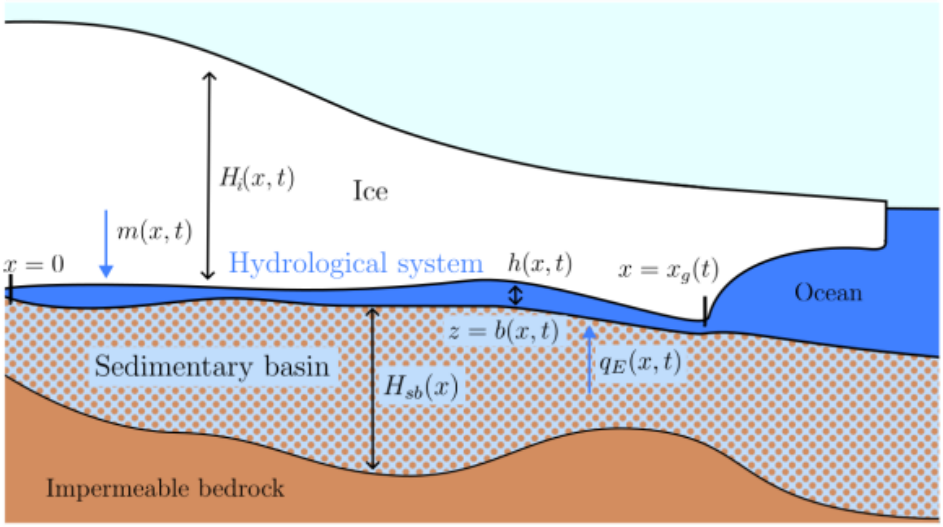


Figure 4.1: Schematic of the model, featuring an ice sheet with thickness $H_i(x,t)$ and hydrological system with effective thickness $h(x,t)$, above the bed elevation $b(x,t)$, with a sedimentary basin of thickness $H_{sb}(x)$ beneath. The grounded portion of the ice occupies $0 < x < x_g(t)$. Melting of the ice supplies a flux of water $m(x,t)$ to the hydrological system, and exfiltration (or infiltration if $q_E < 0$) from the sedimentary basin provides a flux $q_E(x,t)$.

prescribed as the ice sheet model was part of the forcing, but in this chapter the ice sheet must be found by solving a coupled model, in which x_g is a free boundary.)

Beneath the ice is a subglacial hydrological system. For simplicity, this system is modelled using the 'effective' water thickness $h(x,t)$, which represents the average volume of water per unit area. This follows the approach of treating the subglacial hydrological system as a macroporous cavity sheet (*e.g.* Alley, 1996; Creyts and Schoof, 2009; Le Brocq et al., 2009), which achieves comparable results to more complex models over long timescales (De Fleurian, 2018). By a 'macroporous cavity sheet', I mean that the water resides in interconnected cavities between protrusions in the bedrock (*i.e.* the sedimentary basin rock), which directly connect with the ice. (These cavities are however much larger than the pores in the sedimentary rock itself, hence the term 'macroporous'.) The effective water thickness $h(x,t)$ is a larger-scale quantity, presumed to be averaged over a lengthscale much larger than the individual cavities. Melting of the ice supplies a flux $m(x,t)$ of water to the hydrological system.

The model also includes a sedimentary basin, with thickness $H_{sb}(x)$. It is assumed that the effective water thickness $h(x,t)$ is much smaller than $H_i(x,t)$ and $H_{sb}(x)$, so that the top of the sedimentary basin is at approximately the same position $z = b(x,t)$ as the base of the ice sheet. I use q_E to denote the exfiltration (or infiltration when

$q_E < 0$), the flux of water from the sedimentary basin into the hydrological system or vice versa.

4.2.1 Ice sheet

In this chapter, the shallow-shelf approximation is used to model ice flow, as derived in Chapter 2, Section 2.5. The equations for the ice thickness $H_i(x,t)$, velocity $u_i(x,t)$, and grounding line position $x_g(t)$ consist of mass conservation,

$$\frac{\partial H_i}{\partial t} + \frac{\partial}{\partial x}\left(H_i u_i\right) = a, \tag{4.1}$$

along with momentum conservation, which is given by

$$\frac{\partial}{\partial x}\left(2A^{-1/n} H_i \left|\frac{\partial u_i}{\partial x}\right|^{1/n-1} \frac{\partial u_i}{\partial x}\right) - \tau_b(u_i, N) - \rho_i g H_i \frac{\partial}{\partial x}\left(H_i + b\right) = 0, \tag{4.2}$$

where $\tau_b(u_i, N)$ is the basal friction. It is assumed that this stress depends on both the ice velocity $u_i(x,t)$ and the effective pressure $N(x,t)$ within the subglacial hydrological system.

As before, N is defined as the difference between the overburden imposed by the ice and the water pressure p_b in the subglacial water layer

$$N = \rho_i g H_i - p_b. \tag{4.3}$$

Like h, N is a macroscopic quantity over lengthscales larger than individual cavities. The effective pressure is zero when the water pressure is sufficient for the ice to float.

The basal friction is modelled using a 'regularised Coulomb' sliding law (Schoof, 2005; Gagliardini et al., 2007; Zoet and Iverson, 2020),

$$\tau_b = C_C N \left(\frac{|u_i|}{|u_i| + \left(C_C N / C_W\right)^{1/m_W}}\right)^{m_W} \mathrm{sgn}(u_i), \tag{4.4}$$

where C_W and C_C are empirical constants, and the exponent m_W is usually taken to be related to the Glen's law exponent by $m_W = 1/n = 1/3$. The law (4.4) implies that the basal stress τ_b is an increasing function of N, with the limiting behaviour

$$\tau_b \sim \begin{cases} C_W |u_i|^{m_W} \mathrm{sgn}(u_i) & C_C N \gg C_W {u_i}^{m_W}, \\ C_C N \mathrm{sgn}(u_i) & C_C N \ll C_W {u_i}^{m_W}. \end{cases} \tag{4.5}$$

The use of the law (4.4) has been supported over a range of bed types by numerical modelling (Gagliardini et al., 2007; Joughin et al., 2019; Helanow et al., 2021) and

empirical observations (Zoet and Iverson, 2020). For high effective pressures, the law (4.4) recovers the 'Weertman' sliding law (2.103) frequently used in ice sheet models where hydrology has little effect on the sliding of the ice (Weertman, 1957; Fowler, 1981).

The boundary conditions that accompany Equations (4.1) and (4.2) are as in Chapter 2, Section 2.5,

$$u_i = 0 \quad \text{at} \quad x = 0. \tag{4.6}$$

$$\rho_i g H_i = -\rho g b \quad \text{at} \quad x = x_g, \tag{4.7}$$

$$2A^{-1/n} H_i \left| \frac{\partial u_i}{\partial x} \right|^{1/n} \frac{\partial u_i}{\partial x} = \frac{1}{2} \rho_i \left(1 - \frac{\rho_i}{\rho} \right) g H_i^2 \quad \text{at} \quad x = x_g. \tag{4.8}$$

4.2.2 Subglacial hydrological system

The evolution of the effective water thickness $h(x, t)$ in the hydrological system is governed by an equation of mass conservation

$$\frac{\partial h}{\partial t} + \frac{\partial Q_h}{\partial x} = m + q_E. \tag{4.9}$$

Here Q_h is the flux of subglacial water. The source term m describes the supply of water to the hydrological system due to melting of the ice. The exfiltration q_E from the underlying sedimentary basin also appears as a source term.

In this chapter, for simplicity, m is treated as a constant parameter, whose size may be estimated by considering the melting produced by inferred geothermal heat fluxes (McCormack et al., 2022), and whose effect on the ice mass balances is included in the net accumulation a. Assuming a latent heat of fusion of $L = 3.3 \times 10^5$ J kg^{-1} and a density of $\rho_i = 900$ kg m^{-3}, a melt rate of $m = 1$ mm yr^{-1} requires a net heat flux $G = \rho_i L m$ of around 9 mW m^{-2}. Since estimates of geothermal heat flux beneath Antarctica range from 30–150 mW m^{-2} (Burton-Johnson et al., 2020; Stål et al., 2021), a melt rate of a few mm yr^{-1} is reasonable allowing for some heat conduction into the ice. The assumption of constant m neglects the role of frictional heating in meltwater production, which in reality is likely to be significant, if not dominant, in the basal energy budget. In Section 4.6 I discuss the implications of neglecting frictional heating for this model, and possible extensions of the model to include it. I also discuss the relationship between basal melting and geothermal heat further in the following Chapter 5, where I explore how these are modified by groundwater flow.

For the flux Q_h, a Darcy-like law is prescribed

$$Q_h = -\frac{k_h}{\mu} h \frac{\partial \psi}{\partial x}, \tag{4.10}$$

where the hydraulic potential ψ is defined as the difference between the water pressure and hydrostatic pressure

$$\psi = p_b + \rho g b = \rho_i g H_i - N + \rho g b. \tag{4.11}$$

In Equation (4.10), the constant k_h is the effective permeability of the subglacial hydrological system and μ is the viscosity of water. The former is difficult to measure and in theory depends on properties of the macroporous cavity-sheet network such as its average cavity size and connectivity. However, a value of k_h can be estimated based on the fact that the subglacial horizontal water flux must be large enough to evacuate the meltwater produced by geothermal heating. The estimate of k_h does not substantially affect the model, since decreasing k_h causes the effective water thickness h to increase, and vice versa, so that the combination $k_h h$ remains roughly consistent.

As mentioned in Chapter 2, a constitutive law is required to prescribe N, which in this chapter is assumed to take the form of a 'closure relation' linking h to N. It is assumed that this can be written as a decreasing function

$$h = h(N). \tag{4.12}$$

Equation (4.12) is motivated by models of subglacial cavities, in which the rate of cavity closure by viscous creep increases with both effective pressure and the spacing between protruding subglacial obstacles. The latter increases with water film thickness h as the obstacles become more submerged. Assuming that opening and closure of cavities are in quasi-equilibrium and approximating the opening rate as constant leads to a decreasing relationship of the form (4.12) (*e.g.* Creyts and Schoof, 2009; Schoof et al., 2012; Hewitt, 2013; Werder et al., 2013; Kyrke-Smith et al., 2014). A relationship of the form (4.12) also arises in models of subglacial till, if the void ratio of the till is taken as a decreasing function of the effective pressure (Tulaczyk et al., 2000a; Haseloff et al., 2025).

For the examples in this chapter, I use the idealised relationship

$$h = \frac{E}{N}, \tag{4.13}$$

where E is a constant representing the 'stiffness' of the cavity sheet system. Equation (4.13) is intended as a simple relationship that captures the general behaviour of

the more complex models in the above references. A particular feature of Equation (4.13) is that the effective water thickness $h \to \infty$ as $N \to 0$. This means that as the ice approaches flotation, an unbounded amount of water can be stored beneath. An idealisation of the form (4.13) is reasonable when effective water thicknesses are much smaller than the height of the largest bed obstacles. A more physically accurate choice would have $N = 0$ for $h \geq h_c$, where h_c is the maximum height of bed obstacles, since the ice should achieve flotation once all obstacles are submerged. However, it is assumed that h_c can be treated as infinite, since large values of h are limited to a small region close to the grounding line.

Equation (4.9) requires two spatial boundary conditions. As the first of these, it is assumed that the hydrological system begins at the ice divide, so that there is no flux of water there,

$$Q_h = \frac{k_h}{\mu} h \frac{\partial \psi}{\partial x} = 0 \quad \text{at} \quad x = 0. \tag{4.14}$$

For the second, it is required that the effective pressure is zero at the grounding line

$$N = 0 \quad \text{at} \quad x = x_g, \tag{4.15}$$

which is a consequence of the flotation condition (4.7).

4.2.3 Sedimentary basin

The exfiltration from (or infiltration into) the sedimentary basin is determined using the model presented in Chapter 2, Section 2.2, using the Dupuit approximation. After converting to dimensional variables, Equation (2.42) becomes

$$q_E = \frac{\partial}{\partial x}\left[\frac{k_{sb}}{\mu} H_{sb} \frac{\partial}{\partial x}\left(\rho_i g H_i - N + \rho g b\right)\right] - \frac{S_s}{\rho g} H_{sb}\left((1-\xi)\rho_i g \frac{\partial H_i}{\partial t} - \frac{\partial N}{\partial t}\right). \tag{4.16}$$

As described in Chapter 2, the exfiltration in Equation (4.16) consists of a 'topographic' and 'compaction' term respectively. The topographic term is (minus) the divergence of the depth-integrated horizontal Darcy flux through the aquifer, which leads to exfiltration when this total flux is decreasing in the direction of flow. The size of this term is controlled by the sedimentary basin permeability k_{sb}. Values of k_{sb} for coarse-grained sedimentary rocks range from 10^{-17}–10^{-12} m^2, and 10^{-19}–10^{-13} m^2 for glacial tills (Freeze and Cherry, 1979).

The compaction term may be written as

$$q_{Ec} = \frac{S_s}{\rho g} H_{sb}\left(\xi \frac{\partial N}{\partial t} - (1-\xi)\left(\rho_i g \frac{\partial H_i}{\partial t} - \frac{\partial N}{\partial t}\right)\right), \tag{4.17}$$

where the term with prefactor ξ comes from the compression or decompression of the porous medium. This term produces exfiltration when the effective pressure increases ($\partial N/\partial t > 0$), due to contraction of the porous medium. The term with prefactor $(1 - \xi)$ is due to weak compressibility of the water, and produces exfiltration when the pressure decreases, due to expansion of the water.

The size of the compaction term is controlled by the specific storage S_s, and secondarily the loading efficiency ξ. For formerly glaciated aquifers in North America, Neuzil and Provost (2014) measure specific storages ranging from 1×10^{-7} to 3×10^{-5} m^{-1}, and loading efficiencies between 0.3 and 1.0, though generally around 0.75–0.95. However, Stone et al. (1997) use a drainage model with borehole data to infer a specific storage of 1×10^{-4} m^{-1} for subglacial till (although the results of such borehole response tests are subject to high uncertainty, and the reliability of such high values is low (Kulessa et al., 2005, *e.g.*)). A reasonable range is therefore $S_s = 1 \times 10^{-7}$–1×10^{-4} m^{-1}, although in Section 4.5 exaggerated values up to $S_s = 6.8 \times 10^{-4}$ m^{-1} are used for illustrative purposes. The value of ξ is taken to be 0.8 (see Table 1).

The formulation of groundwater flow and exfiltration here neglects certain thermodynamic effects, which fall beyond the scope of the current chapter. For instance, at high effective pressures (larger than 10^4 Pa), ice could infiltrate the porous bed to form a frozen fringe (Rempel, 2008). This reduces the permeability of the frozen region significantly, but also drives a groundwater flow in order to satisfy the required rate of freeze-on. Moreover, the frozen region may inhibit sliding of the ice (Meyer et al., 2018; Hansen et al., 2024). I discuss the implications of such thermodynamic effects further in Section 4.6.

4.2.4 Non-dimensionalisation

It is possible to gain insight into the model of ice and subglacial hydrology described above by non-dimensionalising the governing equations and boundary conditions. The values of imposed scales and parameters are presented in Table 4.1, whereas the resulting values of derived scales and parameters are given in Table 4.2.

The ice sheet model is non-dimensionalised following the scalings and procedures detailed in Chapter 2, Section 2.5. In addition, a scale $[N]$ for the effective pressure is assumed, although its value has not yet been decided. This leads to the dimensionless equations

$$\frac{\partial H_i}{\partial t} + \frac{\partial}{\partial x}(H_i u_i) = a, \tag{4.18}$$

Parameter	Value Used (Range)	Units
$[x]$	5×10^5	m
a	0.3 (0.1–0.5)	m yr^{-1}
g	9.8	m s $^{-2}$
ρ_i	900	kg m^{-3}
ρ	1000	kg m^{-3}
C_W	7.6×10^6	Pa m$^{-\frac{1}{3}}$ s$^{\frac{1}{3}}$
m_W	1/3	
A	1×10^{-25} (6.8×10^{-24}–3.6×10^{-27})	s^{-1} Pa^{-3}
n	3	
C_C	0.42	
E	1×10^5	Pa m
$[m]$	1	mm yr^{-1}
k_h	4.0×10^{-9}	m^2
μ	10^{-3}	Pa s
k_{sb}	(1×10^{-17}–1×10^{-12})	m^2
ξ	0.8 (0.3–1.0)	
S_s	(1×10^{-7}–6.8×10^{-4})	m^{-1}

Table 4.1: Imposed parameters and scalings (given to 2 significant figures where applicable). The accumulation scale a is estimated from Kaspari et al. (2004), and the range of A from Cuffey and Paterson (2010). The chosen value of $A = 1 \times 10^{-25}$ s^{-1} Pa^{-3}, which is selected as an intermediate value from the possible range, corresponds to an average ice temperature of roughly -25° C. The range for k_{sb} is taken from Freeze and Cherry (1979), whereas the estimates for S_s and ξ are based on Neuzil and Provost (2014) and, for the former, Stone et al. (1997).

Parameter	Value Used	Units
$[z]$	2300	m
$[t]$	7800	yr
$[u]$	64	m yr^{-1}
$[N]$	1.1	MPa
$[h]$	0.087	m
$[p_b]$	23	MPa

Parameter	Value Used (Range)
δ_i	0.1
ϵ_i	5.2×10^{-4}
λ	0.011
$\mathcal{E}$	0.05
$\mathcal{C}$	5
κ	(6.1×10^{-5}–6.1)
Σ	(0.070–480)

Table 4.2: Derived parameters and scalings (given to 2 significant figures where applicable).

$$4\varepsilon_i \frac{\partial}{\partial x}\left(H_i \left|\frac{\partial u_i}{\partial x}\right|^{1/n-1} \frac{\partial u_i}{\partial x}\right) - \mathcal{C}N\left(\frac{|u_i|}{|u_i| + (\mathcal{C}N)^{1/m_W}}\right)^{m_W} \mathrm{sgn}(u_i) - H_i \frac{\partial}{\partial x}(H_i + b) = 0. \tag{4.19}$$

where ε_i is as defined in Equation (2.117) and where

$$\mathcal{C} = \frac{C_C[N]}{C_W[u]^{m_W}}. \tag{4.20}$$

The boundary conditions (4.6), (4.22) and (4.8) become

$$u_i = 0 \quad \text{at} \quad x = 0. \tag{4.21}$$

$$H_i = -\frac{b}{1-\delta_i} \quad \text{at} \quad x = x_g. \tag{4.22}$$

$$4\varepsilon_i H_i \left|\frac{\partial u_i}{\partial x}\right|^{1/n-1} \frac{\partial u_i}{\partial x} = \frac{1}{2}\delta_i {H_i}^2 \quad \text{at} \quad x = x_g, \tag{4.23}$$

The dimensionless parameter $\varepsilon_i \ll 1$ represents the size of the extensional stress term compared to the basal stress. Although the extensional stress term is generally small, it becomes important near the grounding line, due to the stress balance boundary condition (4.8). The result is that solutions of this ice-sheet model usually feature an 'extensional stress boundary layer', a small region near the grounding line in which the extensional stress terms become important in Equation (4.19), while these terms remain negligible elsewhere (Schoof, 2007a; Tsai et al., 2015). The dimensionless friction coefficient $\mathcal{C}$ is $O(1)$, and determines how strongly the sliding of the ice is coupled to the subglacial hydrology.

The subglacial hydrology equation (4.9) is non-dimensionalised using the scales described above, taking the vertical lengthscale $[z]$ and timescale $[t]$ obtained from the ice sheet model. It is also assumed that a scale for subglacial water sources $[m]$ is provided, *e.g.* by considering the melt rate expected from estimated geothermal heat fluxes beneath Antarctica (McCormack et al., 2022). (Although m is constant in the below examples, several different values of this constant are considered, so fixing $[m]$ is useful to ensure scalings remain the same.) The exfiltration q_E is scaled with $[m]$, working on the assumption that meltwater fluxes and exfiltration contribute similar amounts to subglacial water budgets (Christoffersen et al., 2014).

It is also assumed that, away from the grounding line, the effective pressure is relatively small compared to the overburden, an assumption consistent with borehole data from West Antarctica (Engelhardt and Kamb, 1997). This means that hydrostatic pressure scale can be chosen as $[p_b] = \rho g[z]$.

Assuming that the source terms m and q_E are balanced by the flux divergence in Equation (4.9) (as is required for a steady state), it is then possible to derive a scale for the subglacial water thickness h, and subsequently the effective pressure N via Equation (4.13)

$$[h] = \frac{\mu[x]^2[m]}{k_h \rho g[z]}, \quad [N] = \frac{E}{[h]}. \tag{4.24}$$

For a general relation $h(N)$, $[N]$ can be determined by inverting this relation to find the $[N]$ such that $[h] = h([N])$. Under these scalings, the mass conservation equation (4.9) and closure relation (4.13) become

$$\lambda \frac{\partial h}{\partial t} = \frac{\partial}{\partial x}\left[h \frac{\partial}{\partial x}\left((1-\delta_i)H_i - \mathcal{E}N + b \right) \right] + m + q_E, \quad N = \frac{1}{h}, \tag{4.25}$$

where the dimensionless parameters are given by

$$\lambda = \frac{[h]}{[m][t]} = \frac{[a][h]}{[m][z]} \ll 1, \tag{4.26}$$

and

$$\mathcal{E} = \frac{[N]}{\rho g[z]}. \tag{4.27}$$

The boundary conditions (4.14) and (4.15) become

$$h \frac{\partial}{\partial x}\left((1-\delta_i)H_i - \mathcal{E}N + b \right) = 0 \quad \text{at} \quad x = 0, \tag{4.28}$$

$$N = 0 \quad \text{at} \quad x = x_g. \tag{4.29}$$

It is noted that the condition (4.29) implies $h \to \infty$ as $x \to x_g$; however, this does not cause an issue in Equation (4.25), since this equation may be regularised by multiplying through by N^2. The numerical method used to solve this equation is detailed in Section A.3 in the Appendix.

The dimensionless timescale $\lambda \ll 1$ represents the ratio of the subglacial hydrology's natural timescale to that of the ice sheet, with the former evolving generally much faster than the latter. The fact that λ is small (see Table 4.2) suggests that the assumption of a balance between the flux divergence and source terms in Equation (4.9) is appropriate.

The parameter $\mathcal{E}$ represents the characteristic size of the effective pressure relative to that of the ice overburden. Since borehole observations by Engelhardt and Kamb (1997) in West Antarctica found effective pressures to be a small percentage of the overburden (< 0.2 MPa beneath 1000 metres of ice, an overburden of around 9 MPa), $\mathcal{E}$ is expected to be small. In particular, a value $\mathcal{E} = 0.05$ is used. However, it is

noted that modelled (rather than observed) effective pressures could equal a larger percentage of the overburden, especially near the grounding line (Ehrenfeucht et al., 2025). Since varying $\mathcal{E}$ is equivalent to varying other parameters of the model (see below), it suffices for the current analysis to consider this single value.

Using the above scalings, and in particular taking $[q_E] = [m]$, the dimensionless version of Equation (4.16) for q_E is

$$q_E = \kappa \frac{\partial}{\partial x}\left[H_{sb}\frac{\partial}{\partial x}\left(H_i - \mathcal{E}N + \frac{b}{1-\delta_i}\right)\right] - \Sigma H_{sb}\frac{\partial}{\partial t}\left((1-\delta_i)(1-\xi)H_i - \mathcal{E}N\right), \tag{4.30}$$

where the dimensionless parameters κ and Σ are given by

$$\kappa = \frac{k_{sb}[z]}{k_h[h]} = \frac{k_{sb}\rho g[z]^2}{\mu[m][x]^2}, \tag{4.31}$$

and

$$\Sigma = \frac{S_s[z]^2}{[m][t]}. \tag{4.32}$$

The permeability ratio κ is the ratio of a typical horizontal flux through the sedimentary basin to that of the subglacial cavity sheet. The size of κ determines the flux of water transported through the sedimentary basin rather than the cavity sheet, along with the overall scale of topographic exfiltration. It is noted in particular that κ is independent of the cavity sheet permeability k_h. This is because the flux through the cavity sheet is determined by the melt rate, so that k_h only influences $[h]$ and by extension λ and $\mathcal{E}$, the latter of which can be adjusted by changing E. Using a range $k_{sb} = 1 \times 10^{-17}$–$1 \times 10^{-12}$ m^2 gives κ ranging from 6.1×10^{-5} to 6. In this chapter, I will generally focus on higher values from this range, as the impact of horizontal groundwater flow is small otherwise, though it is noted that such values are not guaranteed.

The parameter Σ determines the relative size of exfiltration and infiltration driven by compaction. Using a range from $S_s = 1 \times 10^{-7}$ m^{-1} to 1×10^{-4} m^{-1}, as discussed above, leads to Σ between 0.07 and 70.

Substituting Equation (4.30) into Equation (4.25) results in a combined hydrology equation (representing flow in both the subglacial water sheet and in the sedimentary basin)

$$\lambda\frac{\partial h}{\partial t} = \frac{\partial}{\partial x}\left[(h + \kappa H_{sb})\frac{\partial}{\partial x}\left((1-\delta_i)H_i - \mathcal{E}N + b\right)\right] + m \\ - \Sigma H_{sb}\left((1-\delta_i)(1-\xi)\frac{\partial H_i}{\partial t} - \mathcal{E}\frac{\partial N}{\partial t}\right), \tag{4.33}$$

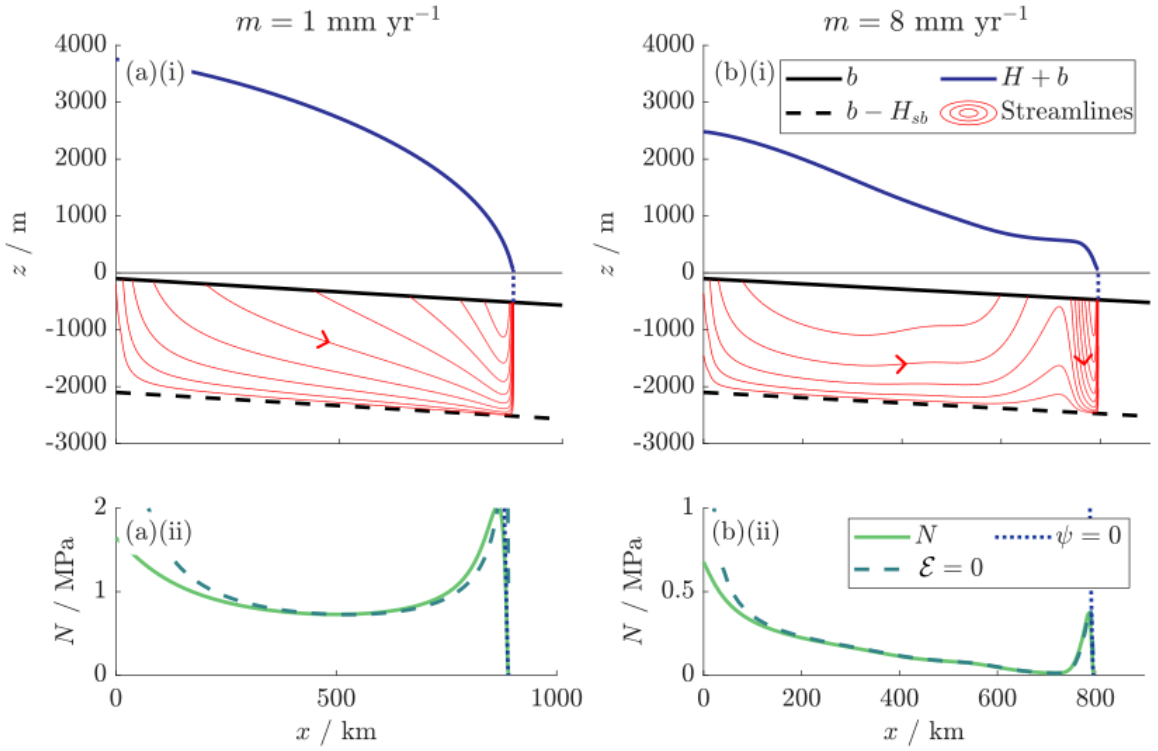


Figure 4.2: (i) Ice sheet profile and groundwater streamlines, and (ii) effective pressure N for (a) $m = 1$ mm yr^{-1} (dimensionless $m = 1$) and (b) $m = 8$ mm yr^{-1} (dimensionless $m = 8$), and for $\kappa \to 0$, with uniform sedimentary basin thickness $H_{sb} = 2000$ m. Inset panels show the ice profile near the grounding line. The effective pressure is compared to the $\mathcal{E} = 0$ and $\psi = 0$ approximations given by Equation (4.35) and (4.36) respectively. The bed is given by $b(x) = (-100 - 230 \times (x/500\,\text{km}))$m. Note that here, and in subsequent figures, the ice shelf beyond the grounding line is not depicted.

along with the relation $h = 1/N$. For a given ice thickness H_i, Equation (4.33) is a nonlinear diffusion equation for N, containing several dimensionless parameters. The fact that λ is small suggests the subglacial hydrological system generally evolves much faster than the ice sheet in the absence of compaction-driven exfiltration, but the presence of $\partial N/\partial t$ in the compaction term produces a slower evolution on a timescale $\Sigma\mathcal{E}$.

4.3 Steady ice sheet with weak groundwater flow

Firstly, to gain an intuition of the model, I consider the steady states in the limit $\kappa \to 0$, in which the sedimentary basin does not exert any effect on the subglacial effective pressure or ice thickness, although it is still possible to plot the limiting

streamlines of groundwater flow. In the steady state, the compaction terms do not play a role, since these require time dependence by definition. Figures for the '$\kappa \to 0$' case are obtained by using the value $\kappa = 0$, although I refrain from referring to them as '$\kappa = 0$' as this would imply no groundwater flow occurs at all. Solutions are considered for the case of a linearly sloping bed $b(x)$ and, initially, for a uniform sedimentary basin thickness H_{sb}. The numerical methods used to obtain solutions for H_i and N in this chapter are described in Sections A.2 and A.3 of the Appendix.

4.3.1 Ice sheet and effective pressure for weak groundwater flow

Figure 4.2(a)(i) and (ii) show a case where the melt rate $m = 1$ mm yr^{-1} (dimensionless $m = 1$) is relatively low. (It is noted that m is not independent of other parameters, so that the same results could be achieved by rescaling other parameters and variables.) As a result, the sliding law (4.4) closely approximates the limiting case $\tau_b \approx |u|^{m_W}$ away from the grounding line, resulting in a 'convex' ice sheet profile, which becomes steeper in the direction of flow.

Near the grounding line, the sliding stress $\tau_b \to 0$, due to the condition (4.15) that $N \to 0$ as $x \to x_g$. This results in a boundary layer near x_g, where $\tau_b \approx \mathcal{C}N$ and the extensional stress terms in (4.19) become significant. This boundary layer, which determines x_g, has been described by Tsai et al. (2015). In this boundary layer, seen in the inset panel in Figure 4.2(a)(i), the ice profile ceases to be 'convex' and flattens out following a point of inflection.

The corresponding effective pressure is shown in Figure 4.2(a)(ii). Integrating the steady state of Equation (4.33) subject to the no-flux condition (4.14) gives

$$h(N)\frac{\partial}{\partial x}\left((1-\delta_i)H_i - \mathcal{E}N + b\right) + mx = 0. \tag{4.34}$$

Since $\mathcal{E}$ is relatively small, the solution for $N(x)$ follows two approximate solutions in different regions. Away from the grounding line $x = x_g$ (and from $x = 0$), the solution is roughly given by the case when $\mathcal{E} = 0$,

$$h(N) \sim mx\left[-\frac{\partial}{\partial x}\left((1-\delta_i)H_i + b\right)\right]^{-1}, \quad \text{for} \quad x_g - x \gg \mathcal{E}. \tag{4.35}$$

Since $h(N)$ is a decreasing function ($h(N) = 1/N$ is used in particular), Equation (4.35) implies that increasing m decreases N away from the grounding line. Equation (4.35) breaks down for small m, as when h becomes small the large effective pressure

N can no longer be neglected in the hydraulic potential. The counterpart of Equation (4.35) for nonzero κ is presented in Section 4.4.

Near the grounding line, provided that $h(N) \to \infty$ as $N \to 0$, as is the case for the above choice of $h(N)$, the solution to Equation (4.34) is approximately given by equating the hydraulic potential $\psi = (1 - \delta_i)H_i - \mathcal{E}N + b = 0$, such that

$$N \sim \frac{1}{\mathcal{E}} \left((1 - \delta_i)H_i + b \right) \quad \text{for} \quad x_g - x \ll \mathcal{E}. \tag{4.36}$$

(If h is finite but large, Equation (4.36) overestimates N by an amount scaling roughly with $1/h(x_g, t)$.) The effective pressure in Figure 4.2(a)(ii) exhibits a local maximum near the grounding line as the solution transitions from Equation (4.35) to Equation (4.36). The local behaviour (4.36) of N near the grounding line can be thought of as a boundary layer associated with the small parameter $\mathcal{E}$, but should not be confused with the extensional stress boundary layer in the ice sheet associated with the small parameter ε_i. A full analysis of this boundary layer is not included in this thesis, as the $\psi = 0$ and $\mathcal{E} = 0$ approximate solutions are sufficient for the analysis in this chapter. Separate cases are possible, depending on whether the extensional stress boundary layer thickness is much less than $\mathcal{E}$ or $O(\mathcal{E})$.

Because the grounding line position of the ice sheet is determined by the extensional stress boundary layer, in which the sliding stress $\tau_b \sim \mathcal{C}N$, Equation (4.36) suggests that the melt rate m and sedimentary basin do not affect the steady grounding line position to leading order, although they may have a small effect via sub-leading order terms.

Figure 4.2(b)(i) and (ii) show the steady state of the ice and hydrology at a higher melt rate $m = 8$ mm yr^{-1} (dimensionless $m = 8$). Although the ice sheet in Figure 4.2(b)(i) follows a similar 'convex' shape to the $m = 1$ mm yr^{-1} case near the ice divide $x = 0$, it assumes a much shallower shape nearer the grounding line before steepening again. As a result of this shallow portion, the ice sheet is thinner overall, reaching a maximum thickness of around 2500 m, rather than 4000 m as for $m = 1$ mm yr^{-1}. Since the steady state ice flux from (4.18) is simply the integral of the accumulation a, thinner ice must also be faster-flowing.

The reason for this changed shape lies in the effective pressure N, seen in Figure 4.2(b)(ii). When m is increased, the overall size of N away from the grounding line is decreased, following the $\mathcal{E} = 0$ approximate solution (4.35). However, the $\psi = 0$ approximate solution (4.36) still holds near the grounding line, meaning that the effective pressure continues to exhibit a maximum near x_g. In this case, N is sufficiently low that the basal stress given by (4.4) behaves as $\tau_b \sim \mathcal{C}N$, rather than

$\tau_b \sim |u|^{m_W}$, over much of the interior of the ice sheet. Since the basal friction balances the driving stress in (4.19), the reduced basal friction results in a lower $|\partial H_i/\partial x|$ and hence a shallower ice profile. However, near the ice divide $x = 0$, the velocity becomes sufficiently low that the behaviour $\tau_b \approx |u|^{m_W}$ takes over once again, resulting in a reversion to the 'convex' ice sheet profile.

There is also a retreat of the grounding line in Figure 4.2(b)(i) compared to Figure 4.2(a)(i), from around 920 km to 830 km. This retreat is due to the sub-leading order effect of m in the behaviour of N near x_g, which reduces the effective pressure and hence the basal friction in the extensional stress boundary layer of the ice (again visible in the inset panel). As shown by Tsai et al. (2015), the reduced basal friction results in a higher ice flux across the grounding line for a given ice thickness, meaning the ice must reduce its thickness at the grounding line in response. This is achieved by grounding in shallower water (due to the flotation condition), and hence at a more retreated position.

4.3.2 Streamlines of groundwater flow

I now consider the groundwater flow, exfiltration and infiltration for $\kappa \to 0$. Equation (4.16), after non-dimensionalising, gives the exfiltration in the steady state as

$$q_E = \kappa \frac{\partial}{\partial x}\left[H_{sb}\frac{\partial}{\partial x}\left((1-\delta_i)H_i - \mathcal{E}N + b\right)\right]. \tag{4.37}$$

Substituting in Equation (4.34) for the hydraulic potential gradient gives

$$\begin{aligned}\frac{q_E}{\kappa} &\sim -\frac{\partial}{\partial x}\left[H_{sb}\frac{mx}{h}\right] \\ &\sim -\frac{mH_{sb}}{h} - mx\frac{\partial}{\partial x}\left(\frac{H_{sb}}{h}\right).\end{aligned} \tag{4.38}$$

Equation (4.38) implies that a necessary (but insufficient) condition for $q_E \geq 0$ (*i.e.* exfiltration) is that

$$\frac{\partial}{\partial x}\left(\frac{H_{sb}}{h(N)}\right) < 0. \tag{4.39}$$

That is, the ratio of the sedimentary basin thickness to that of the cavity sheet system is decreasing. This condition could be satisfied through the sedimentary basin thickness H_{sb} decreasing in the direction of flow, as considered in the previous chapter. The other possibility is that $h(N)$ is increasing, *i.e.* N is decreasing. Although this is generally expected over most of the domain (as the water flux through the domain increases due to melting), this constraint can provide insight into where exfiltration occurs, as seen below.

The streamlines of groundwater flow in the limit $\kappa \to 0$ with constant $H_{sb} = 2000$ m are plotted in Figure 4.2(a)(i) and (b)(i). In the $m = 1$ mm yr^{-1} case (Figure 4.2(a)(i)), groundwater infiltrates into the sedimentary basin almost everywhere, apart from a small region of exfiltration near the grounding line. This is because the condition (4.39) implies for constant H_{sb} that exfiltration can only occur where $\partial N/\partial x < 0$. Since for $x < 500$ km the steepening gradient of the ice overburden drives infiltration, the region of exfiltration is limited to where N decreases sharply near the grounding line following a maximum.

In the $m = 8$ mm yr^{-1} case (Figure 4.2(b)(i)), however, this pattern is modified by an intermediate region of exfiltration, occurring where the flattening of the ice surface leads to decreasing N following the $\mathcal{E} = 0$ approximate solution (4.35). If κ were increased to a non-negligible value, this exfiltration would further reinforce the lowering of N and consequent flattening of the ice.

Another way to think of q_E, alternatively to Equation (4.38), is in terms of the hydraulic potential ψ. For constant H_{sb}, q_E is proportional to $\partial^2\psi/\partial x^2$ by Equation (4.37). Away from the grounding line, ψ is dominated by the ice overburden H_i, so that the 'convex' ice profile in Figure 4.2(a)(i) leads to infiltration. Exfiltration only occurs near the grounding line, where the $\psi \approx 0$ approximate solution (4.36) leads to a change in sign of $\partial^2\psi/\partial x^2$. In Figure 4.2(b)(i), however, the more complex shape of the ice means $\partial^2\psi/\partial x^2$ temporarily changes sign away from the grounding line, leading to an additional region of exfiltration.

4.4 Steady ice sheet with strong groundwater flow

I now consider the steady states of the model when exfiltration and infiltration are strong enough to impact the hydrology and ice sheet, *i.e.* $\kappa = O(1)$. As mentioned above, realistic values of κ include both small values and $O(1)$ values up to around $\kappa \approx 6$. I begin with the case of of a uniform sedimentary basin thickness $H_{sb} = 2000$ m for simplicity, before considering the additional effect of variation in H_{sb}.

In this case, Equation (4.34) instead reads

$$\left(h(N) + \kappa H_{sb}\right) \frac{\partial}{\partial x}\left((1-\delta_i)H_i - \mathcal{E}N + b\right) + mx = 0, \tag{4.40}$$

and the $\mathcal{E} = 0$ approximate solution (4.35) is instead given by

$$h(N) \sim mx \left[-\frac{\partial}{\partial x}\left((1-\delta_i)H_i + b\right)\right]^{-1} - \kappa H_{sb}, \quad \text{for} \quad x_g - x \gg \mathcal{E}. \tag{4.41}$$

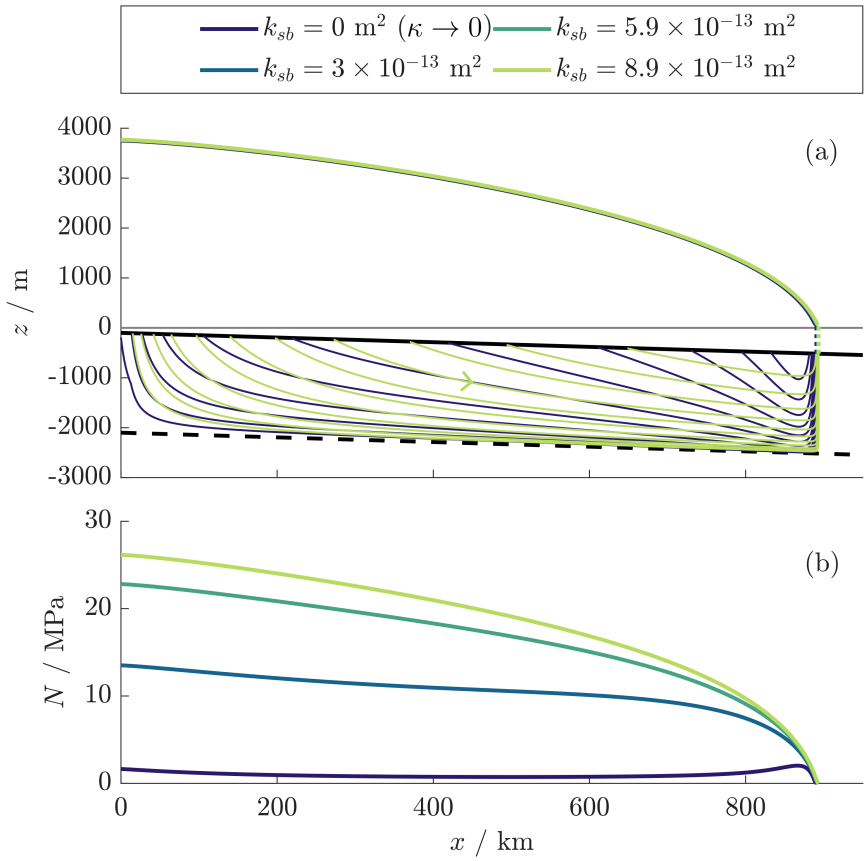


Figure 4.3: (a) Ice sheet profile and sedimentary basins, and (b) effective pressure for a relatively low melt rate $m = 1$ mm yr^{-1} (dimensionless $m = 1$), as in Figure 4.2(a), but with various values of k_{sb} corresponding to $\kappa \ll 1$ and $\kappa = 2, 4, 6$ respectively, and a uniform sedimentary basin thickness $H_{sb} = 2000$ m. The streamlines are only plotted for $k_{sb} = 0$ m^2 and the maximum value of k_{sb}.

4.4.1 Low-moderate melt rate

I first consider the case where $m = 1$ mm yr^{-1} (dimensionless $m = 1$) is sufficiently small that the ice sheet is largely unaffected by subglacial hydrology, as seen previously in Figure 4.2(a). This initial case demonstrates the effect of groundwater on the effective pressure N with the ice sheet held roughly constant. Figure 4.3(a) shows the resulting ice sheet and streamlines, and Figure 4.3(b) shows the effective pressure, for different values of κ.

The main influence of the flow in the sedimentary basin is to increase the effective pressure N, with a greater increase for higher κ. This increase in N can be seen from the $\mathcal{E} = 0$ approximate solution (4.41), and is a consequence of the fact that the total meltwater flux mx must be shared between the sedimentary basin and the cavity sheet, leading to a lower effective water thickness h when κ is larger.

These results can be better understood by considering the limit $\kappa \to \infty$, in which the sedimentary basin dominates subglacial water transport. In this case, Equation (4.38) gives

$$q_E \sim -m + \frac{1}{\kappa}\frac{\partial}{\partial x}\left(\frac{mxh}{H_{sb}}\right) + O\left(\frac{1}{\kappa^2}\right), \tag{4.42}$$

so that the infiltration is simply given by the melt rate at leading order, except in a small region where $h = O(\kappa)$ near the grounding line. In this case, the '$\mathcal{E} = 0$' approximate solution (4.41) away from the grounding line breaks down. Instead, the horizontal groundwater flux is determined by the melt rate, and the effective pressure is determined by the required hydraulic gradient, so Equation (4.40) gives

$$\frac{\partial}{\partial x}\left((1-\delta_i)H_i - \mathcal{E}N + b\right) = -\frac{mx}{h + \kappa H_{sb}} \approx 0 \tag{4.43}$$

This therefore gives

$$N \sim \frac{1}{\mathcal{E}}\left((1-\delta_i)H_i + b\right), \tag{4.44}$$

which resembles the '$\psi = 0$' approximate solution (4.36). This explains why, for the higher values of k_{sb} in Figure 4.3, N closely resembles the ice overburden.

For the nonzero k_{sb} considered in Figure 4.3, N attains very large values. This is partly because the values of k_{sb} used are at the higher end of what is physically realistic. However, it is worth noting that in reality, at high effective pressures the ice would likely infiltrate the upper layers of sediment to form a 'frozen fringe', significantly reducing the permeability, which I discuss further in Section 4.6.

The approximate solution (4.41) suggests for constant H_{sb} that the sedimentary basin has a larger effect when the distance from the ice divide x is small, or the hydraulic potential gradient is steep. When $m = 1$ mm yr^{-1}, the hydraulic potential gradient becomes steeper with increasing x, so that these competing effects even out to a relatively uniform effect of increasing κ. As predicted previously, N follows the $\psi = 0$ approximate solution (4.36) near the grounding line independent of κ, so that the sedimentary basin has little effect on the extensional stress boundary layer of the ice and resulting grounding line position x_g.

4.4.2 High melt rate

Figure 4.4 shows the effect of strong groundwater flow on the steady state ice sheet and hydrology for the higher melt rate $m = 8$ mm yr^{-1} (dimensionless $m = 8$), where the hydrology affects the ice profile, as seen previously in Figure 4.2(b).

When the groundwater flow is weak, the low effective pressure results in a region of the ice with small surface slope, with a localised region of groundwater exfiltration

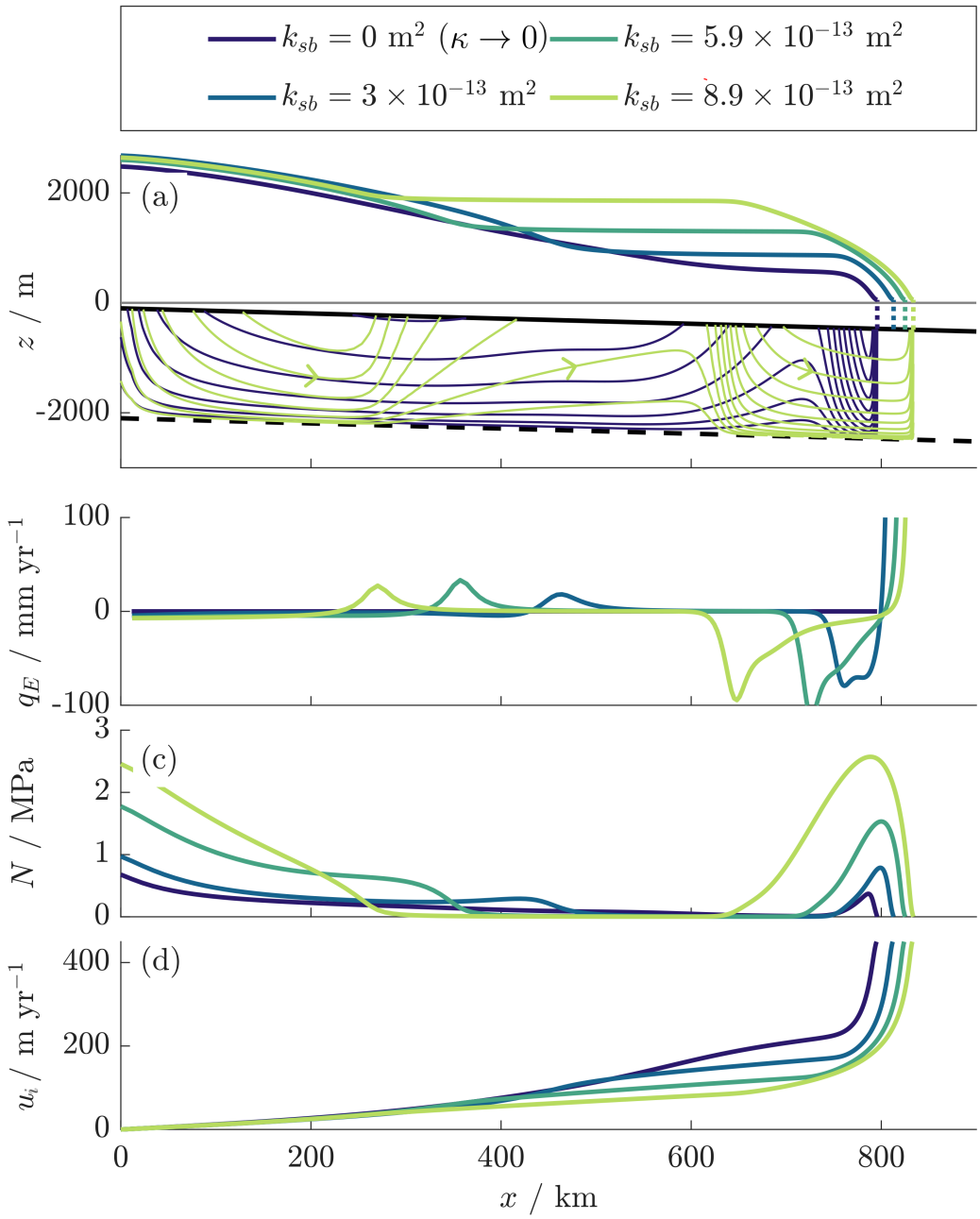


Figure 4.4: (a) Ice sheet profile and sedimentary basin streamlines, (b) exfiltration q_E, (c) effective pressure, and (d) ice velocity for a higher melt rate $m = 8$ mm yr^{-1} (dimensionless $m = 8$), as in Figure 4.2(b). The various values of k_{sb}, the sedimentary basin thickness H_{sb}, and the plotted streamlines are as in Figure 4.3.

slightly upstream. For strong groundwater flow, this exfiltration causes the region of low effective pressure to spread further upstream, in turn causing the region of exfiltration to move upstream, as seen in Figure 4.4(b). The corresponding change in the effective pressure is seen in Figure 4.4(c). Away from this region of low effective pressure, the presence of a more permeable sedimentary basin increases N, with the effect strongest where the hydraulic gradient (*i.e.* the ice sheet profile) is steepest, near the ice divide and grounding line.

The effect on the ice sheet, along with the groundwater flow streamlines, is shown in Figure 4.4(a). As the region of low effective pressure moves upstream with increasing κ, the corresponding region where the ice surface is relatively flat follows. The increase in effective pressure near the grounding line leads to a larger region where the basal friction is high, and the ice profile relatively steep as a result. The larger steep region leads to a larger ice thickness overall, as ice accumulates behind the region of increased friction. Since the ice flux is given by $H_i u_i = ax$ in the steady state, the thickening of the ice sheet when κ is increased corresponds to a reduced ice velocity, as shown in 4.4(d).

Finally, a small advance of the grounding line can be observed as κ is increased. This effect emerges because increasing κ raises the effective pressure close to the grounding line at sub-leading order, similarly to if m were decreased. The increased friction results in a lower ice flux for the same ice thickness, so that the ice is forced to ground in deeper water and hence at a larger x.

As κ increases, both the thickening of the ice and the advance of x_g increase the overall volume of the ice sheet (defined as the integral of H_i with respect to x). The volume of the ice sheet increases relative to the $\kappa \ll 1$ case by 13%, 20% and 37% for $\kappa =$, 2, 4 and 6 respectively.

These results indicate that groundwater flow in sedimentary basins has the potential to significantly affect the steady-state thickness and velocity of an ice sheet. This is because the sedimentary basin can drain water away from certain regions of the subglacial hydrological system, locally increasing the effective pressure, and exfiltrate this water elsewhere to create regions of low effective pressure in a self-reinforcing feedback. The sedimentary basin also results in a slightly more advanced steady grounding line position. It is therefore important to consider sedimentary basin groundwater flow in models for subglacial hydrology and basal friction, and that such groundwater flow could help to explain regions of locally high or low basal friction.

It should be noted, however, that in reality the effect of groundwater flow is unlikely to be as extreme as in Figure 4.4. As mentioned above, this is because this Figure focuses on the highest values of k_{sb} for illustrative purposes. However, this model also neglects certain dynamic effects that would likely prevent the predicted regions of near-flat ice surface from being achieved in reality. Notably, ice streams are typically confined between regions of slower-flowing ice, which restrict sliding of the ice by exerting a lateral shear stress, something that the one-dimensional ice sheet model used above neglects. I discuss this and other limitations of working in a single horizontal dimension in Section 4.6.

4.4.3 Effects of sedimentary basin geometry

So far I have worked with a uniform sedimentary basin thickness H_{sb}. However, in the previous chapter, I found that thinning and thickening of a sedimentary basin can drive exfiltration and infiltration respectively. I therefore investigate the consequences of variations in sedimentary basin geometry in Figure 4.5, using an idealised sedimentary basin thickness $H_{sb} = 750 - 500\cos(2\pi x/250 \text{ km})$ m. The ice sheet profile and streamlines for various κ are shown in Figure 4.5(a), and it can be seen from the latter that several regions of exfiltration and infiltration emerge.

The effective pressure in Figure 4.5(b) shows the effect of this exfiltration and infiltration, which result in local peaks in N where the sedimentary basin is thickening (infiltration) and troughs where the sedimentary basin is thinning (exfiltration). These are most prominent in the middle of the domain.

In the ice sheet in Figure 4.5(a), it is possible to see the effect of these changes in the effective pressure on the ice profile. The local trough in effective pressure produces a plateau-like region of flatter surface slope, whereas the local peak produces a steeper region, resulting in a staggered shape. The net effect of this steepening and flattening on the ice thickness further inland is negligible, so that the effect of the sedimentary basin geometry is localised. The ice thickness at $x = 500$ km increases by around 4%, 10% and 18% for κ =1, 2 and 3 respectively, suggesting that the response of H_i to increasing κ itself becomes stronger as κ increases.

These results suggest, in addition to their permeability, the geometry of sedimentary basins is important in determining their effect on the ice sheet. Moreover, they suggest that the ice sheet profile may give an indication of the properties of the underlying sedimentary basin. In particular, regions of steeper or flatter ice may suggest a change in basal friction, which could be explained by local variations in sedimentary basin geometry driving exfiltration and infiltration.

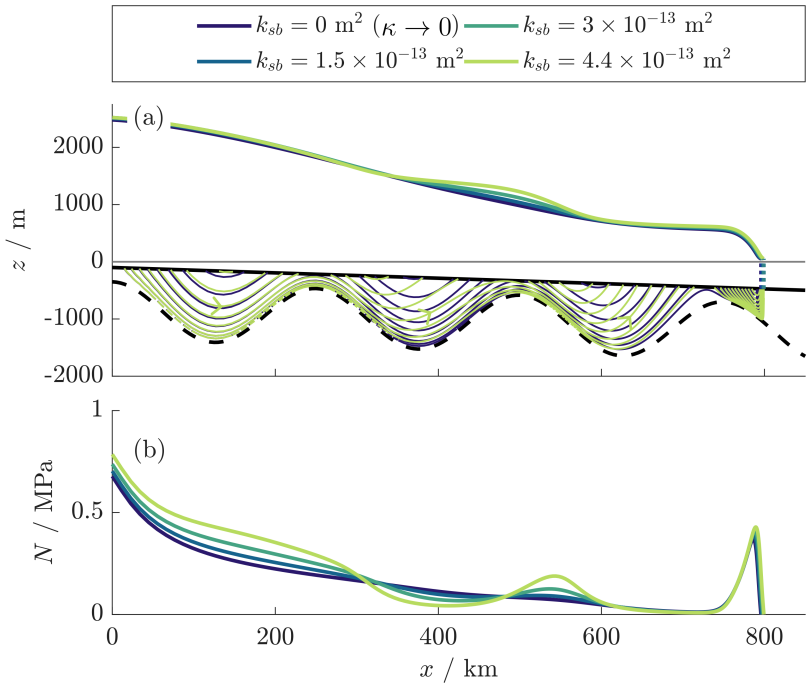


Figure 4.5: (a) Ice sheet profile and sedimentary basin streamlines and (b) effective pressure for a nonuniform sedimentary basin thickness $H_{sb} = 750 - 500\cos(2\pi x/250 \text{ km})$ m, and for a melt rate of $m = 8$ mm yr^{-1} (dimensionless $m = 8$). The various values of k_{sb} correspond to $\kappa \ll 1$ and $\kappa = 1$, 2, 3, and the plotted streamlines are as in Figures 4.3 and 4.4. (Note that in (a), as elsewhere, the aspect ratio is exaggerated for illustrative purposes.)

4.5 Groundwater feedback during grounding line motion

I now turn my consideration to transient solutions of the model, in order to investigate the effect of compaction-driven exfiltration (the second term in Equation (4.16)). Since this depends on $\partial H_i/\partial t$ and $\partial N/\partial t$, it does not appear in the previous steady state solutions, which only include topographically-driven exfiltration. For this section I continue to include the latter (using a modest but nonzero k_{sb}), but focus on the effect of the former.

A canonical transient solution is evolution of the system towards a steady state. This case can be brought about when a parameter of the model, such as the accumulation a, rapidly changes, meaning that the ice sheet is no longer in a steady state and must advance or retreat to a new one. Similar scenarios has been investigated in prior studies of ice and hydrology (*e.g.* Lu and Kingslake, 2023), and additionally resemble the behaviour of the ice after crossing 'tipping points' that can emerge from

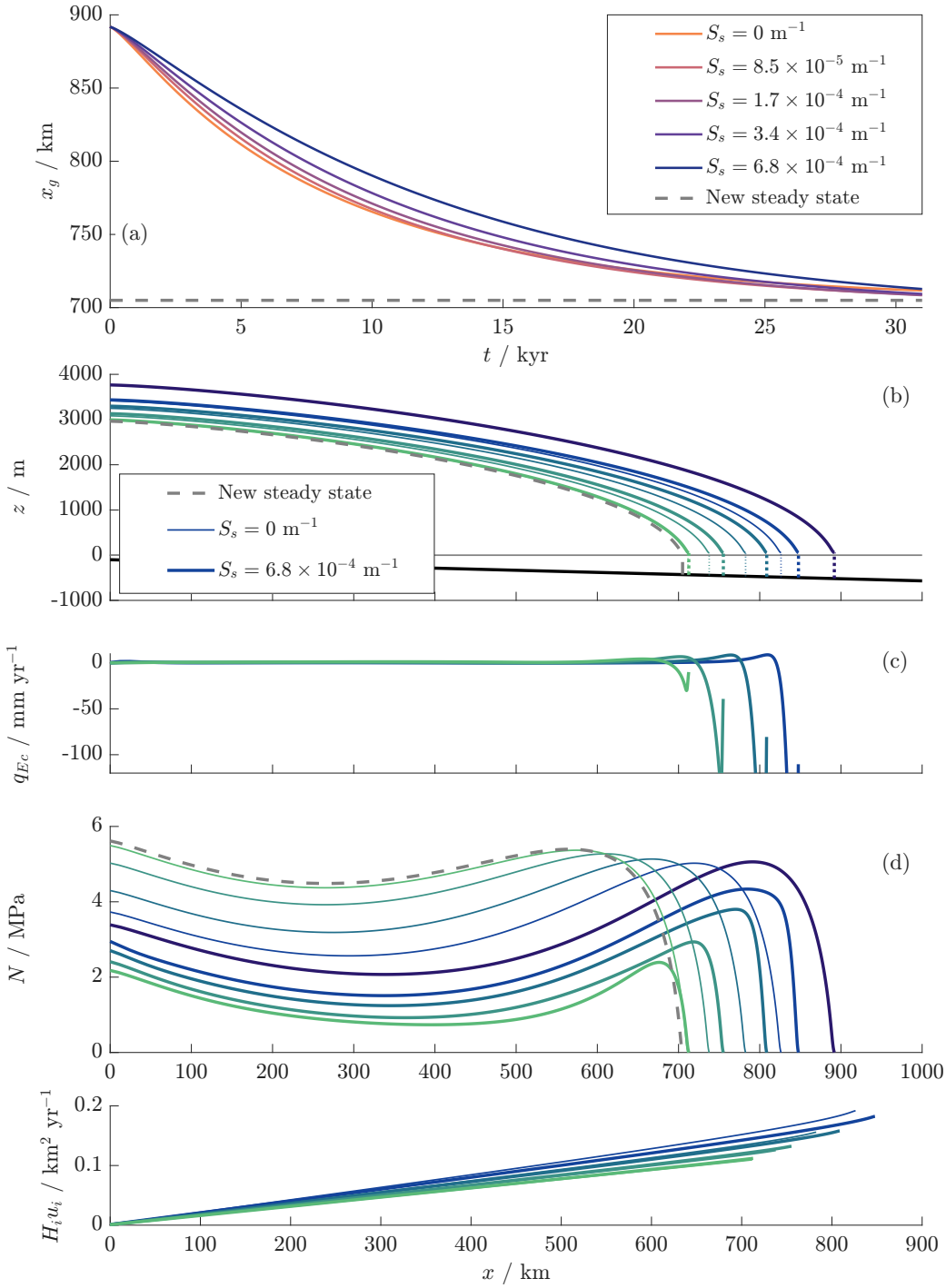


Figure 4.6: (a) Grounding line position $x_g(t)$, retreating to a steady state following a step decrease of the accumulation a, for various values of S_s corresponding to $\Sigma = 0$, 60, 120, 240, 480 respectively, $m = 1$ mm yr^{-1}, $k_{sb} = 1.6 \times 10^{-13}$ m^2, and otherwise as in Figure 4.3. (b) Ice sheet thickness H_i, (c) compaction-driven exfiltration q_{Ec} (see Equation (4.17)), (d) effective pressure N, and (e) ice flux $H_i u_i$ at times $t = 0$, 3.9, 7.8, 15.7 and 31 kyr, for $S_s = 0$ and its maximum value above. A lighter and greener colour indicates later times.

non-monotone bed geometry (Schoof, 2007a). A change in the accumulation a could act as a simple representation of climate change.

In this section, I show that, when the ice is retreating towards a steady state, compaction-driven exfiltration provides a negative feedback that slows this retreat. Using the same linear prograde bed $b(x)$ as above, and with constant sedimentary basin thickness $H_{sb} = 2000$, melt rate $m = 1$ mm yr^{-1} and $k_{sb} = 1.6 \times 10^{-13}$ m^2, the system is initialised in a steady state with $a = 0.3$ m yr^{-1}. The value is then step-changed to $a = 0.15$ m yr^{-1}, so that the steady state grounding line is moved further back, requiring the ice sheet to retreat towards the new steady state. This scenario is repeated for different values of Σ, the parameter determining the strength of compaction-driven exfiltration, which are achieved by varying the parameter S_s. As mentioned previously, realistic values of S_s give Σ ranging from 0.07 to 70, but in this section some larger-than-realistic values of Σ are included for illustrative effect.

The results of this experiment are shown in Figure 4.6. Figure 4.6(a) compares the grounding line position $x_g(t)$ over time for various values of Σ. It can be seen that increasing Σ (via S_s) makes this retreat slower. The largest difference is seen between around 5–15 kyr, roughly following where the curve $x_g(t)$ is steepest. The mechanism behind this acceleration is shown in Figures 4.6(b), (c), (d), and (e), which show the ice sheet profile, the compaction-driven part of the exfiltration q_{Ec} (see Equation (4.17)), the effective pressure N, and the ice flux $H_i u_i$ at selected points in time, for the cases with and without compaction-driven exfiltration ($\Sigma = 0$ and $\Sigma = 480$).

As seen in Figure 4.6(b), the retreat of the ice leads to ice thinning ($\partial H_i/\partial t < 0$), which is most pronounced near the grounding line as the surface slope is steepest. Seen in Figure 4.6(c), this leads to a small amount of exfiltration in the interior of the ice, but a larger amount of infiltration in a small region close to the grounding line. As a result, the effective pressure N (Figure 4.6(d)) is lowered compared to when $\Sigma = 0$ away from the grounding line (as exfiltration increases the effective water thickness h), but increases compared to the $\Sigma = 0$ case within the region of infiltration near the grounding line. The local increase in N increases the basal friction near the grounding line, which decreases the ice flux across the grounding line (Figure 4.6(e)) and hence slows the rate at which the ice retreats.

To explain why compaction drives exfiltration over most of the domain but infiltration near the grounding line, the governing equation (4.33) is revisited. Assuming that $\lambda \ll \Sigma\mathcal{E}$, as is the case for the relatively large Σ considered here, this equation

can be approximately rearranged to

$$0 = \frac{\partial}{\partial x}\left[(h + \kappa H_{sb})\frac{\partial}{\partial x}\left((1-\delta_i)H_i - \mathcal{E}N + b\right)\right] + m \\ - \Sigma H_{sb}\left((1-\delta_i)(1-\xi)\frac{\partial H_i}{\partial t} - \mathcal{E}\frac{\partial N}{\partial t}\right). \quad (4.45)$$

Taking $\lambda \approx 0$ means that h, and hence N, responds instantaneously to the current values of the source terms (melting and exfiltration/infiltration). However, the compaction-driven exfiltration itself depends on the resulting rate of change of N.

Away from the grounding line, $\mathcal{E}N$ is smaller than $(1-\xi)H_i$. This means that ice thinning ($\partial H_i/\partial t < 0$) leads to a net exfiltration, as this term dominates the compaction-driven exfiltration (via the expansion of the pore water). This exfiltration increases h, leading to a decrease in the effective pressure ($\partial N/\partial t < 0$). However, crucially, the rate at which N decreases is not large enough to change the overall sign of the compaction term.

However, close to the grounding line, as in the steady state, N obeys the $\psi = 0$ approximate solution (4.36) as a result of the boundary condition $N = 0$ at $x = x_g$. This implies that when H_i decreases, N must decrease accordingly,

$$\frac{\partial N}{\partial t} \approx \frac{1}{\mathcal{E}}\frac{\partial H_i}{\partial t} \quad \text{near} \quad x = x_g. \quad (4.46)$$

The compaction term is therefore approximately

$$q_{Ec} = -\Sigma H_{sb}\left((1-\delta_i)(1-\xi)\frac{\partial H_i}{\partial t} - \mathcal{E}\frac{\partial N}{\partial t}\right) \approx \Sigma H_{sb}(1-\delta_i)\xi\frac{\partial H_i}{\partial t}, \quad (4.47)$$

so that ice thinning ($\partial H_i/\partial t < 0$) instead leads to a net infiltration. This infiltration is driven by dilation of the porous medium, while the expansion of the pore water is negligible because the pore pressure remains close to hydrostatic. Because this infiltration exceeds the total exfiltration over the interior (*i.e.* $\int_0^{x_g} q_{Ec}\,\mathrm{d}x < 0$), the resulting effect is that N is higher near the grounding line for $\Sigma > 0$ than for $\Sigma = 0$.

It is also to possible consider grounding line advance (rather than retreat) following a step increase in a, a case of which is shown in Figure 4.7. In this case, the ice thickens rather than thins, so that compaction drives infiltration and increased N away from the grounding line, but drives exfiltration and reduced N near the grounding line. The reduced effective pressure lowers the basal friction, increasing the ice flux across the grounding line (Figure 4.7(e)). This leads to slower advance of the ice, because ice flows into the ice shelf rather than accumulating behind the grounding line.

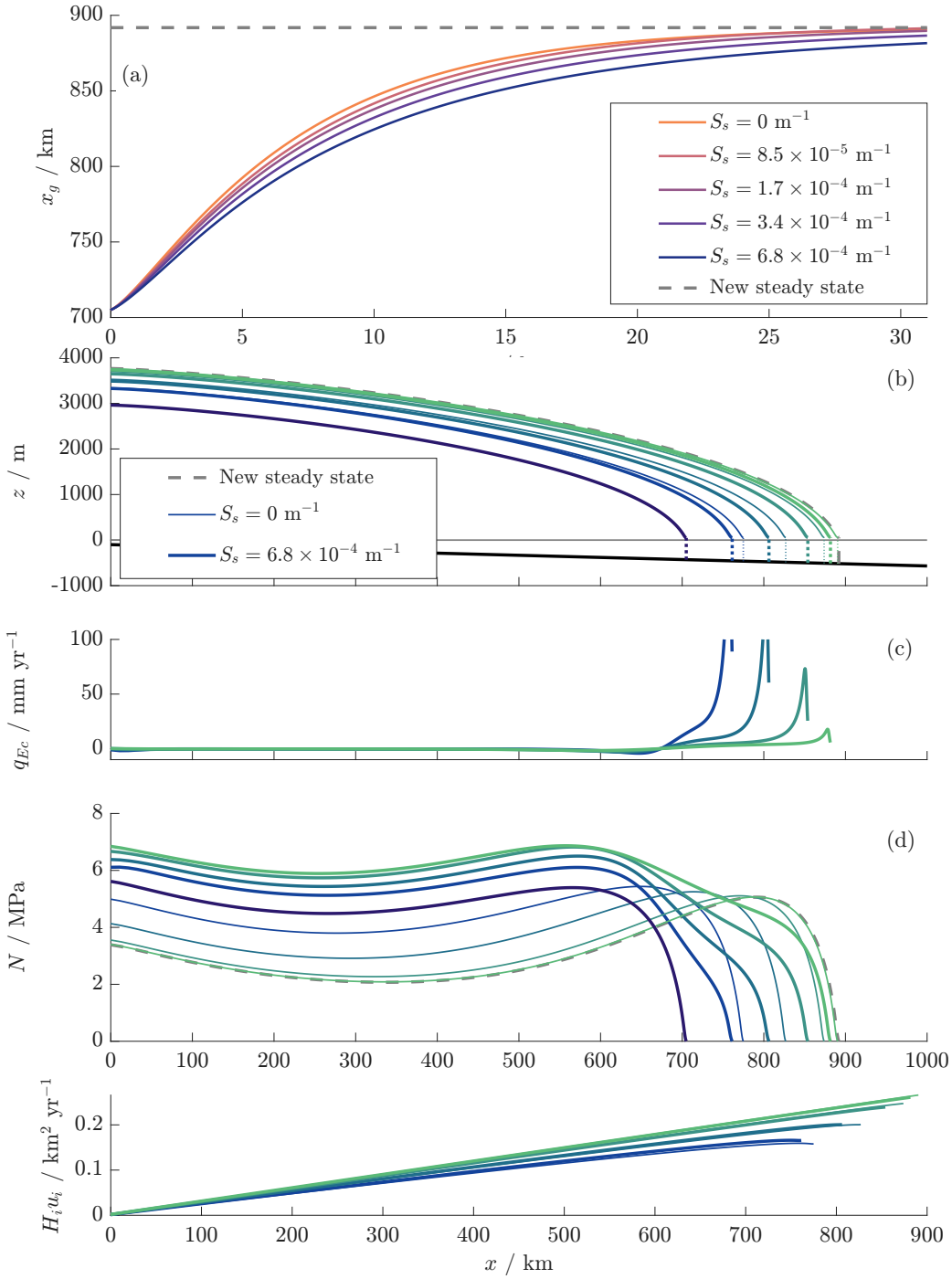


Figure 4.7: (a) Grounding line position $x_g(t)$, advancing to a steady state following a step increase in accumulation from $a = 0.15\,\mathrm{m\,yr^{-1}}$ to 0.3 m yr^{-1} at time 0, and otherwise as in Figure 4.6. (b) Ice sheet thickness H_i, (c) compaction-driven exfiltration q_{Ec}, and (d) effective pressure N, as in Figure 4.6.

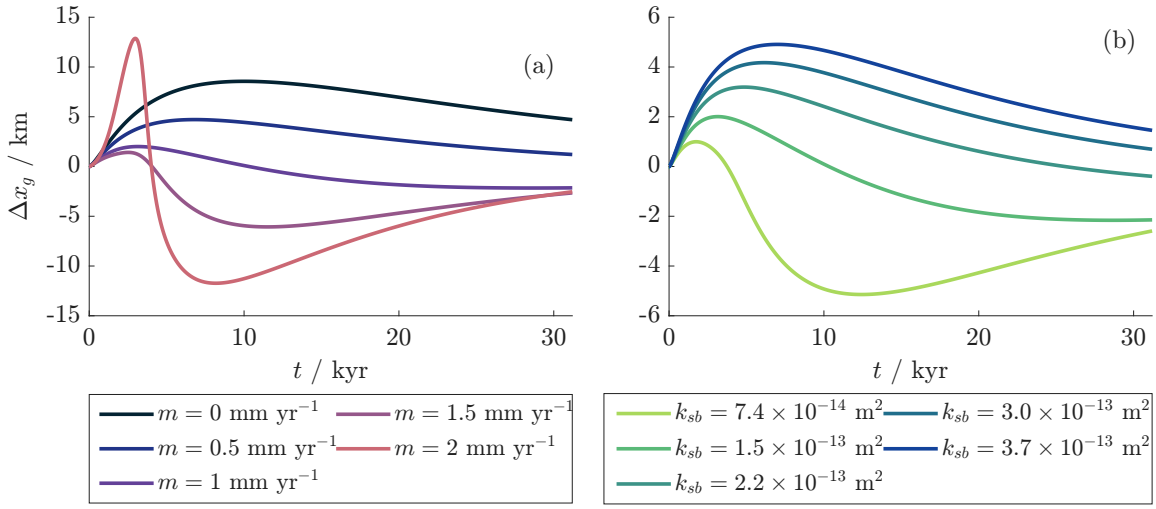


Figure 4.8: Difference in grounding line position $\Delta x_g(t) = x_g(t; \Sigma = 30) - x_g(t; \Sigma = 0)$ between the cases when $S_s = 4.3 \times 10^{-5}$ m^{-1} and $S_s = 0$ m^{-1} ($\Sigma = 30$ and $\Sigma = 0$) for the retreat scenario considered in Figure 4.6. The value of $\Delta x_g(t) > 0$ if the retreat is slowed, as in Figure 4.6. This is plotted for (a) varying m corresponding to dimensionless $m = 0$, 0.5, 1, 1.5, 2 with fixed $k_{sb} = 1.6 \times 10^{-13}$ m^2 (b) varying k_{sb} corresponding to $\kappa = 0.5$, 1, 1.5, 2, 2.5 with fixed $m = 1$ mm yr^{-1}.

A remaining question is how the strength of the response to compaction-driven exfiltration and infiltration varies with m and κ. Figure 4.8 shows plots of $\Delta x_g(t) = x_g(t; \Sigma = 30) - x_g(t; \Sigma = 0)$, the relative difference in the grounding line positions between the cases when $S_s = 4.3 \times 10^{-5}$ m^{-1} and $S_s = 0$ m^{-1} ($\Sigma = 30$ and $\Sigma = 0$), over time for a range of m (Figure 4.8(a)) and k_{sb} (Figure 4.8(b)). A positive value of Δx_g implies that retreat is slowed. Generally, the effect is stronger if less water is present at the bed overall, since compaction-driven exfiltration then has a larger effect on the subglacial hydrology. This means the feedback is stronger if m is lower or if κ is higher. However, for higher values of m, or lower values of κ, the effect is weakened or even reversed, so that compaction accelerates retreat rather than slowing it. I hypothesise that this is because when the effective pressure is lower overall, the compaction-driven exfiltration beneath the interior of the ice sheet is strengthened, whereas the infiltration close to the grounding line is weakened and more localised. Once m is sufficiently high (or κ sufficiently low), the overall exfiltration exceeds the infiltration (*i.e.* $\int_0^{x_g} q_{Ec}\,\mathrm{d}x > 0$), so that N is lowered overall at the grounding line rather than increased.

The results of this section indicate that, as well as affecting the steady states, sedimentary basins can also influence the transient dynamics of the ice-sheet-hydrology system through the separate process of compaction-driven exfiltration and infiltration.

In particular, these processes provide a feedback that slows both retreat and advance of the grounding line, which has potential significance when projecting the future of Antarctic ice streams that overlie sedimentary basins and are currently undergoing grounding line motion. These results depend on the behaviour of the effective pressure near the grounding line, and are sensitive to the melt rate and sedimentary basin permeability as a result.

4.6 Discussion

In this chapter, I have developed an idealised two-way coupled model of ice flow and subglacial hydrology, including a sedimentary basin which exchanges groundwater with the subglacial hydrological system. I found that exfiltration generally occurs close to the grounding line and infiltration close to the ice divide, but that exfiltration can also occur inland if the ice profile is becoming flatter in the direction of flow. Exfiltration and infiltration can also be driven by thinning and thickening of the sedimentary basin respectively.

Due to their effect on the water balance in the subglacial drainage system, regions of exfiltration locally lower the effective pressure, and infiltration increases the effective pressure. If the sliding of the ice is dominated by the subglacial effective pressure, then these changes in effective pressure in turn lead to a steeper ice profile above areas of infiltration and a shallower plateau-like profile above areas of exfiltration. Overall, a thinner or more permeable sedimentary basin leads to thicker and slower-flowing ice in the steady state, due to certain localised increases in effective pressure.

Transient changes in the basal water pressure and effective pressure also produce compaction-driven exfiltration and infiltration. During ice sheet retreat (for example due to a changing climate), compaction-driven exfiltration near the grounding line can decelerate the process of retreat by increasing the effective pressure, and hence the basal friction, near the grounding line. Conversely, compaction-driven infiltration near the grounding line can decelerate grounding line advance by reducing the effective pressure. These results suggest that groundwater feedback could help to delay the sea-level rise and ice loss resulting from climate change, although further modelling work is required to determine whether this effect could be significant for existing Antarctic glaciers undergoing retreat.

The model in this chapter includes a number of idealising assumptions, in order to be simple to use and easy to interpret. However, there are a number of ways in which

the theory in this chapter could be extended to represent other features of Antarctic groundwater flow.

Firstly, the model considers only one horizontal dimension, limiting its ability to be applied in modelling specific Antarctic ice streams. Lateral variations in topography could influence both ice flow and the routing of subglacial water. Moreover, laterally-confining shear stresses could play a significant role on ice stream dynamics, and in particular could explain why regions of flat ice surfaces as seen in this chapter are seldom observed in practice. In addition, lateral narrowing or broadening of the sedimentary basin could drive groundwater exfiltration or infiltration respectively, similarly to vertical thinning and thickening. Future work could therefore use the expression for the exfiltration q_E derived in Chapter 2, Section 2.2, within a three-dimensional model for subglacial hydrology and ice flow.

This model also assumes an isotropic and homogeneous permeability of the sedimentary basin, although this assumption is unlikely to be accurate in reality. The generalisation of the groundwater flow model to include heterogeneity presented in Chapter 2, Section 2.4, could be used to investigate the importance of heterogeneity for the feedbacks presented in this chapter, provided that the Dupuit model remains valid for the cases considered.

In this chapter, I have only considered one choice of bed topography $b(x)$, given by a linear prograde bed. Previous studies have shown that more realistic bed topographies can lead to complex ice dynamics, such as multiple steady states, hysteresis, and bifurcations as parameters are varied (Schoof, 2007a). Although such cases are beyond the scope of this chapter, the findings here concerning the steady states and dynamic behaviour of this model generalise to more complex geometries. For instance, compaction-driven exfiltration and infiltration ought to decelerate the grounding line retreat or advance that occurs after a bifurcation emerging from bed topography is crossed.

I have also only considered a single sliding law, the regularised Coulomb law (4.4), in coupling the ice sheet to the hydrological system. A more comprehensive study could consider a range of sliding laws, along with different values of parameters such as $\mathcal{C}$ and m_W (as in *e.g.* Brondex et al., 2019; Gregov et al., 2023). However, the results of this study should generalise to any sliding law in which the basal stress is an increasing function of effective pressure, with the caveat that the parameters of the sliding law will determine the overall strength of the coupling.

The treatment of subglacial hydrology in this chapter, based on a simple cavity-sheet model, is also deliberately simplified in order to be easy to solve and understand.

While a simple model of this form ought to broadly agree with more complex models over the long timescales I consider (De Fleurian, 2018), it may not be appropriate if the drainage system is dominated by flow in subglacial channels. Channels would be expected to form if the subglacial water flux becomes sufficiently large, and lead to an instability where larger channels drain water away from smaller ones (Flowers, 2015). Due to their dynamics, effective pressure is generally increased near to such channels and lowered between them (Boulton et al., 2007; Rempel, 2009). However, the modelling of subglacial channels requires consideration of thermodynamic effects, since channels open by melting in response to heat dissipation by the subglacial flow, which I discuss further below.

Even within the cavity-sheet framework, I have made simplifying assumptions, such as the form of the relationship $h(N)$, and in particular the fact that $h \to \infty$ as $N \to 0$. As mentioned above, a more accurate model would have $N \to 0$ once h exceeds a finite height corresponding to the thickness at which topographic obstacles are completely submerged. The use of such a model may modify the '$\psi = 0$' approximate solution for N here (Equation (4.36)), and consequent results such as the feedbacks on grounding line motion considered in Section 4.5, although the '$\psi = 0$' approximate solution should remain roughly accurate provide the limiting value of h is relatively large. These considerations highlight the need for future work incorporating groundwater flow into a wider range of subglacial hydrology models, in particular models that are able to account for different modes of subglacial water transport.

For simplicity, I have treated the melt rate as spatially uniform and prescribed, for example by a uniform geothermal heat flux. This neglects melting due to frictional heating, which depends on the ice velocity and basal stress, introducing another coupling to the model. However, for fast-flowing ice streams, such heating is likely to be significant, and even to dominate the energy budget. For example, for a Weertman sliding law (2.103) with the above choice of C_W, a sliding velocity of 200 m yr^{-1} implies a frictional heat flux of $\tau_b u = C_W u^{m_W+1} = 890$ mW m^{-2}, compared to estimated geothermal heat fluxes ranging from 30–150 mW m^{-2} across Antarctica (Burton-Johnson et al., 2020; Stål et al., 2021).

A more accurate modelling approach would calculate the melt rate m using an energy balance at the bed. This energy balance, which I consider in the following chapter, should include geothermal heating and basal friction, as well as conduction into the ice. Calculated in this way, m would increase with x following the ice velocity over most of the domain, but decrease near the grounding line, where the friction vanishes. Such an energy balance would introduce further coupling between the ice

and hydrology, since for rapid sliding the friction τ_b is approximately $C_C N$, yet a higher friction leads to a lower N by increasing the melt rate m. A model for an ice stream coupled via sliding to subglacial hydrology that includes such an energy balance among other thermal effects has been considered by Haseloff et al. (2025). Including such an energy balance could allow for further investigation of thermal effects, such as the feedback of groundwater flow on basal melting via modification of geothermal heat flux, which forms the focus of the following chapter.

Incorporating thermodynamics into the model could moreover allow for a description of basal freeze-on and frozen fringe formation, which would be expected for the higher effective pressures in this chapter (Rempel, 2008). Where the bed is frozen, the permeability of the subglacial hydrological system is effectively zero, and the sliding of the ice is also inhibited (Meyer et al., 2018; Hansen et al., 2024). In such a region, the 'exfiltration' must match the rate at which ice is accreted onto the frozen fringe (Christoffersen and Tulaczyk, 2003b). In reality, large parts of the Antarctic ice-bed interface are likely to be frozen, and a hydrology model incorporating this should include a frozen region as a free boundary. This free-boundary problem is important in enabling ice streaming, with ice streams above thawed bed confined by slower-moving ice above frozen bed (Schoof and Mantelli, 2021). A potential consequence of groundwater flow for this problem is that groundwater can flow beneath regions of frozen bed. This allows for the thawed and frozen regions to exchange water and heat with one another, and could moreover enable water transport between two thawed regions separated by a frozen region.

4.7 Conclusions

In this chapter, I have coupled groundwater flow into a model of subglacial hydrology and ice sliding. I have found that groundwater exfiltration promotes sliding by reducing basal friction, whereas infiltration increases friction. The presence of a sedimentary basin leads to thicker and slower-flowing ice in the steady state due to groundwater infiltration away from the grounding line. In addition, compaction-driven infiltration and exfiltration near the grounding line can slow down ongoing grounding line retreat and advance respectively. The latter feedback is of wider interest for ice sheet modelling, as it may be able to partially counteract existing positive feedback mechanisms in ice sheet retreat, such as the marine ice sheet instability (Schoof, 2007a).

Chapter 5

Modification of Antarctic geothermal heat flux by groundwater flow

5.1 Introduction

As previously discussed, a further way in which Antarctic sedimentary basins could influence ice dynamics is through their potential effect on heat transport to the ice bed. In particular, groundwater could advect heat as it circulates, thereby producing local variations in geothermal heat flux to the ice bed (Gooch et al., 2016; Tankersley et al., 2022). However, existing models of Antarctic geothermal heat flux have not yet accounted for possible effects of groundwater (Reading et al., 2022), and the presence of groundwater in Antarctic sedimentary basins is a source of uncertainty in current models of Antarctic geothermal heat flux (Aitken et al., 2023).

Geothermal heat flux consists of conduction from the mantle, alongside radiogenic heat production in the crust (Stål et al., 2021), and influences ice flow through its effect on the ice temperature and energy balance at the bed. The ice temperature is important because the ice rheology is temperature-dependent. Geothermal heat flux can also facilitate sliding of the ice by thawing the bed, and by contributing to the production of meltwater, which enters the subglacial hydrological system (Burton-Johnson et al., 2020). As a result, localised regions of elevated geothermal heat flux can significantly influence ice dynamics (Pittard et al., 2016). Moreover, resolving small-scale variations in geothermal heat flux can lead to higher overall estimated melt rates (McCormack et al., 2022). A map of estimated geothermal heat flux beneath Antarctica is shown, and is compared with estimated sedimentary basin thickness, in Figure 5.1.

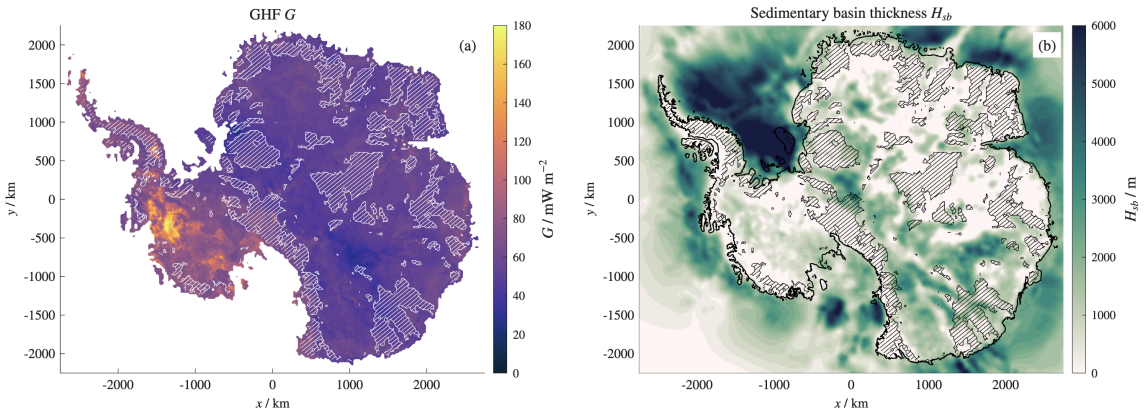


Figure 5.1: (a) Modelled Antarctic geothermal heat flux (without modification by groundwater flow) from Stål et al. (2021). (b) Modelled sedimentary basin thickness from Li and Aitken (2024). Probable frozen regions of the ice bed, based on Seiner et al. (2025), are masked with hatches in both instances.

Overall, the thermal state of the ice bed is considered one of the largest sources of uncertainty in predicting future Antarctic ice loss, with a warmer ice bed leading to higher predicted ice loss (Dawson et al., 2022). Therefore, it is important to predict and constrain geothermal heat flux could be locally modified by groundwater flow.

Although groundwater flow has been considered in models of localised freezing and thawing near the ice bed (*e.g.* Christoffersen and Tulaczyk, 2003b), considerations of heat transport in existing models of large-scale groundwater flow in Antarctic sedimentary basins are currently limited. In a notable exception, Gooch et al. (2016) found, using a one-dimensional vertical model, that groundwater flow upwards and downwards could significantly enhance or reduce geothermal heat flux. By incorporating a horizontal dimension into a similar model, Li et al. (2022) found that groundwater flow during ice sheet retreat could enhance heat flux to the ice bed by up to 5 mW m^{-2} (in supplementary material). However, these investigations are currently limited to realisations of individual numerical experiments, which cannot straightforwardly be generalised to make predictions.

In this chapter, I present a mathematical model for groundwater flow in a sedimentary basin, including both horizontal and vertical flow and compaction of the basin, combined with heat transport. I firstly explore the predictions of this model in an idealised cross-section of an Antarctic sedimentary basin, and derive a reduced-order approximation for the modification of the geothermal heat flux by groundwater flow. I then apply this approximation to existing geophysical models of Antarctic heat flux and sedimentary basin thickness, in order to investigate the extent to which

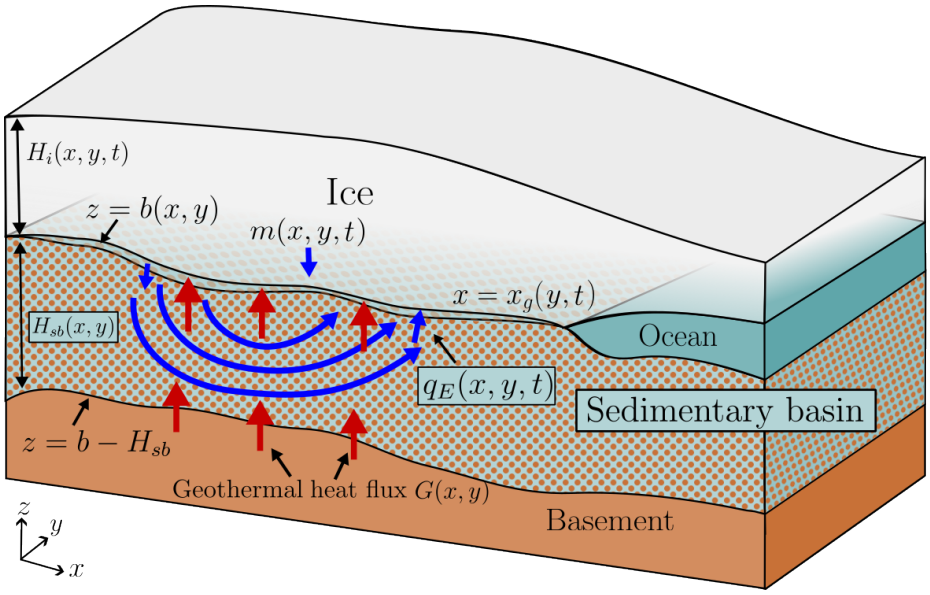


Figure 5.2: Schematic of the model. The ice sheet has thickness H_i and bed at $z = b$. It overlies a sedimentary basin with thickness H_{sb} and an impermeable lower boundary. There is a geothermal heat flux G into the sedimentary basin, which is modified by groundwater flow on its way to the ice bed.

groundwater flow could modify the heat flux. I find that, for realistic parameter values, groundwater flow has the potential to significantly enhance or reduce heat flux in large regions of both East and West Antarctica, with the resulting difference in basal melting comparable in size to the exfiltration of water from the sedimentary basin. In particular, topographically-driven groundwater flow enhances heat flux in the centre of ice streams and reduces it at the margins, potentially helping the ice stream to self-reinforce. Meanwhile, compaction-driven groundwater flow provides a positive feedback by enhancing heat flux beneath thinning ice and reducing it beneath thickening ice.

In Section 5.2 I describe the governing equations of the model, in dimensional and dimensionless form, and in Section 5.3 I provide an example solution for a synthetic geometry in two dimensions. In Section 5.4 I then derive an approximate solution for the modification of the geothermal heat flux, and compare this approximate solution with the numerical solution for the aforementioned example. I then evaluate this approximate modified heat flux for Antarctic data across the whole continent in Section 5.5, and discuss my findings.

5.2 Model

For this chapter, I incorporate energy transport into the Dupuit model of groundwater flow described in Chapter 2, Section 2.2, but work in two horizontal dimensions rather than one (in order to use Antarctic data across the whole continent later). The sedimentary basin therefore has thickness $H_{sb}(x, y)$, the ice-bed interface is $z = b(x, y)$, and the bottom of the sedimentary basin is at $z = b - H_{sb}$. Above the sedimentary basin is an ice sheet with thickness $H_i(x, y, t)$, and between the sedimentary basin and the ice is a subglacial hydrological system, which is modelled as a thin layer of pressurised water. Subscripts sb, i, h, w and r are used for properties of the sedimentary basin, ice, hydrological system, water and sedimentary rock. This chapter considers longer timescales (*i.e.* hundreds to thousands of years), so that annual variability is not important. In particular, it will generally be assumed that groundwater and heat dynamics are in a quasi-steady state.

A consequence of the Dupuit approximation is that horizontal diffusion of heat is negligible compared to vertical diffusion; however, vertical and horizontal advection are generally comparable. This model therefore improves on existing one-dimensional models that do not include horizontal advection (*e.g.* Gooch et al. (2016)).

5.2.1 Governing equations

The temperature in the sedimentary basin $T_{sb}(x, y, z, t)$ is governed by an advection-diffusion equation,

$$\rho_{sb} c_{sb} \frac{\partial T_{sb}}{\partial t} + \rho c_w \mathbf{u} \cdot \nabla T_{sb} + \rho c_w w \frac{\partial T_{sb}}{\partial z} = k^T_{sb} \frac{\partial^2 T_{sb}}{\partial z^2} + Q_r + D_{sb}. \tag{5.1}$$

Here $\mathbf{u}(x, y, z, t)$ and $w(x, y, z, t)$ are the horizontal and vertical components of the Darcy flux in the sedimentary basin, and $\nabla = (\partial/\partial x, \partial/\partial y)$ is the horizontal component of the gradient. A source term Q_r is included for radiogenic heating, and D_{sb} for dissipation in the groundwater flow. In this chapter ρ, c and k^T refer to density, specific heat and thermal conductivity, all assumed constant for simplicity. (The latter should not be confused with the permeability of the porous medium, which in this chapter is referred to as k^p_{sb}.) The bulk quantities $\rho_{sb} c_{sb}$ and k^T_{sb} are defined in terms of the porosity ϕ as

$$\rho_{sb} c_{sb} = \rho_r c_r (1 - \phi) + \rho c_w \phi, \quad k^T_{sb} = k^T_r (1 - \phi) + k^T_w \phi. \tag{5.2}$$

Equation (5.1) includes heat transport via advection by groundwater, which only occurs in water phase, and via conduction, which occurs through both the water and

rock phases and which produces the diffusive term. Heat can also be transported by dispersion, the spreading of heat due to the heterogeneity of fluid velocity on the pore scale, which effectively modifies the conductivity k_{sb}^T to (Bear, 2013)

$$k_{\text{eff}}^T = k_r^T(1-\phi) + k_w^T\phi\left(1 + \frac{\text{Pe}_{\text{dis}}^2}{48}\right), \tag{5.3}$$

where the pore-scale Peclet number is (under the Dupuit approximation)

$$\text{Pe}_{\text{dis}} = \frac{\rho_w C_w |\mathbf{u}| r_p}{k_w^T}, \tag{5.4}$$

and r_p is the pore radius. For the values in Table 5.1 below, assuming the size $|\mathbf{u}|$ is represented by its scale $[\mathbf{u}]$, and for a pore radius $r_p = 10^{-7}$ m, this number is $\text{Pe}_{\text{dis}} = 1.3 \times 10^{-9}$. The effect of thermal dispersion ought to therefore be negligible compared to advection and diffusion, and this is subsequently neglected henceforth.

For simplicity, the assumption is made of a temperate (thawed) bed, and ignore the dependence of the melting temperature on pressure. Although large regions of Antarctica likely possess a frozen bed, the assumption of a thawed bed is reasonable beneath most outlet glaciers where ice dynamics are of most concern. It is therefore imposed that the top of the sedimentary basin is at a uniform melting temperature T_m,

$$T_{sb} = T_m \quad \text{on} \quad z = b. \tag{5.5}$$

At the bottom, a conductive heat flux is prescribed, given by the geothermal heat $G(x, y)$,

$$-k_{sb}^T \frac{\partial T_{sb}}{\partial z} = G \quad \text{on} \quad z = b - H_{sb}. \tag{5.6}$$

This chapter continues to use the Dupuit model of groundwater flow from Chapter 2, so that the horizontal Darcy flux is given by

$$\mathbf{u} = -\frac{K_{sb}}{\rho g}\nabla\psi, \tag{5.7}$$

where K_{sb} is the hydraulic conductivity and

$$\psi = p_b + \rho g b = \rho_i g H_i - N + \rho g b, \tag{5.8}$$

is the hydraulic potential. The hydraulic conductivity is given by

$$K_{sb} = \rho g k_{sb}^p / \mu, \tag{5.9}$$

where k_{sb}^p denotes the permeability of the porous medium, and μ is the viscosity of water. Throughout this chapter I work in terms of K_{sb} rather than k_{sb}^p, in order to avoid confusion with the thermal conductivity.

The vertical Darcy flux is given by Equation (2.43),

$$w = (z - b + H_{sb}) \left(\frac{K_{sb}}{\rho g} \nabla^2 \psi - \frac{S_s}{\rho g} \frac{\partial \psi_c}{\partial t} \right) - \frac{K_{sb}}{\rho g} \nabla (b - H_{sb}) \cdot \nabla \psi, \tag{5.10}$$

where the 'compaction potential' is defined as

$$\psi_c = p_b - \xi \rho_i g H_i = (1 - \xi) \rho_i g H_i - N. \tag{5.11}$$

Throughout this chapter, a model for N is used that ensures $N < (1-\xi)\rho_i g H_i$, so that the compaction term produces upward flow where the ice is thinning ($\partial H_i / \partial t < 0$) and downward flow where it is thickening. However, it is noted that $N < (1 - \xi)\rho_i g H_i$ might not always hold in glaciological settings (especially if ξ is close to 1). For instance, in the previous chapter, the effective pressure model was such that $N > (1 - \xi)\rho_i g H_i$ near the grounding line, leading to the opposite response locally.

As previously, a range of values is considered for both K_{sb} and S_s (the former of which may vary because it depends on k^p_{sb}). Values of K_{sb} for coarse-grained sedimentary rocks range from 10^{-10}–10^{-5} ms^{-1} (Freeze and Cherry, 1979). For formerly glaciated aquifers in North America, Neuzil and Provost (2014) measure values of S_s between 10^{-7}–3×10^{-5} m^{-1}, along with ξ ranging from 0.3–1.0.

The exfiltration q_E is given by

$$q_E = (w - \mathbf{u} \cdot \nabla b)|_{z=b} = \nabla \cdot \left(\frac{K_{sb}}{\rho g} H_{sb} \nabla \psi \right) - \frac{S_s}{\rho g} H_{sb} \frac{\partial \psi_c}{\partial t}. \tag{5.12}$$

Finally, the dissipative heating term in the energy balance is given by (Bear, 2013)

$$D_{sb} = -\mathbf{u} \cdot \nabla \psi = \frac{K_{sb}}{\rho g} |\nabla \psi|^2, \tag{5.13}$$

assuming that the horizontal fluxes are much larger than the vertical flux under the Dupuit approximation.

Under the assumption that the bed is at a uniform melting temperature T_m, the melt rate $m(x, y, t)$ is determined by the energy balance at the ice bed $z = b$, which reads

$$\rho m L = -k^T_{sb} \frac{\partial T_{sb}}{\partial z} + k_i \frac{\partial T_i}{\partial z} + \boldsymbol{\tau_b} \cdot \mathbf{u_b} + D_h, \tag{5.14}$$

where the terms are as follows:

- $\rho m L$ is the energy used to melt or freeze the ice, with m the melt rate and L the latent heat,
- $-k^T_{sb} \partial T_{sb} / \partial z$ is the conductive heat flux upwards from the sedimentary basin,

- $k_i \partial T_i / \partial z$ is the conductive heat flux into the ice,
- $\boldsymbol{\tau}_\mathbf{b} \cdot \mathbf{u}_\mathbf{b}$ is the frictional heating from the sliding of the ice (and resulting deformation of the till, etc.), where $\boldsymbol{\tau}_\mathbf{b}$ and $\mathbf{u}_\mathbf{b}$ are the basal shear stress and ice velocity,
- D_h is the heat produced by dissipation from the flow in the hydrological system.

Conduction into the ice is a sink, whereas the other terms are heat sources. The conductive heat flux from the sedimentary basin (the first term on the right) is of primary interest here. In the absence of groundwater flow, this is equal to the geothermal heat flux at the bottom of the sedimentary basin, along with a possible radiative heating contribution,

$$-k_{sb}^T \frac{\partial T_{sb}}{\partial z} = G + \int_{b-H_{sb}}^{b} Q_r \, \mathrm{d}z. \tag{5.15}$$

The groundwater flow modifies this term, and this chapter will focus on the change in the basal melt rate m that results from this. The other terms in Equation (5.14) are assumed unaffected by groundwater flow, and therefore are ignored when considering the resulting modification Δm. As such, they are not needed for the present work and are hence not modelled any further. However, it is noted that there could be additional feedbacks; for example, modified sliding rates could change the frictional heating term.

The model solved in this chapter consists of Equation (5.1), subject to the provided boundary conditions, with ψ, $\mathbf{u}$ and w assumed known. The ice thickness H_i must therefore be either provided by data or prescribed using an ice sheet model. In the 2D example solutions (using a synthetic geometry) that follow, a shallow-shelf ice sheet model with a Weertman sliding law is used, as in Chapter 2, Section 2.5. Equation (5.8) also requires a prescription of the effective pressure N. A simple parameterisation is to take the effective pressure as a fixed fraction of the overburden (*e.g.* Gregov et al., 2023),

$$N = \nu \rho_i g H_i, \tag{5.16}$$

where the value $\nu = 0.1$ is taken throughout this chapter. In this case, the 'compaction potential' simplifies to

$$\psi_c = (1 - \xi - \nu) \rho_i g H_i. \tag{5.17}$$

A more detailed model of the effective pressure could relate N to the distribution of water in the subglacial hydrological system, as in the previous chapter. This requires solving a mass conservation equation for basal water, in which m and q_E are source

terms. However, as mentioned in the previous chapter, subglacial hydrology and thermodynamics interact in numerous ways that would complicate this analysis, and as such are presently ignored. I discuss these further in Section 5.6.

5.2.2 Non-dimensionalisation

The above model may now be non-dimensionalised, writing variables as

$$x = [x]\hat{x}, \quad z = [z]\hat{z}, \quad T_{sb} - T_m = [\Delta T]\hat{T} \quad \ldots, \tag{5.18}$$

where square brackets [] denote constant scales and hats denote dimensionless variables. The choice of scales follows that in Chapter 2, Section 2.2. In addition, a known scale $[G]$ for the geothermal heat flux is assumed, and the temperature relative to melting point $T_{sb} - T_m$ is scaled with

$$[\Delta T] = [G][z]/k_{sb}^T. \tag{5.19}$$

Following Equation (5.14), a scale for the melt rate is chosen based on the heat flux from the sedimentary basin

$$[m] = [G]/\rho L. \tag{5.20}$$

The melt rate scale $[m]$ is also used as the scale $[q_E]$ for q_E, so that the two source terms may be straightforwardly compared.

Under this choice of scalings, the dimensionless exfiltration is given by

$$\hat{q}_E = \kappa\hat{\nabla} \cdot \left(\hat{H}_{sb}\hat{\nabla}\hat{\psi}\right) - \Sigma\hat{H}_{sb}\frac{\partial\hat{\psi}_c}{\partial\hat{t}}, \tag{5.21}$$

where

$$\kappa = \frac{[w]}{[m]} = \frac{K_{sb}[z]^2\rho L}{[x]^2[G]}, \quad \Sigma = \frac{S_s[z]^2\rho L}{[G][t]}. \tag{5.22}$$

Taking a range $K_{sb} = 10^{-10}$–10^{-5} ms^{-1} (Freeze and Cherry, 1979) and $S_s = 10^{-7}$–3×10^{-5} m^{-1} (Neuzil and Provost, 2014) gives κ ranging from 1.7×10^{-7}–0.017 and Σ from 0.0046–1.37. This chapter therefore focuses on the higher range of possible values for K_{sb}, since for the lower end the importance of topographic groundwater flow is negligible. The dimensionless hydraulic potential (scaled with $[p] = \rho g[z]$) is

$$\hat{\psi} = (1 - \delta_i)\hat{H}_i - \hat{N} + \hat{b} = (1 - \nu)(1 - \delta_i)\hat{H}_i + \hat{b}, \tag{5.23}$$

and the 'compaction potential' is

$$\hat{\psi}_c = (1 - \xi)(1 - \delta_i)\hat{H}_i - \hat{N} = (1 - \xi - \nu)(1 - \delta_i)\hat{H}_i. \tag{5.24}$$

Parameter	Value(s) used	Units
ρ	1000	kg m^{-3}
ρ_r	2000	kg m^{-3}
ρ_i	900	kg m^{-3}
c_w	4200	J kg^{-1} K^{-1}
c_r	700	J kg^{-1} K^{-1}
ϕ	0.2	
k_r^T	2.8	W m^{-1} K^{-1}
k_w^T	0.56	W m^{-1} K^{-1}
g	9.81	m s^{-2}
S_s	3×10^{-6}–3×10^{-5}	m^{-1}
ξ	0.8	
K_{sb}	1×10^{-6}–5×10^{-6}	m s^{-1}
k_{sb}^p	1×10^{-13}–5×10^{-13}	m^2
μ	1×10^{-3}	Pa s
$[x]$	5×10^5	m
$[z]$	871	m
$[\mathbf{u}]$	1.7×10^{-9}–8.7×10^{-9}	m s^{-1}
$[t]$	2900	yr
$[G]$	60	mW m^{-2}
$[\Delta T]$	25	K
$[m]$	5.7	mm yr^{-1}

Table 5.1: Physical parameters and scales used in the model. The values of ϕ, k_r^T and c_r are representative values for sedimentary rocks based on Bear (2013), and ρ_r based on Manger (1963). The values of S_s and ξ are based on Neuzil and Provost (2014). The values of K_{sb} are based on the upper range of values for coarse-grained sedimentary rock in Freeze and Cherry (1979). The scale $[G]$ is inferred from data (Stål et al., 2021) and $[x]$ based as before on the size of the continent, whereas the scales $[z]$, $[t]$, $[\mathbf{u}] = K_{sb}[z]/[x]$, $[\Delta T]$ and $[m]$ are derived from other parameters and scales. In particular, $[z]$ and $[t]$ are found based on a shallow-shelf ice sheet model (Equations (2.110) and (2.111)), whose parameters are described at the start of Section 5.3.

Parameter	Value(s) used
κ	0.017—0.084
Σ	0.14—1.4
δ_i	0.1
λ_{sb}	340–1700
Pe	0.0047—0.024
Ξ_{sb}	0.083

Table 5.2: Derived dimensionless parameters used in the model.

The dimensionless Darcy flux components are

$$\hat{\mathbf{u}}_{\mathbf{sb}} = -\hat{\nabla}\hat{\psi}, \quad \hat{w}_{sb} = \left(\hat{z} - \hat{b} + \hat{H}_{sb}\right)\left(\hat{\nabla}^2\hat{\psi} - \frac{\Sigma}{\kappa}\frac{\partial\hat{\psi}_c}{\partial\hat{t}}\right) - \hat{\nabla}\left(\hat{b} - \hat{H}_{sb}\right)\cdot\hat{\nabla}\hat{\psi}. \quad (5.25)$$

Equation (5.1) for the temperature in the sedimentary basin becomes

$$\lambda_{sb}\frac{\partial\hat{T}_{sb}}{\partial\hat{t}} + \hat{\mathbf{u}}_{\mathbf{sb}}\cdot\hat{\nabla}\hat{T}_{sb} + \hat{w}_{sb}\frac{\partial\hat{T}_{sb}}{\partial\hat{z}} = \frac{1}{\mathrm{Pe}}\left(\frac{\partial^2\hat{T}_{sb}}{\partial\hat{z}^2} + \hat{Q}_r\right) + \Xi_{sb}\left(\frac{\partial\hat{\psi}}{\partial\hat{x}}\right)^2, \quad (5.26)$$

where

$$\lambda_{sb} = \frac{\rho_{sb}c_{sb}[x]^2}{\rho c_w K_{sb}[z][t]}, \quad \mathrm{Pe} = \frac{K_{sb}\rho c_w[z]^3}{k_{sb}^T[x]^2}, \quad \hat{Q}_r = \frac{Q_r[z]}{[G]}, \quad \Xi_{sb} = \frac{g[z]}{c_w[T]}. \quad (5.27)$$

The parameter λ_{sb} represents the timescale of heat flow in the sedimentary basin relative to evolution of the ice sheet, $\hat{Q}_r$ is the dimensionless radiative heating, and Ξ_{sb} represents the size of the dissipation. The parameter Pe is the Péclet number of the sedimentary basin, representing the importance of heat advection compared to diffusion, and, like κ, Pe scales linearly with k_{sb}. The boundary conditions are

$$\hat{T}_{sb} = 0 \quad \text{on} \quad \hat{z} = \hat{b}. \quad (5.28)$$

$$\frac{\partial\hat{T}_{sb}}{\partial\hat{z}} = -\hat{G} \quad \text{on} \quad \hat{z} = \hat{b} - \hat{H}_{sb}, \quad (5.29)$$

where

$$\hat{G} = G/[G]. \quad (5.30)$$

Equation (5.14) can also be written non-dimensionally as

$$\hat{m} = -\left.\frac{\partial\hat{T}_{sb}}{\partial\hat{z}}\right|_{\hat{z}=\hat{b}} + \alpha_i\left.\frac{\partial\hat{T}_i}{\partial\hat{z}}\right|_{\hat{z}=\hat{b}} + \alpha_f\hat{\boldsymbol{\tau}}_{\mathbf{b}}\cdot\hat{\mathbf{u}}_{\mathbf{b}} + \alpha_d\hat{D}_h, \quad (5.31)$$

where α_i, α_f and α_d are suitable dimensionless parameters that depend on how the other heat sources are scaled.

5.3 Example solution for a synthetic geometry in 2D

As an illustrative example, a steady-state solution of Equation (5.26) is considered in two dimensions (x, z), representing a cross-section of an ice stream along a flow-line, which is shown in Figure 5.3. The sedimentary basin thickness H_{sb} is given by

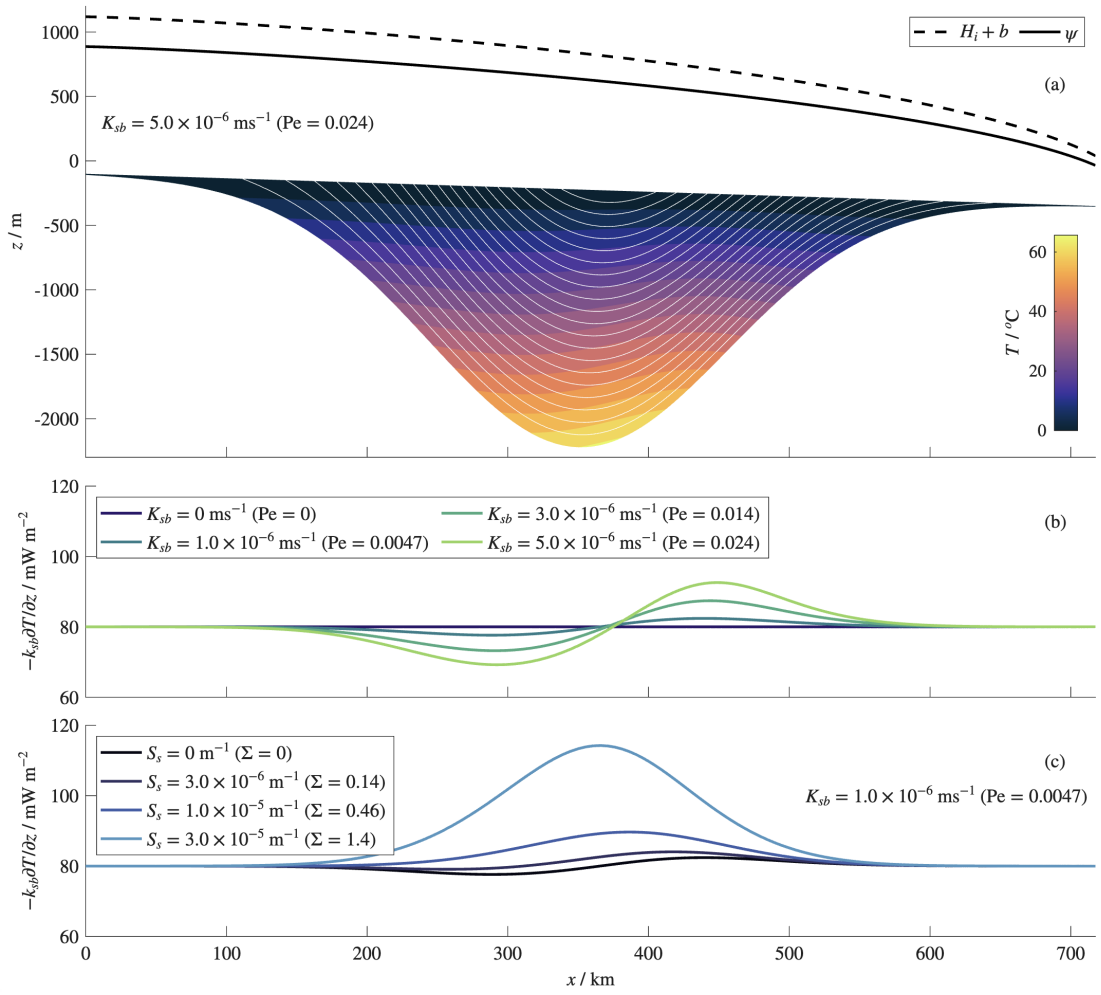


Figure 5.3: Steady state solution for a test case with sedimentary basin thickness $H_{sb} = (2000 \exp(-((x - 350\text{km})/150\text{km}))^2)$ m, and geothermal heat flux $G = 80\,\text{mW m}^{-2}$. (a) shows the ice profile and hydraulic potential ψ, along with the temperature in the sedimentary basin at 5° contours and streamlines of the groundwater flow for a relatively high hydraulic conductivity K_{sb} with $S_s = 0$. (b) and (c) show the modified heat flux to the ice bed for various values of K_{sb} with $S_s = 0$, and for various values of the specific storage S_s for a fixed K_{sb} and for a uniform quasi-steady ice thinning rate $\partial H_i/\partial t = -1$ m yr^{-1}.

a Gaussian function, whose thickening and thinning in the direction of groundwater flow drives infiltration and exfiltration of groundwater. This shape is chosen purely in order to illustrate the typical influence of groundwater flow. The ice sheet thickness is found by solving a shallow-shelf ice sheet model with a Weertman (*i.e.* decoupled) sliding law (Equations (2.112) and (2.113)), using the parameters $a = 0.3$ m yr^{-1}, $A = 4.227 \times 10^{-25}$ Pa^{-1} s^3, $C_W = 7.624 \times 10^6$ Pa m$^{-1/3}$ s$^{1/3}$, and a topography $b(x) = -100\text{m} - x/2870$ m. The numerical method used to obtain this solution, and others in this chapter, is detailed in the Appendix, Section A.4.

Figure 5.3(a) shows the streamlines of this groundwater flow, driven by the hydraulic gradient. This flow advects heat, causing the temperature to deviate from the unmodified solution $T_{sb} = G(b - z)/k^T_{sb}$. When heat is advected downwards, the thermal gradient $\partial T_{sb}/\partial z$ at the top of the sedimentary basin becomes smaller. Conversely, when heat is advected upwards, the thermal gradient at the top of the sedimentary basin is larger.

This results in a modification of the heat flux to the ice bed, seen in Figure 5.3(b). The heat flux is lowered in regions of groundwater infiltration, but elevated in regions of exfiltration. A higher value of the hydraulic conductivity K_{sb}, hence the Péclet number Pe, amplifies this change, with the difference between the modified and unmodified flux approximately scaling with Pe.

In Figure 5.3(c), the effect of compaction-driven exfiltration is seen, for groundwater flow equivalent to that produced by a spatially-uniform steady ice thinning rate $\partial H_i/\partial t < 0$ (and corresponding effective pressure rate of change $\partial N/\partial t < 0$). This 'ice thinning' is assumed to be maintained indefinitely, but with negligible resulting change in H_i (*i.e.* H_i still satisfies the steady state of Equations (2.112) and (2.113)), so that Equation (5.26) can reach a quasi-steady state. This solution is obtained by solving the steady state of Equation (5.26) ($\partial \hat{T}_{sb}/\partial \hat{t} = 0$) with $\partial \hat{\psi}_c/\partial \hat{t} = (1 - \xi - \nu)(1 - \delta_i)\partial H_i/\partial t$ treated as a constant forcing.

The ice thinning increases vertical groundwater flux in the upwards direction, enhancing the heat flux relative to the case with $S_s = 0$. The enhancement to the heat flux again scales with S_s (*i.e.* with Σ). Because the compaction-driven part of the groundwater flow scales with the sedimentary basin thickness H_{sb}, the overall heat flux enhancement is largest where the sedimentary basin is thickest.

5.3.1 Additional example

In Figure 5.4, a second example of a 2D steady state solution is provided for a more complex setup. The sedimentary basin includes a bottleneck at $x = 200$ km, driving

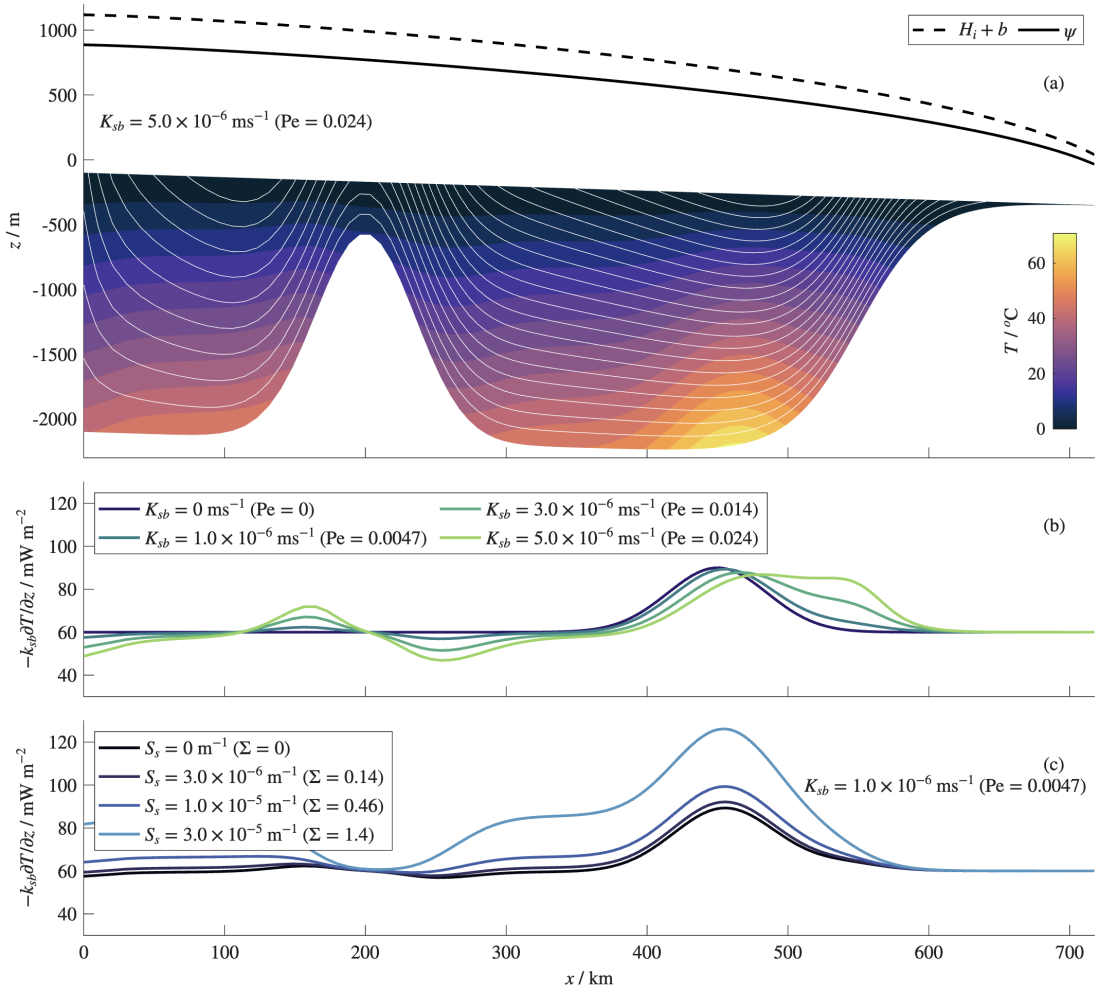


Figure 5.4: As in Figure 5.3, except using a sedimentary basin thickness $H_{sb} = (1000 - 1000\tanh((x - 550\text{km})/50\text{km}) - 1600\exp(-((x - 200\text{km})/50\text{km})^2))$ m, and a geothermal heat flux $G = (60 + 30\exp(-((x - 450\text{km})/50\text{km})^2)))$ mW m^{-2}.

exfiltration and subsequent infiltration, and reduces in thickness approaching the grounding line, driving further exfiltration. The prescribed geothermal heat flux G is nonuniform, with a local peak at $x = 450$ km. Figure 5.4(a) shows the streamlines of this groundwater flow, which advects heat, reducing the thermal gradient where groundwater flows downwards and increasing it when groundwater flows upwards as in Figure 5.3.

Figure 5.4(b) shows the resulting modification to the heat flux, with the difference between the modified and unmodified flux approximately scaling with Pe as before. The horizontal component of the groundwater flow also plays a role, as the basal heat flux enhancement from $x = 500$–600 km is magnified by the region of elevated geothermal heat upstream of this region.

Figure 5.4(c) shows the effect of compaction-driven exfiltration, again for a spatially uniform steady ice thinning rate $\partial H_i/\partial t < 0$ in a quasi-steady state. The ice thinning again increases vertical groundwater flux in the upwards direction, enhancing the heat flux by an amount that scales with S_s (*i.e.* with Σ), and is also largest where the sedimentary basin is thickest.

5.4 Asymptotic solution for small Péclet number

Realistic values of the hydraulic conductivity suggest the Péclet number of the sedimentary basin is relatively small. Taking a possible range $K_{sb} = 10^{-10}$–10^{-5} ms^{-1} (Freeze and Cherry, 1979) gives Pe ranging from 4.7×10^{-7}–0.047. It therefore makes sense to consider the behaviour of the problem when Pe is asymptotically small. In the following calculation, the radiogenic heating $\hat{Q}_r$ is ignored for simplicity, although the result can easily be generalised to include $\hat{Q}_r$. Dissipative heating is also neglected, which is justified provided that the parameter Ξ_{sb} (= 0.083 for the chosen parameter values) is small. In addition to Pe $\ll 1$ t is assumed that $\Sigma \mathrm{Pe}/\kappa \ll 1$ for the following working, so that heat advection due to the compaction-driven part of the groundwater flow is small similarly to the topographically-driven part. The alternative case, in which compaction-driven vertical advection of heat is comparable with diffusion, requires a separate consideration that is not included in this chapter.

In the limit Pe = 0, the temperature profile is simply given by

$$\hat{T}_{sb} = \hat{T}_0 := \hat{G}(\hat{b} - \hat{z}), \tag{5.32}$$

so that the heat flux at the ice-bed interface is just the geothermal heat $\hat{G}$, with no perturbation due to groundwater flow. For small but nonzero Pe, $\hat{T}_{sb}$ may be expanded as an asymptotic series

$$\hat{T}_{sb} \sim \hat{T}_0 + \mathrm{Pe}\hat{T}_1 + \ldots \tag{5.33}$$

At leading order $\hat{T}_0$ is as above, and at first order $\hat{T}_1$ obeys (from Equation (5.26), assuming a quasi-steady state, *i.e.* $\partial T_{sb}/\partial t = 0$, and that Ξ_{sb} is negligibly small)

$$\frac{\partial^2 \hat{T}_1}{\partial \hat{z}^2} = \hat{\mathbf{u}}_{\mathbf{sb}} \cdot \hat{\nabla}\hat{T}_0 + \hat{w}_{sb}\frac{\partial \hat{T}_0}{\partial \hat{z}}. \tag{5.34}$$

Substituting in the Darcy flux components given by Equation (5.25) and $\hat{T}_0$, it is

found that

$$\frac{\partial^2 \hat{T}_1}{\partial \hat{z}^2} = -\hat{\nabla}\hat{\psi} \cdot ((\hat{b} - \hat{z})\hat{\nabla}\hat{G} + \hat{G}\hat{\nabla}\hat{b}) - \left((\hat{z} - \hat{b} + \hat{H}_{sb}) \left(\hat{\nabla}^2 \hat{\psi} - \frac{\Sigma}{\kappa} \frac{\partial \hat{\psi}_c}{\partial \hat{t}} \right) - \hat{\nabla}\hat{\psi} \cdot \hat{\nabla}(\hat{b} - \hat{H}_{sb}) \right) \hat{G}. \quad (5.35)$$

Simplifying and integrating gives that

$$\frac{\partial \hat{T}_1}{\partial \hat{z}} = \frac{1}{2} \left((\hat{z} - \hat{b})^2 - \hat{H}_{sb}^2 \right) \hat{\nabla}\hat{\psi} \cdot \hat{\nabla}\hat{G} - (\hat{z} - \hat{b} + \hat{H}_{sb})\hat{G} \left(\hat{\nabla}\hat{\psi} \cdot \hat{\nabla}\hat{H}_{sb} \right) + \frac{1}{2}(\hat{z} - \hat{b} + \hat{H}_{sb})^2 \hat{G} \left(\hat{\nabla}^2 \hat{\psi} - \frac{\Sigma}{\kappa} \frac{\partial \hat{\psi}_c}{\partial \hat{t}} \right). \quad (5.36)$$

Evaluating at the ice-bed interface, it can be found after further simplifying that

$$-\frac{\partial \hat{T}_1}{\partial \hat{z}}\bigg|_{\hat{z}=\hat{b}} = \hat{\nabla} \cdot \left(\frac{1}{2} \hat{G} \hat{H}_{sb}^2 \hat{\nabla}\hat{\psi} \right) - \frac{1}{2} \frac{\Sigma}{\kappa} \hat{G} \hat{H}_{sb}^2 \frac{\partial \hat{\psi}_c}{\partial \hat{t}}, \quad (5.37)$$

where there are terms originating from the topographically-driven (involving $\hat{\nabla}\hat{\psi}$) and compaction-driven (involving $\partial\hat{\psi}_c/\partial\hat{t}$) groundwater flow respectively, similarly to the exfiltration q_E (Equation (5.21)). In dimensional variables,

$$-k_{sb}^T \frac{\partial T}{\partial z}\bigg|_{z=b} \sim G + \frac{c_w}{2g k_{sb}^T} \left(\nabla \cdot \left(K_{sb} G H_{sb}^2 \nabla \psi \right) - S_s G H_{sb}^2 \frac{\partial \psi_c}{\partial t} \right). \quad (5.38)$$

This heat flux modification results in a modification Δm to the melt rate at the ice bed. Specifically, defining the unperturbed melt rate as

$$m_0 = \frac{1}{\rho L} \left(G + k_i \frac{\partial T_i}{\partial z} + \boldsymbol{\tau_b} \cdot \mathbf{u_b} + D_h \right), \quad (5.39)$$

Equation (5.14) gives that

$$m = m_0 + \Delta m, \quad \Delta m = \frac{c_w}{2\rho g k_{sb}^T L} \left(\nabla \cdot \left(K_{sb} G H_{sb}^2 \nabla \psi \right) - S_s G H_{sb}^2 \frac{\partial \psi_c}{\partial t} \right). \quad (5.40)$$

The asymptotic approximation (5.37) is tested using the 2D example previously shown in Figure 5.3, in order to determine the scope of its validity. The results are shown in Figure 5.5. Figure 5.5(a) shows the performance of the asymptotic approximation for various hydraulic conductivities K_{sb} and hence Péclet numbers Pe. The asymptotic approximation fits the numerical solution very well for $K_{sb} = 1 \times 10^{-6}$ (Pe = 0.0047), but begins to deviate from the numerical solution for Pe > 0.01. The

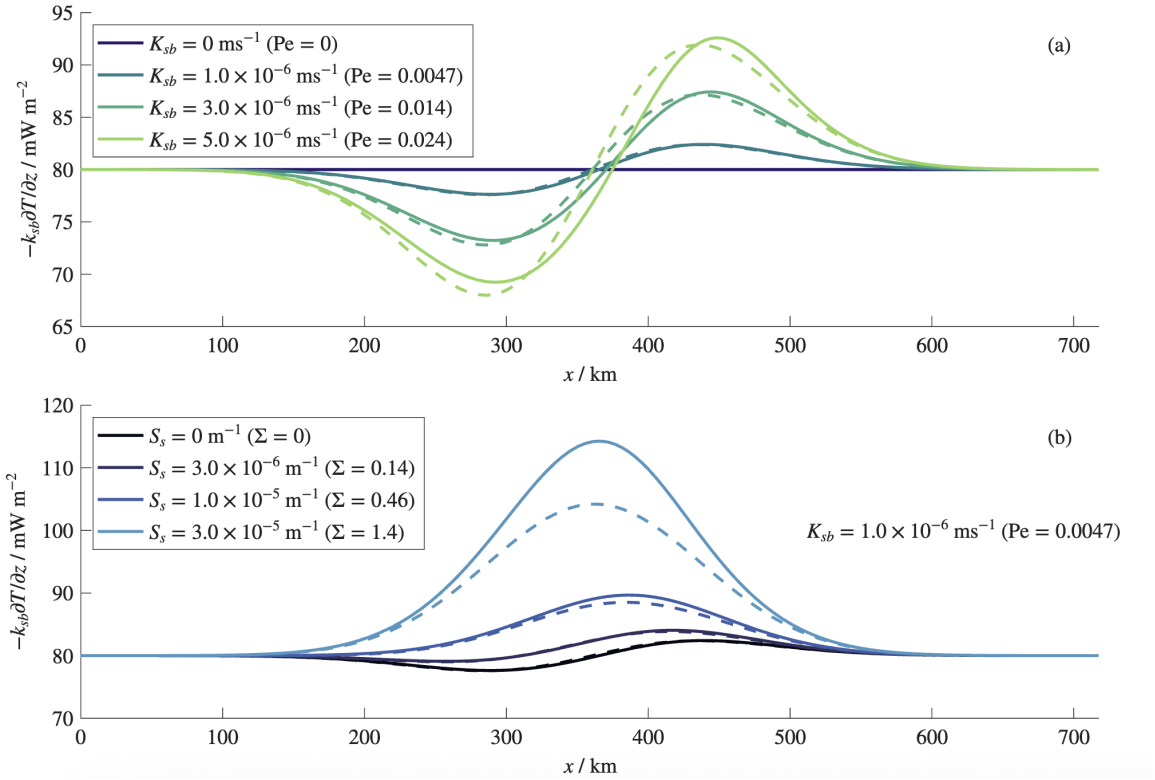


Figure 5.5: Comparison of asymptotic solution (dashed line) with the numerical solution (solid line), for the example shown in Figure 5.3. Panel (a) tests the asymptotic solution for varying K_{sb} / Pe, whereas (b) tests the asymptotic solution for varying S_s / Σ and a fixed value of K_{sb}.

Péclet number at which the solutions differ noticeably will vary slightly depending on specifics of the problem such as H_{sb}, G, and the hydraulic gradient.

In Figure 5.5(b), the asymptotic solution is compared to the numerical solution for different values of the specific storage S_s, leading to different values of Σ, with a fixed K_{sb}. This time, the approximation agrees well with the numerical solution up to and including $\Sigma = 0.46$, but for $\Sigma = 1.4$ the asymptotic approximation underestimates the perturbation to the flux. This means that, as well as Pe being small, this approximation also requires small Σ in order to be accurate, so that the compaction-driven contribution to the groundwater flow is not too large. Taken together, these results suggest that Equation (5.37) is a reliable approximation to the solution of the heat equation (5.26), provided that K_{sb} and S_s are not too large.

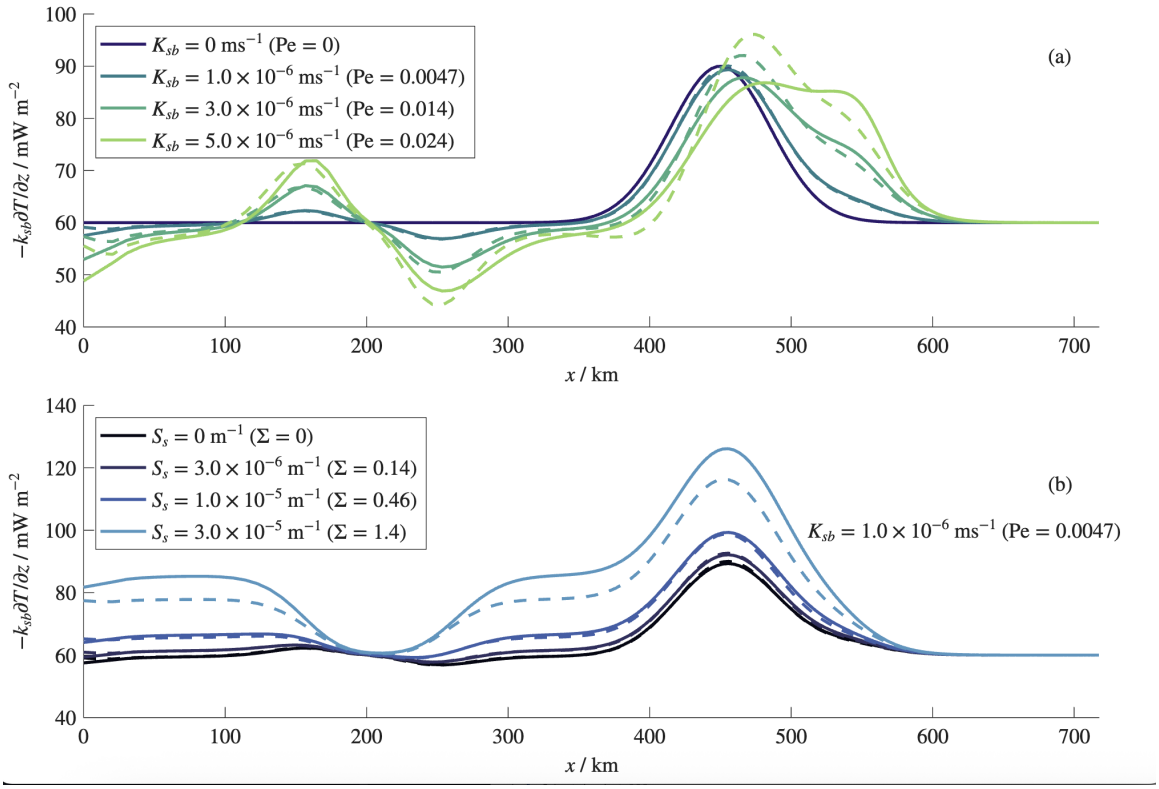


Figure 5.6: Comparison of asymptotic solution (dashed line) with the numerical solution (solid line), for the example shown in Figure 5.4. The heat flux at the ice-bed interface is shown for (a) varying K_{sb} (Pe), and (b) varying S_s (Σ) and a fixed value of K_{sb}.

5.4.1 Additional example

Figure 5.6, similarly to Figure 5.5, shows a comparison of the numerical solution for the heat flux with the approximate solution (5.37), this time for the case in Figure 5.4. In Figure 5.6(a), which shows the effect of varying K_{sb} (hence Pe) for $S_s = 0$, it can once more be seen that the approximation matches the numerical solution well roughly for Pe< 0.01, but becomes less accurate for higher values of Pe.

Figure 5.6(b) shows the effect of varying S_s (hence Σ) for a fixed K_{sb}. Again, the approximate solution agrees well with the numerical solution for Σ up to 0.46, but overestimates the heat flux modification for the higher value $\Sigma = 1.1$. These results provide further support for using Equation (5.37) to approximate the full solution of the heat equation (5.26) provided Pe and Σ are sufficiently small, and in particular that this approximation is reliable for a case where G is non-uniform.

5.5 Application to Antarctic data

The approximate expression (5.38) for the heat flux modification for small Péclet number is useful insofar that it enables an approximate calculation of the effect of groundwater flow on subglacial heating without needing to solve a PDE. This expression can therefore be evaluated using estimated subglacial heat flux and sedimentary basin thickness from Antarctica. When estimating the heat flux modification by groundwater beneath Antarctica, the main source of uncertainty comes from the values of K_{sb} and S_s. These are here taken as constant in space for simplicity, and large but realistic values are used, while noting that the topographically-driven and compaction-driven terms scale linearly with K_{sb} and S_s respectively.

For simplicity, the effective pressure is parameterised as above as 10% of the overburden ($N = 0.1\rho_i g H_i$). A thawed bed is assumed everywhere, although it is noted significant regions of Antarctica are likely to have a frozen bed. The regions where the bed is likely to be frozen are designated with hatching (Seiner et al., 2025), in which the results are less likely to be reliable.

In this section, the geothermal heat flux model of Stål et al. (2021) and the sedimentary basin thickness from Li et al. (2022) are used, both of which have 20-kilometer resolution. This geothermal heat flux model is used as the prescribed heat flux at the base of the sedimentary basin, meaning that radiogenic heat production in the sedimentary basin is neglected as a result. The compaction component uses the ice thickness rate of change $\partial H_i/\partial t$ (assumed steady) from ICESAT satellite data (Smith et al., 2020). The coverage excludes a region around the South Pole, which is denoted with a dashed circle, and in which it is assumed $\partial H_i/\partial t = 0$ for simplicity. (A plot of these data was provided in Chapter 1, Figure 1.1(a).) The ice thickness H_i and bed elevation b are taken from Bedmap3 (Pritchard et al., 2025).

5.5.1 Heat flux modification

Figure 5.7 shows the result of applying the asymptotic solution for the heat flux modification for values $K_{sb} = 10^{-6}\,\mathrm{m\,s^{-1}}$ and $S_s = 10^{-4}\,\mathrm{m^{-1}}$. These values correspond to $\mathrm{Pe} = 4.7 \times 10^{-3}$, $\kappa = 0.017$ and $\Sigma = 4.56$, and are intended to represent an upper bound on possible values. Although it is noted that this value of Σ is higher than those for which the approximate solution was reliable in the previous section (and the value $\Sigma\mathrm{Pe}/\kappa = 1.29$ is not small, as required by the asymptotic theory), the approximate solution tended to under-predict the heat flux modification in these cases. Despite the small Péclet number, it can be seen that the asymptotic solution

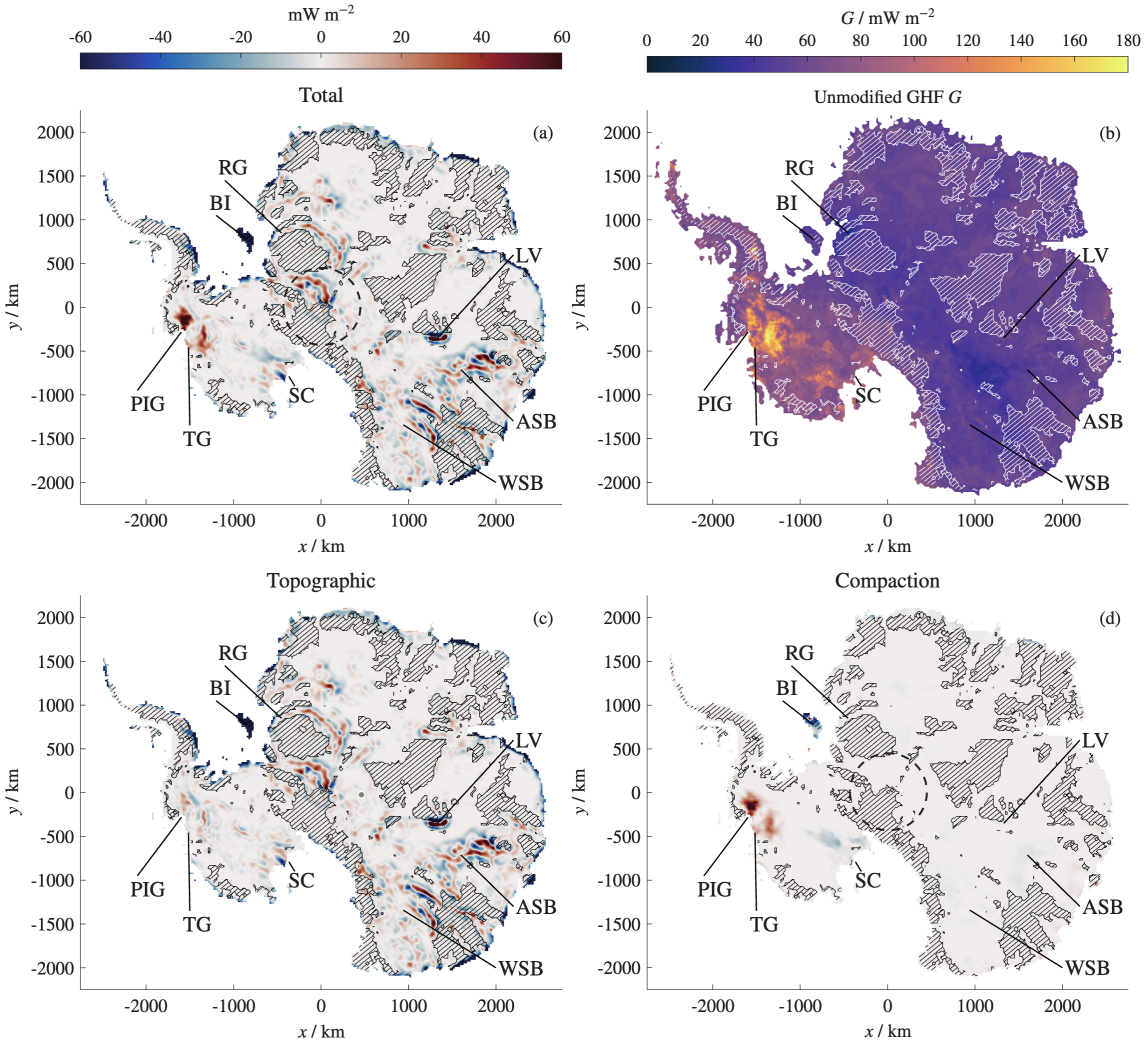


Figure 5.7: Geothermal heat flux modification (5.37) for $K_{sb} = 10^{-6}$ m s^{-1} and $S_s = 10^{-4}$ m^{-1}. Panel (a) shows the total modification, compared to the unmodified heat flux G in (b). Panel (c) shows the topographic term and (d) the compaction term. Selected locations are marked by abbreviations. The dashed circle around the South Pole marks a gap in the thinning rate data, wherein it is assumed that $\partial H_i/\partial t = 0$. Hatched regions denote regions where the bed is likely frozen (Seiner et al., 2025).

predicts that geothermal heat can be modified by tens of mW m^{-2} in either direction, representing a substantial modification, for these large but realistic parameter values. The compaction term is discussed first, before the topographic term is examined region by region.

Due to the high ice thinning rates beneath Pine Island Glacier and Thwaites Glacier (PIG and TG), the effect of compaction-driven groundwater flow is strongest here (Figure 5.7(d)). The ice thinning drives groundwater flow vertically upwards, which results in a further enhancement of heat flux from its already high value. This compaction-driven enhancement of heat flux in response to ice thinning could act as a positive feedback mechanism that accelerates basal melting, leading to further sliding and ice loss. Conversely, however, this feedback could help to reduce ice flow in regions where the ice is thickening, leading to heat flux reduction by groundwater infiltration. This predicted effect is most visible beneath the stagnated Kamb Ice Stream on the Siple Coast (SC), which is currently undergoing thickening.

The topographic component (Figure 5.7(c)) includes a thin region of significant heat flux reduction around the grounding line, particularly in East Antarctica. This is because the sedimentary basin underlies most of the ocean, meaning that a steep increase in sedimentary basin thickness occurs around the grounding line. However, the extent of the sedimentary basin beyond the grounding line may be uncertain and may depend on how the data has been processed. Moreover, certain assumptions of the model are likely to break down within a few kilometres of the grounding line: in particular, the effective pressure N may become comparable to the overburden (*i.e.* a much larger ν in Equation (5.16)) as the ice approaches flotation, and groundwater flow may be influenced by seawater intrusion into the sedimentary basin (as considered in Chapter 3).

A dramatic effect is also seen around Lake Vostok (LV) in East Antarctica, where there is a significant topographic minimum. In addition, substantial geothermal cooling is seen beneath Berkner Island (BI) in the Filchner-Ronne Ice Shelf, where the sedimentary basin is thought to be extremely thick. In these regions, the predicted groundwater flow velocities are large, meaning that the small Péclet number approximation may not be accurate.

Setting aside these uncertain regions, the topographic component of the groundwater flow has a noticeable effect across both East and West Antarctica, which can be seen in more detail in the zoomed-in regions of Figure 5.8. In East Antarctica, where the heat flux is relatively low, the groundwater-induced effect is strongest beneath Wilkes Subglacial Basin (WSB) and Aurora Subglacial Basin (ASB) (Figure

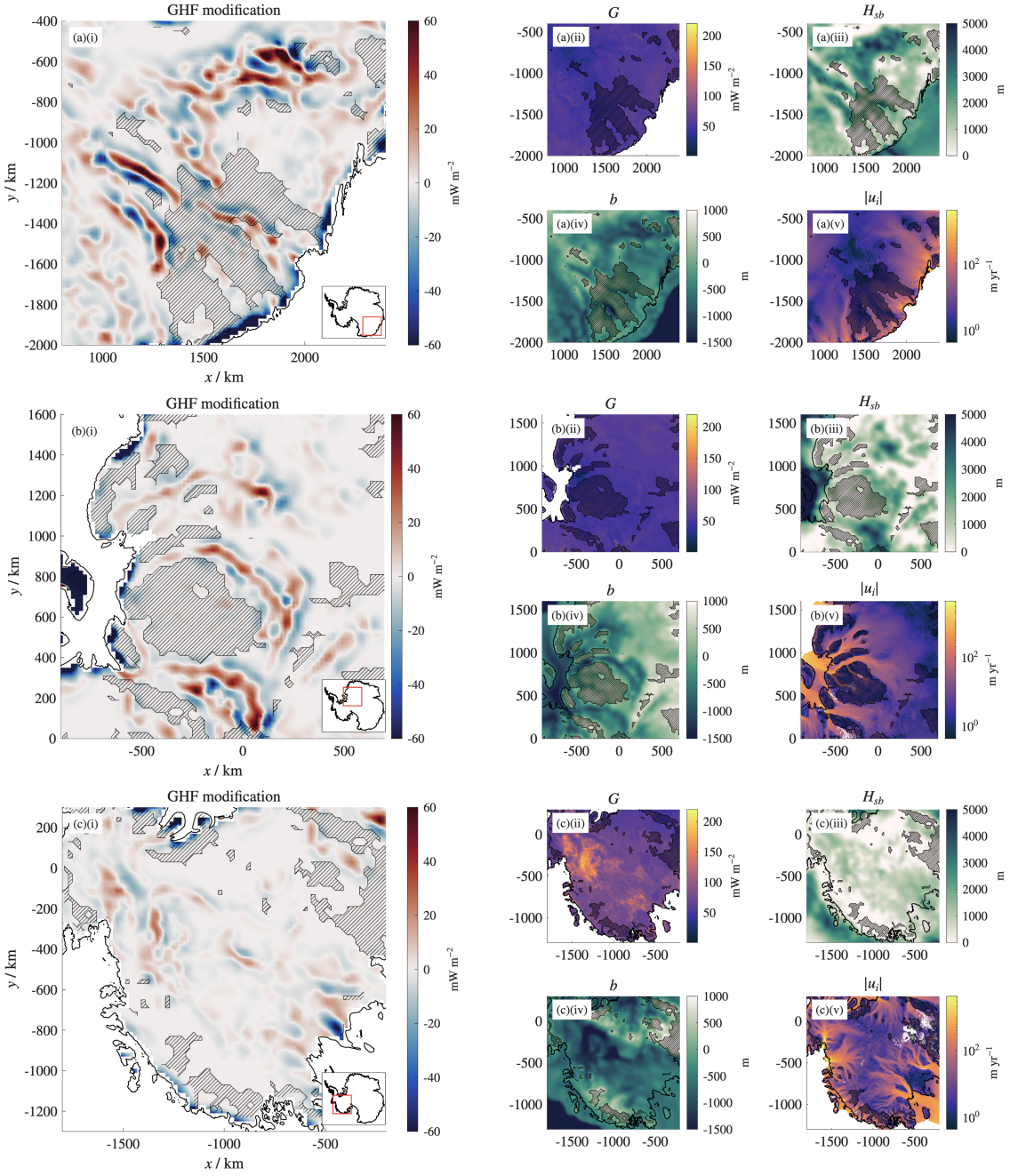


Figure 5.8: (i) Zoomed-in regions of the topographic heat flux modification, compared with (ii) the geothermal heat G, (iii) the sedimentary basin thickness H_{sb}, (iv) the ice bed topography b and (v) the ice velocity (Mouginot et al., 2017). The regions respectively cover (a) Wilkes Subglacial Basin (WSB) and Aurora Subglacial Basin (ASB) , and (b) Recovery Glacier (RG), both in East Antarctica, and (c) the majority of West Antarctica.

5.8(a)), because this region includes the thickest sedimentary basins in Antarctica. These sedimentary basins form bands roughly parallel to the ice flow (panel (iii)), corresponding to topographic lows in the ice bed (panel (iv)), and to the location of ice streams (panel (v)). Topographic highs have little to no sedimentary basin coverage, and in many cases correspond to regions where the bed is predicted to be frozen. Beneath Recovery Glacier (RG) and the surrounding land (Figure 5.8(b)), the distinction is even clearer between sedimentary basins below fast-flowing ice in topographic lows and topographic highs with a frozen bed and little sedimentary basin coverage (comparing panels (iii)–(v)).

In both Figure 5.8(a) and Figure 5.8(b), the variations in bed elevation b (panel (iv)) produce a variation in the hydraulic potential (because the ice surface $H_i + b$ is relatively flat). This hydraulic gradient drives a groundwater flow, which results in heat flux enhancement in the centre of the ice stream and reduction at the margins. Such heat flux enhancement via groundwater flow could therefore act as a self-reinforcing mechanism for ice streams, which naturally create sedimentary basins in topographic lows over time by erosion and deposition. Once a sedimentary basin is in place, groundwater flow helps transport heat to the bed of the ice stream and away from its surroundings, making it more likely that the central bed will remain thawed and the surrounding bed remain frozen.

This mechanism is illustrated in Figure 5.9 by another example solution to the model for a cross-section of an idealised ice stream, which shows the numerical solution of the steady state of Equation (5.26) (in 2 dimensions) rather than the asymptotic solution. The idealised ice stream is taken to be uniform in the longitudinal x-direction (into-page), and in the transverse y-direction includes a topographic trough, with a sedimentary basin below that is thickest in the centre of the stream. The ice surface is taken to be uniform in the transverse direction, but the density difference between ice and water (along with the effective pressure) leads to a non-uniform hydraulic potential, which is lowest in the middle of the ice stream. Groundwater infiltrates near the margins of the ice streams driven by the thickening of the sedimentary basin towards the centre, but exfiltrates in the centre due to the shallowing of the hydraulic gradient. As predicted, this leads to heat flux enhancement in the centre of the ice stream and reduction at the margins, with amplitude up to 40 mW m^{-2} for $K_{sb} = 3 \times 10^{-6}$ m s^{-1} and around 10 mW m^{-2} for $K_{sb} = 1 \times 10^{-6}$ m s^{-1}.

In West Antarctica, a similar banded pattern of heat enhancement in the centre of ice streams and reduction at their margins can be seen along the Siple Coast (SC) (Figure 5.8(c)). In this case, the variations in bed topography are smaller than the

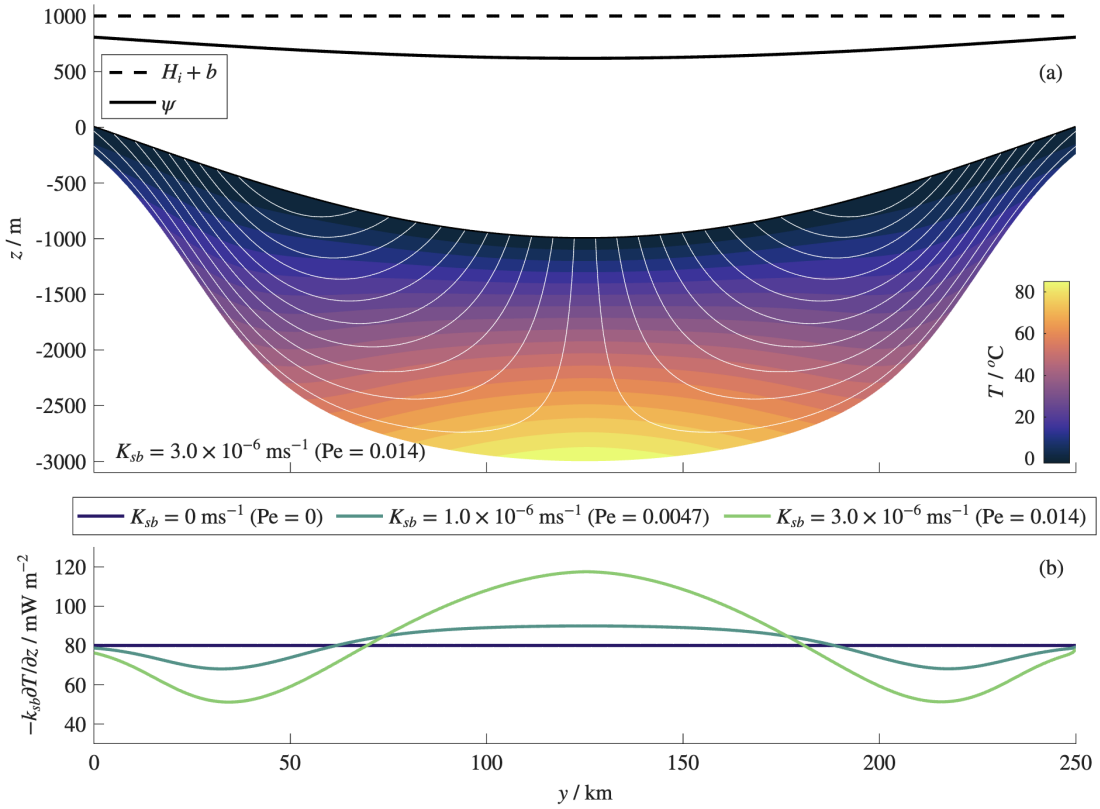


Figure 5.9: Numerical solution for an idealised cross-section of an ice stream. The topography is given by $b(y) = -1000\sin(\pi y/250\text{km})$ m, the ice thickness by $H_i(y) = 1000\text{m} - b(y)$, and the sedimentary basin thickness $H_{sb}(y) = 1000(1 + \tanh\big((y - 25\text{km})/25\text{km}\big)\tanh\big((225\text{km} - y)/25\text{km}\big))$ m. The heat flux is uniformly given by $G = 80$ mW m^{-2}, the effective pressure is taken as $N = 0.1\rho_i g H_i$ as elsewhere, and there is no thinning rate of the ice ($\partial H_i/\partial t = 0$). Panel (a) shows the geometry, streamlines of the groundwater flow in white, and temperature at 5°C contours for a particular K_{sb}. Panel (b) compares the heat flux through the top of the sedimentary basin for various K_{sb}.

aforementioned locations in East Antarctica, but the background geothermal heat flux is larger and more important in determining the location of ice streams (panel (ii)). Again, the areas of geothermal heat flux enhancement generally coincide with topographic lows beneath active ice streams, and heat flux reduction coincides with topographic highs near their margins. The highest heat flux is found beneath Pine Island Glacier and Thwaites Glacier (PIG and TG), which also comprise the fastest-thinning regions of the grounded Antarctic Ice Sheet. Similar bands of heating and cooling are seen beneath these glaciers, owing to variations in the sedimentary basin thickness (panel (iii)), but do not correspond as clearly to the topography and the location of ice streams.

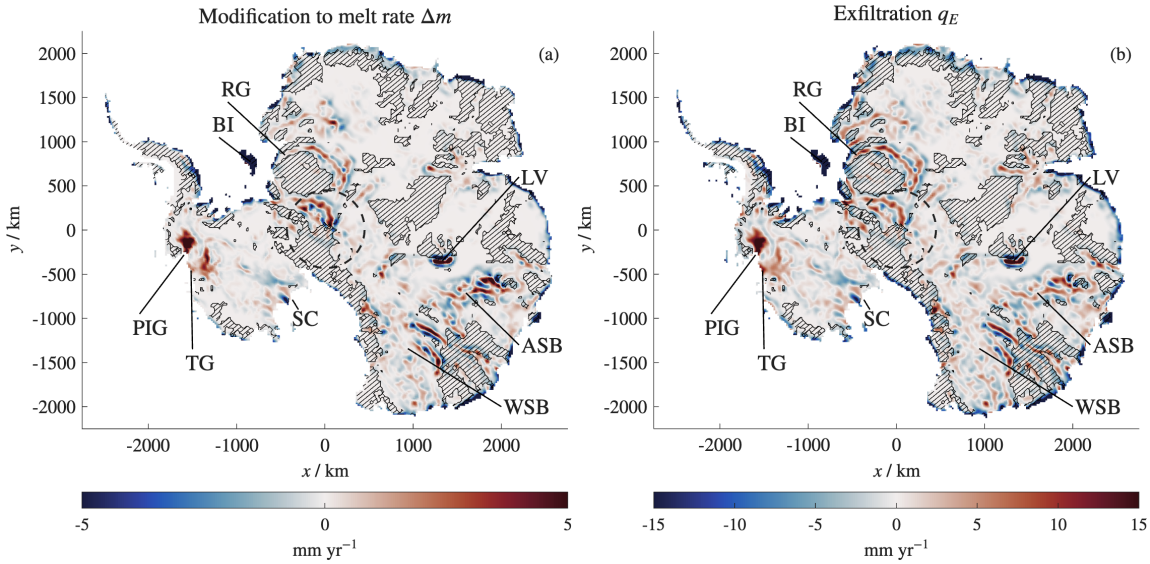


Figure 5.10: (a) Asymptotic modification to melt rate based on the heat flux modification above, compared with (b) the exfiltration q_E, for the K_{sb} and S_s in Figure 5.7.

5.5.2 Basal melt modification correlates with exfiltration

Assuming a thawed bed, modification of the geothermal heat flux results in a corresponding modification of the basal melt rate. Figure 5.10(a) shows the resulting modification Δm in the melt rate from the estimated heat flux modification in Figure 5.7, obtained using Equation (5.40). For the same parameter values, Figure 5.10(b) shows the exfiltration q_E, obtained using Equation (5.21). From a visual inspection Δm and q_E are closely correlated, but q_E is 2–3 times larger. This suggests that the leading-order contribution of groundwater to subglacial water budgets is through exfiltration and infiltration, but that the modification to the melt rate through geothermal heat flux modification is also significant.

The correlation between Δm and q_E can be understood by referring to Equations (5.12) and (5.40), which are almost identical except that the factor H_{sb} in the former is replaced with $c_p G H_{sb}^2 / 2k_{sb}^T L$ in the latter. This suggests that the size of the melt modification relative to the exfiltration roughly scales with the parameter $\Lambda = c_p G H_{sb} / k_{sb}^T L$. This has the form of a Stefan number, where $G H_{sb} / k_{sb}^T$ is the natural scale for the change in temperature across the depth of the basin.

The parameter Λ, plotted in Figure 5.11, is highest where the heat flux is high, such as beneath Pine Island Glacier and Thwaites Glacier (PIG and TG), and where the sedimentary basins are thickest, such as beneath Wilkes Subglacial Basin and Aurora Subglacial Basin (WSB and ASB), and near the South Pole (within the dashed

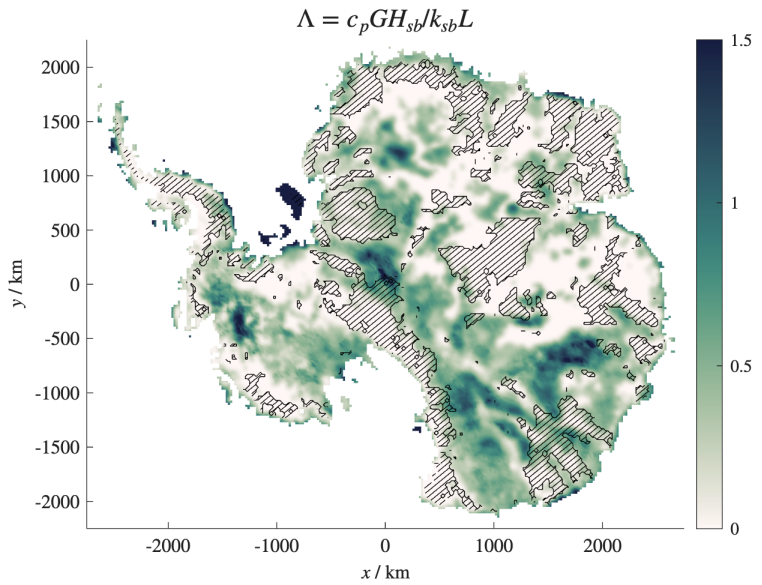


Figure 5.11: Parameter $\Lambda = c_p G H_{sb}/k_{sb}^T L$, which roughly determines the size of the melt rate modification relative to the exfiltration.

circle). In these locations, the ratio of Δm to q_E ought to be relatively high. This can be seen in Figure 5.10, where these locations exhibit particularly high values of Δm compared to other regions (*e.g.* Recovery Glacier (RG)) with similar values of q_E but lower values of Λ.

5.6 Discussion

In this chapter I have described a simple model for three-dimensional heat transport and groundwater flow in a sedimentary basin, including both topography and compaction as drivers of flow. This model predicts that heat flux is typically enhanced where groundwater is exfiltrated and reduced where groundwater infiltrates. I have derived an asymptotic approximation for the modification to the groundwater flux for small Péclet numbers, and shown that this approximates the numerical solution well for realistic parameter values.

For large but realistic values of the parameters K_{sb} and S_s, the heat flux beneath Antarctica could be modified by tens of mW m^{-2} in either direction, representing a significant alteration. This highlights the need to account for groundwater flow in models of Antarctic geothermal heat flux. Topographically-driven groundwater flow tends to enhance heat flux in topographic lows at the centre of glaciers, and reduce heat flux at the margins, providing a potential self-reinforcing mechanism for ice streams across much of both West and East Antarctica. Compaction-driven

groundwater flow also provides a potential positive feedback by enhancing heat flux below ice that is already thinning, an effect that is currently concentrated beneath Thwaites Glacier and Pine Island Glacier.

A number of simplifying assumptions have been made in order to obtain these results. First is the use of an asymptotic solution for the heat flux modification in Section 5.5 (rather than the full solution of the equations). This asymptotic solution may prove inaccurate when groundwater fluxes are large, and in particular may underestimate the magnitude of the perturbation (see Figure 5.5). However, this approximation is unlikely to substantially affect the qualitative behaviour, and likely has less impact than other assumptions.

Another assumption is that of an isothermal thawed bed, when in reality large regions of the Antarctic bed are likely to be frozen. Where the bed is frozen, the permeability of the frozen rock is reduced to almost zero. Modelling of this region would require introducing a free boundary representing the extent of the frozen region, whose position is determined by balances of energy and water mass across the boundary. It can be noted (referring to Figure 5.1(b)) that the overlap of sedimentary basins with frozen bed regions is small, partly because sedimentary basins are formed by the deposition of sediments in topographic lows, whereas the bed is more likely to be frozen in topographic highs. This suggests that bed freezing need not be a concern over many of the smaller-scale regions of interest here, although there are some exceptions *e.g.* in Wilkes Land and near the South Pole.

The treatment of the basal temperature above overlaps with the simplifying assumptions about the basal effective pressure, which has been parameterised here in a simple way. This avoids the need to solve a PDE (or system of PDEs) to describe the subglacial drainage system. An effective pressure equal to 10% of the overburden (as assumed) is a reasonable value for most of Antarctica, but near the grounding line in particular the effective pressure is likely to be a significantly higher fraction of the overburden (Ehrenfeucht et al., 2025). This suggests that the above modelling overestimates the hydraulic potential gradient, and thus the groundwater fluxes, in this region. Moreover, the compaction-driven groundwater flow can vary significantly and even change direction at high flotation fractions, as seen in Section 4.5 of the previous chapter. The work in this chapter therefore could be developed by including a simple coupled model of subglacial hydrology (*e.g.* Kazmierczak et al., 2024), or by incorporating the effect of groundwater flow into a more involved hydrology model (*e.g.* GlaDS (Werder et al., 2013) or SHAKTI (Sommers et al., 2018)).

As discussed in the previous chapter, subglacial hydrology and thermodynamics are interconnected in several ways. For instance, high effective pressures lead to the formation of frozen fringe as ice infiltrates the underlying sediment (Meyer et al., 2018). In addition, basal water is unable to be transported through regions of frozen bed (although as previously discussed, groundwater flow could enable water to flow underneath such regions). When the bed temperature is non-uniform, the subglacial hydrological system takes on an important role in transporting heat across the ice bed (*e.g.* Schoof and Mantelli, 2021). For large fluxes of basal water, the water flow itself may dissipate significant heat; this underpins the formation of subglacial conduits, which grow by melting in response to such dissipation (Flowers, 2015).

These considerations are also relevant to the above prediction of the modification to basal melt Δm due to groundwater, based on Equation (5.14). In predicting this modification, it was assumed that the other sources of heat to the ice bed were unaffected by groundwater, which is unlikely to be accurate in reality. Firstly, as mentioned above, the dissipation D_h depends on the water flux through the subglacial hydrological system, which is directly affected by exfiltration and infiltration. For the large water fluxes associated with subglacial conduits, this dissipation is a significant heat source. The frictional heating could also depend on groundwater, via the subglacial hydrology, if the sliding law depends on the effective pressure N, as considered in Chapter 4. Frictional heating often dominates geothermal heat flux, especially beneath rapidly-flowing ice (Reading et al., 2022), so even modest changes in the friction may be important to the basal thermal budget. Finally, in Chapter 4 it was observed that groundwater could influence the ice thickness H_i and velocity u_i, which would affect heat transport within the ice and hence conduction into the ice, although this feedback is likely less significant than those named above.

This chapter has also only considered steady- or quasi-steady-state models. In reality, grounding line motion and ice thickness changes will introduce transience into the groundwater flow over timescales of centuries to millennia. Evolution of the subglacial hydrological system will also induce changes in the effective pressure over much faster timescales of months to years. While exploring time-dependent solutions is beyond the scope of this chapter, it could provide further insight into the feedbacks associated with ice streams and ice thinning suggested by the results above. In addition, the slow response time of groundwater in sedimentary basins could mean that groundwater flow and thus temperature profiles in sedimentary basins are still responding to historic ice sheet changes, rather than being in a steady state (similarly

to Chapter 3). This delay between forcing and response could be significant when considering groundwater flow coupled to ice sheet models.

Outside of the modelling assumptions, the work in this chapter is also limited by current knowledge of the geology and hydraulic properties of sedimentary basins. A spatially uniform hydraulic conductivity has been assumed in the calculations, although the permeability and hence conductivity of sedimentary basins is likely to be highly heterogeneous even on small scales. For instance, faults could act as highly localised regions of high permeability, concentrating groundwater flow and hence heat flux enhancement (Tankersley et al., 2022). Until the hydraulic properties of sedimentary basins are better known, the work here can provide at best an order-of-magnitude estimate of the importance of groundwater and a qualitative description of its likely behaviour. However, provided the Dupuit assumption remains valid, the asymptotic solution presented in this chapter can be generalised to heterogeneous and anisotropic K_{sb} using the groundwater flow model described in Chapter 2, Section 2.4.

All in all, however, my work in this chapter expands the existing scientific framework for modelling the effect of groundwater flow on Antarctic geothermal heat flux, and demonstrates the need for further investigation into this topic. The development of more complex mathematical models, alongside further advances in using geophysical methods to investigate Antarctic sedimentary basins, will enable future breakthroughs in understanding the basal conditions of Antarctica and the future of the Antarctic Ice Sheet.

Chapter 6

Conclusions

6.1 Summary

In this thesis, I have sought to investigate the possible role and importance of groundwater in sedimentary basins beneath Antarctica using mathematical modelling. My first aim was to develop a theoretical framework for modelling subglacial groundwater flow, and obtain analytical expressions for the exfiltration and infiltration. In particular, I set out to investigate the importance of horizontal groundwater flow, since existing analytical work (Robel et al., 2023) considers only vertical flow. Since including groundwater flow allows for the modelling of seawater intrusion, I then sought to use this model to estimate the permeability of Antarctic sedimentary basins by comparing to inferred groundwater salinity from field observations by Gustafson et al. (2022). This in turn would enable estimation of the water flux due to exfiltration and infiltration.

I also sought to investigate the effects of coupling groundwater flow to a model of subglacial hydrology, addressing an existing gap in the literature, and further coupling this to the sliding of the ice. Finally, motivated by existing work investigating the effect of groundwater on geothermal heat flux (Gooch et al., 2016; Li et al., 2022, supplementary material), I sought to develop this work by obtaining generalised predictions of the heat flux modification and by incorporating horizontal groundwater flow.

I begun my investigations in Chapter 2 by deriving a suitable model for groundwater flow, driven by both horizontal pressure gradients and by compaction. While the resulting 'groundwater flow equation' (2.21) is well-known, its application in a subglacial context required novel consideration of how to implement a non-zero effective pressure at the ice bed. Using the Dupuit approximation, I obtained from this model a closed expression for the exfiltration q_E, along with the Darcy flux components,

which can be evaluated from suitable data or incorporated into other models. The most uncertain parameters in this expression are the permeability k_{sb} and specific storage S_s of the sedimentary basin, which control the size of topographically-driven and compaction-driven groundwater flow respectively (the latter alongside the loading efficiency ξ). The expression for q_E can also be generalised to an anisotropic and heterogeneous aquifer.

While the Dupuit approximation is suitable for a wide range of problems involving subglacial groundwater due to the small aspect ratio $\varepsilon = [z]/[x]$, there are some further restrictions on its use. Firstly, the timescale needs to be sufficiently large that the quantity $\varepsilon^2\zeta = S_s\mu[z]^2/k_{sb}\rho g[t]$ is also small, which is potentially restrictive if the hydraulic diffusivity $k_{sb}\rho g/S_s\mu$ of the porous medium is relatively low. Secondly, if the sedimentary basin is anisotropic with vertical and horizontal permeabilities k^V_{sb} and k^H_{sb}, the quantity $\varepsilon^2 k^H_{sb}/k^V_{sb}$ must also be small, which could fail if the rock consists of strata with large variations in permeability. In the case where $\varepsilon^2 k^H_{sb}/k^V_{sb}$ is not small, the Dupuit regime may still be applicable on sufficiently long timescales once the pressure has become roughly hydrostatic (*e.g.* Benham et al., 2022), but, as in Chapter 3, changes in the ice sheet forcing over these timescales may prevent this regime from being realised in a glaciological setting.

In Chapter 3, by modelling seawater intrusion, I aimed to constrain the permeability of a sedimentary basin by comparing modelled seawater intrusion to observed groundwater salinity by Gustafson et al. (2022), and moreover to predict the topographically-driven exfiltration resulting from horizontal groundwater flow. It was found that periodic grounding line motion could cause seawater to become trapped in regions of the sedimentary basin that are freshwater-saturated in the steady state (for the most advanced grounding line position). The results of this approach suggested a permeability at the high end of realistic ranges was most appropriate, suggesting that horizontal groundwater flow and resulting exfiltration are important to account for. Seawater intrusion also had a significant effect on the topographically-driven exfiltration, particularly in the unsteady state where the freshwater lens occupies a relatively small portion of the aquifer. The predicted influence of seawater intrusion on groundwater flow is worthy of note, as subsequent chapters do not account for this.

However, the estimated permeability includes substantial uncertainty, in which potential heterogeneity of the sedimentary basin is a particularly important factor. Additional uncertainty results from the reconstruction of the history of the ice sheet,

the use of a cross-sectional model, the neglect of subglacial hydrology and compaction-driven groundwater flow, and the current sparsity of field observations. With this said, the results of this chapter demonstrate the viability of seawater intrusion modelling for estimating the permeability of subglacial sedimentary basins, and possible developments of this approach are discussed in the 'Future Work' section below.

Chapter 4 addresses the coupling of groundwater flow to basal hydrology and to the sliding of the ice. In this chapter, I showed that infiltration into the sedimentary basin could drain water away from the ice bed, locally increasing effective pressure and hence basal friction. Likewise, localised exfiltration could reduce the basal effective pressure, promoting sliding by reducing the friction. I also showed that compaction-driven groundwater flow could affect ongoing grounding line motion, slowing both retreat and advance of the grounding line via localised infiltration and exfiltration respectively. This result highlighted the subtle dependence of the compaction-driven exfiltration on both effective pressure and overall water pressure, which in this case exhibited competing effects. It also suggests that sedimentary basins could play a role in the response of the Antarctic Ice Sheet to climate change, in this case by slowing the rate of ice loss and resulting sea level rise. The results of this chapter invite further investigations into the interaction between groundwater and basal hydrology, for instance by including a more complex hydrological system, thermodynamic effects, or a second horizontal dimension.

Finally, in Chapter 5 I investigated the effect of groundwater flow on heat flux to the ice bed. In this chapter I derived an approximate analytical expression for the modification to the heat flux by groundwater flow, which is accurate provided that the Péclet number of the heat flow is small (as is the case for realistic permeabilities k_{sb}) and that the compaction-driven groundwater flow is not too large. This approximate heat flux modification could be calculated across Antarctica, allowing some potential feedback mechanisms to be identified. In particular, the usual topography of ice streams drives a groundwater flow that elevates heat flux in their centre and reduces it at the margins, and compaction-driven groundwater flow can enhance heat flux beneath ice that is already thinning. The latter is of particular concern to the future of the Antarctic Ice Sheet, as it suggests that sedimentary basins could provide a positive feedback that accelerates ice loss. These results suggest that more detailed modelling of the interaction between groundwater and thermodynamics warrants investigation, including effects such as bed freezing that are important to the formation of ice streams. The results also highlight the need to better constrain the permeability and

specific storage of Antarctic sedimentary basins, in order to more accurately estimate their effect on basal heat flux.

6.2 Future work

The results of this thesis provide a number of possible directions for future work, some of which I discuss here.

Firstly, it is noted that remote sensing and geophysics are crucial in providing the data used to explore models of groundwater flow. While there has been substantial recent progress in estimating the thickness and extent of Antarctic sedimentary basins using a range of methods (*e.g.* Tankersley et al., 2022; Li et al., 2022; Zhou et al., 2022; Li and Aitken, 2024), these data sets are themselves the outputs of models subject to their own uncertainty. Continued work is therefore required to constrain the thickness of sedimentary basins, and evaluate the uncertainty therein. This could use the indirect methods applied in existing studies (*e.g.* gravity and magnetic anomalies, seismic methods, magnetotelluric imaging), or integrate data from various data sets (Aitken et al., 2023). Obtaining direct observations, *i.e.* samples of the sedimentary rock itself, is also a priority for future studies.

Much uncertainty has originated from not just the values of the permeability and specific storage for sedimentary basins across Antarctica, but how these properties likely vary across and throughout the depth of the sedimentary basin. Accounting for anisotropy and heterogeneity within a model introduces significant uncertainty in how these properties should be represented. Therefore, geophysical methods that can yield insight into these properties are of particular importance. For instance, seismic methods can be used to identify different strata within an aquifer, and magnetotelluric resistivity also depends strongly on porosity (Siegert et al., 2018). The results of Chapter 3 suggest that remote sensing of salinity, which can be estimated using magnetotelluric imaging, could also provide insight into sedimentary basin permeability, and a greater number of point measurements would enable better comparison to model outputs.

There are also several ways in which the modelling approaches in this thesis could be developed. For instance, future models of seawater intrusion could explore a far wider range of parameterisations of heterogeneity than those considered in Chapter 3. One possible approach could be to prescribe a probability distribution for the permeability profile, and run the model on a random sample of cases from this distribution (Benham et al., 2021; Harris et al., 2021). In addition, future modelling work should

account for transverse geometry, which could be achieved via a width-averaged model as proposed in Section 3.6, or by solving the full model in two horizontal dimensions derived in Chapter 2, Section 2.3. Since the results of Chapter 3 suggested the possibility that saltwater could be exfiltrated to the basal hydrological system, possible future modelling work could also explore the impacts of saltwater at the ice bed on subglacial drainage and basal melting.

A natural development of the work in Chapter 4 is to implement groundwater flow within a model of subglacial hydrology in a more realistic glaciological context, by using more complex models of basal hydrology and ice flow, and by doing so in two horizontal dimensions. Such models could be solved in an idealised geometry to further investigate the effect of groundwater infiltration and exfiltration on subglacial drainage and basal sliding. Another possibility would be to incorporate exfiltration and infiltration into a catchment-scale or even continent-scale model of subglacial drainage, which could in turn be coupled to ice flow. A challenge for such work is to account for the fact that compaction-driven groundwater flow requires time-dependent evolution of the ice thickness and/or effective pressure, rendering steady-state models unsuitable. However, a coupled time-dependent model of ice dynamics and subglacial drainage is likely to be computationally costly to implement.

Although many existing models assume zero effective pressure at the ice bed, the dependence of compaction-driven groundwater flow on both overburden and effective pressure suggests that evolution of the subglacial hydrological system should be an important consideration in future models of groundwater flow in sedimentary basins. The results of Section 4.5 suggest in particular that the effective pressure does not just act as a small correction to the overburden, but under certain circumstances can be the dominant driver of groundwater flow, even overriding the effect of the overburden altogether.

Finally, there are several thermodynamic processes that have been omitted from the models used in this thesis but whose interaction with groundwater flow merits investigation. In particular, developing the modelling approach to allow for a partially frozen bed could allow the investigations in this thesis to be improved upon, as well as enabling consideration of further problems. For example, the results in Chapter 5 regarding heat flux modification beneath ice streams suggest that incorporating groundwater flow into a model of ice stream formation could provide insight into the feedbacks and instabilities governing this process. Other possible considerations include whether sedimentary basins could enable water transport across regions of

frozen bed, or whether basal freezing and thawing could act as drivers of large-scale groundwater flow.

One approach to such models could be to allow for only the ice-bed interface to be frozen, resulting in a complementarity problem where the basal water thickness, temperature and pressure obey a different set of equations in two distinct 'frozen' and 'thawed' regimes. This assumes the thickness of the frozen region is much smaller than that of the sedimentary basin, which is true of typical subglacial frozen fringe (Meyer et al., 2018; Hansen et al., 2024). Even without considering the case of a frozen bed, simply allowing a variable bed temperature and including a detailed model of basal hydrology could affect the findings of Chapter 5, such as the predicted basal melt rate modification due to groundwater flow.

6.3 Concluding remarks

Groundwater flow in sedimentary basins beneath Antarctica has the potential to influence ice dynamics in numerous ways via the water and energy budgets at the ice bed, and is associated with several potential feedbacks related to contemporary ice loss. Mathematical modelling can provide useful insights into the dynamics of subglacial groundwater, and the effect thereof on the overlying ice. However, much is still unknown about the properties of Antarctic sedimentary basins, and the precise nature of their potential role. These open questions provide rich opportunities for future research into Antarctic sedimentary basins, including both observational and modelling work, in order to better understand and constrain the future of the Antarctic Ice Sheet.

Appendix A

Numerical methods

In this appendix, I describe the numerical methods used to obtain the solutions presented in this thesis. Throughout this thesis, the equations are discretised spatially using finite volume schemes (a subclass of finite difference methods), and they are then evolved forward in time using a one-step fully implicit method. Numerical methods are implemented in MATLAB, with the inbuilt 'fsolve' function used to solve the implicit equations at each time step. (Manual time stepping is favoured over an inbuilt ODE solver for the ability to explicitly prescribe time steps and sample the solution at specified times.)

Many of the Equations considered in this thesis are solved on a variable domain $0 < x < x_g(t)$. To address this, the coordinate transformation is used

$$x = x_g(t)X, \tag{A.1}$$

which changes the domain to $0 < X < 1$, while introducing x_g and $\dot{x}_g = \mathrm{d}x_g/\mathrm{d}t$ into the equations themselves.

A.1 Saltwater intrusion

Chapter 3 included numerical solutions the complementarity problem given by Equation (3.12). To account for the two possible cases, two auxiliary variables U and V are defined, and the system of equations are solved for h, U and V

$$U^2 = -\frac{\partial h}{\partial t} + \kappa \frac{\partial}{\partial x}\left(h\frac{\partial}{\partial x}\left(p_b + (1+\delta_s)b + \delta_s h\right)\right) \tag{A.2}$$

$$V^2 = H_{sb} - h, \tag{A.3}$$

$$UV = 0, \tag{A.4}$$

using the fact that $s(x,t) = h(x,t) + b(x)$. This formulation ensures that both the constraints of Equation (3.12) are satisfied (upon enforcing that U and V remain real-valued), and that one of the two cases applies at all times.

After applying the transformation (A.1), the definition of U can be written as

$$U^2 = -\frac{\partial h}{\partial t} + \frac{\dot{x}_g}{x_g} X \frac{\partial h}{\partial X} + \frac{\partial}{\partial X}\left(\kappa \frac{h}{x_g^2}\frac{\partial}{\partial X}\left(p_b + (1+\delta_s)b + \delta_s h\right)\right) \tag{A.5}$$

$$= -\frac{\partial h}{\partial t} + \frac{\partial}{\partial X}\left(h\left(\frac{\kappa}{x_g^2}\frac{\partial}{\partial X}\left(p_b + (1+\delta_s)b\right) + \frac{\dot{x}_g}{x_g}X\right) + \frac{\kappa\delta_s}{x_g^2} h \frac{\partial h}{\partial X}\right) - \frac{\dot{x}_g}{x_g} h. \tag{A.6}$$

This is implemented as a finite volume scheme on a uniform spatial mesh grid, with the time derivative approximated using an implicit (backward) method on a variable time mesh. The finite volume method requires the flux to be evaluated at staggered edges, between the mesh points at which h is discretised. Zero flux is imposed into the leftmost cell (Equation (3.14)), along with $h = H_{sb}$ in the rightmost cell (Equation (3.15)). As written in Equation (A.5), the flux between adjacent cells consists of an 'advective' term,

$$h\left(\frac{\kappa}{x_g^2}\frac{\partial}{\partial X}\left(p_b + (1+\delta_s)b\right) + \frac{\dot{x}_g}{x_g}X\right), \tag{A.7}$$

which is approximated using a first-order upwind scheme, and a 'diffusive' term,

$$\frac{\kappa\delta_s}{x_g^2} h \frac{\partial h}{\partial X}, \tag{A.8}$$

in which $\partial h/\partial X$ is approximated using a central difference method, and h using a midpoint arithmetic mean. (It is noted that higher-order methods exist for equations of this form which are more accurate, although the method described above is sufficient for the cases considered in this thesis.)

The solutions in Chapter 3 use between 100 and 200 spatial mesh points, with variable time steps generally between 0.001 and 0.01 (though larger steps are used for the late stages of the long-term simulation shown in Figure 3.5). Smaller time steps are required when the advection rate in Equation (A.7) is large (*e.g.* during rapid grounding line movement), in order to ensure stability of the first-order upwind method.

A.2 Shallow-shelf ice sheet model

Section 4 (along with the idealised solutions in Section 5) used the solution of the shallow-shelf ice sheet model, whose non-dimensional governing equations are given

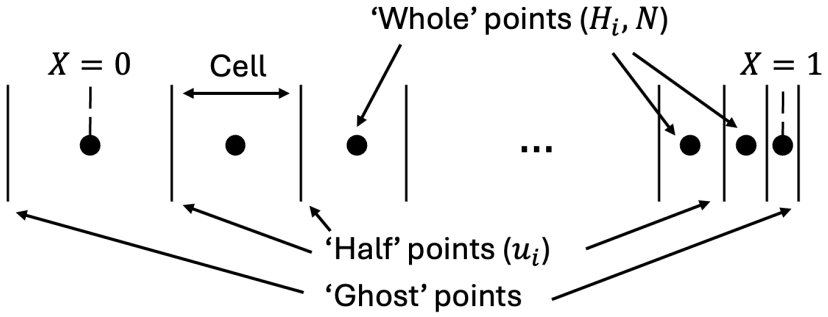


Figure A.1: Schematic of the staggered mesh grid used to obtain numerical solutions for H_i, u_i, x_g and N in Chapter 4.

by Equations (4.18) and (4.19). The procedure used here for solving these equations numerically is based on that described in Schoof (2007a).

After applying the transformation (A.1), Equation (4.1) becomes

$$\frac{\partial H_i}{\partial t} - \frac{\dot{x}_g}{x_g} X \frac{\partial H_i}{\partial X} + \frac{1}{x_g} \frac{\partial}{\partial X}(H_i u_i) = a. \tag{A.9}$$

Equation (A.9) is discretised using a first-order upwind scheme. The velocity u_i is calculated at 'half' mesh points, which are spaced halfway between the 'whole' mesh points at which H_i is found. Figure A.1 shows a depiction of the staggered mesh grid used for this numerical method. Equation (A.9) is solved at every 'whole' mesh point, and it is imposed in addition that $H_i = b/(1-\delta_i)$ at the rightmost mesh point $X = 1$ (Equation (4.22)), which implicitly determines the evolution of x_g.

The ice velocity u_i is found by solving the transformed version of Equation (4.19) at each time step,

$$\frac{4\varepsilon_i}{{x_g}^{1/n+1}} \frac{\partial}{\partial X} \left(H_i \left| \left(\frac{\partial u_i}{\partial X} \right)^2 + \varepsilon_R^2 \right|^{(1-n)/2n} \frac{\partial u_i}{\partial X} \right) - \mathcal{C} N \left(\frac{|u_i|}{|u_i| + (\mathcal{C}N)^{1/m_W}} \right)^{m_W} \operatorname{sgn}(u_i) - \frac{1}{x_g} H_i \frac{\partial}{\partial X}(H_i + b) = 0. \tag{A.10}$$

Following Haseloff et al. (2025), a regularisation parameter $\varepsilon_R = 0.01$ is introduced to ensure smoothness when $\partial u_i / \partial X = 0$. Discretised versions of the boundary conditions (4.21) and (4.23) are imposed at 'ghost' mesh points just outside the domain on either side. In discretising Equation (A.10), spatial derivatives $\partial/\partial X$ are estimated using a central difference. The factor of H_i in the driving stress is found as a midpoint arithmetic mean, as is N in the basal friction.

Equations (A.9) and (A.10) are solved on a 300-point variable grid, with mesh points more tightly spaced towards the grounding line and a mesh spacing decreasing to 10^{-4} in the rightmost cell. This ensures that the extensional stress boundary layer near the grounding line is accurately resolved. The numerical method was validated for the case of a Weertman sliding law using the results of Schoof (2007a).

Because steady states of the shallow-shelf model are non-unique in general, steady-state solutions are obtained by evolving the model forward in time until successive time steps satisfy (in discretised form)

$$\int_0^{x_g} \left(\left(\frac{\partial H_i}{\partial t} \right)^2 + \left(\frac{\partial u_i}{\partial t} \right)^2 + \left(\frac{\partial N}{\partial t} \right)^2 \right) \mathrm{d}x + \left(\frac{\mathrm{d}x_g}{\mathrm{d}t} \right)^2 < 0.001^2. \tag{A.11}$$

In order to promote fast convergence, an artificially small value of the parameter λ is used in the subglacial hydrology equation (see below) when finding these solutions. An initial condition is obtained by solving the approximate steady state equation for x_g found by Tsai et al. (2015), and then by integrating the ice sheet model ignoring the extensional stress terms as in Chapter 3. To obtain the time-dependent solutions in Section 4.5, a variable time step is used, with shorter time steps early on in order to accurately resolve the initial behaviour.

A.3 Subglacial hydrology model

The evolution of the subglacial hydrological system in Chapter 4 is given by Equation (4.33). Applying the transformation (A.1), this becomes

$$\begin{aligned} -\left(\frac{\lambda}{N^2} + \Sigma \mathcal{E} H_{sb} \right) \left(\frac{\partial N}{\partial t} - \frac{\dot{x}_g}{x_g} X \frac{\partial N}{\partial X} \right) = \\ \frac{1}{{x_g}^2} \frac{\partial}{\partial X} \left[\left(\frac{1}{N} + \kappa H_{sb} \right) \frac{\partial}{\partial X} \left((1 - \delta_i) H_i - \mathcal{E} N + b \right) \right] + m \\ - \Sigma H_{sb} (1 - \delta_i)(1 - \xi) \left(\frac{\partial H_i}{\partial t} - \frac{\dot{x}_g}{x_g} X \frac{\partial H_i}{\partial X} \right). \end{aligned} \tag{A.12}$$

This equation is implemented as a finite volume method, with N solved at 'whole' meshpoints, using the same grid as for H_i above. Equation (A.12) is solved at all except the rightmost mesh point ($X = 1$), where N is set to be 0 (Equation (4.29)). In calculating the fluxes between cells, $1/N$ is estimated using its left-hand value in order to avoid a singularity from the rightmost grid cell. The flux into the leftmost cell is imposed to be minus the outgoing flux, to satisfy the zero-flux condition at $X = 0$ (Equation (4.28)).

A.4 Heat equation in sedimentary basin

The example solutions in Chapter 5 require solving the heat equation (5.26) in the steady state and in one horizontal dimension. For simplicity, the source terms due to radiative and dissipative heating are neglected. After these simplifications, and dropping hats in the notation, the equation may be written as

$$u_{sb}\frac{\partial T_{sb}}{\partial x} + w_{sb}\frac{\partial T_{sb}}{\partial z} = \frac{1}{\mathrm{Pe}}\frac{\partial^2 T_{sb}}{\partial z^2}, \tag{A.13}$$

where $u_{sb}(x)$ and $w_{sb}(x,z)$ are known functions in terms of the overburden and effective pressure. This is implemented within a finite volume scheme as

$$\frac{\partial}{\partial x}\left(u_{sb}T_{sb}\right) + \frac{\partial}{\partial z}\left(w_{sb}T_{sb} - \frac{1}{\mathrm{Pe}}\frac{\partial T_{sb}}{\partial z}\right) - \left(\frac{\partial u_{sb}}{\partial x} + \frac{\partial w_{sb}}{\partial z}\right)T_{sb} = 0, \tag{A.14}$$

noting that the groundwater flow is not incompressible in general because of the compaction terms. In particular,

$$\frac{\partial u_{sb}}{\partial x} + \frac{\partial w_{sb}}{\partial z} = -\frac{\Sigma}{\kappa}\frac{\partial \psi_c}{\partial t}. \tag{A.15}$$

In order to work within the non-uniform sedimentary basin geometry, the transformation is introduced

$$Z = \frac{z - b + H_{sb}}{H_{sb}}, \tag{A.16}$$

so that the domain is $0 < x < x_g$, $0 < Z < 1$. (Since this equation is not solved for time-varying x_g, there is no need to rescale the x variable as above.) Under this transformation, Equation (A.14) becomes

$$\left(\frac{\partial}{\partial x} - \frac{1}{H_{sb}}\left(\frac{\partial b}{\partial x} - \frac{\partial H_{sb}}{\partial x}\right)\frac{\partial}{\partial Z}\right)\left(u_{sb}T_{sb}\right) + \frac{1}{H_{sb}}\frac{\partial}{\partial Z}\left(w_{sb}T_{sb} - \frac{1}{\mathrm{Pe}\,H_{sb}}\frac{\partial T_{sb}}{\partial Z}\right) + \frac{\Sigma}{\kappa}\frac{\partial \psi_c}{\partial t}T_{sb} = 0. \tag{A.17}$$

The advective heat fluxes $u_{sb}T_{sb}$ and $w_{sb}T_{sb}$ are discretised using a first-order upwind scheme in each case, and the conductive heat flux $\partial T_{sb}/\partial z$ using a central difference. The boundary conditions are given by Equations (5.28) and (5.29), which together define the fluxes into the lowermost and out of the uppermost row of cells. In addition, the definitions of u_{sb} and w_{sb} automatically impose no normal advective flux through $x = 0$ and $z = b - H_{sb}$. The mesh grid consists of the 300-point non-uniform grid used to solve for H_i above in the horizontal, and 20 equally-spaced points in the vertical, for a total of 6000 mesh points.

Bibliography

Aitken, A. R., Li, L., Kulessa, B., Schroeder, D., Jordan, T. A., Whittaker, J. M., Anandakrishnan, S., Dawson, E. J., Wiens, D. A., Eisen, O., et al. (2023). Antarctic sedimentary basins and their influence on ice-sheet dynamics. *Reviews of Geophysics*, 61(3):e2021RG000767.

Alley, R. B. (1996). Towards a hydrological model for computerized ice-sheet simulations. *Hydrological Processes*, 10(4):649–660.

Anandakrishnan, S. (2003). Dilatant till layer near the onset of streaming flow ofIce Stream C, West Antarctica, determined by AVO (amplitude vs offset) analysis. *Annals of Glaciology*, 36:283–286.

Aquilina, L., Vergnaud-Ayraud, V., Les Landes, A. A., Pauwels, H., Davy, P., Pételet-Giraud, E., Labasque, T., Roques, C., Chatton, E., Bour, O., et al. (2015). Impact of climate changes during the last 5 million years on groundwater in basement aquifers. *Sci. Rep.-UK*, 5(1):1–12.

Arias, P., Bellouin, N., Coppola, E., Jones, R., Krinner, G., Marotzke, J., Naik, V., Palmer, M., Plattner, G.-K., Rogelj, J., et al. (2021). Climate change 2021: the physical science basis. contribution of working group i to the sixth assessment report of the intergovernmental panel on climate change; technical summary.

Athy, L. F. (1930). Density, porosity, and compaction of sedimentary rocks. *Aapg Bulletin*, 14(1):1–24.

Audet, D. and Fowler, A. (1992). A mathematical model for compaction in sedimentary basins. *Geophysical Journal International*, 110(3):577–590.

Bamber, J. L., Ferraccioli, F., Joughin, I., Shepherd, T., Rippin, D. M., Siegert, M. J., and Vaughan, D. G. (2006). East Antarctic ice stream tributary underlain by major sedimentary basin. *Geology*, 34(1):33–36.

Bear, J. (2013). *Dynamics of fluids in porous media*. Courier Corporation.

Bell, R., Blankenship, D., Finn, C. A., Morse, D., Scambos, T., Brozena, J., and Hodge, S. (1998). Influence of subglacial geology on the onset of a West Antarctic ice stream from aerogeophysical observations. *Nature*, 394(6688):58–62.

Bell, R. E., Studinger, M., Shuman, C. A., Fahnestock, M. A., and Joughin, I. (2007). Large subglacial lakes in East Antarctica at the onset of fast-flowing ice streams. *Nature*, 445(7130):904–907.

Benham, G. P., Bickle, M. J., and Neufeld, J. A. (2021). Two-phase gravity currents in layered porous media. *Journal of Fluid Mechanics*, 922:A7.

Benham, G. P., Neufeld, J. A., and Woods, A. W. (2022). Axisymmetric gravity currents in anisotropic porous media. *Journal of Fluid Mechanics*, 952:A23.

Bense, V. and Person, M. (2008). Transient hydrodynamics within intercratonic sedimentary basins during glacial cycles. *Journal of Geophysical Research: Earth Surface*, 113(F4).

Beyer, S., Kleiner, T., Aizinger, V., Rückamp, M., and Humbert, A. (2018). A confined–unconfined aquifer model for subglacial hydrology and its application to the Northeast Greenland Ice Stream. *The Cryosphere*, 12(12):3931–3947.

Bougamont, M., Price, S., Christoffersen, P., and Payne, A. (2011). Dynamic patterns of ice stream flow in a 3-D higher-order ice sheet model with plastic bed and simplified hydrology. *J. Geophys. Res.-Earth*, 116(F4).

Boulton, G. and Caban, P. (1995). Groundwater flow beneath ice sheets: part ii—its impact on glacier tectonic structures and moraine formation. *Quaternary Science Reviews*, 14(6):563–587.

Boulton, G., Caban, P., and Van Gijssel, K. (1995). Groundwater flow beneath ice sheets: Part i—large scale patterns. *Quaternary Science Reviews*, 14(6):545–562.

Boulton, G. and Dobbie, K. (1993). Consolidation of sediments by glaciers: relations between sediment geotechnics, soft-bed glacier dynamics and subglacial groundwater flow. *Journal of Glaciology*, 39(131):26–44.

Boulton, G., Lunn, R., Vidstrand, P., and Zatsepin, S. (2007). Subglacial drainage by groundwater–channel coupling, and the origin of esker systems: part ii—theory and simulation of a modern system. *Quaternary Science Reviews*, 26(7-8):1091–1105.

Brondex, J., Gillet-Chaulet, F., and Gagliardini, O. (2019). Sensitivity of centennial mass loss projections of the Amundsen basin to the friction law. *The Cryosphere*, 13(1):177–195.

Bueler, E. and van Pelt, W. (2015). Mass-conserving subglacial hydrology in the Parallel Ice Sheet Model version 0.6. *Geoscientific Model Development*, 8(6):1613–1635.

Burton-Johnson, A., Dziadek, R., and Martin, C. (2020). Geothermal heat flow in Antarctica: Current and future directions. *The Cryosphere Discussions*, 2020:1–45.

Cairns, G., Benham, G., and Hewitt, I. (2025). Groundwater dynamics beneath a marine ice sheet. *The Cryosphere*, 19(9):3725–3747.

Christoffersen, P., Bougamont, M., Carter, S., Fricker, H., and Tulaczyk, S. (2014). Significant groundwater contribution to Antarctic ice streams hydrologic budget. *Geophysical Research Letters*, 41(6):2003–2010.

Christoffersen, P. and Tulaczyk, S. (2003a). Response of subglacial sediments to basal freeze-on 1. Theory and comparison to observations from beneath the West Antarctic Ice Sheet. *Journal of Geophysical Research: Solid Earth*, 108(B4).

Christoffersen, P. and Tulaczyk, S. (2003b). Thermodynamics of basal freeze-on: predicting basal and subglacial signatures of stopped ice streams and interstream ridges. *Annals of Glaciology*, 36:233–243.

Cook, S., Christoffersen, P., Todd, J., Slater, D., and Chauché, N. (2020). Coupled modelling of subglacial hydrology and calving-front melting at Store Glacier, West Greenland. *The Cryosphere*, 14(3):905–924.

Cooper Jr, H. H. (1959). A hypothesis concerning the dynamic balance of fresh water and salt water in a coastal aquifer. *Journal of Geophysical Research*, 64(4):461–467.

Creyts, T. and Schoof, C. (2009). Drainage through subglacial water sheets. *Journal of Geophysical Research: Earth Surface*, 114(F4).

Croucher, A. and O'Sullivan, M. (1995). The Henry problem for saltwater intrusion. *Water Resour. Res.*, 31(7):1809–1814.

Cuffey, K. M. and Paterson, W. S. B. (2010). *The physics of glaciers*. Academic Press.

Dawson, E. J., Schroeder, D. M., Chu, W., Mantelli, E., and Seroussi, H. (2022). Ice mass loss sensitivity to the Antarctic ice sheet basal thermal state. *Nature Communications*, 13(1):4957.

de Fleurian, B., Gagliardini, O., Zwinger, T., Durand, G., Le Meur, E., Mair, D., and Råback, P. (2014). A double continuum hydrological model for glacier applications. *The Cryosphere*, 8(1):137–153.

De Fleurian, B. e. a. (2018). SHMIP the subglacial hydrology model intercomparison project. *Journal of Glaciology*, 64(248):897–916.

Dentz, M., Tartakovsky, D., Abarca, E., Guadagnini, A., Sánchez-Vila, X., and Carrera, J. (2006). Variable-density flow in porous media. *J. Fluid Mech.*, 561:209–235.

Dow, C. (2022). The role of subglacial hydrology in Antarctic ice sheet dynamics and stability: a modelling perspective. *Annals of Glaciology*, 63(87-89):49–54.

Dow, C., Ross, N., Jeofry, H., Siu, K., and Siegert, M. (2022). Antarctic basal environment shaped by high-pressure flow through a subglacial river system. *Nature Geoscience*, 15(11):892–898.

Edwards, T. L., Nowicki, S., Marzeion, B., Hock, R., Goelzer, H., Seroussi, H., Jourdain, N. C., Slater, D. A., Turner, F. E., Smith, C. J., et al. (2021). Projected land ice contributions to twenty-first-century sea level rise. *Nature*, 593(7857):74–82.

Ehrenfeucht, S., Dow, C., McArthur, K., Morlighem, M., and McCormack, F. (2025). Antarctic wide subglacial hydrology modeling. *Geophysical Research Letters*, 52(1):e2024GL111386.

Engelhardt, H., Humphrey, N., Kamb, B., and Fahnestock, M. (1990). Physical conditions at the base of a fast moving Antarctic ice stream. *Science*, 248(4951):57–59.

Engelhardt, H. and Kamb, B. (1997). Basal hydraulic system of a West Antarctic ice stream: constraints from borehole observations. *Journal of Glaciology*, 43(144):207–230.

Flowers, G. (2015). Modelling water flow under glaciers and ice sheets. *Proceedings of the Royal Society A: Mathematical, Physical and Engineering Sciences*, 471(2176):20140907.

Flowers, G. E. (2008). Subglacial modulation of the hydrograph from glacierized basins. *Hydrological Processes*, 22(19):3903–3918.

Flowers, G. E. and Clarke, G. K. (2000). An integrated modelling approach to understanding subglacial hydraulic release events. *Annals of Glaciology*, 31:222–228.

Flowers, G. E. and Clarke, G. K. (2002a). A multicomponent coupled model of glacier hydrology 1. theory and synthetic examples. *Journal of Geophysical Research: Solid Earth*, 107(B11):ECV–9.

Flowers, G. E. and Clarke, G. K. (2002b). A multicomponent coupled model of glacier hydrology 2. application to trapridge glacier, yukon, canada. *Journal of Geophysical Research: Solid Earth*, 107(B11):ECV–10.

Fowler, A. (1981). A theoretical treatment of the sliding of glaciers in the absense of cavitation. *Philosophical Transactions of the Royal Society of London. Series A, Mathematical and Physical Sciences*, 298(1445):637–681.

Fowler, A. and Noon, C. (1999). Mathematical models of compaction, consolidation and regional groundwater flow. *Geophysical Journal International*, 136(1):251–260.

Freeze, R. and Cherry, J. (1979). *Groundwater*. Prentice-Hall.

Fretwell, P., Pritchard, H. D., Vaughan, D. G., Bamber, J. L., Barrand, N. E., Bell, R., Bianchi, C., Bingham, R. G., Blankenship, D. D., Casassa, G., et al. (2013).

Bedmap2: improved ice bed, surface and thickness datasets for Antarctica. *The Cryosphere*, 7(1):375–393.

Fricker, H., Galton-Fenzi, B., Walker, C., Freer, B., Padman, L., and DeConto, R. (2025). Antarctica in 2025: Drivers of deep uncertainty in projected ice loss. *Science*, 387(6734):601–609.

Gagliardini, O., Cohen, D., Råback, P., and Zwinger, T. (2007). Finite-element modeling of subglacial cavities and related friction law. *Journal of Geophysical Research: Earth Surface*, 112(F2).

Gerber, D., Wilen, L. A., Poydenot, F., Dufresne, E. R., and Style, R. W. (2022). Stress accumulation by confined ice in a temperature gradient. *Proceedings of the National Academy of Sciences*, 119(31):e2200748119.

Gooch, B., Young, D., and Blankenship, D. (2016). Potential groundwater and heterogeneous heat source contributions to ice sheet dynamics in critical submarine basins of East Antarctica. *Geochemistry, Geophysics, Geosystems*, 17(2):395–409.

Gowan, E., Hinck, S., Niu, L., Clason, C., and Lohmann, G. (2023). The impact of spatially varying ice sheet basal conditions on sliding at glacial time scales. *Journal of Glaciology*, 69(276):1056–1070.

Gregov, T., Pattyn, F., and Arnst, M. (2023). Grounding-line flux conditions for marine ice-sheet systems under effective-pressure-dependent and hybrid friction laws. *Journal of Fluid Mechanics*, 975:A6.

Gustafson, C., Key, K., Siegfried, M., Winberry, J., Fricker, H., Venturelli, R., and Michaud, A. (2022). A dynamic saline groundwater system mapped beneath an Antarctic ice stream. *Science*, 376(6593):640–644.

Hansen, D., Warburton, K., Zoet, L., Meyer, C., Rempel, A., and Stubblefield, A. (2024). Presence of frozen fringe impacts soft-bedded slip relationship. *Geophysical Research Letters*, 51(12):e2023GL107681.

Harris, C., Jackson, S. J., Benham, G. P., Krevor, S., and Muggeridge, A. H. (2021). The impact of heterogeneity on the capillary trapping of CO2 in the Captain Sandstone. *International Journal of Greenhouse Gas Control*, 112:103511.

Haseloff, M., Hewitt, I., and Katz, R. (2025). Subglacial hydrology regulates oscillations in marine ice streams. *EGUsphere*, 2025:1–28.

Hayden, A.-M., Pelle, T., and Dow, C. (2025). The past, present, and future evolution of Aurora Subglacial Basin's subglacial drainage system. *Nature Communications*, 16(1):2747.

Helanow, C., Iverson, N., Woodard, J., and Zoet, L. (2021). A slip law for hard-bedded glaciers derived from observed bed topography. *Science Advances*, 7(20):eabe7798.

Hewitt, I. (2013). Seasonal changes in ice sheet motion due to melt water lubrication. *Earth and Planetary Science Letters*, 371-372:16–25.

Huybrechts, P. (2002). Sea-level changes at the LGM from ice-dynamic reconstructions of the Greenland and Antarctic ice sheets during the glacial cycles. *Quatenary Sci. Rev.*, 21(1-3):203–231.

Joughin, I., Smith, B., and Schoof, C. (2019). Regularized Coulomb friction laws for ice sheet sliding: Application to Pine Island Glacier, Antarctica. *Geophysical research letters*, 46(9):4764–4771.

Joughin, I., Tulaczyk, S., Bamber, J. L., Blankenship, D., Holt, J. W., Scambos, T., and Vaughan, D. G. (2009). Basal conditions for Pine Island and Thwaites Glaciers, West Antarctica, determined using satellite and airborne data. *J. Glaciol.*, 55(190):245–257.

Kaspari, S., Mayewski, P. A., Dixon, D. A., Spikes, V. B., Sneed, S. B., Handley, M. J., and Hamilton, G. S. (2004). Climate variability in west antarctica derived from annual accumulation-rate records from itase firn/ice cores. *Annals of Glaciology*, 39:585–594.

Kazmierczak, E., Gregov, T., Coulon, V., and Pattyn, F. (2024). A fast and unified subglacial hydrological model applied to Thwaites Glacier, Antarctica. *EGUsphere*, 2024:1–36.

Ketabchi, H., Mahmoodzadeh, D., Ataie-Ashtiani, B., and Simmons, C. T. (2016). Sea-level rise impacts on seawater intrusion in coastal aquifers: Review and integration. *J. Hydrol.*, 535:235–255.

Killingbeck, S. F., Kulessa, B., Pearce, R., Brisbourne, A., Borthwick, L., Napoleoni, F., Anandakrishnan, S., Unsworth, M., and Muto, A. (2026). Distinct groundwater regimes in west antarctic sedimentary basins inferred from magnetotelluric imaging. *Journal of Geophysical Research: Solid Earth*, 131(9):e2026JB033859.

Kingslake, J., Scherer, R., Albrecht, T., Coenen, J., Powell, R., Reese, R., Stansell, N., Tulaczyk, S., Wearing, M., and Whitehouse, P. (2018). Extensive retreat and re-advance of the West Antarctic ice sheet during the Holocene. *Nature*, 558(7710):430–434.

Koussis, A. D. and Mazi, K. (2018). Corrected interface flow model for seawater intrusion in confined aquifers: relations to the dimensionless parameters of variable-density flow. *Hydrogeol. J.*, 26(8).

Kulessa, B., Hubbard, B., Williamson, M., and Brown, G. H. (2005). Hydrogeological analysis of slug tests in glacier boreholes. *Journal of Glaciology*, 51(173):269–280.

Kyrke-Smith, T., Katz, R., and Fowler, A. (2014). Subglacial hydrology and the formation of ice streams. *Proceedings of the Royal Society A: Mathematical, Physical and Engineering Sciences*, 470(2161):20130494.

Le Brocq, A., Payne, A., Siegert, M., and Alley, R. (2009). A subglacial water-flow model for West Antarctica. *Journal of Glaciology*, 55(193):879–888.

Lemieux, J.-M. (2006). *Impact of the Wisconsinian glaciation on Canadian continental groundwater flow*. University of Waterloo Waterloo, Ont., Canada.

Lemieux, J.-M., Sudicky, E., Peltier, W., and Tarasov, L. (2008a). Dynamics of groundwater recharge and seepage over the Canadian landscape during the Wisconsinian glaciation. *Journal of Geophysical Research: Earth Surface*, 113(F1).

Lemieux, J.-M., Sudicky, E., Peltier, W., and Tarasov, L. (2008b). Simulating the impact of glaciations on continental groundwater flow systems: 1. Relevant processes and model formulation. *J. Geophys. Res.-Earth*, 113(F3).

Lemieux, J.-M., Sudicky, E. A., Peltier, W. R., and Tarasov, L. (2008c). Simulating the impact of glaciations on continental groundwater flow systems: 2. model application to the wisconsinian glaciation over the canadian landscape. *Journal of Geophysical Research: Earth Surface*, 113(F3).

Li, L. and Aitken, A. (2024). Crustal heterogeneity of Antarctica signals spatially variable radiogenic heat production. *Geophysical Research Letters*, 51(2):e2023GL106201. e2023GL106201 2023GL106201.

Li, L., Aitken, A., Lindsay, M., and Kulessa, B. (2022). Sedimentary basins reduce stability of Antarctic ice streams through groundwater feedbacks. *Nature Geoscience*, 15(8):645–650.

Lowry, D. P., Golledge, N. R., Bertler, N. A., Jones, R. S., and McKay, R. (2019). Deglacial grounding-line retreat in the Ross Embayment, Antarctica, controlled by ocean and atmosphere forcing. *Sci. Adv.*, 5(8):eaav8754.

Lu, G. and Kingslake, J. (2023). Coupling between ice flow and subglacial hydrology enhances marine ice-sheet retreat. *EGUsphere*, 2023:1–31.

MacAyeal, D. (1989). Large-scale ice flow over a viscous basal sediment: Theory and application to ice stream B, Antarctica. *Journal of Geophysical Research: Solid Earth*, 94(B4):4071–4087.

Manger, G. E. (1963). *Porosity and bulk density of sedimentary rocks*. Number 1144. US Government Printing Office.

McCormack, F., Roberts, J., Dow, C., Stål, T., Halpin, J., Reading, A., and Siegert, M. (2022). Fine-scale geothermal heat flow in Antarctica can increase simulated subglacial melt estimates. *Geophysical Research Letters*, 49(15):e2022GL098539.

McKay, R., Naish, T., Powell, R., Barrett, P., Scherer, R., Talarico, F., Kyle, P., Monien, D., Kuhn, G., Jackolski, C., and Williams, T. (2012). Pleistocene variability of Antarctic ice sheet extent in the Ross embayment. *Quatenary Sci. Rev.*, 34:93–112.

Meyer, C. R., Downey, A. S., and Rempel, A. W. (2018). Freeze-on limits bed strength beneath sliding glaciers. *Nature communications*, 9(1):3242.

Mondal, R., Benham, G., Mondal, S., Christodoulides, P., Neokleous, N., and Kaouri, K. (2019). Modelling and optimisation of water management in sloping coastal aquifers with seepage, extraction and recharge. *J. Hydrol.*, 571:471–484.

Morlighem, M., Rignot, E., Binder, T., Blankenship, D., Drews, R., Eagles, G., Eisen, O., Ferraccioli, F., Forsberg, R., Fretwell, P., et al. (2020). Deep glacial troughs and stabilizing ridges unveiled beneath the margins of the Antarctic ice sheet. *Nature geoscience*, 13(2):132–137.

Mouginot, J., Scheuchl, B., and Rignot, E. (2017). MEaSUREs Antarctic boundaries for IPY 2007-2009 from satellite radar, version 2.

Muszynski, I. and Birchfield, G. (1987). A coupled marine ice-stream–ice-shelf model. *Journal of Glaciology*, 33(113):3–15.

Neuhaus, S. U., Tulaczyk, S. M., Stansell, N. D., Coenen, J. J., Scherer, R. P., Mikucki, J. A., and Powell, R. D. (2021). Did Holocene climate changes drive West Antarctic grounding line retreat and readvance? *The Cryosphere*, 15(10):4655–4673.

Neuzil, C. (2012). Hydromechanical effects of continental glaciation on groundwater systems. *Geofluids*, 12(1):22–37.

Neuzil, C. E. and Provost, A. M. (2014). Ice sheet load cycling and fluid underpressures in the Eastern Michigan Basin, Ontario, Canada. *Journal of Geophysical Research: Solid Earth*, 119(12):8748–8769.

Otosaka, I. N., Shepherd, A., Ivins, E. R., Schlegel, N.-J., Amory, C., van den Broeke, M., Horwath, M., Joughin, I., King, M., Krinner, G., et al. (2022). Mass balance of the Greenland and Antarctic ice sheets from 1992 to 2020. *Earth System Science Data Discussions*, 2022:1–33.

Paster, A. and Dagan, G. (2007). Mixing at the interface between two fluids in porous media: a boundary-layer solution. *J. Fluid Mech.*, 584:455–472.

Pelle, T., Greenbaum, J., Ehrenfeucht, S., Dow, C., and McCormack, F. (2024). Subglacial discharge accelerates dynamic retreat of Aurora subglacial basin outlet glaciers, East Antarctica, over the 21st century. *Journal of Geophysical Research: Earth Surface*, 129(7):e2023JF007513.

Person, M., Bense, V., Cohen, D., and Banerjee, A. (2012). Models of ice-sheet hydrogeologic interactions: A review. *Geofluids*, 12(1):58–78.

Person, M., McIntosh, J., Bense, V., and Remenda, V. (2007). Pleistocene hydrology of north america: The role of ice sheets in reorganizing groundwater flow systems. *Reviews of Geophysics*, 45(3).

Peters, L. E., Anandakrishnan, S., Alley, R. B., Winberry, J. P., Voigt, D. E., Smith, A. M., and Morse, D. L. (2006). Subglacial sediments as a control on the onset and location of two Siple Coast ice streams, West Antarctica. *J. Geophys. Res.-Solid*, 111(B1).

Pittard, M., Galton-Fenzi, B., Roberts, J., and Watson, C. (2016). Organization of ice flow by localized regions of elevated geothermal heat flux. *Geophysical Research Letters*, 43(7):3342–3350.

Pollard, D. and DeConto, R. M. (2009). Modelling West Antarctic ice sheet growth and collapse through the past five million years. *Nature*, 458(7236):329–332.

Pritchard, H. D., Fretwell, P. T., Fremand, A. C., Bodart, J. A., Kirkham, J. D., Aitken, A., Bamber, J., Bell, R., Bianchi, C., Bingham, R. G., et al. (2025). Bedmap3 updated ice bed, surface and thickness gridded datasets for Antarctica. *Scientific data*, 12(1):414.

Reading, A. M., Stål, T., Halpin, J. A., Lösing, M., Ebbing, J., Shen, W., McCormack, F. S., Siddoway, C. S., and Hasterok, D. (2022). Antarctic geothermal heat flow and its implications for tectonics and ice sheets. *Nature Reviews Earth & Environment*, 3(12):814–831.

Rempel, A. (2008). A theory for ice-till interactions and sediment entrainment beneath glaciers. *Journal of Geophysical Research: Earth Surface*, 113(F1).

Rempel, A. W. (2009). Effective stress profiles and seepage flows beneath glaciers and ice sheets. *Journal of Glaciology*, 55(191):431–443.

Revil, A. and Cathles III, L. (1999). Permeability of shaly sands. *Water resources research*, 35(3):651–662.

Richardson, C., Davis, K., Ruiz-González, C., Guimond, J. A., Michael, H., Paldor, A., Moosdorf, N., and Paytan, A. (2024). The impacts of climate change on coastal groundwater. *Nat. Rev. Earth Environ.*, 5:1–20.

Robel, A., Sim, S., Meyer, C., Siegfried, M., and Gustafson, C. (2023). Contemporary ice sheet thinning drives subglacial groundwater exfiltration with potential feedbacks on glacier flow. *Science Advances*, 9(33):eadh3693.

Scambos, T. A., Berthier, E., and Shuman, C. A. (2011). The triggering of subglacial lake drainage during rapid glacier drawdown: Crane Glacier, Antarctic Peninsula. *Annals of Glaciology*, 52(59):74–82.

Schoof, C. (2005). The effect of cavitation on glacier sliding. *Proceedings of the Royal Society A: Mathematical, Physical and Engineering Sciences*, 461(2055):609–627.

Schoof, C. (2007a). Ice sheet grounding line dynamics: Steady states, stability, and hysteresis. *Journal of Geophysical Research: Earth Surface*, 112(F3).

Schoof, C. (2007b). Marine ice-sheet dynamics. Part 1. The case of rapid sliding. *Journal of Fluid Mechanics*, 573:27–55.

Schoof, C., Hewitt, I. J., and Werder, M. A. (2012). Flotation and free surface flow in a model for subglacial drainage. part 1. distributed drainage. *Journal of Fluid Mechanics*, 702:126–156.

Schoof, C. and Mantelli, E. (2021). The role of sliding in ice stream formation. *Proceedings of the Royal Society A*, 477(2248):20200870.

Seiner, O., Hugney, A., Seroussi, H., and MacGregor, J. A. (2025). A synthesis of the basal thermal state of the Antarctic ice sheet. *Journal of Glaciology*, pages 1–30.

Seroussi, H., Nowicki, S., Simon, E., Abe-Ouchi, A., Albrecht, T., Brondex, J., Cornford, S., Dumas, C., Gillet-Chaulet, F., Goelzer, H., et al. (2019). initMIP-Antarctica: an ice sheet model initialization experiment of ISMIP6. *The Cryosphere*, 13(5):1441–1471.

Seroussi, H., Pelle, T., Lipscomb, W. H., Abe-Ouchi, A., Albrecht, T., Alvarez-Solas, J., Asay-Davis, X., Barre, J.-B., Berends, C. J., Bernales, J., et al. (2024). Evolution of the antarctic ice sheet over the next three centuries from an ismip6 model ensemble. *Earth's Future*, 12(9):e2024EF004561.

Seroussi, H., Verjans, V., Nowicki, S., Payne, A. J., Goelzer, H., Lipscomb, W. H., Abe-Ouchi, A., Agosta, C., Albrecht, T., Asay-Davis, X., et al. (2023). Insights into the vulnerability of Antarctic glaciers from the ISMIP6 ice sheet model ensemble and associated uncertainty. *The Cryosphere*, 17(12):5197–5217.

Shoemaker, E. (1986). Subglacial hydrology for an ice sheet resting on a deformable aquifer. *Journal of Glaciology*, 32(110):20–30.

Siegert, M. J., Kulessa, B., Bougamont, M., Christoffersen, P., Key, K., Andersen, K. R., Booth, A. D., and Smith, A. M. (2018). Antarctic subglacial groundwater: a concept paper on its measurement and potential influence on ice flow. *Geol. Soc. Spec. Publ.*, 461(1):197–213.

Siegfried, M. R., Fricker, H. A., Carter, S. P., and Tulaczyk, S. (2016). Episodic ice velocity fluctuations triggered by a subglacial flood in West Antarctica. *Geophysical Research Letters*, 43(6):2640–2648.

Smith, A. M., Jordan, T. A., Ferraccioli, F., and Bingham, R. G. (2013). Influence of subglacial conditions on ice stream dynamics: Seismic and potential field data from Pine Island Glacier, West Antarctica. *Journal of Geophysical Research: Solid Earth*, 118(4):1471–1482.

Smith, B., Fricker, H. A., Gardner, A. S., Medley, B., Nilsson, J., Paolo, F. S., Holschuh, N., Adusumilli, S., Brunt, K., et al. (2020). Pervasive ice sheet mass loss reflects competing ocean and atmosphere processes. *Science*, 368(6496):1239–1242.

Sommers, A., Rajaram, H., and Morlighem, M. (2018). SHAKTI: Subglacial Hydrology and Kinetic, Transient Interactions v1.0. *Geoscientific Model Development*, 11(7):2955–2974.

Stål, T., Reading, A. M., Halpin, J. A., and Whittaker, J. M. (2021). Antarctic geothermal heat flow model: Aq1. *Geochemistry, Geophysics, Geosystems*, 22(2):e2020GC009428.

Stearns, L. A., Smith, B. E., and Hamilton, G. S. (2008). Increased flow speed on a large East Antarctic outlet glacier caused by subglacial floods. *Nature Geoscience*, 1(12):827–831.

Stone, D., Clarke, G., and Ellis, R. (1997). Inversion of borehole-response test data for estimation of subglacial hydraulic properties. *Journal of Glaciology*, 43(143):103–113.

Tankersley, M., Horgan, H., Siddoway, C., Caratori Tontini, F., and Tinto, K. (2022). Basement topography and sediment thickness beneath Antarctica's Ross ice shelf. *Geophysical Research Letters*, 49(10):e2021GL097371.

Tsai, V., Stewart, A., and Thompson, A. (2015). Marine ice-sheet profiles and stability under Coulomb basal conditions. *Journal of Glaciology*, 61(226):205–215.

Tulaczyk, S., Kamb, W., and Engelhardt, H. (2000a). Basal mechanics of ice stream B, West Antarctica: 1. Till mechanics. *Journal of Geophysical Research: Solid Earth*, 105(B1):463–481.

Tulaczyk, S., Kamb, W., and Engelhardt, H. (2000b). Basal mechanics of Ice Stream B, West Antarctica: 2. Undrained plastic bed model. *Journal of Geophysical Research: Solid Earth*, 105(B1):483–494.

Van Duijn, C. and Peletier, L. A. (1992). A boundary-layer problem in fresh-salt groundwater flow. *Q.J. Mech. Appl. Math.*, 45(1):1–24.

Venturelli, R., Siegfried, M., Roush, K., Li, W., Burnett, J., Zook, R., Fricker, H., Priscu, J., Leventer, A., and Rosenheim, B. (2020). Mid-Holocene grounding line retreat and readvance at Whillans Ice Stream, West Antarctica. *Geophys. Res. Lett.*, 47(15):e2020GL088476.

Venturelli, R. A., Boehman, B., Davis, C., Hawkings, J. R., Johnston, S. E., Gustafson, C. D., Michaud, A. B., Mosbeux, C., Siegfried, M. R., Vick-Majors, T. J., et al. (2023). Constraints on the timing and extent of deglacial grounding line retreat in West Antarctica. *AGU Adv.*, 4(2):e2022AV000846.

Wearing, M., Dow, C., Goldberg, D., Gourmelen, N., Hogg, A., and Jakob, L. (2024). Characterizing subglacial hydrology within the Amery ice shelf catchment using numerical modeling and satellite altimetry. *Journal of Geophysical Research: Earth Surface*, 129(4):e2023JF007421. e2023JF007421 2023JF007421.

Weertman, J. (1957). On the sliding of glaciers. *Journal of Glaciology*, 3(21):33–38.

Werder, M., Hewitt, I., Schoof, C., and Flowers, G. (2013). Modeling channelized and distributed subglacial drainage in two dimensions. *Journal of Geophysical Research: Earth Surface*, 118(4):2140–2158.

Werner, A. D., Bakker, M., Post, V. E., Vandenbohede, A., Lu, C., Ataie-Ashtiani, B., Simmons, C. T., and Barry, D. A. (2013). Seawater intrusion processes, investigation and management: Recent advances and future challenges. *Adv. Water Resour.*, 51:3–26.

Willeit, M., Ganopolski, A., Calov, R., and Brovkin, V. (2019). Mid-Pleistocene transition in glacial cycles explained by declining CO2 and regolith removal. *Sci. Adv.*, 5(4):eaav7337.

Zhang, Y., Moore, J., Zhao, L., Werder, M., Gladstone, R., and Wolovick, M. (2024). The role of hydraulic conductivity in the Pine Island Glacier's subglacial water distribution. *Science of The Total Environment*, 927:172144.

Zhou, Z., Wiens, D. A., Shen, W., Aster, R. C., Nyblade, A., and Wilson, T. J. (2022). Radial anisotropy and sediment thickness of West and Central Antarctica estimated from Rayleigh and Love wave velocities. *Journal of Geophysical Research: Solid Earth*, 127(3):e2021JB022857. e2021JB022857 2021JB022857.

Zoet, L. and Iverson, N. (2020). A slip law for glaciers on deformable beds. *Science*, 368(6486):76–78.